A Fundamental Investigation Into Electron Beam Induced Deposition

James Bishop

A thesis submitted to the Faculty of Science of the University of Technology Sydney in partial fulfilment of the requirements for the degree of:

Master of Science

University of Technology Sydney, Australia

June 2012

CERTIFICATE OF AUTHORSHIP/ORIGINALITY

I certify that the work in this thesis has not previously been submitted for a degree nor has it been submitted as part of requirements for a degree except as fully acknowledged within the text.

I also certify that the thesis has been written by me. Any help that I have received in my research work and the preparation of the thesis itself has been acknowledged. In addition, I certify that all information sources and literature used are indicated in the thesis.

Signed: Production Note:
Signature removed prior to publication.

Acknowledgments

First of all I would like send thanks to my supervisor Professor Matthew Phillips. The broad project proposal he created allowed minimal restrictions upon my research and also for his help in many areas and in the preparation of this thesis. I would also like to thank all the staff at the Microstructural Analysis Unit of UTS: Katie Mcbean, Mark Berkahn, Richard Wuhrer and Geoff McCredie for instruction with instrument usage and help in various areas. A special mention has to be given to Geoff McCredie, his help with construction of experimental apparatus and general workshop wizardry made the research possible. The ESEM cell was mostly his work and this project would not have succeeded without the equipment and apparatus which he created. Geoff taught me much about working metal and all things technical and the MAU surely could not function without him. Greg and Greg of the science workshop also provided much help with apparatus manufacturing and I would like to express my gratitude.

I would like to thank my fellow students at the MAU, Richard Crendal and Aiden Martin. Aiden deserves a special mention as he taught me much about electron microscopy, vacuum systems and experimental apparatus development. Aiden was instrumental in performing the upgrades to the XL30 ESEM and in constructing the excellent experimental apparatus which is described in the thesis. Aiden also performed the EDS compositional analysis on some of my experimental samples for me which added useful data to this thesis. It was a pleasure working with you guys and thankyou Richard for being my Australian correspondent whilst I was finishing this thesis from a dingy Spanish hotel room.

My two apprentices Chris Badawi and Douglas Gregory-Jones I would like to thank for some of the tedious work they did for me including the analysis of some experimental data. It also felt good to pass on the knowledge I have gathered and experimental procedures I developed over the course of this project concerning EBID experimentation.

I would like to thank Professor Charlene Lobo for help with EBID modelling work and creation of the main paper which was produced as a result of this project.

Above all I would like to thank Professor Milos Toth. The majority of the work of this thesis would not have been possible without the arrival of Milos at the MAU. The funding that was secured through an agreement with FEI company by the arrival of Milos at the MAU, allowed for the costly apparatus development. Milos has been an excellent role model for me as a scientist and has inspired me to want to become a scientist and make an impact in the world. Apart from that, Milos's expertise in the field of EBEID research and broad scientific knowledge allowed the maximum amount of data to be collected from each experiment. The project would surely have stumbled along blindly without help and direction from Milos.

The project was funded by the Australian Research Council (ARC) and FEI company. The ARC provided a grant which paid for my scholarship and FEI provided much of the equipment used for the research along with one of their best researchers. I would like to express gratitude to both FEI and the ARC.

TABLE OF CONTENTS

List of Figures

Chapter 1:

Chapter 2:

Chapter 3:

Chapter 4:

Chapter 5:

Chapter 6:

Appendix I:

Appendix II:

List of Commonly Used Acronyms

AFM – Atomic force microscopy.
AOCVD – Atomic oxygen induced chemical vapour deposition.
BSE – Backscattered electron.
CID – Collision induced desorption.
CIM – Collision induced migration (impact enhanced diffusion).
CIP – Collision induced processes.
CL – Cathodoluminescence.
CNT – Carbon nanotube.
CVD – Chemical vapour deposition.
D – Deposit.
DEAL – Digital electrostatic array lithography.
EBID – Electron beam induced deposition.
EBIE – Electron beam induced etching.
EBIED – Electron beam induced etching and deposition.
EBIH – Electron beam induced heating.
EBL – Electron beam lithography.
EDS – Energy dispersive x-ray spectroscopy.
EL – Electron limited.
ESD – Electron stimulated desorption.
ESEM – Environmental scanning electron microscope.
EUV – Extreme ultraviolet.
FE – Field emission.
FEBID – Focused electron beam induced deposition.
FEG – Field emission gun.
GIS – Gas injection system.
GSED – Gaseous secondary electron detector.
HIVAC – High Vacuum.
HV – High vacuum.
IC – Integrated circuit.
KE – Kinetic energy.
LAOCVD – Localised atomic oxygen induced chemical vapour deposition.
MFC – Mass flow Controller.
MTL – Mass transport limited.
NI – National Instruments.
ODP – Oil diffusion pump.
PBG – Photonic band-gap.
PD – Partially depleted.

PDS – Precursor delivery system.
PE – Primary electron.
PECVD – Plasma enhanced chemical vapour deposition.
PVP – Pre-vacuum pump.
RGA – Residual gas analysis.
RT – Room temperature (≈ 300 K).
S2N – Signal to noise (ratio).
SE – Secondary electron.
SEBIED – Simultaneous electron beam induced etching and deposition.
SEM – Scanning electron microscopy.
STEM – Scanning transmission electron microscopy.
STM – Scanning tunnelling microscopy.
TC – Thermocouple.
TEM – Transmission electron microscopy.
TEOS – Tetraethoxysilane.
TMP – Turbo molecular pump (high vacuum pump).
TPD – Temperature programmed desorption.
UHV – Ultra high vacuum.
UV – Ultraviolet.
UVPL – Ultraviolet photolithography.
VACNF – Vertically aligned carbon nanofibers.
VCR – Vacuum coupling radiation (High vacuum fittings).
XPS – X-ray photoelectron spectroscopy.

Symbols for Commonly Referred Parameters/Species

e^- – Electron.
T_s – Substrate temperature.
T_g – Gas temperature.
t_g – Growth time.
I_b – Electron beam current.
I_e – Emitted current.
I_t – Transmitted current.
P_T – Total pressure in cell.
P_{TEOS} – TEOS partial pressure.
P_{O2} – O_2 partial pressure.
$O^\cdot$ – Atomic oxygen (radical).
σ – Effective cross-section for electron induced dissociation.
D – Diffusion co-efficient.

τ – Residence time.

L_d – Mean diffusion length.

V_0 – Acceleration voltage.

Abstract:

Electron beam induced deposition (EBID) is a maskless, direct-write nanofabrication technique. It is capable of very high resolution and deposition of a wide variety of materials. It is a widely used technique for nanoprototyping and has several current applications in industry including the repair of photolithographic masks for integrated circuit (IC) production. Despite the widespread usage of EBID, the fundamental mechanisms which govern the process are not sufficiently well understood.

In this thesis, an experimental-based investigation is undertaken in order to obtain a greater understanding of fundamental factors which govern the EBIED process and particularly those factors not accounted for by current models of EBIED. A world-class and possibly unique experimental apparatus is developed which allows quantitative EBID experimentation. The conclusions reached demonstrate the importance of a previously neglected fundamental aspect of EBID: the adsorption kinetics of precursor molecules. The findings have significant importance for EBID and the sister technique of electron beam induced etching (EBIE).

The first chapter presents a thorough general background and introduction to electron beam induced etching and deposition (EBIED) and literature review with a focus on EBID. Chapter two discusses theoretical aspects of EBIED and current models. Chapter three is a record of the apparatus and experimental procedures which were developed and can be considered as a recipe for reliable EBID experimentation.

Experiments were performed as a function of substrate temperature in chapters four and five. The results which were not predicted by current models of EBID demonstrate the effect of activated chemisorption. A new model is developed which correctly predicts the generic temperature dependence of the EBID process. Activated chemisorption is found to allow simultaneous high purity and high growth rates of EBID deposits. FEBID at high T_s with TEOS precursor was found to result in complex unexpected growth and mechanisms involving diffusion, electron beam induced heating (EBIH) and charging are presented and discussed to explain this growth in chapter five.

Chapter six involves TEOS EBID with gas mixing. The growth rate was found to be significantly enhanced or suppressed with O_2 or Ar mixing respectively. A new mechanism (termed LAOCVD) is proposed to explain O_2 mediated purity and EBID rate enhancement with organosilane precursors as reported in literature and demonstrated by my results. The effects of EBID system parameters are characterised and explained in the appendix.

1. Introduction

1.1 Electron Beam Induced Deposition & Etching

Electron beam induced etching and deposition (EBIED) is a maskless lithography technique capable of creating nanoscale structures of a wide range of compositions. It is not a recently developed process, however the technique has only recently gained considerable attention and significant research initiated in the field. A major motivation for increasing research in EBIED is that the resolution limits of conventional methods of lithography and micro/nanofabrication (e.g. ultraviolet photolithography (UVPL) and electron beam lithography (EBL)) are starting to be realised. EBIED has the potential to be a useful technique for many research and manufacturing industries. Rapid, single-step, direct-write fabrication of micro/nanostructures of a wide range of compositions is the key advantage of EBIED over other lithography techniques. The major disadvantage (compared to other lithography techniques) is low throughput which currently restricts EBIED to prototyping applications.

Stewart [1] was the first to publish material concerning EBID in 1934 where he noted that insulating films were deposited upon a substrate under electron irradiation. He discovered that these insulating films were carbonaceous and concluded that they were formed by polymerisation of residual organic vapours in the vacuum chamber by the electron beam. Such “contamination” deposition has long been considered the bane of electron microscopy as residual organic vapours are generally present in most vacuum systems. Much technology has since been developed to minimise the amount of residual hydrocarbon vapours present in a vacuum chamber including oil free high-vacuum pumping systems such as the scroll pump and magnetically levitated turbo-molecular pump (TMP), as well as high-vacuum cleaning techniques such as radio frequency plasma cleaning systems. Contamination deposition due to residual organic vapours remains a significant issue in all forms of scanning electron microscopy (SEM). Contamination deposition continually forms an amorphous carbon film during imaging, lowering practical resolution and contrast, as well as total secondary electron (SE) and backscattered electron (BSE) signal yield. SEM based analysis techniques such as energy-dispersive x-ray spectroscopy (EDS) and cathodoluminescence spectroscopy

(CL) suffer heavily at high chamber contamination levels. With much care concerning what is placed into the SEM, coupled with cleaning techniques contamination deposition can be minimised.

It was not until the 1960's that EBID was considered as a potential technique for the intentional deposition and fabrication of micro and nanoscale structures of various compositions. The first in-depth EBID experimentation work was performed by Cristy [2] and Baker *et al.*[3]. Cristy was the first to characterise carbonaceous deposition including the formulation of an expression to describe EBID growth rates with respect to deposition parameters. Baker *et al.* deposited bulk metallic films via the decomposition of various organometallic precursors demonstrating for the first time that EBID could potentially be used to deposit functional materials. The 1970's, 80's and 90's then saw a steady increase in experimental work to investigate the feasibility of EBID as a direct write micro/nanofabrication technique. Deposits of metallic [3], semiconducting [4, 5], insulating [7, 8] and carbonaceous [9, 10] materials were fabricated in modified SEM's. As a result EBID was confirmed as a promising potential technique for maskless nanoprototyping.

A simple description of the EBID and electron beam induced etching (EBIE) process can be stated as thus: gaseous precursor molecules which contain the atomic and molecular species of interest for deposition are injected into a vacuum chamber and adsorbed upon a substrate surface. Electron beam irradiation is used to dissociate the adsorbates (only at and near the beam impact point) into volatile and non-volatile fragments. In the case of deposition (EBID), volatile fragments are desorbed and leave the substrate while the non-volatile component/s bond to the substrate forming a deposit. For the case of etching, reactive species created by precursor dissociation react with the substrate to form volatile components which subsequently desorb thus giving rise to substrate etching.

Potential applications for EBIED are many and varied. One of the most important and promising applications to date is in the repair of UV photomasks used in integrated circuit (IC) fabrication. Small defects in these masks are common during fabrication and/or use. Tolerance for defects is very low and can result in faulty IC

devices. Furthermore, these masks are very expensive to manufacture and thus an optimised repair process is desirable. EBIED is currently used commercially for this purpose and some companies are now manufacturing and selling EBIED UV photomask repair systems [10].

Despite the use of EBIED in industry, considerable research is still needed to understand the EBIED process. A common material used for transparent regions of UV photomasks is SiO_2. EBID and EBIE of SiO_2 is therefore of particular interest for mask repair [11]. EBID of SiO_2 could also be useful for deposition of dielectric, insulating layers and structures in IC's [12]. Other applications of EBIED include: fabrication of nanoscale functional structures such as field emission devices [13], production of nanoparticles of various compositions [14], fabrication of super-sharp atomic force microscopy (AFM) tips [15], fabrication of interconnects for IC's [16] and as an adherent (amorphous carbon deposition) to selectively immobilise nanoparticles or nanofibers to substrates [17].

EBIED research has been sparsely ongoing for decades. However, due to the inherent complexity of the process coupled with a lack of standardised experimental methods and instrumentation between EBIED research groups, technology in the field has been slow to develop. Development of a complete model of EBIED remains an important goal and much research is needed for the potential of the technique to be realised.

1.2 Experimental Setups for EBIED Research

a. Gas Injection System (GIS)

There are two main experimental configurations for performing EBIED experiments. The most commonly used and least expensive setup involves the addition of a Gas Injection System (GIS) to a standard SEM. A crucible holds the precursor which can be gaseous, liquid or solid as long as it has a high enough vapour pressure to provide a sufficient flow rate of precursor molecules to a substrate. Precursor vapour is delivered into an SEM chamber via a thin needle which is positioned close (typically < 0.5 mm) to the substrate surface. The flow rate is typically controlled by varying the crucible temperature while that of high vapour pressure liquids and solids is often

reduced by a mass flow controller (MFC) or needle valve. The microscope chamber is pumped to high vacuum to minimise the amount of residual impurities such as water and hydrocarbon vapours. Plasma cleaning and baking of the sample is recommended before deposition to further minimise non-precursor residual gases. The needle-sample geometry results in localised region of higher pressure at the substrate surface and the corresponding pressure distribution can be estimated via a simple mathematical model [18]. Disadvantages of this configuration (when compared to other EBIED configurations) include: a varying pressure distribution at the substrate surface which can be important when depositing large structures such as horizontal lines and area depositions, a lower level of control of precursor gas composition than the ESEM cell configuration, minimal charging compensation and lower workable precursor partial pressure.

b. ESEM EBIED

Environmental scanning electron microscopy (ESEM) in which gas fills the SEM chamber (typically 0.1 – 10 torr) and gas cascade amplification is used for the imaging signal [19] can also be used for EBIED. An external precursor delivery system (PDS) configured for higher flow rates than a GIS is attached to the ESEM and used to fill the chamber to a certain pressure with precursor gas. Maximum pressures as high as 10 torr can be used with some ESEM differential pumping systems. This configuration ensures a uniform precursor pressure over the entire substrate surface. Charging compensation by the gas ionisation cascade is beneficial as charging during EBIED can cause beam drift amongst other undesirable effects. An ESEM detector is a simple anode with positive bias (typically 50 – 500 V) which is also beneficial as it is less susceptible to damage by precursor gases than high vacuum detectors. The major disadvantage of the ESEM configuration for EBIED study is the low level of control over unwanted residual gases present in the ESEM chamber during EBIED. The proportion of residual gases is higher with ESEM EBIED than with GIS setups. Precursor consumption is also much higher. Plasma cleaning can minimise residual hydrocarbon vapours but residual air incorporation is problematic due to the slow pumping speed

of the chamber during ESEM EBIED (roughing pump only due to the large gas volumes involved).

c. "ESEM Cell" EBIED Sub-Chamber

A sub-chamber within a high vacuum SEM chamber can overcome many of the limitations inherent to ESEM EBIED whilst maintaining the benefits of ESEM. The sub-chamber is connected directly to the external gas injection system via feed-throughs in SEM blanking plates. This configuration is known as the "ESEM cell". It can be installed in a standard SEM or ESEM. ESEM level pressures (0.05 – 10 torr) can be maintained inside the cell while the SEM chamber outside the cell is pumped to high vacuum. An aperture of 50 – 500 µm in the top of the cell admits the electron beam. The large negative pressure differential from the sub-chamber to SEM chamber inhibits the diffusion of residual gases into the cell ensuring the highest possible purity of precursor gas. The benefits of ESEM such as charge compensation, high precursor pressure and gas ionisation cascade imaging can be utilised whilst maintaining high precursor gas purity.

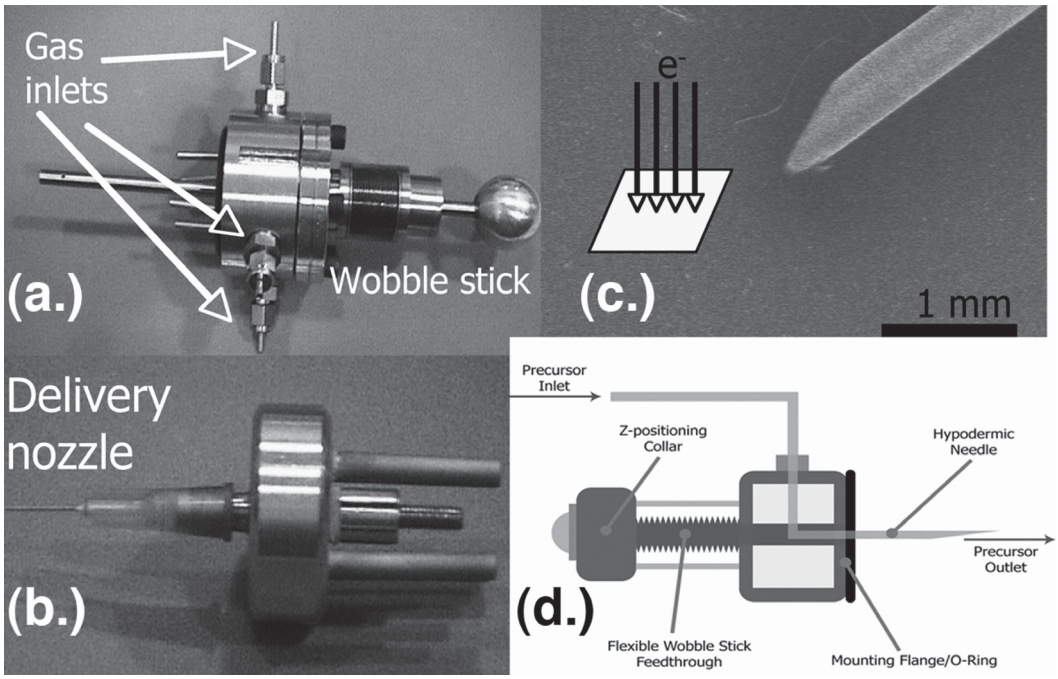

Figure 1.1: (a.): *GIS feed-through piece.* ***(b.):*** *Delivery nozzle.* ***(c.):*** *SEM image of injection needle close to substrate. (****d.):*** *Schematic of GIS. Schematic and images from Randolph et al. [20].*

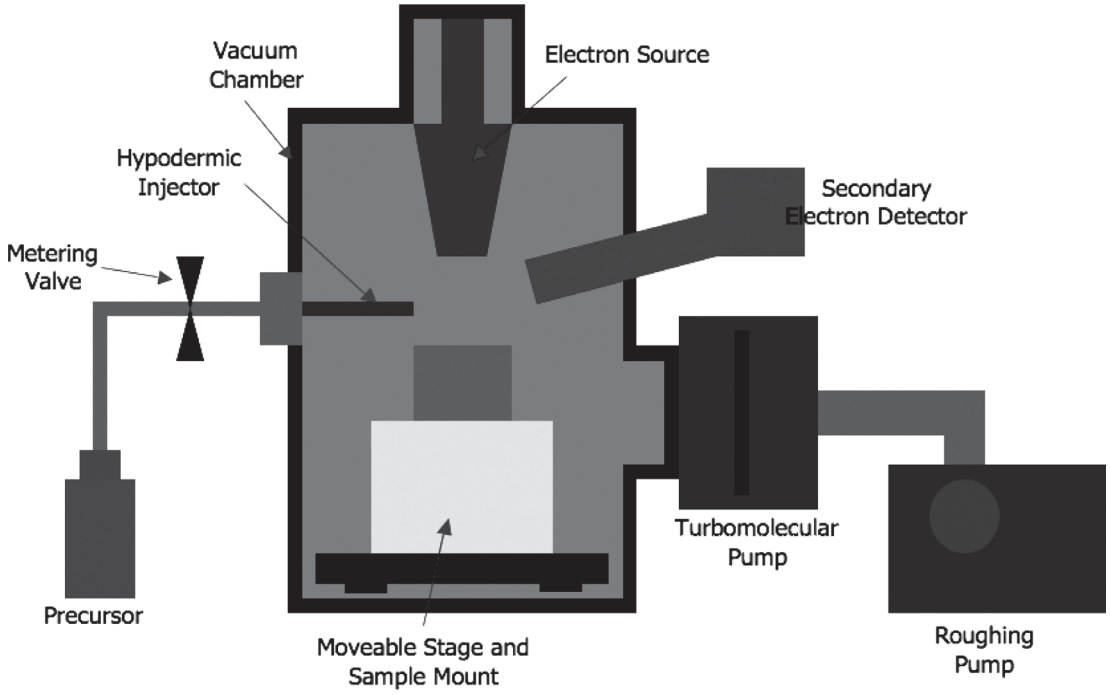

Figure 1.2: *Schematic showing a simple version of the Gas Injection System to perform EBIED experiments. The only modification to the microscope is the attachment of the GIS. Randolph et al. [20].*

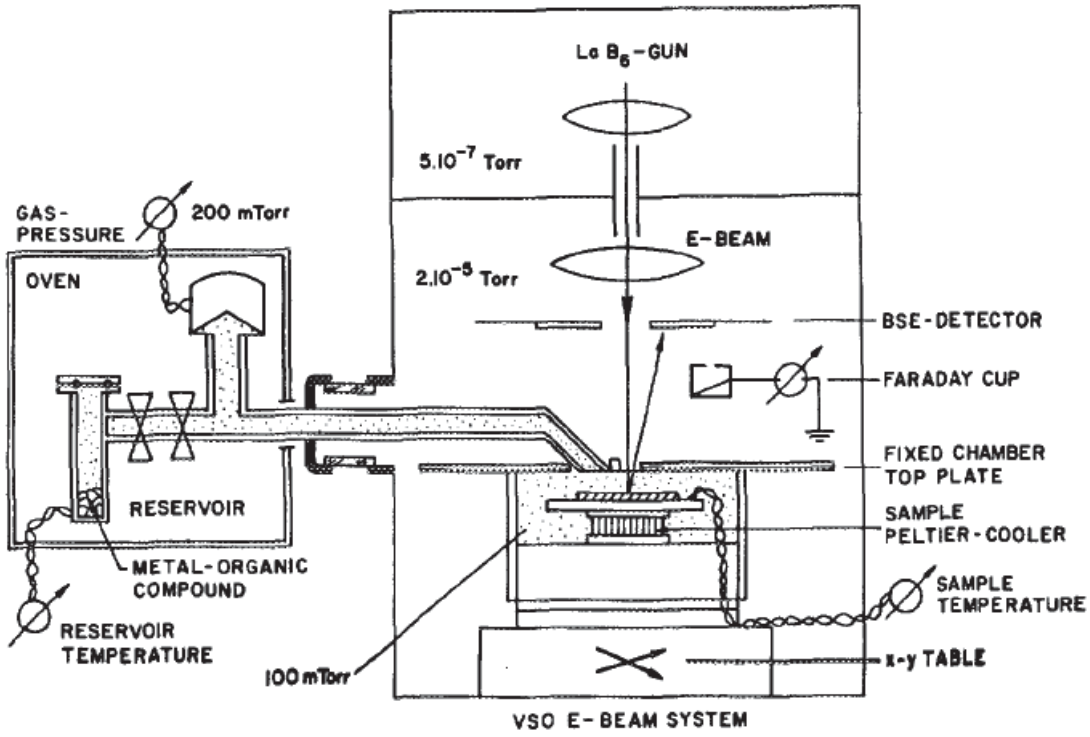

Figure 1.3: *Schematic showing an early example of an ESEM cell EBIED sub-chamber from [21].*

d. Other Experimental Configurations for EBIED Study

Generally a modified SEM or ESEM is used for the study of EBIED. However, any electron source can be used for EBIED. Transmission Electron Microscopy (TEM) has been used for several EBID studies [22]. Deposits with diameters < 1 nm have been created on thin substrates using extremely small diameter electron beams only achievable with the high acceleration voltages (50 – 300 kV) used in TEM. Scanning Transmission Electron Microscopy (STEM) [23], Scanning Tunnelling Microscopy (STM) [24] and electrostatic field emission (FE) sources [25] have all been used as electron sources for EBID. Other EBIED configurations such as those mentioned above have not been extensively studied and a modified SEM or ESEM remains the most common experimental configuration for EBIED study. The large chamber size, acceleration voltage and beam current range as well as in-situ imaging immediately after deposition, are some of the advantages of SEMs and ESEMs for EBIED experimentation.

1.3 The EBIED Process

As was mentioned briefly in section 1.1, the EBIED process involves the electron induced dissociation of gaseous precursor molecules adsorbed to a substrate into volatile and non-volatile fragments. Dissociation and ionisation of precursor molecules will also occur in the gas phase but do not directly contribute to the EBIED process. EBIED can be described as analogous to a localised chemical vapour deposition (CVD) process. In CVD, thermal energy causes the dissociation of precursor molecules adsorbed to a heated substrate causing the deposition of a film over the entire substrate. Since the energy is supplied thermally, predictions of dissociation kinetics can be easily made as molecular bond strengths can be correlated to available thermal energy (kT). With EBIED, the energy for precursor dissociation is supplied by primary (PE), secondary (SE) and backscattered (BSE) electrons. There is some debate [26] as to which electron species are responsible for the majority of the EBIED process but generally SEs (< 50 eV) are assumed to fulfil this role [27]. This assumption is based upon e^- dissociation cross-sectional data which is available in the literature for a few of the precursors used for EBIED. Electron dissociation cross sections generally peak

below 50 eV for the molecules used in EBIED for which e^- dissociation cross-sectional data is available [28].

Due to the broad range of electron energies incident upon and emitted by a substrate under e^- irradiation, all bonds of a precursor molecule can be broken during EBIED. This results in many different fragment species after dissociation. Some of these species may be unstable and react further. Furthermore, the ratio of volatile reaction products to total gas pressure in chamber is generally very low (as the amount of total precursor dissociated by e^- beam is small) and as a result techniques like residual gas analysis (RGA) which are useful in CVD analysis, do not work. These factors make the EBIED process significantly more complex than the CVD process, thus creating difficulties in understanding EBIED reaction mechanisms and for accurate modelling.

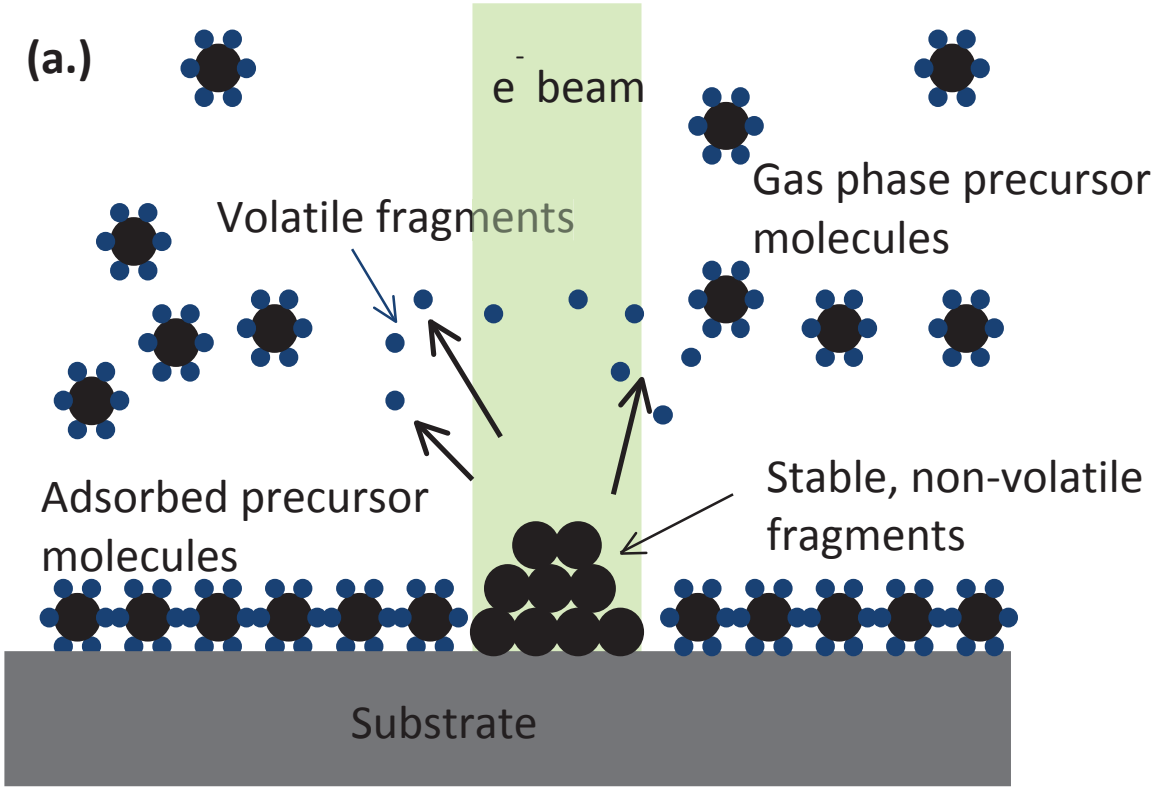

Figure 1.4: *Simple illustrations representing the EBIED process.* ***(a.):*** *Electron beam induced deposition (EBID). (****(b.)*** *next page): Electron beam induced etching (EBIE).*

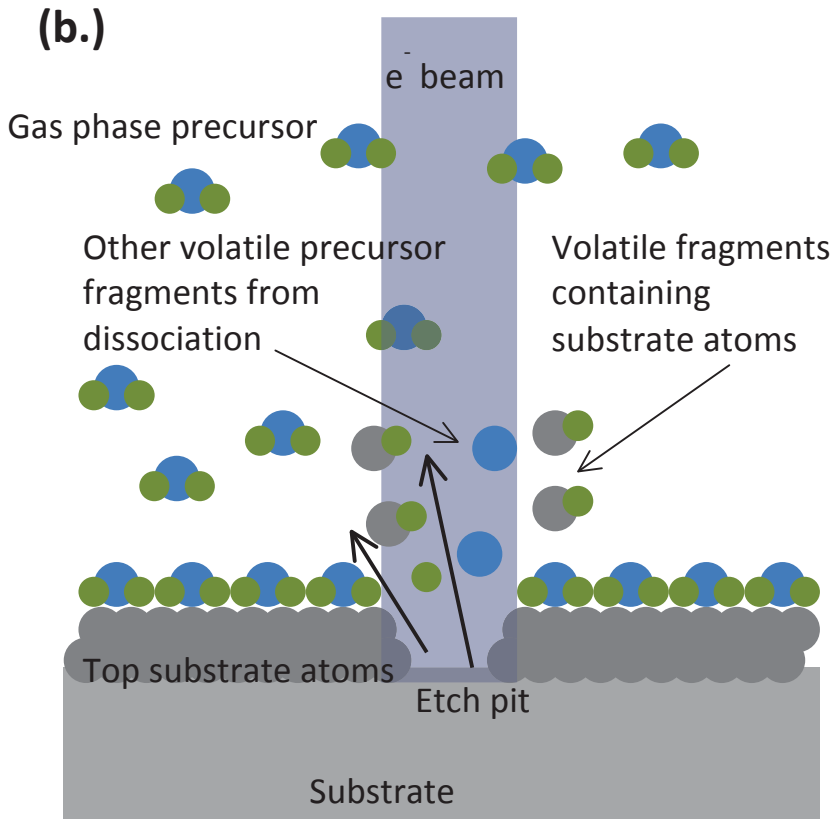

1.4 Current EBID Research

Research in the field of electron beam induced etching and deposition (EBIED) has increased significantly in the last decade. Advances in other fields of nanotechnology have fuelled increasing interest in EBIED research. It has much potential as a complementary technique for nanofabrication processes. The major research areas of interest for EBID are: Developing techniques to deposit high purity material, increasing resolution of EBID processes and increasing throughput of EBID processes.

High Purity EBID

The EBID process results in deposits composed of the atoms of gaseous molecules present in the chamber, which will include the precursor gas and any contaminants present such as residual hydrocarbons. Generally the element/s of

interest for deposition exist in a minority atomic ratio in the precursor molecule, e.g W from WF_6 or SiO_2 from $Si(OC_2H_5)$. Developing methods to create high purity deposits by EBID is one of the main goals of EBID research. Repairing/writing interconnects in integrated circuits is an example of an application for which high purity metallic EBID would be necessary. For an extensive literature review on this topic see [44]. EBID parameters and processes which can be applied that affect the final purity of EBID deposits include:

Precursors

The first step that must be taken to achieve EBID deposits of favourable purity is to start with a very clean microscope chamber, precursor injection lines and substrate. Plasma, cleaning, heating of gas lines and substrate and pumping with an oil-free high-vacuum pumping system for days to achieve best possible vacuum conditions is essential to eliminate as much residual contaminant vapours from the deposition chamber as possible prior to insertion of precursor in order to maintain purity of precursor gas.

Vapour pressure and toxicity, as well as composition are important considerations when choosing EBID precursors. A precursor must contain the target element/s desired for deposition (EBID) and the less other atoms present on the molecule the better. The vapour pressure of the molecule must be high enough to provide a reasonable flow of precursor molecules (higher pressures are needed for ESEM EBID than for the GIS setup). If an EBIED precursor is toxic the equipment required to limit exposure to humans will increase cost and lower throughput.

The most common EBID precursors are organometallics. These are organic-metal complexes that contain the target EBID metal atom bonded to a number of organic ligands. They are used more for their favourable vapour pressures, low toxicity, availability and low cost rather than for the composition of EBID deposits which they produce. Typical structures of EBID deposits from these precursors consist of nanocrystals of the desired metal dispersed in an amorphous carbon matrix [45]. Compositions are typically around 70 atomic % C. The precursor tetraethoxysilane

(TEOS) is the main precursor used in this work and is an organosilane. Organosilanes are Si analogues of organometallics.

Inorganic precursors which contain no carbon such as tungstenhexafluoride (WF_6) [46] or Tetrakis (triflurophosphine)platinum($F_{12}P_4Pt$) [47] are good precursors for achieving higher purity deposits by EBID. Tetrakis(triflurophosphine)platinum for example, can result in EBID deposits of 90 % platinum without further purification [47]. These precursors also have some disadvantages, namely their higher cost (($F_{12}P_4Pt$) ≈ $1500 for 5g) and incorporation of inorganic impurities in the deposit.

In-situ Purity Enhancing Techniques

Some techniques can be applied in-situ during deposition to increase the purity of material being deposited. Deposition on a heated substrate can lower the incorporation of organic species in EBID deposits generally at the cost of a lower growth rate [53]. The addition of reactive gases such as O_2, N_2O, H_2 or H_2O can be very effective in increasing the purity of deposits. O_2, H_2O or N_2O (i.e. an oxidant) mixing during EBID has been shown to minimise or even eliminate C incorporation [48]. Higher beam currents during deposition are generally reported to improve purities of deposits. Optimisation of EBIED parameters for maximum purity is a very active area of EBIED research.

Ex-situ Purification techniques

Ex-situ processing can be applied after deposition to remove some impurities from EBID deposits. Annealing in vacuum or in an atmosphere such as O_2 or H_2 has been reported to remove carbon and inorganic impurities from deposits [44]. Large shrinkage and deformation can occur if the deposit has a large amount of impurity to begin with. Treatment with oxygen or hydrogen plasmas can also remove impurities. Many groups have experimented with various ex-situ heat and plasma treatments in order to remove impurities from deposits [10]. It is likely that the mechanism of impurity removal is similar for both annealing in reactive atmosphere or plasma treatment .Reactive radicals are formed by dissociative adsorption or electron dissociation of the purification gas which form volatile species such as CO, CO_2 or CH_4 when reacting with embedded impurities. The same mechanism would likely be active

during in-situ contaminant removal by gas mixing and/ or heat treatment. Botman *et al.* [52] used a flux of hydrogen radicals to remove inorganic impurities from Pt EBID deposits. They found dense, pure Pt was formed but only to a depth of 30 nm which they suggested was the penetration depth of the H radicals.

EBID Resolution Limits

The diameter of deposits created by EBID is always greater than that of the electron beam diameter. SEs and BSEs will be emitted from the substrate/EBID deposit over the whole of the interaction volume. Thus the factor which limits the maximum resolution of the EBIED process is the radial distance (from the beam axis) where backscattered and secondary electrons excited by the beam cross the substrate/vacuum interface. This is determined by the diameter of the primary beam and the size of the interaction volume within the substrate which is itself determined by the energy of the electrons in the primary beam.

Deposits with diameters as small as 1 nm have been made by various groups [49]. The ability to create features of sub 10 nm diameter is one of the main advantages of EBID as a nanofabrication technique. If pure semiconductors can be deposited it could enable direct writing of quantum confined structures. To create such small structures high energy beams around 200 – 300 kV have been used to achieve sub nm beam diameters with thin (< 50 nm) substrates to limit the radial distance to which backscattered and secondary electrons leave the substrate surface. Simulations have been developed [49] to predict the achievable resolution for a given set of beam and substrate parameters. Since high accelerating voltages are needed for small beam diameters and interaction volumes are large for high accelerating voltages, thin substrates in a TEM are the best way thus far to create the smallest diameter EBID deposits.

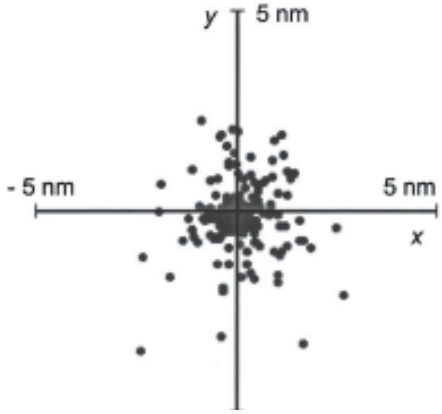

Figure 1.5: *Monte-Carlo simulation showing positions of electrons emitted from a surface. A point source electron beam at 20 kV was modelled. Even with an electron beam of zero diameter, SEs and BSEs are emitted up to 5 nm away from the beam axis. Maximum resolution of the deposits would be ≈ 5 nm. From [49]*

EBIED Process Throughput

The major disadvantage of EBIED as a nanofabrication technique is the low throughput of the process. With a single electron beam only one feature can be created at a time which limits EBIED to prototyping and repair applications. One possible path to high throughput EBIED is multiple electron beam array systems. Several groups are developing such systems for a process called digital electrostatic electron beam array lithography (DEAL) [50, 51]. The concept behind DEAL is the creation a dense array of millions of nanoscale field emission electron sources on a single chip. Integrated electrostatic lenses would focus the beams. The EBID process would be performed by millions of beams simultaneously to directly write millions of features to the surface of a substrate. Multiple electron beam systems such as DEAL are a very promising avenue of research and could make the EBIED process a viable manufacturing technique for the fabrication of devices such as integrated circuits. However, such systems are still in the early development stages.

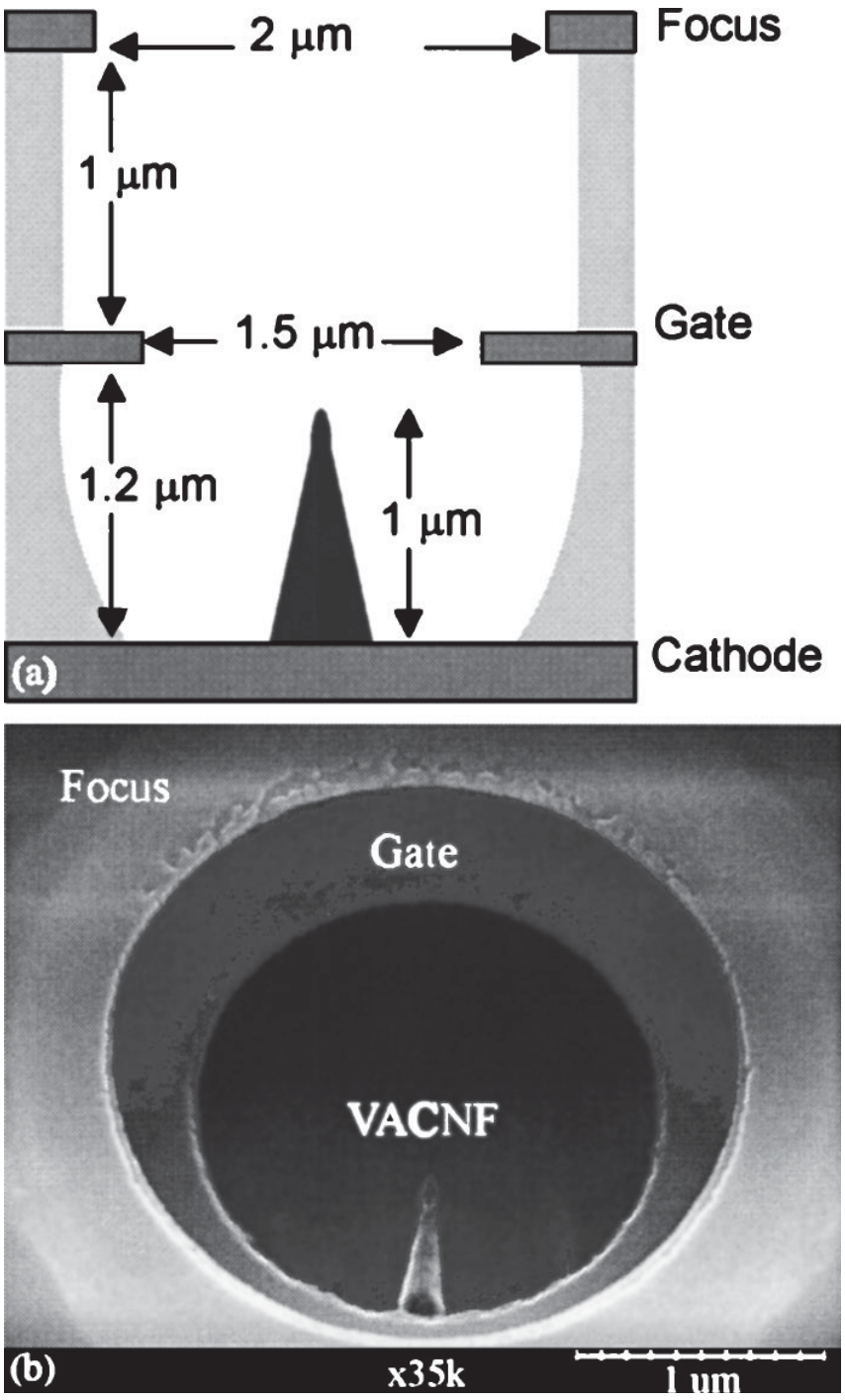

Figure 1.6: *Schematic and SEM image of one FE electron source in a prototype DEAL system. A vertically aligned carbon nanofiber (VACNF) forms the cathode and a Mo focus electrode electrostatically focuses the beam. From [51].*

1.5 Industry Potential and Practical Applications of EBIED

Mask Repair

EBIED is currently used by some integrated circuit (IC) manufacturers for the repair of UV photolithography masks. The masks are expensive and time consuming to fabricate and defects can render them useless. Ion-beam induced deposition is often used for mask repair although the implantation of ions into the mask can be a significant problem. UV opaque materials deposited by EBID such as amorphous carbon can suffice to repair certain defects on a mask and without the problem of ion implantation. Other kinds of defects can be repaired using EBIE techniques [10]. Chemical means have previously been the industry standard for mask repair. Extreme ultraviolet masks (EUV) have smaller, more delicate features and it has been shown that conventional techniques do not suffice for repair [10]. A commercially available system for mask repair utilising EBIED and IBID has been developed by Zeiss [10].

Figure 1.7: *The Carl Zeiss SMS MeRiT HR 32 UV photomask repair instrument. From [10].*

The deposition of UV and EUV transparent materials is also of high importance to mask repair. Pure SiO_2 is a likely material. EBID of pure SiO_2 has been

achieved with various organosilane precursors including TEOS [48] and has shown suitable EUV transmission to be applied to mask repair.

Other Applications for EBIED

EBID has been used to deposit metals like gold and platinum of high enough purity to serve as interconnects in micro-circuits [52, 16]. Amorphous carbon deposited by EBID has been shown to have powerful adhesive properties and has been used as an adherent to immobilise nanofibers, CNTs and nanoparticles to substrates [55]. EBID has also shown potential as a means for depositing catalytic materials to enable seeded CVD growth [56]. Periodic structures for optical applications such as a photonic band gap structure have been created purely by EBID [57]. A nanoparticle separator prototype device for micofluidic applications was recently created by Rack *et al.* utilising EBID [58]. Very sharp, high aspect ratio AFM tips have been created and have demonstrated excellent performance and ability to map very small sharp features due to their high-aspect ratio [59]. Many complex nanosized 3D objects have been created by various groups including a nanosized topographical world map, a DNA shaped and sized helix pattern and even a nanoscopic wineglass [60]. EBIED as a nanoprototyping technique is gaining considerable attention around the world.

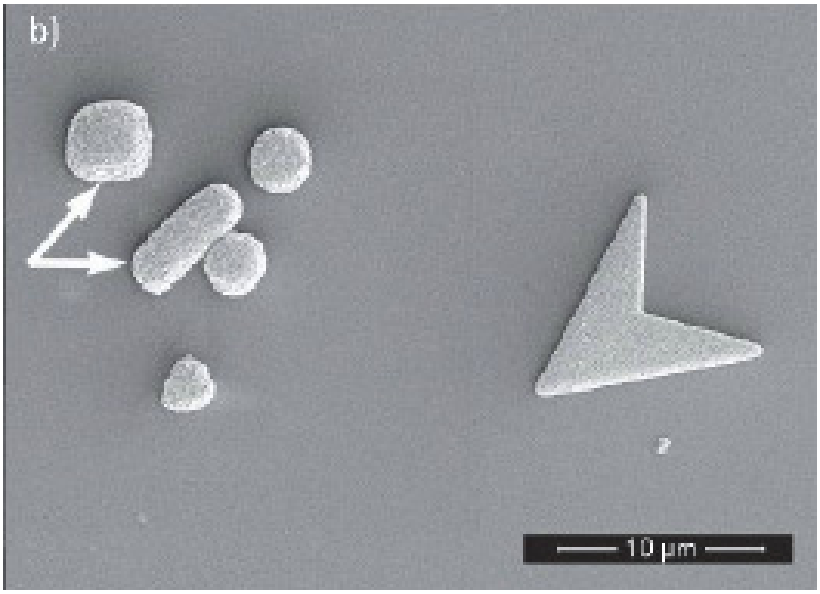

Figure 1.8: *High purity cobalt produced by seeded CVD of $Co_2(CO)_8$. The thermal decomposition of the precursor is catalysed by an EBID deposited amorphous carbon seed layer and the thermal decomposition temperature is lowered [56]. The cobalt grows only in the pre-seeded regions.*

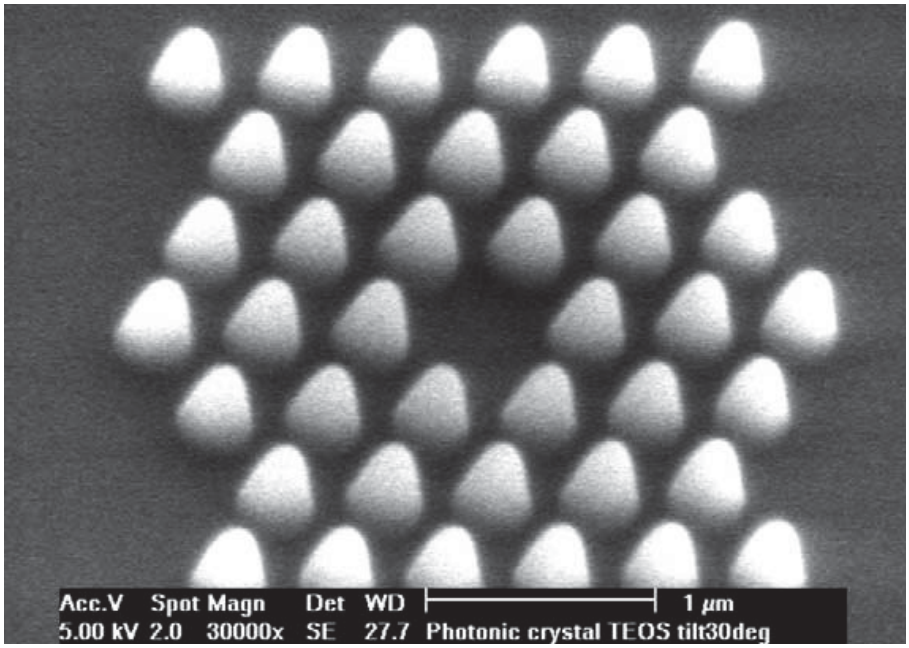

Figure 1.9: *Photonic band-gap (PBG) structure created by EBID with TEOS/O_2 precursor mix. Deposits are transparent and suitable for optical applications [57].*

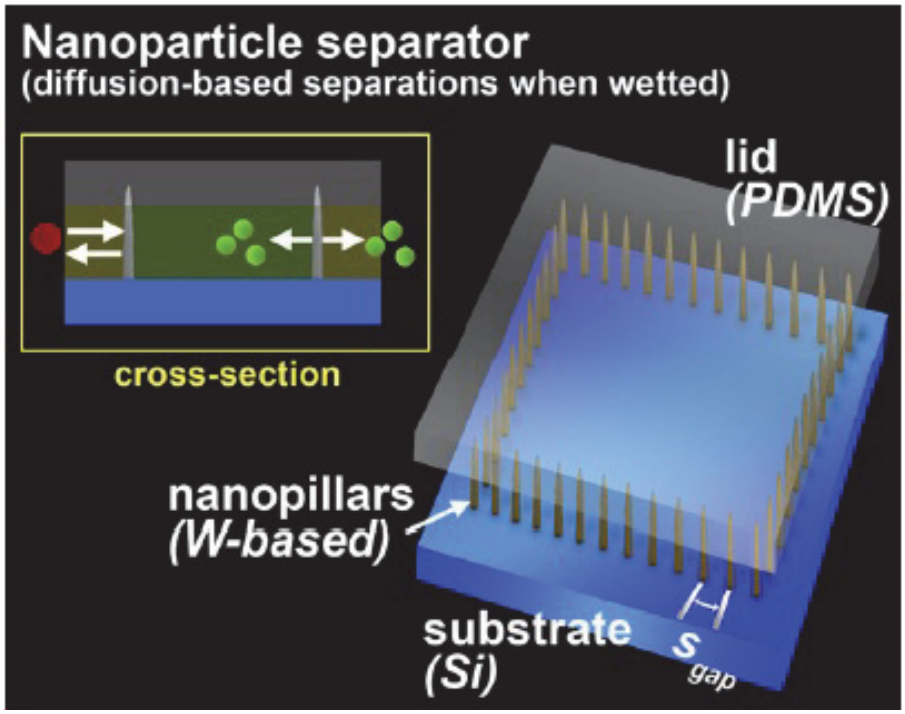

Figure 1.10: *Schematic of nanoparticle separator prototype device for microfluidic applications. The nanopillars are created by EBID with WF_6 precursor and particles larger in diameter than the gap size s do not pass the wall of pillars [58].*

Another very promising potential application for EBID is in the creation of nanoscale field emission (FE) devices. Nanoscale FE electron sources have been fabricated purely by EBID and shown good performance [61, 62]. It has been suggested that EBID could be a "self-sustaining" technology for FE device fabrication. Arrays created by EBID in a format similar to the DEAL system could perform parallel EBID to create even more massive arrays.

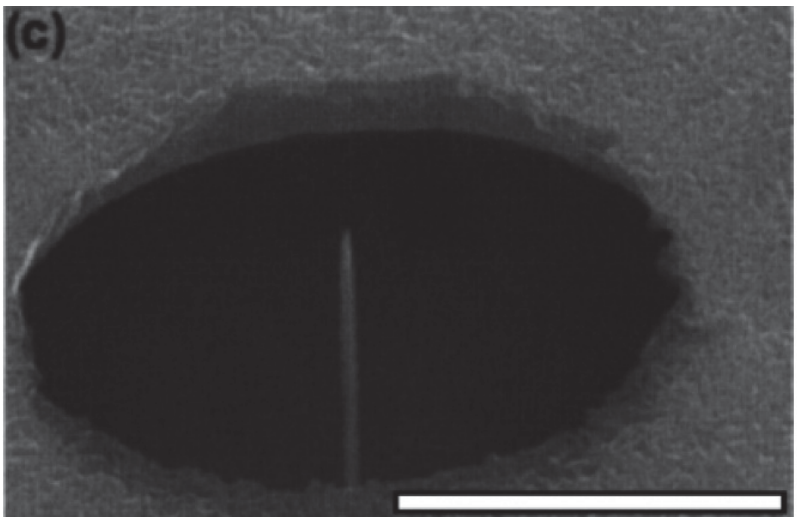

Figure 1.11: *SEM Image of a nanoscale gated-cathode field emission device made by EBID deposition of emitter inside aperture etched by ion beam sputtering [61].*

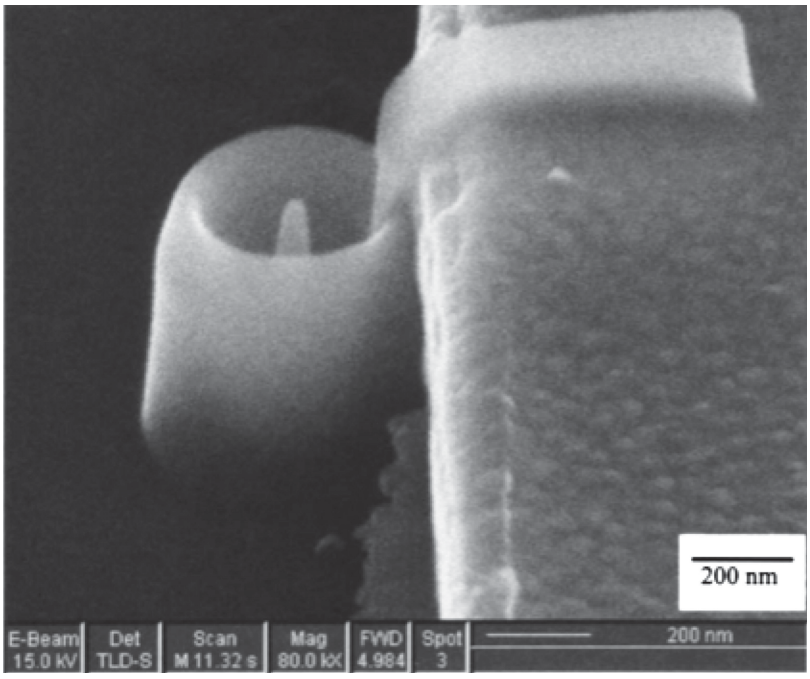

Figure 1.12: *Nanoscale field emission device fully fabricated by EBID [62]*

1.6 Motivation for the Research of This Thesis

The sections above should provide the reader with a satisfactory introduction to the EBIED process. A brief literature review is included to outline the major EBID research areas as well as the currently used and potential applications of the technique for industry. The use of EBIED in industry is highly developed for certain applications and has seen much research and development in recent years. Examples include: UV photolithography mask repair, nanoprototyping and direct deposition of magnetically confined structures. However, EBIED fundamental theory and model development has not progressed at a comparable rate.

There is much motivation for performing fundamental EBIED study. The state of EBIED technology although highly developed for specific applications, remains limited in the range of materials which can be deposited. Increasing the understanding of the fundamentals of the EBIED process should allow improvements to current EBIED technology as well as opening up new areas of application. It also will allow the development of better models. With more accurate, more robust models of the EBIED process it should be possible to save much time and money in EBIED research.

The ultimate motivation for me for performing this fundamental EBIED research project is to experimentally identify the factors which need to be considered for the creation of new models of EBIED. The ultimate goal is to eventually create a model of EBIED which can be used to accurately predict the outcome of an EBIED experiment over a large volume of parameter space (e.g different precursors, temperatures, electron beam conditions, scan strategies etc). Such a model could be used to simulate EBIED experiments and complement future EBIED nanofabrication systems. The work of this thesis is only one step towards this ultimate goal.

During the course of the project another motivation for fundamental EBIED research became apparent. This new motivation is the possibility of using EBIED as a fundamental technique for the investigation of material specific, gas molecule – surface interactions. An example of this is explored in chapter 4 where the EBID technique is used to estimate values for the energy of desorption of the TEOS

molecule. Research is being planned for future investigations into the feasibility of using EBIED as an analytical technique as well as a nanofabrication technique.

There are many EBID precursors which could have been used for this project. The motivation to work with the tetraethoxysilane (TEOS) precursor initially included the low cost, low toxicity and high EBID growth rate obtained using the precursor. The comparatively large amount of supporting literature available concerning CVD and EBID with TEOS was another motivation. During the course of the project, the interesting adsorption kinetics of the TEOS molecule became another motivation.

In summary, this thesis contains the results of an experimental EBID investigation and the conclusions drawn as a result of the experimental work. It is a fundamental study with the primary intent of identifying factors which are not included in current models of EBIED in order to contribute towards the goal of the creation of a high accuracy, robust model of the EBIED process.

2. Theoretical Aspects of EBIED

With this chapter I shall attempt to familiarise the reader with EBIED theory and the model which has been developed over the course of decades of research. The model provides the basis for EBIED simulation work and displays excellent agreement with experimental results over a broad range of system parameters. However, the model does not account for all factors which can influence an EBIED system and significant deviation from model behaviour can be observed under certain experimental conditions. Some examples of experimental conditions which can result in deviation from model behaviour shall be presented in later chapters. The formulation of a "complete" model of EBIED is a major motivation for performing fundamental EBIED research.

2.1 Physical interactions involved in the EBIED Process

Many factors influence the EBIED process. Electron induced reaction mechanisms which give rise to EBIED are different for each precursor. Even without an electron beam, each precursor will interact uniquely with different surfaces. Furthermore, parameters which describe interactions of molecules with surfaces such as sticking co-efficient and the desorption energy are very difficult to determine accurate values for experimentally and generally require expensive UHV apparatus. The variables and interactions which are of importance to the EBIED process can be classed into several categories which will be discussed below.

a. Interaction of precursor Molecules with Substrate

The first category of interactions to consider when performing an experiment involving EBIED (or any CVD process) is the interactions of the gaseous precursor molecules with the substrate. A flux of precursor molecules is incident upon the substrate from gas phase and this flux is a function of the partial pressure of the precursor. This is designated J_d. An expression for J_d inside a chamber with precursor partial pressure P_p is:

$$J_d = \frac{P_p}{2\pi mkT} \qquad (2.1)$$

where: *m, k* and *T* are the mass of one molecule of the gas, Boltzmann's constant and temperature of the gas respectively.

The precursor molecules will then either adsorb (physisorption or chemisorption) or not adsorb to the substrate surface with a probability which is described by the sticking co-efficient, s_d. The sticking co-efficient is the ratio of the number of gas molecules that adsorb to a certain surface, to the total number of molecules incident upon that surface and is a function of the adsorption energy (E_d, usually referred to as desorption energy) , surface coverage *(ϑ),* substrate temperature (T_s) and the momentum vector of impinging precursor molecules. Direct, accurate experimental determination of s_d is difficult and requires UHV conditions [29].Thus values of s_d are available in the literature only for some commonly used precursors.

After a precursor molecule adsorbs to the substrate surface it will diffuse across the surface for a certain time (mean residence time τ) before desorbing or being dissociated by electrons (if beam present). The average distance diffused across the substrate in τ is the mean diffusion length L_d . Both L_d and τ are different for each precursor and substrate combination and is strongly dependent upon the substrate temperature. Surface diffusion (diffusion co-efficient D) and mean residence time (τ) generally display Arrhenius behaviour and can be modelled with standard Arrhenius expressions:

$$D = D_0 e^{\frac{-E_d}{kT}} \qquad (2.2)$$

$$\tau = \tau_0 e^{\frac{E_D}{kT}} \qquad (2.3)$$

where: D_0 and τ_0 are the attempt frequency of the processes (determined by frequencies of different modes of molecular vibrations), E_d and E_D are the diffusion energy barrier (energy required to initiate diffusion of molecule across surface) and desorption energy (energy required to desorb a molecule from the surface) respectively, k is Boltzmann's constant and T the temperature in Kelvin.

After a certain length of time (see figures below) the coverage of adsorbed precursor molecules upon the substrate will reach equilibrium between adsorption from gas phase and thermally induced desorption. This is termed the *initial coverage (ϑ_0).* Isotherms are used to model of the initial coverage on surfaces and the Langmuir isotherm is used most

often in EBIED modelling [30]. The Langmuir model is a simple model of adsorption and makes four key assumptions: that the surface is uniform, adsorbates do not interact, only one mechanism of adsorption occurs and adsorption is limited to a monolayer. All four assumptions will be extremely unlikely to be true during EBIED and some precursors may adsorb and form multiple layers.

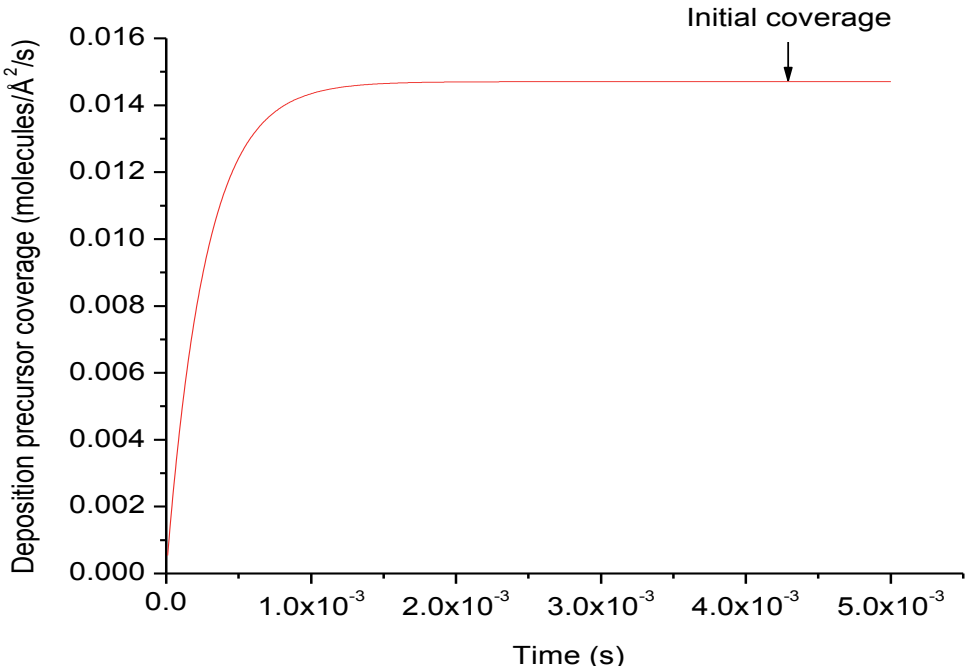

Figure 2.1: *Simulated precursor coverage before e^- irradiation assuming Langmuir adsorption. Equilibrium coverage is reached quickly and is a single monolayer. The coverage will change when e^- irradiation is introduced to the system. From [40].*

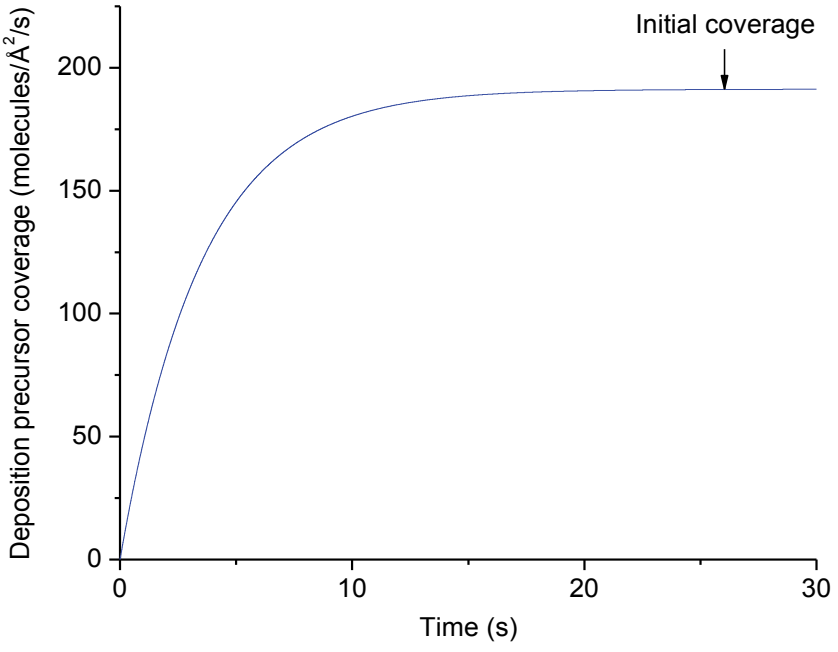

Figure 2.2: *Simulated initial coverage assuming multi-layer adsorption. Equilibrium coverage is much higher and takes a much longer time to be reached. From [40].*

b. Electron beam interaction with substrate

An electron beam incident upon a substrate will penetrate to a certain depth which is termed the *penetration range*. The penetration range is a function of the kinetic energy of the primary electrons in the beam as well as the density and average atomic number of the substrate material. It can be approximated by the Kanaya-Okayama equation [31]:

$$R_{KO} = \frac{27.6AE_L^{5/3}}{\rho Z^{8/9}} \qquad (2.4)$$

where: E_L is the landing energy of the electrons in the beam (keV, equivalent to the accelerating voltage of the beam), A is the average atomic weight (g/Mol), ρ the density (g/cm^3) and Z the average atomic number of the substrate material.

The primary electrons from the beam are scattered elastically and inelastically by the substrate atoms and the maximum distance that can be travelled by primary electrons inside the substrate forms a teardrop shaped volume termed the *interaction volume*. Some electrons are scattered at angles greater than 90 °, leave the substrate with much of their energy intact and are termed *backscattered electrons* (BSE). Primary (PE) electrons within the interaction volume also continuously cause secondary electrons (SE1) to be emitted by atoms due to ionisation events. BSEs will also cause SE emission and these electrons are referred to as SE2s. Secondary electrons are of low energy (<50 eV) and thus only those emitted by atoms within the uppermost portion of the interaction volume will escape the sample surface. Photons are also generated throughout the interaction volume via processes such as cathodoluminescence.

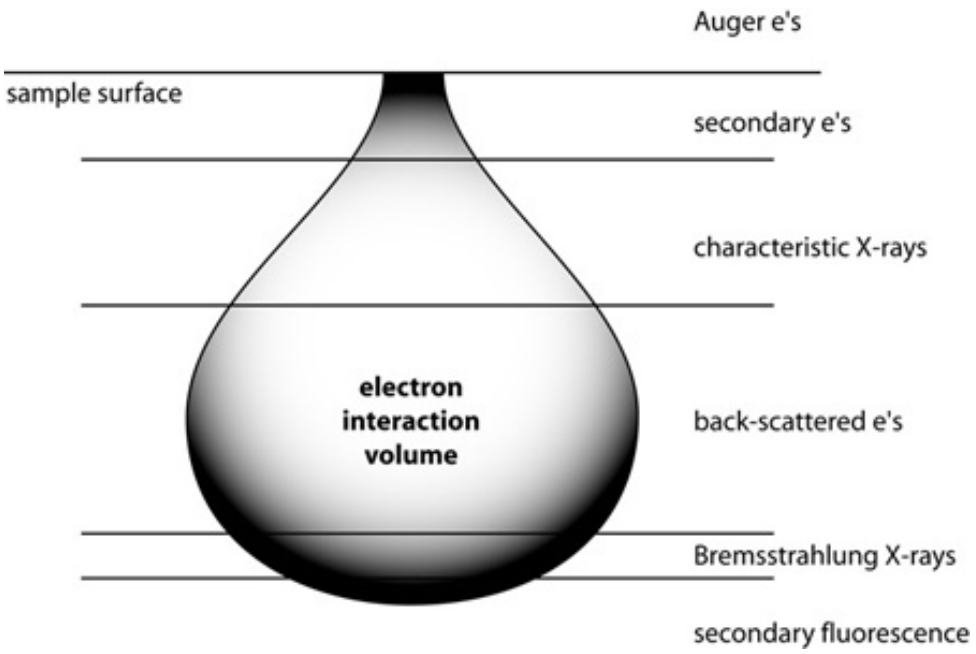

Figure 2.3: *Simple representation of the interaction volume within a flat substrate under focused electron beam irradiation. The various signals that are generated within the interaction volume and their general regions of origin are shown. From [70].*

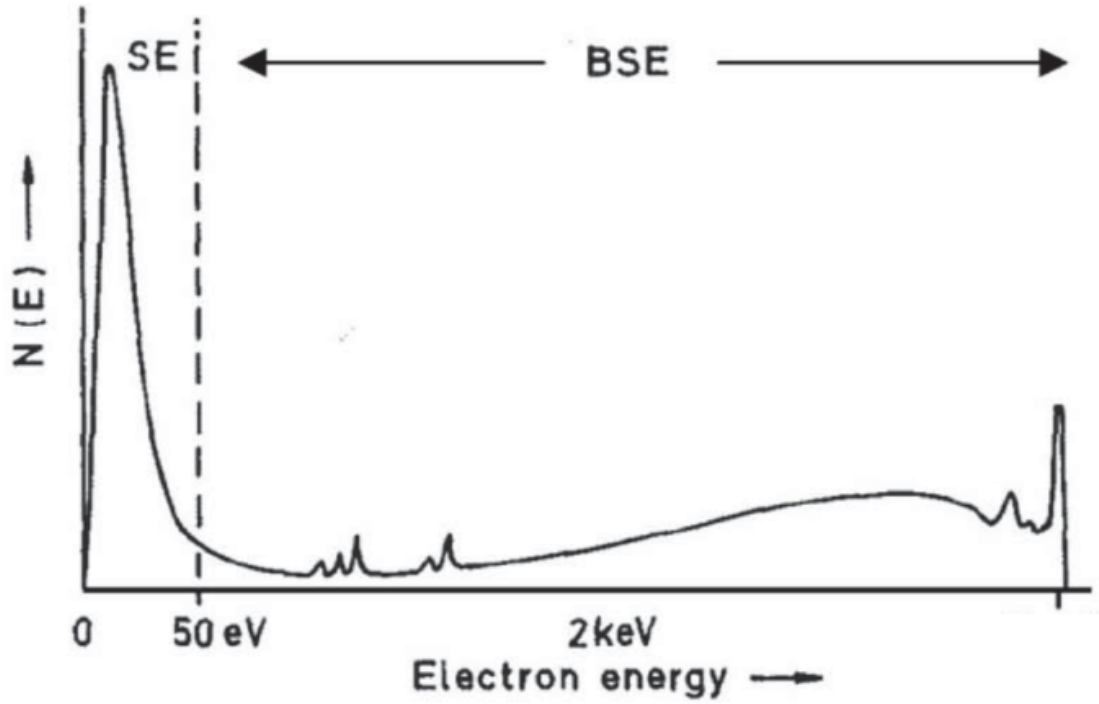

Figure 2.4: *Characteristic curve of the electron emission from a flat substrate under electron beam irradiation at typical energies used in SEM (1 – 30 kV). Electrons under 50 eV are classed as secondary electrons and all above 50 eV as backscattered electrons. From [20].*

For the case of EBID, the growing EBID deposit will further complicate the matter. As a deposit forms, the interaction volume will become increasingly contained within the EBID deposit rather than the substrate. If the EBID material is different to the substrate, which is likely, then the yield of SEs and BSEs as well as the size of the interaction volume itself will be altered. High aspect ratio deposits (e.g. nanopillars) also have a higher yield of emitted SEs and BSEs due to their higher (compared to a flat substrate) surface area to volume ratio. The emitted electron yield will directly affect the EBIED rate.

As well as exciting secondary electrons and causing photon emissions, the energy deposited into the substrate by the electron beam will have a significant portion dissipated as heat. This heating is proportional to the electron flux and thus it is generally negligible for low beam currents, de-focused beams and rastered beams. However, it can be significant for a high current stationary beam [32] which is often the case during EBIED. Electron beam induced heating (EBIH) during EBIED can result in a localised temperature increase in the EBIED region which will affect most of the parameters which control the EBIED process and give unexpected results. Hochleitner *et al.* [33] observed spontaneous, directionless, polycrystalline Fe growth du ring EBID of nanopillars with $Fe(CO)_5$ precursor. They attributed the growth to thermal decomposition of precursor molecules adsorbed to the surface of the growing nanopillar which reached a significantly higher temperature than the substrate due to EBIH during EBID. Similar behaviour may be expected of any EBID precursor with low thermal decomposition temperatures. EBIH is certainly an important factor for any scientist performing EBIED research to consider

c. Interaction of adsorbed precursor molecules with electron beam

When an electron beam is introduced, adsorbed precursor molecules adsorbed to the substrate will then begin to be dissociated, ionised and desorbed by primary, secondary and backscattered electrons. Photons generated during e^- irradiation may also play a role in precursor dissociation in some cases [34]. Cross-sections are used in particle physics to predict the probabilities of certain interactions occurring between particles. An effective cross section for dissociation by electrons is used to predict probabilities of dissociation events for EBIED modelling. This effective cross-section σ, describes only the probability of a

dissociation event occurring for a given set of EBIED parameters and may or may not be close to a true cross-section for any single dissociation reaction as the overall EBIED reaction is likely to be the combination of several reactions.

The cross-section, *σ,* can be estimated for a particular precursor, electron beam energy and surface through careful EBIED experimentation and fitting to theoretical models [35, 36]. True cross-sections for some beam induced reactions for some precursors can be determined experimentally in UHV conditions [28]. True cross-sections for electron induced reactions are available in literature only for some simple molecules such as H_2O [37, 38].

Dissociation cross-sections are available in the literature for several common CVD precursors, compiled from experimental and theoretical calculations but often only for molecules in the gas phase. General practice for EBIED modelling is to use gas phase dissociation cross-sections from CVD literature if available, or of molecules that bear some similarity to the precursor. Plasma processing literature is another source for molecular parameters such as dissociation cross sections which could apply to EBIED. W.L Morgan compiled much data upon the molecules CF_4, SiH_4 & CH_4 for plasma modelling in a 1991 paper [39].

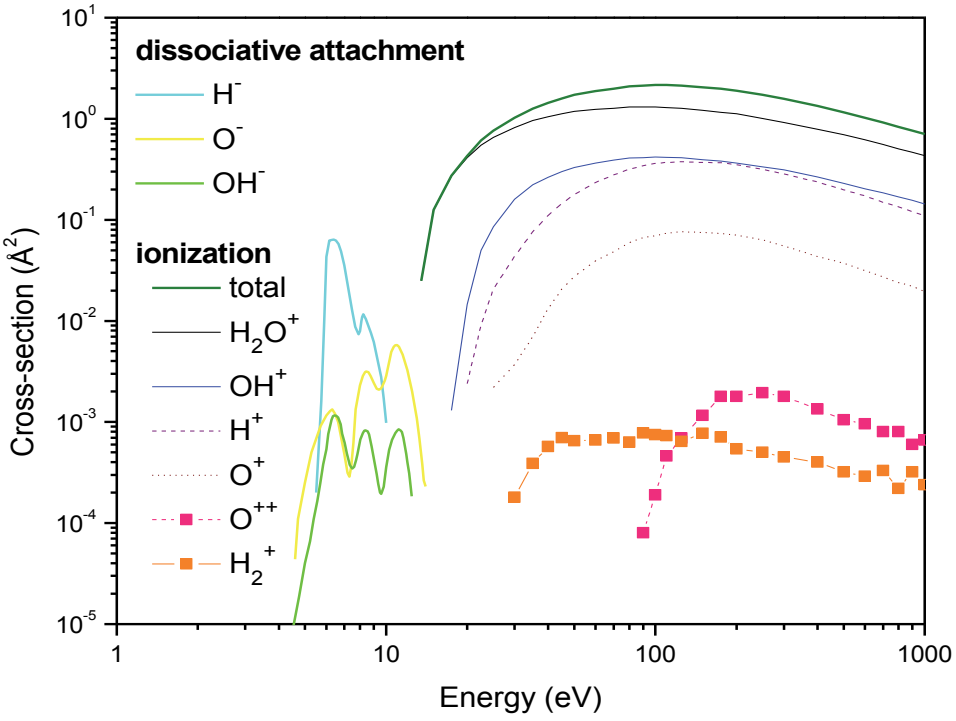

Figure 2.5: *Cross-sections of various electron induced reactions of H_2O. H_2O is a common EBIE precursor for carbon containing material. Compiled by Itikawa et al. [37].*

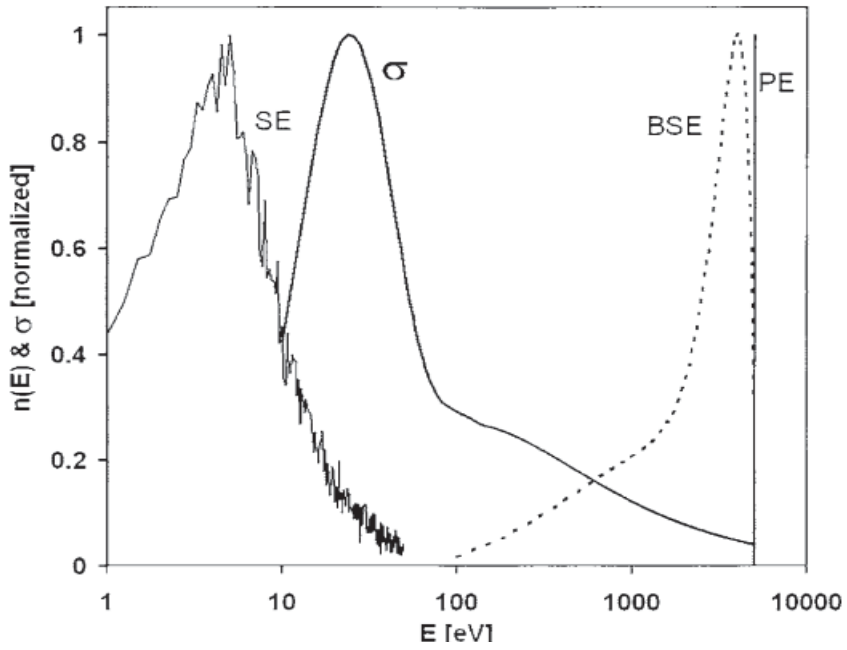

Figure 2.6: *Estimated effective cross-section for dissociation of WF_6, a common inorganic deposition precursor. A simulated emitted electron energy distribution profile of a 20 kV beam incident upon a flat Ge substrate is overlayed to highlight the low number of electrons with energy similar to the peak position of the cross section. From [26]*

Although dissociation cross-sectional data is available only for some EBIED precursors, the dissociation cross-sections that are available generally have their maximum (peak) position below 50 eV. This indicates that the chance for an electron-induced dissociation event occurring is higher for SEs (defined as electrons < 50 eV) than it is for backscattered electrons. As a result, it has generally been assumed that SEs are mainly responsible for and dominate the EBIED process. It has been suggested that primary and backscattered electrons also contribute significantly to precursor dissociation due to the larger number of higher energy electrons available at typical EBID beam energies (10 – 30 kV). Randolph *et al.* [26] demonstrated through modelling and experiment that this scenario is likely.

EBIED Regimes

Prior to electron beam irradiation, the substrate will have the initial coverage of precursor molecules. When electron irradiation begins, precursor molecules will be dissociated, ionised and desorbed by electron impact. These processes will deplete the concentration of adsorbed precursor molecules in the electron irradiation region. A new equilibrium is reached after a short time (≈ ms) between the depletion mechanisms (e^-

induced dissociation & thermal desorption) and replenishment effects (adsorption from gas phase & diffusion into irradiation region). This new equilibrium coverage under e^- irradiation is termed the *steady state coverage* $(N_d)_{ss}$.

Using a low beam current with sufficient precursor pressure, depletion is lower than replenishment and the steady state concentration $((N_d)_{ss})$ is approximately equal to the initial coverage (ϑ_0). The growth/etch rate will be determined by the electron flux *f* (incident electrons/ unit area) for this case. This is termed the *reaction rate limited regime* or *electron limited regime (EL).* The growth/etch rate increases linearly with electron flux and is unaffected by increasing precursor pressure, in this regime.

As electron flux is increased for a constant precursor pressure (or pressure reduced for constant e^- flux), the rate of depletion will begin to exceed the rate of replenishment and $(N_d)_{ss} < (\vartheta_0)$. The growth/etch rate in this regime will increase sub-linearly with *f*. It will also increase sub-linearly with increasing precursor pressure (P_p). We shall term this regime the *partially depleted regime (PD).*

As *f* is further increased (or P_p reduced), the depletion will increase and $(N_d)_{ss} \rightarrow 0$. This means that precursor molecules are dissociated as soon as they enter the irradiation region. The growth/etch rate will be determined by the precursor supply to the irradiation region. This regime is termed the *mass-transport limited regime (MTL)* and the growth/etch rate increases linearly with P_p and be unaffected by increasing *f*.

Any parameter of the EBIED system which can alter *f* or the precursor supply to irradiation region will affect the degree of depletion and thus the regime. For example, increasing the substrate temperature T_s reduces the residence time τ of adsorbed precursor molecules, lowering $(N_d)_{ss}$ and increasing depletion. Defocusing the electron beam reduces e^- flux and lowers depletion. Electron beam induced heating will increase the temperature locally to the irradiation region and increase depletion. Different geometries of deposits are typical of different EBID growth regimes and the highest possible aspect ratio for nanopillars can only be achieved in the EL regime. EBIED experimentation often requires a good knowledge of the EBIED regime under which a particular deposition/etching experiment is occurring. Furthermore, it is often beneficial to work within a particular regime.

2.2 Theoretical Model of the EBIED Process

**The following model is published in reference [40]. It shall be referred to throughout the rest of the thesis as "the standard model".*

Rate of change of precursor adsorbates N_d:

$$\frac{\partial N_d(r,t)}{\partial t} = s_d J_d (1 - N_d(r,t) A_d) - \frac{N_d(r,t)}{\tau_d} + D_d \left[\frac{\partial^2 N_d(r,t)}{\partial r^2} \frac{1}{r} \frac{\partial N_d(r,t)}{\partial r} \right] - \sigma_d f(r) N_d(r,t) \quad (2.5)$$

where: s_d is the sticking coefficient, J_d the flux of precursor molecules from vacuum and A_d the precursor molecule surface area. τ_d is the residence time. r is the radial distance from the beam axis and t is time. D_d is the diffusion co-efficient of the precursor molecules on the surface (eq. 2.2). Each highlighted term accounts for each of the main processes which are occurring during EBIED as shown below.

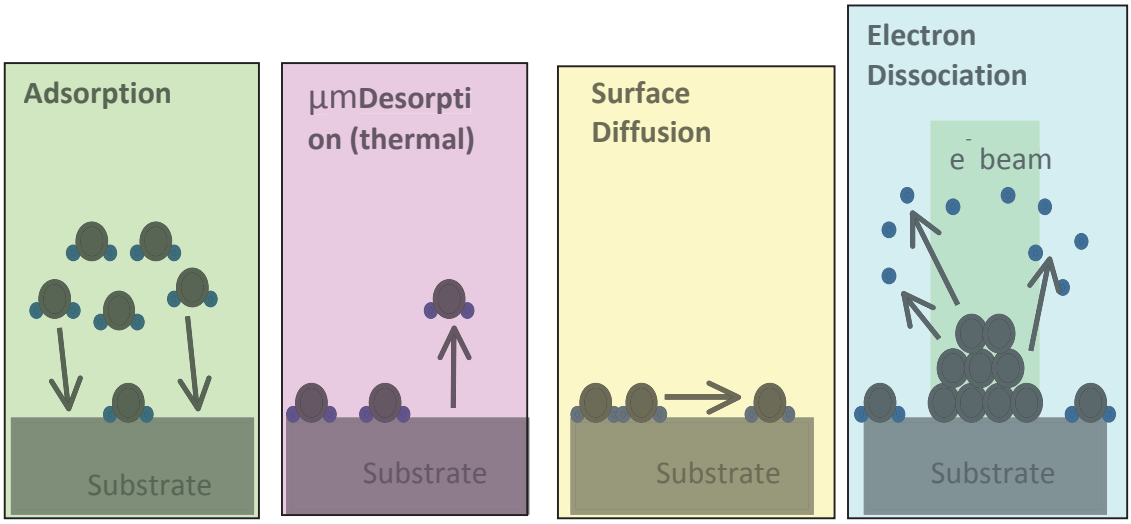

Figure 2.7: *The main processes which occur during EBIED. The illustration representing each process is colour – coded to indicate which term represents the process in the adsorbate concentration expression above (2.5).*

Rate of change of concentration of deposited molecules N_D:

$$\frac{\partial N_D(r,t)}{\partial t} = \sigma_d f(r) N_d(r,t) \quad (2.6)$$

where: σ_d is the effective cross section for dissociation by electrons and *f* the electron flux. The equations can be solved numerically if all parameters are known. To reproduce EBIED experimental data, one must use parameters which represent the system. The electron flux

f, is the *incident electron beam current per unit area* and can be derived from measurements of beam current (I_b) and diameter (L). J_d can be calculated from measurement of the P_p. The rest: s_d, D_d, σ_d, and A_d are available in literature for some precursor/surface combinations or must be estimated. Guidelines exist for making estimations of such parameters [81]. Solved numerically the equations will yield the spatial and temporal evolution of the precursor coverage N_d, deposit coverage N_D, growth rate $\frac{\partial N_D(r,t)}{\partial t}$ and deposit height h:

$$h(r,t) = V_D N_D(r,t) = V_D \int_0^t \frac{\partial N_D(r,t)}{\partial t} dt \qquad (2.7)$$

where: V_D is the volume of a deposited molecule/atom (or the volume removed by each EBIE reaction). These equations can be easily modified to simulate the EBIE process simply by inserting the molecular parameters of an etch precursor in place of the parameters of a deposition precursor and by replacing V_D with the volume removed from the substrate by each etching event. The subscript d is usually replaced by the subscript e to indicate etchant parameters.

EBIED Regimes

As discussed in section 2.1 c, three EBIED regimes exist and are defined by the degree of precursor depletion occurring within the irradiation area which is itself governed by the precursor supply and electron flux. If we remove the diffusion term from equation 2.5 it can be solved analytically to give the steady state concentration (neglecting diffusion) of precursor molecules.

$$(N_d)_{ss} = \frac{s_d J_d}{\left(s_d A_d J_d + \frac{1}{\tau_d} + \sigma_d f\right)} \qquad (2.8)$$

The steady state growth/etch rate is given by:

$$\left(\frac{dN_D}{dt}\right)_{ss} = \sigma_d f N_d = \frac{\sigma_d f s_d J_d}{\left(s_d A_d J_d + \frac{1}{\tau_d} + \sigma_d f\right)} \qquad (2.9)$$

Electron Limited Regime

In the electron limited regime, the growth rate is determined by the electron flux (*f)* and increases linearly with flux as the dissociation rate of precursor molecules is negligible

compared to the arrival rate (by adsorption from gas phase). This means that the term $\sigma_d f$ in the denominator of equation 2.9 is negligible compared to the rest of the terms and can be discarded. Neglecting diffusion for EBID in the EL regime is a valid assumption since there will be no diffusion into the irradiation region. Once equilibrium precursor concentration has been reached no diffusion will occur unless an adsorbate gradient is present [41]. Since $(N_d)_{ss} \approx \vartheta_0$ for EL regime no adsorbant gradient exists. The steady state deposition/etch rate in this regime is given by:

$$\left(\frac{dN_D}{dt}\right)_{ss} \approx \frac{\sigma_d f s_d J_d}{\left(s_d A_d J_d + \frac{1}{\tau_d}\right)} = \sigma_d f \theta_0 \qquad (2.10)$$

Mass-Transport Limited Regime

With MTL EBIED all terms in the denominator of equation 2.9 are negligible compared to the $\sigma_d f$ term. Neglecting diffusion will cause some error for this regime as diffusion into the irradiation region is at a maximum as depletion and therefore adsorbant gradient are at maximum. The approximate steady state growth rate (neglecting diffusion) is:

$$\left(\frac{dN_D}{dt}\right)_{ss} \approx s_d J_d \qquad (2.11)$$

When the EBIED process is in the PD regime all terms in the denominator of equation 2.9 are significant and no simplification can be made. The approximate growth/etch rate is given by equation 2.9.

Multiple Gaseous Species EBIED Modelling

Multiple gaseous precursor species present at appreciable concentrations in an EBID/EBIE system can result in competing electron beam induced processes occurring. Generally the residual gaseous species present will be H_2O, O_2, N_2, Ar (i.e. air) and organic vapours. Measures must be taken to minimise the quantity of residual vapours present in your SEM chamber for EBIED to avoid the effects of multiple gaseous species.

A good example of multi-species EBIED competition is EBID of carbonaceous material with a focused (Gaussian flux distribution) beam whilst H_2O is also present in the EBID chamber. This system has been investigated in detail by Toth *et al.* [42, 43]. Carbonaceous EBID dominates on the periphery of the irradiation region where the e^- flux is low whilst etching of carbon by H_2O dominates in the centre where the flux is higher. The organic vapour (deposition precursor) partial pressure must be much lower than the H_2O (etch precursor) P_p for this behaviour to occur due to the higher efficiency of the EBID reaction. A volcano or ring shaped structure grows as there is zero net growth in the centre and net deposition around the beam periphery. Toth *et al.* contributed this behaviour to competing EBID and EBIE. As electron flux is increased (moving in towards the beam axis) the EBID reaction saturates due to precursor depletion whilst the EBIE reaction continues to increase. The behaviour was termed "simultaneous electron beam induced deposition and etching (SEBIED)".

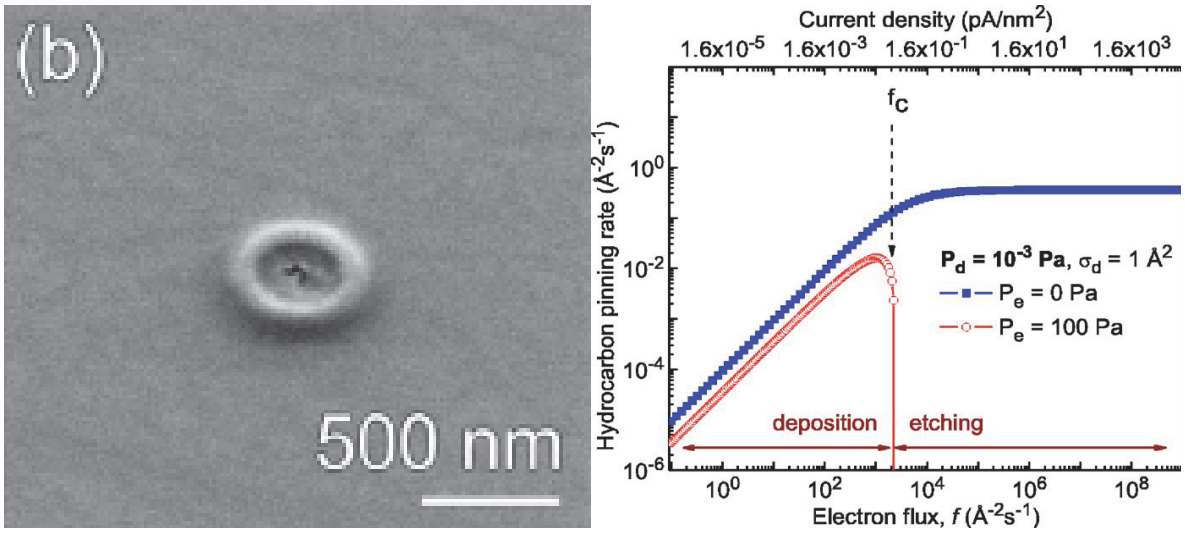

Figure 2.8 Left: *Ring deposit formed as result of SEBIED.* ***Right:*** *Carbonaceous deposition rate calculated from a multi-species model with residual hydrocarbons and H_2O. The carbonaceous EBID reaction is more efficient than the H_2O EBIE reaction but saturates at higher electron fluxes due to lack of precursor. The EBIE reaction does not saturate with increasing e^- flux due to abundant precursor molecules (at 100 pa H_2O). A net deposition rate of zero occurs in the centre. From [42].*

2.3 EBID Experimental Instrumentation Theory

In-situ EBID Monitoring Theory

The In-situ EBID monitoring system which is used for all experiments is described in chapter 3. The system involves measuring and logging the emitted (I_e) and transmitted (I_t) electron currents during EBID experiments. This allows real-time identification of experimental process errors. Apart from this the I_e and I_t curves collected during experiment can be analysed and compared to post-deposition images to yield much information concerning growth processes occurring during EBID.

When spot-mode EBID is commenced the stationary electron beam is initially incident upon a flat substrate (Si in the case of this work) and there will be a corresponding emitted electron yield (BSE yield + SE yield) yield for this situation. The yield is dependent upon substrate material dependant factors such as the atomic number (z) or average atomic number and density (ρ) as well as electron beam parameters such as the beam energy (V_0), beam current (I_b) and electron flux (f). The EBID material being deposited will have a different electron yield (compared to the substrate) due to different material properties assuming it is a different material. As the EBID pillar grows the interaction volume of the electron beam will become increasingly contained within the EBID material rather than the substrate. When the pillar reaches a height equal to the penetration depth of the electron beam within the EBID material, the SE and BSE yield will originate from the EBID pillar only and the substrate will no longer contribute. At this point the I_e signal will stop increasing and the I_e curve will saturate. A change in I_e signal after saturation indicates a process error (e.g change in I_b or P or beam movement) or a change in the tip geometry of the growing EBID pillar.

The emitted electron yield from a high aspect ratio structure such as an EBID pillar is much greater than that of a flat bulk substrate. This is due to the contribution of forward scattered electrons (FSE) emitted from sidewalls and SE's emitted by FSE's. Some FSE's will also then be backscattered by the substrate. Every EBID deposit – vacuum or substrate – vacuum transition event by FSE's or BSE's will also generate SE's. Thus the I_e signal will still increase during spot mode EBID even if the material being deposited has an electron yield ≤

the substrate electron yield. As a result the monitoring process should work for all EBID material – substrate combinations.

During EBID the emitted electron yield will gradually change from the case of a flat bulk substrate to the EBID pillar case and will stop changing after the point where the interaction volume is inside the EBID pillar only. Thus the saturation of the curves corresponds to a certain pillar height which is fixed for a given electron beam energy and EBID material. This I_e curve saturation pillar height corresponds to the penetration depth of the electron beam inside the EBID material. This allows estimation of the penetration depth of the electron beam within the EBID material by determination of the pillar height at which curve saturation occurs. This may allow estimation of parameters such as the density (ρ) of an EBID material.

Transmitted current (I_t) curves are essentially the inverse of the I_e curves. I_t decreases as I_e increases during pillar growth as less and less electrons penetrate the substrate and are transmitted as the pillar grows. Thus the same information can be extracted via the I_t curves.

Practical Example: Estimating Penetration Depth

Figure 2.8 below shows the first four deposits of an experimental set which was made as a function of beam diameter. The beam diameter was controlled by adjusting the position of the focal point of the beam. As the beam diameter increases the aspect ratio and vertical growth rate of the deposits is decreased. The vertical growth rate can be inferred from the gradient of the I_e curve prior to saturation. As can be seen above, the vertical growth rate was high for D1 (focused) and the I_e curve quickly saturated. As the beam is defocused, vertical growth rate slows and D3 and D4 do not reach saturation height. The penetration range of the 25 kV electrons within the TEOS grown EBID material can be roughly estimated from this data. Since the saturation of the curve corresponds with the penetration range and D3 almost reaches saturation, the range can be estimated as ≈ 4 – 5 μm. The height of the deposits is measured ex – situ from images taken after deposition.

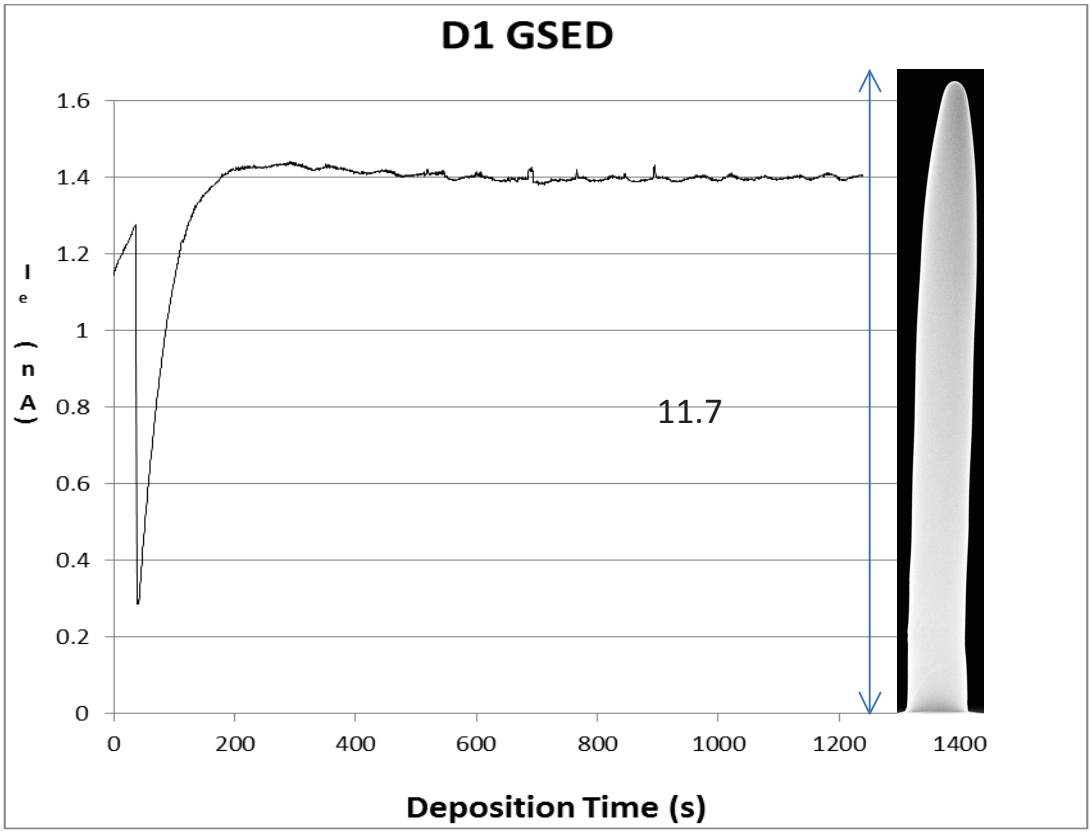

Figure 2.9 (above & below): *I_e curves recorded during deposition by EBID with TEOS precursor. SEM images of the deposits and heights are overlayed. Data is an extract from experimental set with beam diameter as the changing parameter. Aspect ratio of deposits decreases with increasing beam diameter.*

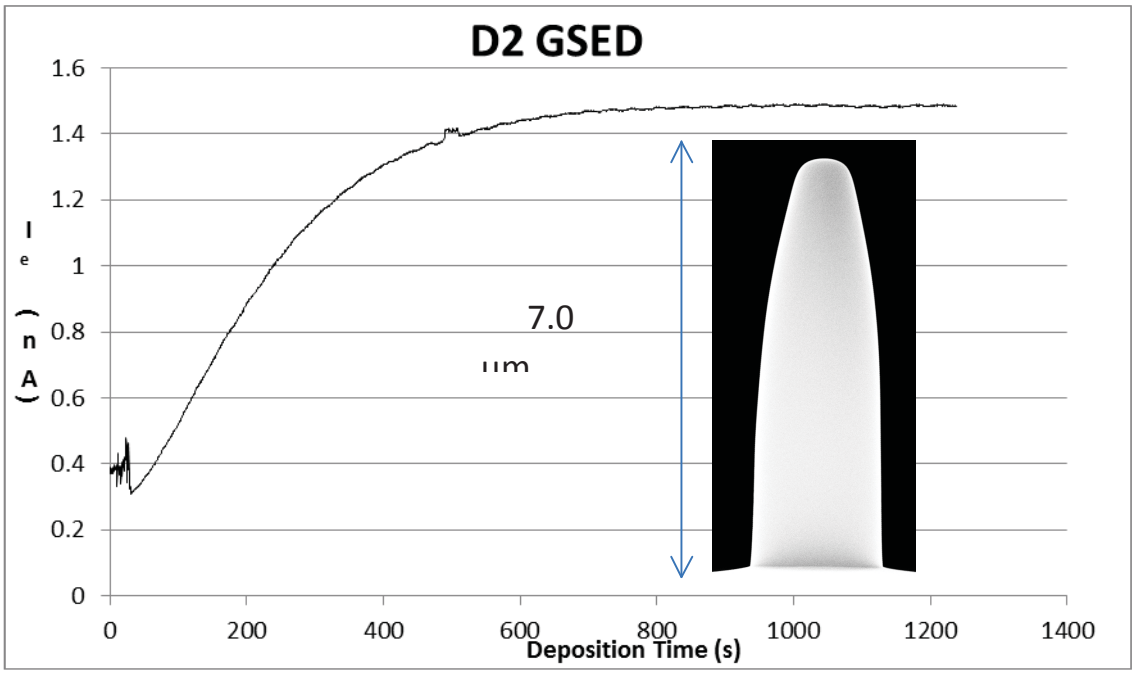

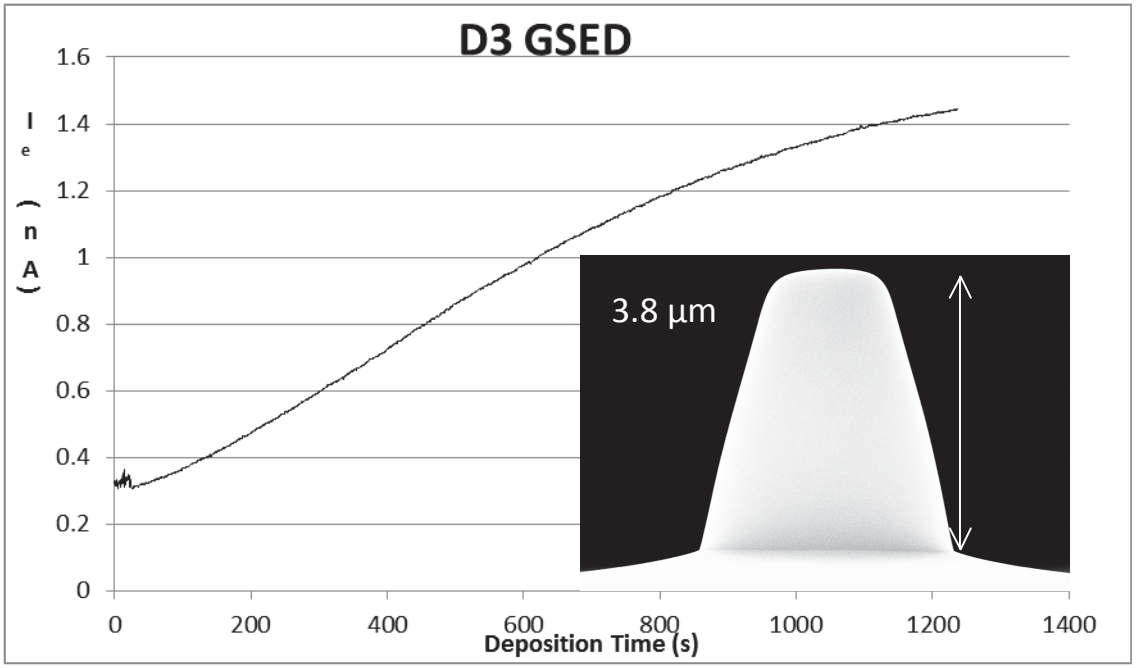
D3 GSED
1.6
1.4
1.2
1
0.8
0.6
0.4
0.2
0
I e) n A (
0
200
400
600
800
1000
1200
1400
Deposition Time (s)
3.8 µm

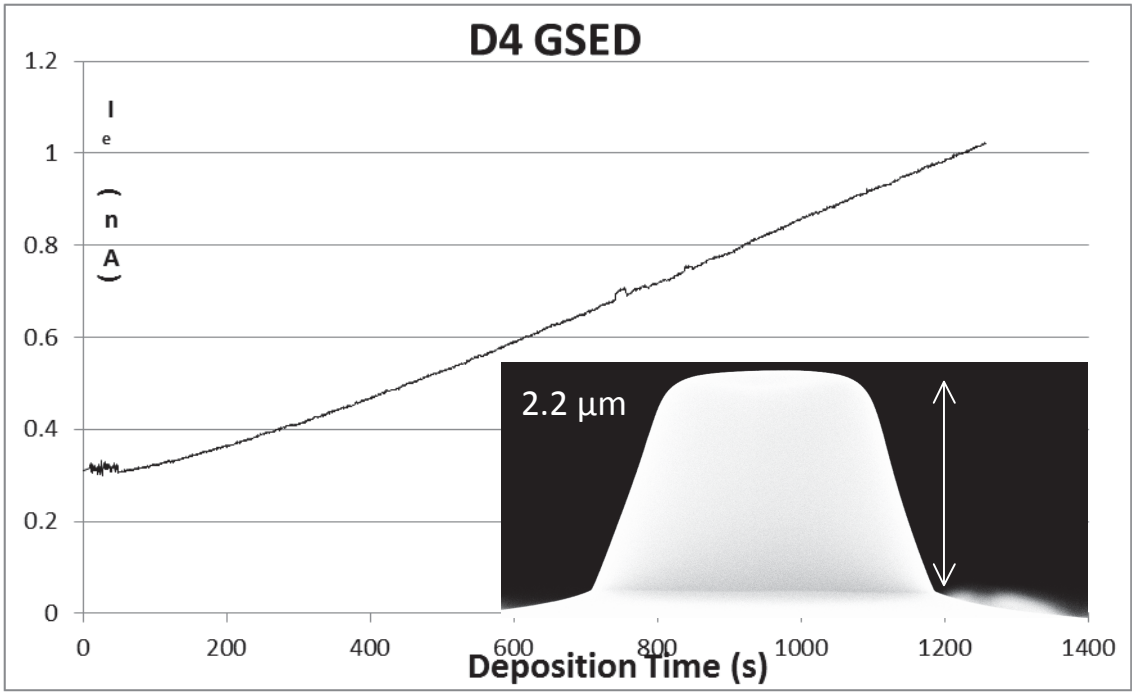
D4 GSED
1.2
1
0.8
0.6
0.4
0.2
0
I e) n A (
0
200
400
600
800
1000
1200
1400
Deposition Time (s)
2.2 µm

2.4 Literature and Theory Most Relevant To the Work of This Thesis

The main body of work in this thesis concerns EBID with an ESEM cell setup using the precursor tetraethoxysilane (TEOS) to deposit $Si_xO_yC_z$ structures. Investigating thermal effects, adsorption kinetics and gas mixing is the focus. Literature concerning silane precursors, thermal effects on EBID, reactive gas mixing and adsorption kinetics is of vital importance to support conclusions reached as a result of experimental work in this project. Surface science literature is an important source of information as is the field of chemical vapour deposition (CVD). Much information concerning organosilane precursors such as TEOS can be found within CVD literature. The majority of the most relevant literature shall be referenced and reviewed in later chapters when discussing the results to which the literature best applies.

CVD Studies concerning Tetraethoxysilane

TEOS has been used as a precursor for the deposition of SiO_2 via CVD since the 70's [63]. It is an organosilane complex with the empirical formula $SiO_4C_8H_{20}$. There is much published work concerning CVD with TEOS precursor and it has also been used as an EBID precursor by several groups [48]. Surface science and CVD studies have indicated thermal decomposition from TEOS to SiO_2 is complex with multiple steps activated at different substrate temperatures. Spitzmüller *et al.* [64] studied the adsorption and thermal decomposition up to 850 K of TEOS on a silicon (111) surface with native oxide using STM and XPS. They found that TEOS adsorbs molecularly via an initial physisorption step. At higher T_s the physisorbed TEOS molecule can react with the substrate and dissociatively chemisorb. The TEOS molecule loses one or more ligands as ethyl or ethyl or ethoxy groups during dissociative adsorption [74]. Crowell *et al.*[65] found that after adsorption of TEOS upon SiO_2 at T_s = 450 K, the majority adsorbed species were di & triethoxysiloxanes and ethyl groups.

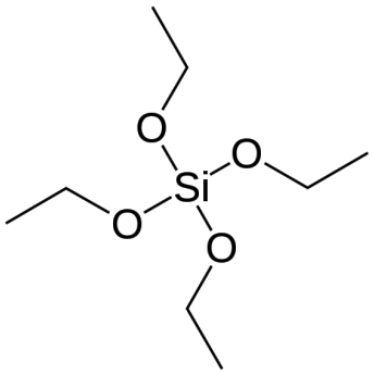

Figure 2.10: *Structure of the TEOS molecule.*

TEOS can decompose thermally to produce SiO_2 at high temperatures (≈1000 K). It can also be combined with other gases which catalyse the reaction and lower the decomposition temperature. The addition of oxygen is common practice with TEOS CVD [66] and helps increase the uniformity and purity of deposited CVD films. Direct-plasma assisted CVD of TEOS with or without oxygen can be used to deposit SiO_2 films at room temperature. The direct plasma case can be considered as equivalent to EBID of TEOS. Deposition of SiO_2 from TEOS at room temperature can also be achieved with an atomic oxygen source (e.g. remote plasma CVD). This suggests that atomic oxygen can directly decompose TEOS molecules to SiO_2. Svetlichnnyi *et al.* [67] proposed the following model of TEOS decomposition to SiO_2 catalysed by atomic oxygen:

Firstly, one or more ligands of a TEOS molecule are substituted for hydroxyl groups via attack by an oxygen radical:

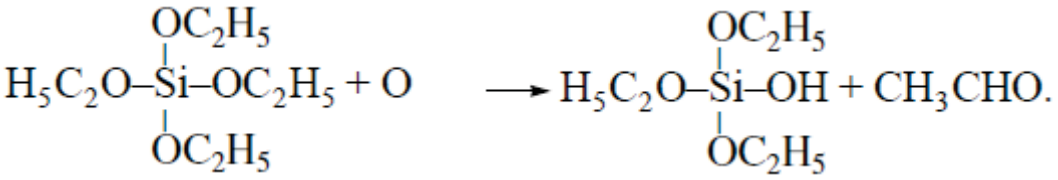

(I)

Silanol groups then undergo dehydration to link the Si:

(II)

Acetate aldehyde produced by the original interaction of TEOS and O radicals (1) is proposed to be further oxidised to formaldehyde and then to H_2O and CO_2:

$$CH_3CHO + 3O \longrightarrow HCHO + CO_2 + H_2O,$$
$$HCHO + 2O \longrightarrow CO_2 + H_2O. \quad \text{(III)}$$

With the stoichiometric oxygen radical assisted TEOS CVD reaction being:

$$Si(OC_2H_5)_4 + 24O \longrightarrow SiO_2 + 8CO_2 + 10H_2O. \quad \text{(IV)}$$

The true reaction scheme is likely to be more complex than the simple model described above however, the model provides a starting point for a more detailed analysis of O radical induced decomposition of TEOS.

Adsorption Kinetics during EBIED

Adsorption kinetics will play a large role in the EBIED process. The particular mechanism of adsorption will affect the growth rate and composition of EBID deposits. For the most part, details of adsorption mechanisms have not been considered in previous EBIED studies. The latest models of EBIED consider only the physisorption of precursor molecules. If a precursor chemisorbs upon EBID deposited surfaces then significant deviation from model behaviour may result. In this thesis, EBID experiments are performed which suggest an activated dissociative chemisorption of TEOS precursor. Literature concerning the adsorption kinetics of the TEOS molecule shall be reviewed in later chapters so as to support the conclusions drawn from my experimental work. The work should highlight the significance of the consideration of adsorption kinetics of precursors for future EBIED research.

3. Experimental Apparatus and Procedures

3.1 Practical Necessities for Reliable EBIED

Reliable EBIED study cannot be performed without a significant investment in equipment. The following list should be considered the minimum requirements for reliable EBIED experimentation:

- Well maintained SEM with minimal chamber and vacuum line contamination which can provide stable beam currents. Preferentially the SEM should be dedicated to the study of EBIED and related techniques only*.
- GIS system (cheaper yet limited) or external precursor delivery system preferably with ESEM cell EBIED sub-chamber within SEM chamber.
- Sealed box for N_2 atmosphere precursor loading.
- Plasma cleaning system.
- Cleaning equipment and solvents to provide super clean substrates.

The practical necessities listed above were discovered through attempted EBID experimentation prior to system upgrades. An FEI XL30 ESEM was the SEM used for all EBID experimentation. The final apparatus developed makes possible the quantitative study of EBIED. The initial apparatus was unable to maintain precursor gas purity due to several critical design flaws. The flaws in the initial apparatus will be discussed in order to provide the reader with a means to avoid the same mistakes in the design of an EBIED system. The following can be considered a guide for the development of a high-quality apparatus for reliable EBIED study.

** **Note upon SEM instrument lab usage:** It is best to have an instrument which is dedicated to the study of EBIED and related techniques only. This is due to the need to maintain an uncontaminated SEM chamber for EBIED work. Methods for maintaining an uncontaminated SEM chamber as well as possible alternative arrangements (to having the SEM dedicated for EBIED only) are discussed in section ____.*

3.2 Initial Experimental Apparatus for EBID

The instrument designated for EBID study was a Phillips Electron Optics XL30 Environmental Scanning Electron Microscope Many upgrades, modifications and repairs were performed over the course of the last 2 years and it is now an instrument devoted purely to the study of EBIED.

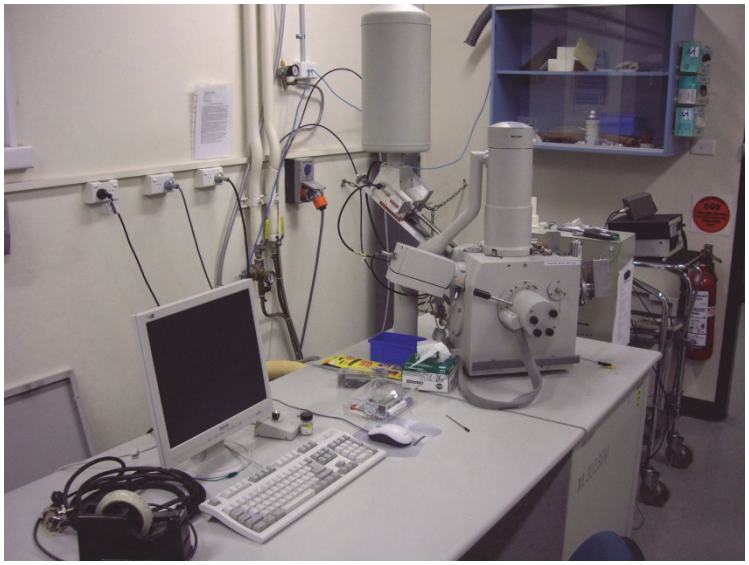

Figure 3.0: *The XL30 ESEM with original PDS prior to modifications and upgrades.*

Environmental Scanning Electron Microscopy (ESEM)

The XL30 ESEM is a thermionic tungsten filament electron source ESEM with a simple column structure. Pressure limiting apertures and differential pumping allow the tungsten filament to remain in high vacuum with up to 10 torr of gas in the specimen chamber. This allows imaging of delicate structures which may be damaged by high vacuum and is referred to as “environmental” SEM [19]. Imaging with gas in the chamber is achieved with a different detector to the Everhart-Thornley detectors used in HIVAC SEM (which directly detects SEs emitted from the sample). An ionisation cascade is induced in the gas by secondary electrons emitted from the sample. Each ionisation event emits more SEs which ionise further gas molecules causing a “cascade”. A positively biased plate measures the gas amplified emitted current at the end of the cascade which forms the imaging signal. Positively ionised gas molecules resulting from the cascade are attracted to the sample as it is negatively charged

relative to the positively biased GSED detector. This allows significant charge neutralisation of non-conductive samples which accumulate charging under electron illumination. ESEM thus allows the imaging of non-conductive samples and even biological structures which would be impossible with other forms of electron microscopy.

Contamination deposition (amorphous carbon EBID from residual organic vapours in the chamber), which is generally problematic in HIVAC SEM can also be minimised using H_2O vapour as the ESEM imaging gas (standard procedure). H_2O is known to etch carbon under electron beam irradiation (EBIE) and deposited carbon is simultaneously etched whilst being deposited resulting in a lower net contamination deposition rate. ESEM is now a standard form of electron microscopy and widely used around the world.

Figure 3.1: *Series of simple diagrams illustrating how ESEM works.*

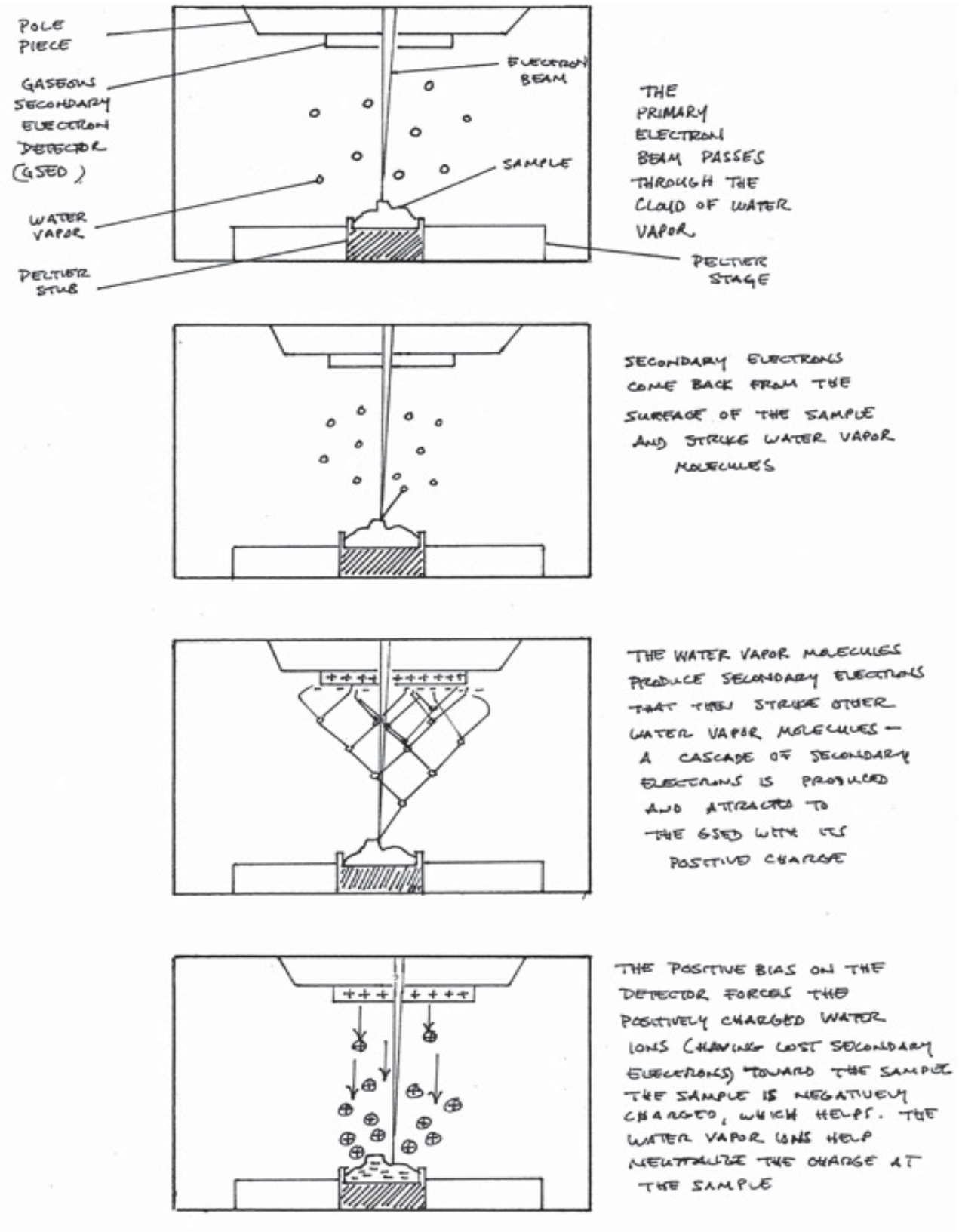

Initial EBIED System Apparatus Flaws

The simple precursor delivery system (PDS) already present on the XL30 ESEM was used for initial experimentation using the ESEM EBID experimental configuration. The system was constructed by a technical officer and honour student with no prior EBIED experience. Critical flaws in the design of the PDS (resulted in an inability to provide pure precursor gas to the chamber. This resulted in somewhat irreproducible EBID results as levels of contaminants (such as H_2O vapour, air and residual organic vapours) mixed with the precursor gas in the ESEM chamber were significant and would vary on a daily basis. A precursor gas environment of high purity is essential for quality EBIED experimentation and especially if quantitative comparison of results is intended.

The flaws in the original EBIED system and experimental procedure were:

- Flaws in design and construction of PDS:
  - Constructed with insufficiently clean tubing (need HV grade cleanliness).
  - Some non metal-metal connections resulting in leaks.
  - Rotary oil roughing pump used for pumping chamber during EBIED.
    - Back diffusion of pump oil → contamination.
  - Precursor crucible contained non high-vacuum rated plastic and a very leaky plastic – metal connection.
  - No high vacuum gauge (must have high vacuum in lines prior to precursor flow).
- Loading precursor into crucible in atmosphere (must load under dry N_2 environment).
- Use of ESEM EBIED experimental configuration. This results in significant residual atmospheric gas contamination due to the slow pumping speed of roughing pumps compared to high vacuum pumps (the large gas volumes involved with this configuration precludes the use of HV pumps).
- Use of oil – diffusion high vacuum pump as the primary high vacuum pump of ESEM.
  - Back diffusion of pump oil → contamination.

- Significant chamber contamination introduced by other users (as microscope was available for non EBIED usage including organic sample analysis) and frequent venting.

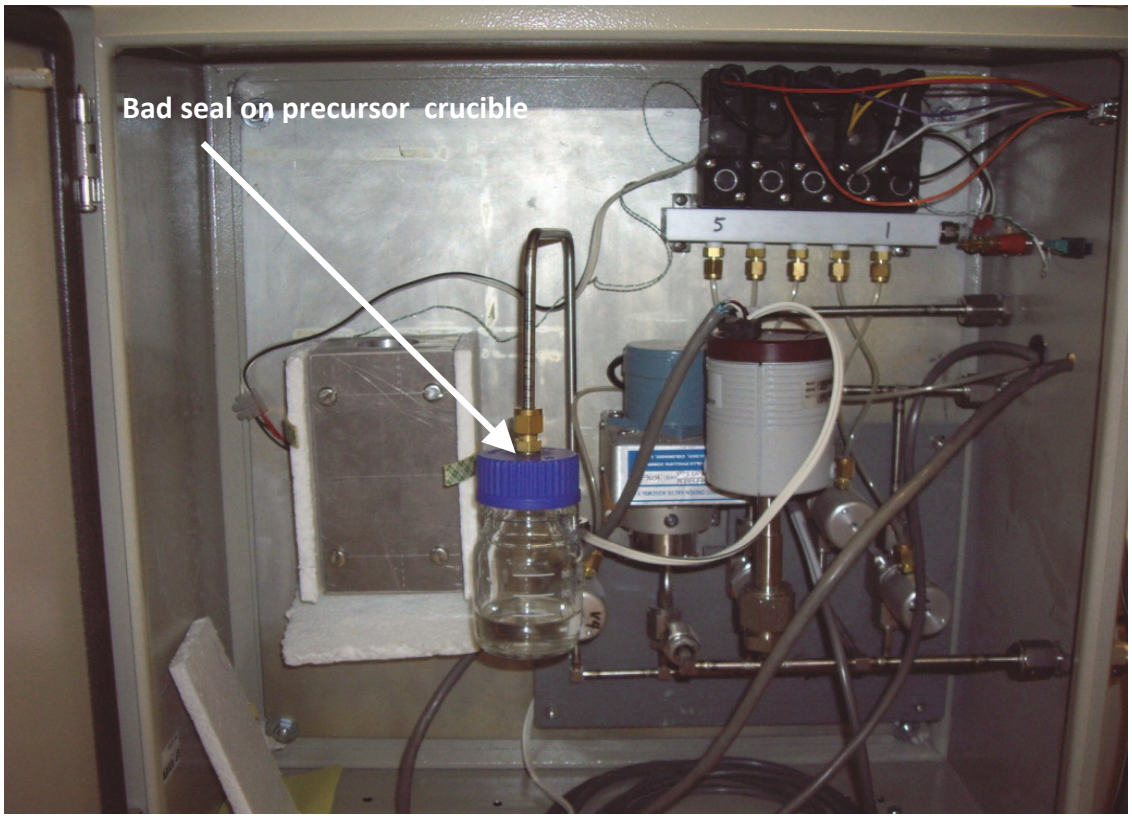

Figure 3.2: *Photograph of the initial precursor delivery system. Leaks in the system allowed contamination by atmosphere. Seal on precursor crucible was likely the worst leak.*

Irreproducibility of initial EBID experiments can be attributed to the system flaws listed above. However, the experiments were necessary for the flaws to become apparent. Since there is minimal data available in literature concerning the construction of a quality EBIED system, the hardware specifics necessary for quality EBIED had to be determined through experimentation.

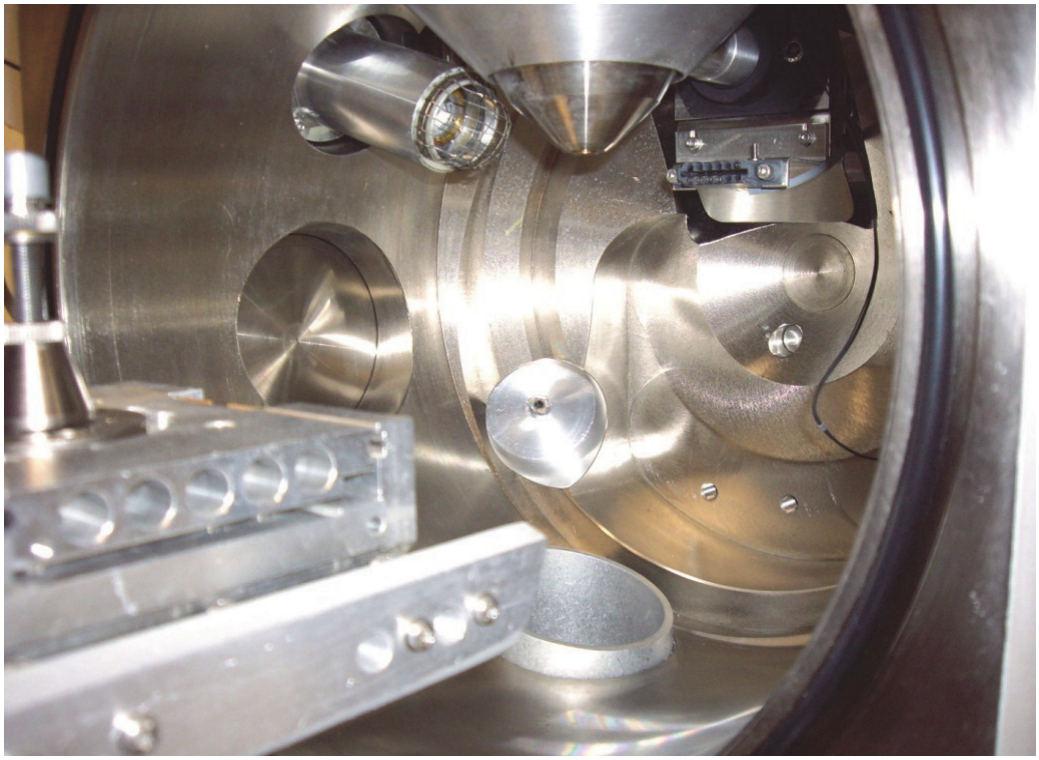

Figure 3.3: *Photograph of the interior of the XL30 ESEM specimen chamber. Many O-ring seals are present and they may add to precursor gas contamination by diffusion of atmosphere into chamber through O-rings.*

3.3 EBIED Experimental Apparatus Upgrades

Motivation

As discussed above, the experimental apparatus which was previously installed on the XL30 ESEM was rudimentary and resulted in irreproducible results. The presence of H_2O & O_2 vapours mixed with carbonaceous or silane precursors will have a dramatic effect on the EBID process. It is well known that H_2O is an etch gas for carbon [42]. It is also documented in literature that H_2O and O_2 have a large effect on the EBID process with organosilane precursors such as TEOS [68, 87].

Quantitative EBIED study requires a high purity precursor environment as well as stable pressures and beam currents. The decision was made to invest in a high quality system for EBIED study.

Vacuum Upgrade

The XL30 ESEM was previously equipped with an oil diffusion pump (ODP). Oil diffusion pumps have the advantage of high pumping speeds for all gases , long service life and low cost however back diffusion of the pumping oil inevitably results in contamination of the microscope chamber with organic vapours. This is unacceptable for quality EBIED experimentation. The organic contamination in the XL30 ESEM chamber was found to be significant due to several sources. These sources include: back diffusion of pump oil, residual carbonaceous precursor vapours and contamination introduced by the many people who used the machine for SEM imaging and compositional analysis.

A clean chamber with minimal contamination is essential for quality EBIED experimentation. The old oil diffusion pump was replaced by a new Edwards magnetic-bearing, turbo-molecular high vacuum pump. The two old rotary oil backing pumps were replaced by new Edwards scroll pumps to back the TMP. Custom vacuum components were manufactured and most vacuum lines replaced.

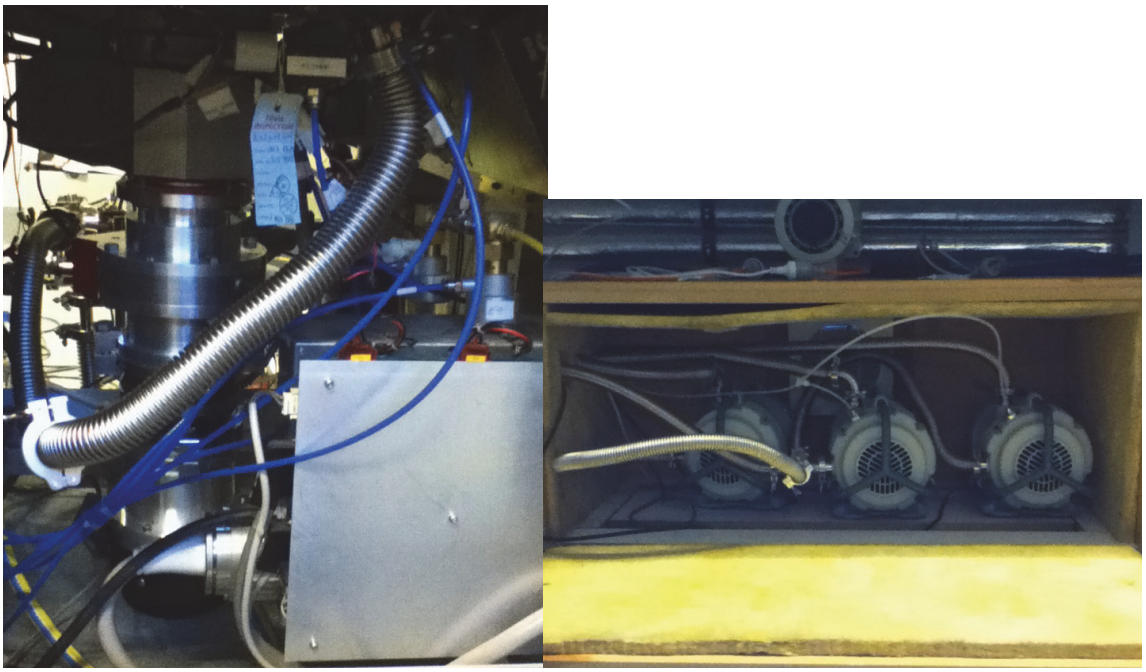

Figure 3.4 (left): *Edwards TMP installed on XL30 ESEM.* ***(right):*** *Edwards scroll pumps for TMP backing.*

Precursor Gas Delivery System

A new external precursor delivery system (PDS) was constructed. The use of only vacuum coupling radiation (VCR) fittings ensured leak-free connections between components. Precursors are housed in stainless steel crucibles and cooled by a Peltier array. Cooling allows adjustment of precursor vapour pressure. Precursor gas passes through an automatic needle valve to limit the flow. Stainless-steel gas lines connect directly to ESEM cell (discussed below) via a feed-through in the ESEM chamber wall. A 10 torr baratron measures pressure in the cell and provides feedback to the needle valve controller. A sealed, nitrogen atmosphere glove box was constructed to load precursor materials into crucibles. This minimises contamination of precursors before use. Gas lines of the system are heated to around 50 °C to increase desorption and increase vacuum prior to precursor flow. Gas line heating also prevents condensation precursor. The system ensures minimum contamination and stable pressures.

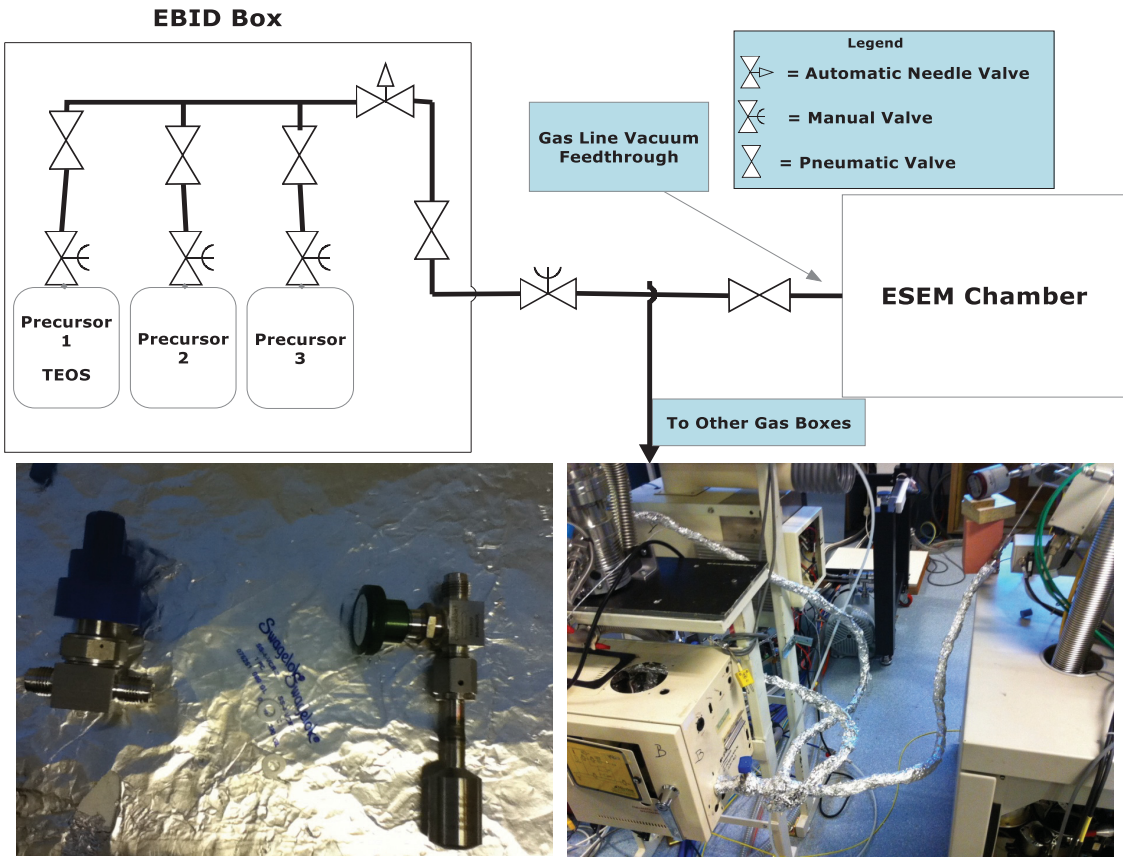

Figure 3.5 (Clockwise from top): *Precursor delivery system schematic (mixing gases can be added via line to other gas boxes), photo of system, precursor crucible with VCR valves and gaskets.*

The "ESEM Cell"

A custom sub-chamber was constructed of stainless steel and secured on the stage of the XL30 ESEM. A custom made "bullet" with thread at both ends holds the lid of the cell and the final column aperture. Sealing surfaces of cell are polished to minimise leakage. Within the cell the sample holder is positioned atop a heating element and has a built in faraday cup for measuring electron beam current. K-type thermocouples to measure substrate temperature are secured in the sample holder. The TCs also serve as grounding wires. A 1 mm thick stainless steel wire is positioned above the plane of the sample to serve as the GSED detector (when biased). Feed throughs in the cell walls allow heater current cables, TCs and GSED detector wire to enter cell with minimal gas leakage. High vacuum rated sealant resin is used to seal wires within feed throughs. Pipes welded into sidewalls of the cell connect with VCR fittings to precursor supply lines from external system. The setup allows ESEM pressures (0.1 – 10 torr) to be maintained inside the cell whilst the pressure in the ESEM chamber remains in medium to high vacuum. No residual contaminants present in the SEM chamber can diffuse into the cell due to the positive pressure gradient. This apparatus allows the highest possible level of control of gas composition.

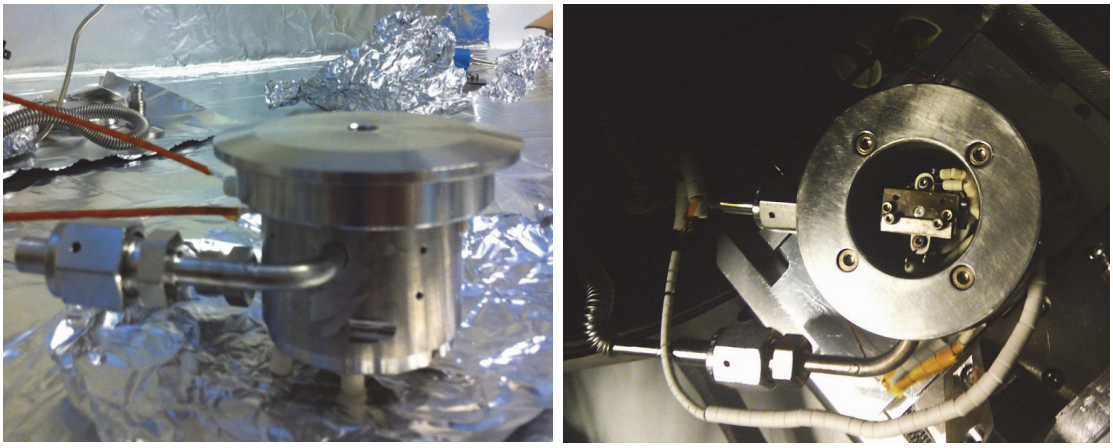

Figure 3.6 (Top): *Custom made "ESEM cell" constructed from stainless steel in science workshop at UTS. Cell is shown before installation inside the XL30 ESEM.* **(Bottom):** *ESEM Cell installed on XL30 ESEM stage. The cell lid remains fixed in place at the base of the electron column pole piece. The stage is moved in the positive z direction to close the cell during experiments.*

The ESEM cell was custom built to fit the dimensions of the XL30 ESEM vacuum chamber. The cell is small due to the constraints of the XL30 chamber. A larger cell is desirable and would allow more flexibility for customisation and instrumentation. A larger area for the sealing surface between the cell and lid would also be desirable to decrease gas leakage and increase stability. It is important to use non-magnetic stainless steel for cell and bullet construction as stray magnetic fields within the SEM chamber may cause electron beam astigmatism. A simple cross-sectional schematic of the ESEM cell is shown below. Dimensions are not included as these will vary depending upon the size A simple schematic of the sample holder is included in chapter 4.

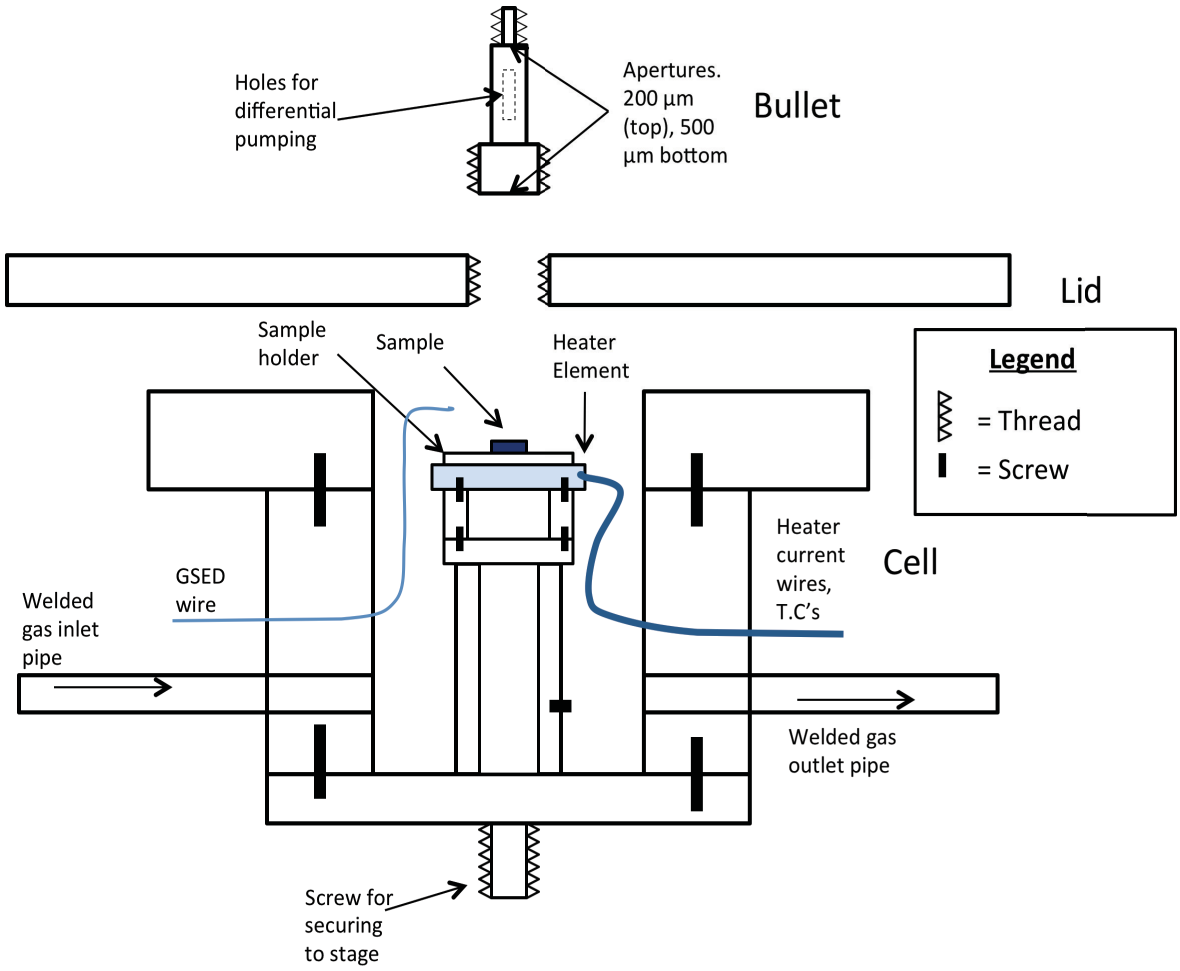

Figure 3.7: *Simple cross-sectional schematic of the ESEM cell.*

Other Upgrades

In-situ EBIED process monitoring system:

A system was developed to monitor EBIED experiments performed inside the ESEM cell on the XL30 ESEM. This consisted of the integration of a support PC with the control PC of the XL30 and the use of an NI USB 6251 BNC data-acquisition device to provide an interface between the raw voltage data collected during in-situ monitoring and the support PC. A program utilising the NI Labview graphical development environment was written and used to record the experimental data to a text file. Using this system it is possible to log data in real time for many different parameters of an EBIED experiment. These include: GSED detector current (I_e), transmitted specimen current (I_t), substrate temperature (T_s), pressure in cell (P_T), pressure in SEM chamber and bias voltage supplied to GSED detector. The really useful parameters to record are the emitted (GSED) and transmitted currents I_e and I_t. These allow the real time monitoring of the deposition or etching process.

Auxiliary Turbomolecular Pump:

A second TMP was used to pump the chamber outside the cell during EBIED experiments. The main TMP installed on the XL30 was used to pump the electron beam column only whilst this second TMP pumped the chamber outside the cell. This setup ensures the maximum positive pressure gradient from outside to inside the cell is maintained. An electrically operated valve and switch were installed on the microscope vent line to prevent unauthorised venting of ESEM due to power being cut.

Sample stage replacement:

The sample stage and the entire door assembly was replaced with a newer version (that came from a disused XL30 over at FEI headquarters in Oregon, US). The old stage had stopped functioning properly due to grit and contamination which had built up over years of use by many users.

Everhart-Thornley Secondary Electron Detector Replacement:

The old secondary electron detector was replaced with a newer one. This resulted in much better signal to noise levels.

Extensive Cleaning and Reassembly of XL30 ESEM:

The whole electron column was dismantled and each part cleaned as best as possible. An automatic plasma cleaning device was fitted to the microscope as a permanent attachment and used periodically. The whole chamber was thoroughly cleaned with IPA soaked lint-free wipes as well as 72+ hours plasma cleaning with O_2 plasma. Column and bullet apertures were replaced. All alignment and column optimisation procedures were performed. The extensive upgrading, cleaning and configuring procedures performed resulted in the XL30 performing better than it had in years.

EBIED Team Dedication of XL30 ESEM:

It was decided the XL30 would be dedicated to be used for EBIED experimentation only. This was necessary as constant venting as well as many samples of differing composition being placed in the chamber would make high quality EBIED experimentation impossible.

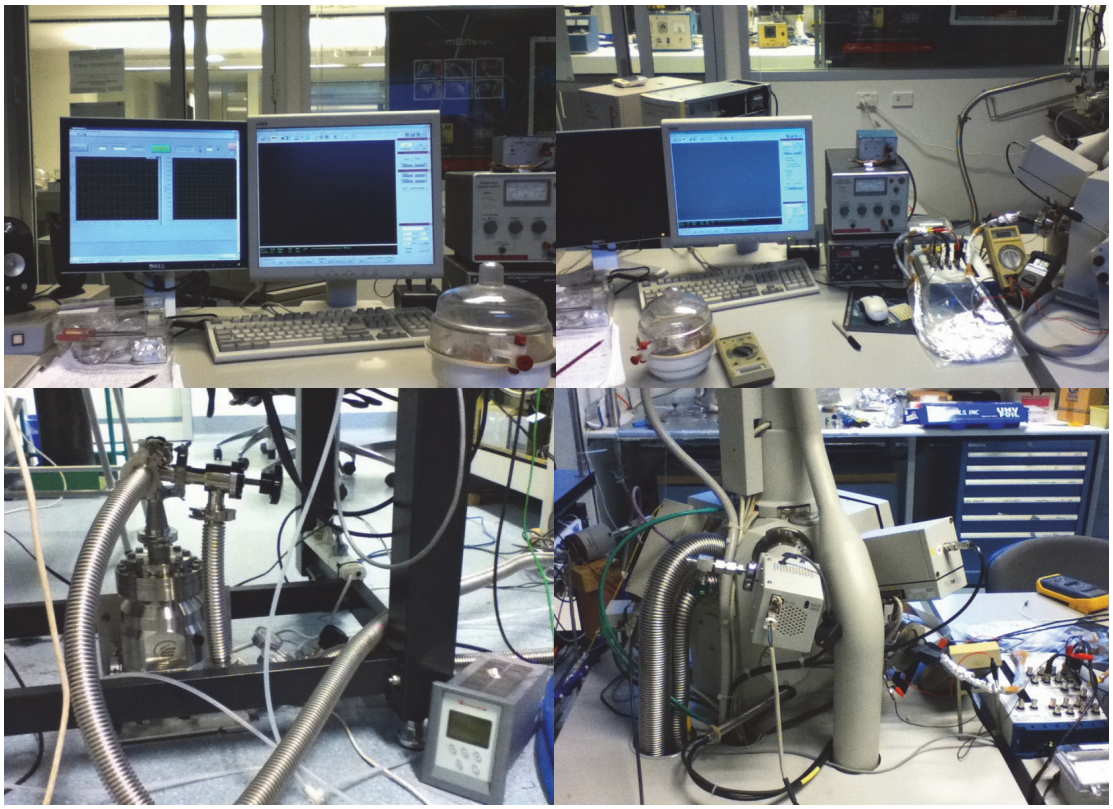

Figure 3.8 (Clockwise from top left): (1) *Screen of support PC that has been interfaced with control PC (screen on right) of XL30 ESEM showing screenshot of EBIED in-situ*

monitoring Labview program. ***(2)*** *Support and monitor hardware including NI USB 6251 BNC DAQ device, specimen current meter and heater power source.* ***(3)*** *Auxiliary TMP with controller and vacuum lines to microscope.* ***(4)*** *Plasma cleaner and secondary electron detector installed on XL30 ESEM.*

3.4 Performing ESEM Cell EBID Experiments

Considerable care has to taken when performing EBID experiments. The time-consuming construction of the complicated and expensive system described in the previous section was necessary for valid experimentation. Proper EBIED apparatus and experimental procedures are not so widely known and some contradictory results found in EBIED literature can be attributed to deficiencies in apparatus and procedure. Below I shall outline the procedure used for ESEM EBID experiments performed.

Ensuring System Cleanliness

Initial Measures Before First Precursor Loading:

It is necessary to minimise contamination in EBIED reaction chamber prior to experiment. Plasma cleaning and extensive pumping (72 hrs) was performed after every ESEM vent. Anything placed in chamber and all components of the external precursor delivery system were cleaned by a half hour ultrasonication in each acetone, iso-propyl alcohol and then de-ionised water followed by high temperature baking in an oven (standard cleaning procedure for all vacuum components). Baking of the substrate prior to EBID at around 300 °C for 12 hrs was always performed in-situ prior to experiment. All gas lines of the precursor delivery system (PDS) and the precursor crucible itself were heated to around 60 °C and pumped with the TMP on the XL30 until the pressure in the lines was the same as the base pressure of ESEM chamber (3 x 10^{-6} mbar). With a high vacuum of this level and a working precursor pressure of 0.05 torr for experiments, contamination due to residual gaseous species should be lower than 0.006 %. The TEOS precursor purchased from Sigma-Aldrich is specified at > 99.9 % purity and thus this purity should be maintained.

Sample Preparation and Precursor Loading:

EBID deposits were made on single-crystal Si (111) n-type substrates with a resistivity of 5 – 10 Ωcm. The thickness of the substrates is 1 mm. The following process was repeated for each substrate used for EBID experiments:

Fine scratches were made on the substrate using a diamond tipped pen to provide rough surfaces for focusing the electron beam during experiments. The substrate was then immersed in a beaker of acetone and ultrasonicated for a half hour. This was then repeated using isopropylalcohol followed by rinsing with de-ionised water and drying with strong nitrogen flow. It was then placed on the sample holder of the ESEM cell and baked overnight in high vacuum at around 250 °C. This process should ensure minimal contamination introduction to the system via insertion of the substrate and also provide a flat surface free of particles to perform EBID upon.

The precursor tetraethoxysilane is liquid at room temperature with a vapour pressure of around 1 torr. It will react with water vapour and must not be exposed to atmosphere whilst being transferred to the crucible. A sealed glove box was constructed for this purpose. The precursor crucible was cleaned, baked and pumped to high vacuum (3 x 10^{-6} mbar). It was then sealed with a manual VCR valve and transferred to the glove box along with sealed precursor bottle and clean pipettes. The precursor is then transferred to the crucible under pure N_2 atmosphere, the crucible sealed and reconnected to the PDS. The precursor is then run through the PDS and ESEM cell for up to an hour to remove any N_2 in the crucible. This process should ensure that the purity of the precursor is not compromised.

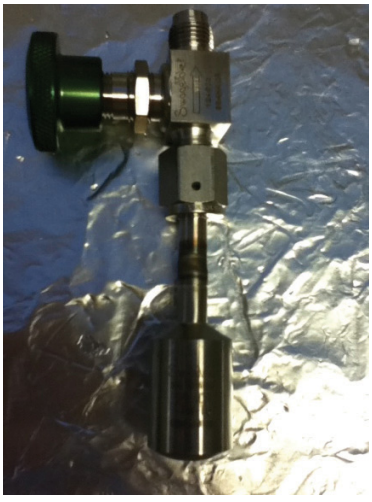

Figure 3.9 (previous page): *N_2 atmosphere glove box used for precursor loading (left), precursor crucible used to hold TEOS precursor (right).*

Standard EBID Experimental procedure

Before each experiment was performed the microscope and gas lines were pumped at least overnight to ensure that the maximum vacuum conditions (≈10^{-6} mbar) are present before precursor is introduced. This will ensure the minimum amount of contaminants incorporated with precursor gas.

Stabilisation of electron beam:

The electron beam was run in spot mode inside faraday cup (to measure beam current change) for up to 3 hours prior to each experiment. This was found to be necessary as the beam current decays with time and a stable beam current is a necessity for any EBIED experiment. The rate of decay can be significant at first but decreases with time and is generally negligible after 3 hours of beam operation. The reason for this long period of instability is unknown. A possible reason is thermal disequilibrium due to electron beam induced heating of certain components in the column and thermal equilibrium being reached after hours.

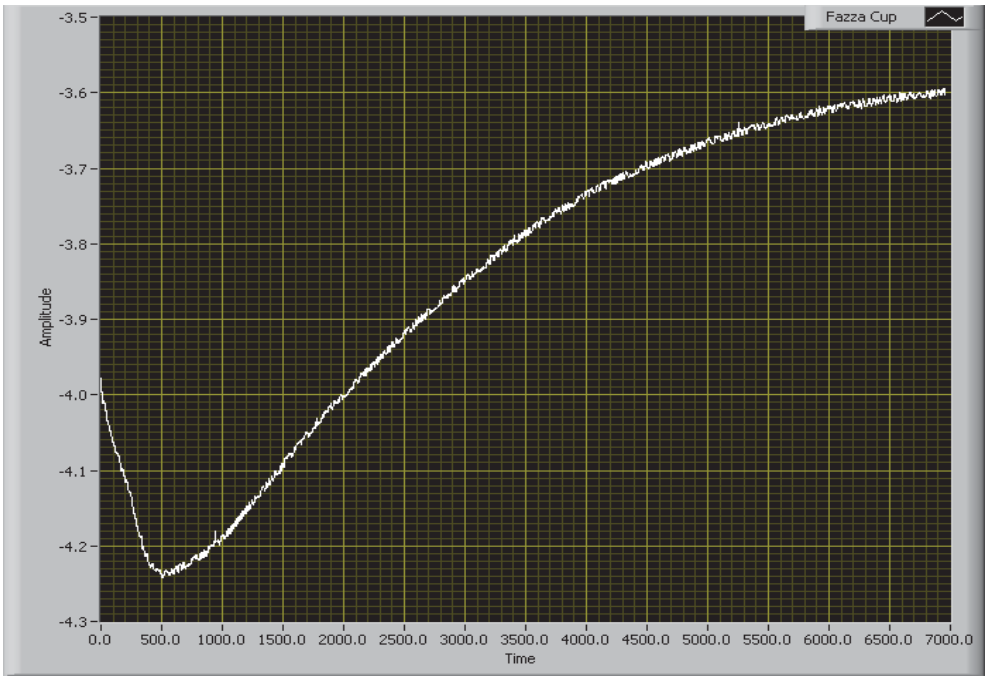

Figure 3.10 (previous page): *A typical beam current profile as the column reaches stability. The electron beam current is negative so the profile indicates beam current decay. When the decay rate reaches a low value experiments can proceed.*

EBID experimental Procedure:

A silicon substrate is placed in ESEM cell days prior to beginning a set of experiments and is baked at around 250 °C in high vacuum for at least 10 hours. On the day of an experiment the electron beam is turned on in the morning. Once the electron beam has reached stability the ESEM cell is then closed by moving the stage in the negative z direction approximately 6 mm. The working distance/electron beam gas path length is ≈ 14 mm and cannot be changed. The beam current is then measured in high vacuum before and after the EBID experiment to determine the current used for the EBID growth and the level of current decay (generally negligible after ≈ 3 hrs operation). The auxiliary TMP (on auxiliary vacuum line) is then turned on and N_2 ballast opened to flow. The N_2 ballast is a low flow rate of N_2 that is added to the TMP pump line in order to mix with the TEOS precursor in a 10:1 ratio (N_2: TEOS). This ensures minimisation of damage to the TMP. The chamber isolation valve E7 is then closed manually and the auxiliary vacuum line opened by opening valve E4. This configuration allows the use of 2 TMP's with the primary TMP pumping the electron beam column and the auxiliary TMP pumping the ESEM chamber.

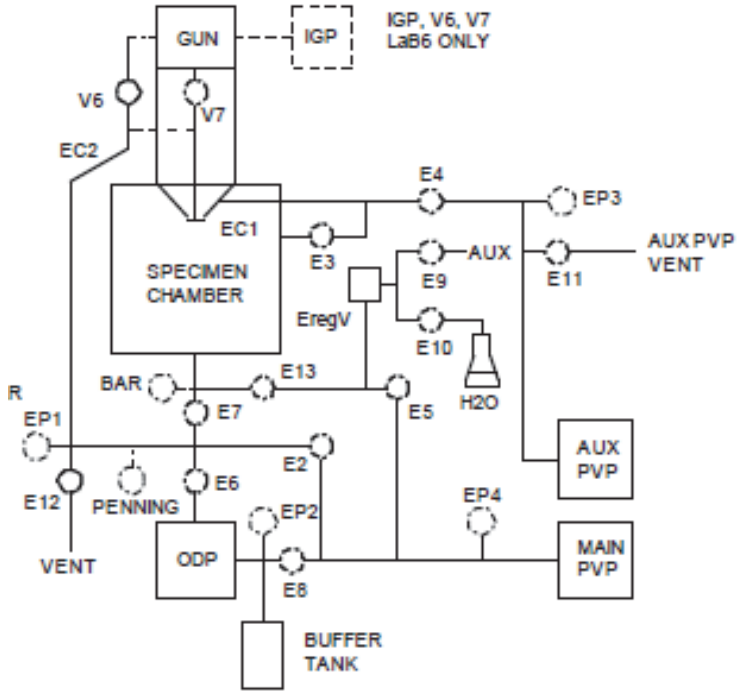

Figure 3.11 (previous page): *Simple Schematic of XL30 Vacuum System. E indicates valve while EP indicates a thermocouple vacuum gauge. The ODP has been replaced with a TMP and the auxiliary TMP is on aux PVP line. Auxiliary scroll pump backs auxiliary TMP.*

The needle valve controller is then initiated and valves opened to allow precursor flow. A baratron measures cell pressure and provides feedback to the needle valve controller. High precision control of the cell pressure (to within 0.001 torr) was made possible with this configuration and reproducible constant precursor pressures were achieved. After the precursor pressure has stabilised the beam is focused and EBID depositions are performed. The beam is generally left in spot mode near the top of the frame whilst preparing for deposits to be made rather than using the beam blanker. This has resulted in deposits in the background seen in most SEM images of EBID experimental sets. Using beam blanker would result in EBID within electron beam column and cause problems. Experiments were performed as a function of deposition parameters, substrate temperature (T_s) and with extra mixing gases such as O_2.

In-situ Monitoring of EBIED experiments

During each EBID experiment, the transmitted (I_t) and emitted (I_e) current are measured and recorded. Both signals provided much the same information and the I_t curve generally had a better signal to noise (S2N) ratio than the I_e curve. The changing I_t and I_e signals provide much information about the EBID growth. It also provided a means of indicating process errors as they occurred. e.g pressure drop due to precursor supply being depleted, change of focus due to slight cell movement. Thus errors during deposition would not pass unnoticed. Typical I_e and I_t curves collected

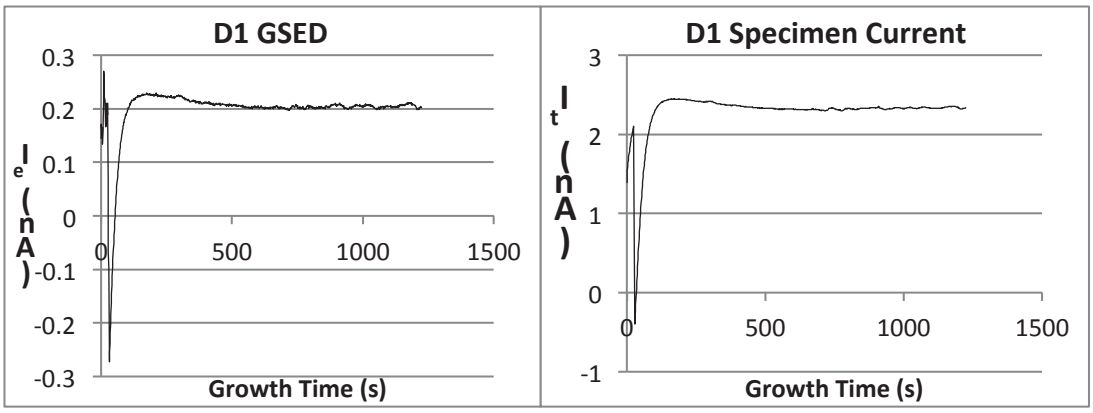

Figure 3.12a (previous page): *Typical I_e curve (left) and I_t curve (right) collected during FEBID with TEOS.*

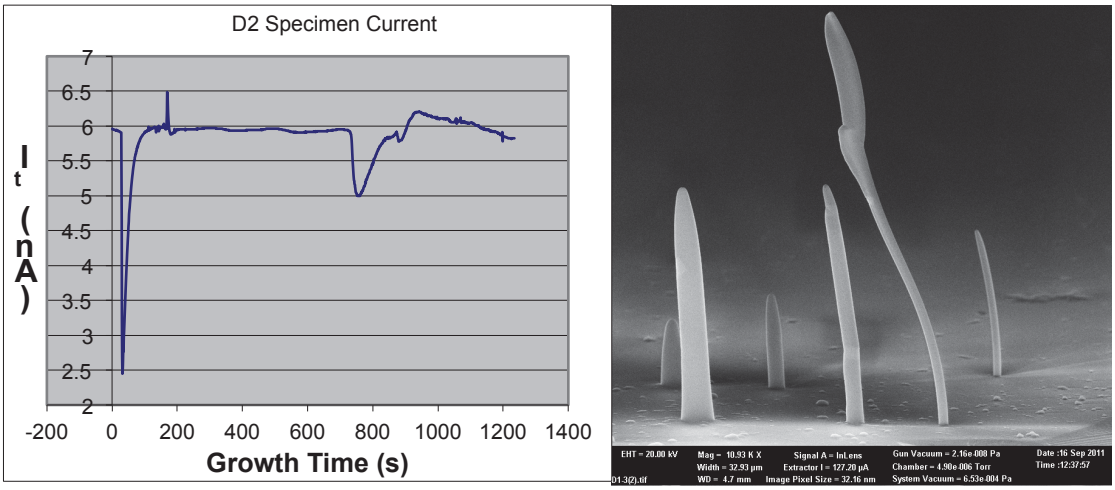

Figure 3.12b: *I_t curve indicating unexpected process/error (left) during EBID. In this case, proximity charging effects during EBID of middle pillar (image on right) caused bending of pillar already deposited at right. Pillar bent towards the growing pillar until it overshadowed it and intercepted beam. Growth continued atop the bent pillar D1 instead of the middle pillar D2.*

Immediate detection of experimental process errors is essential for any scientific experiment. For the case of EBID experiments much time is saved by in-situ monitoring. Without the monitoring system, experimental errors would not be detected until after deposition of an entire experimental set for the system I have used for the work of this thesis. Experimental errors are quite common with my system and thus much time was saved by immediate error detection. The in-situ monitoring system is an essential part of the EBIED system used for my experiments and I recommend any experimentalist to construct a similar system if intending to perform experiments in EBIED.

3.5 EBID Experimental Analysis Procedures

After carrying out upgrades of the XL30 ESEM and construction of other EBIED equipment followed by extensive troubleshooting and system optimisation, the system was finally ready for EBID experimentation. An experimental and data analysis procedure was developed and refined over the course of experimentation. Generally several EBID experimental sets were deposited on a single substrate using the XL30 EBIED apparatus. The machine was then vented and substrate transferred to an imaging stub which holds the substrate vertically without adhesive. The sample was then transferred to another SEM for high-resolution imaging. The transferral procedure is a delicate matter and a steady hand is necessary to successfully transfer the substrate without damaging the delicate EBID deposits. Several times EBID sets had to be repeated due to damage incurred during transferral.

High resolution, tilted imaging was performed on the Zeiss LEO SEM. It is equipped with a field emission gun (FEG) and capable of 1 nm resolution. Images were recorded at a variety of tilt levels and high contrast images of single deposits (at ≈ 0° tilt) recorded with high pixel resolution for volumetric analysis. The substrate was then transferred to a flat sample holder for top-down imaging. Images were usually taken at 20 kV with the high-vacuum SE detector however BSE imaging and variable voltage SE imaging were sometimes performed as these techniques can provide information on properties such as density and compositional variation.

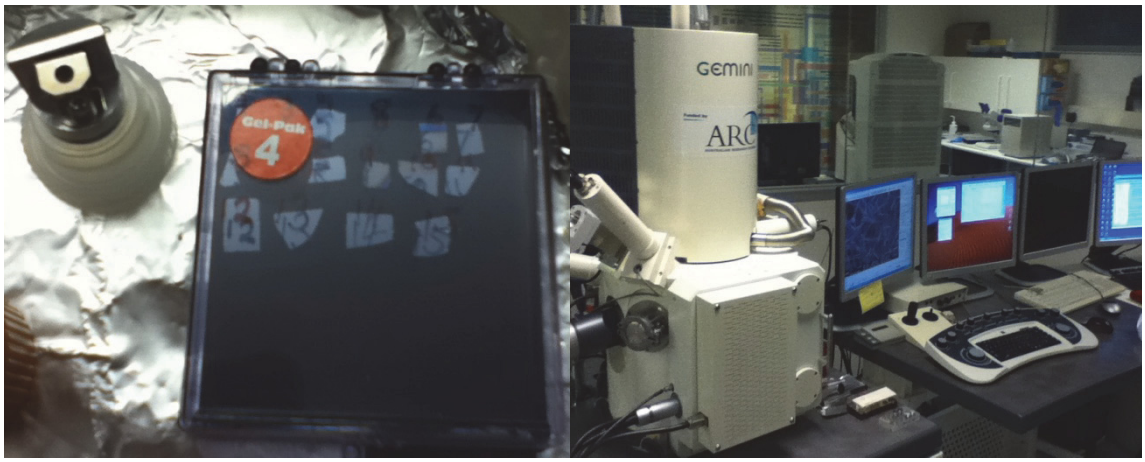

Figure 3.13 (previous page): *(Left): 90° Tilted imaging sample holder and gel-pack used to store substrates after imaging. (Right): Zeiss LEO FEG SEM used for EBID deposit imaging.*

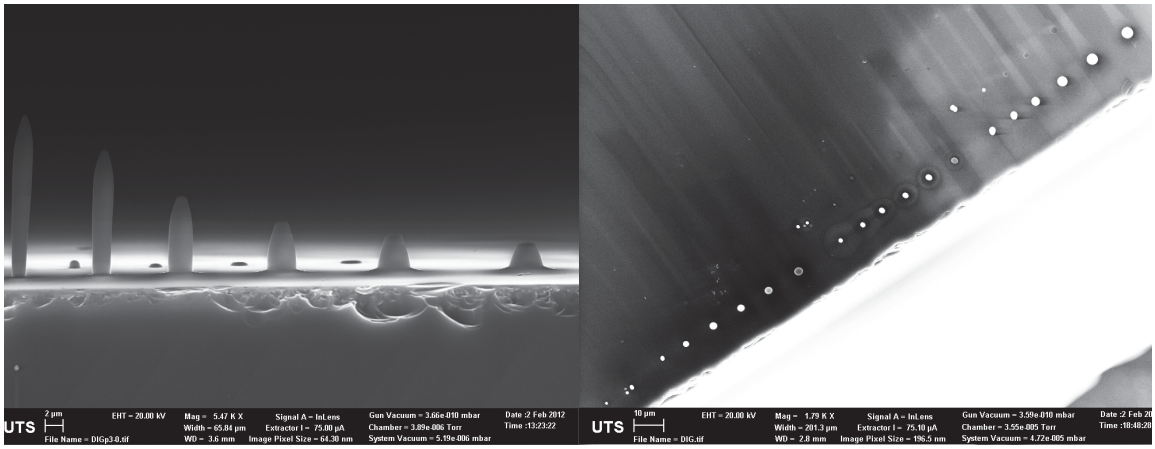

Fig. 3.14: *Examples of images taken with the ZEISS LEO FEG SEM. (Left): Horizontal imaging via 90° Tilt. (Right): Top-down imaging with substrate on flat sample holder.*

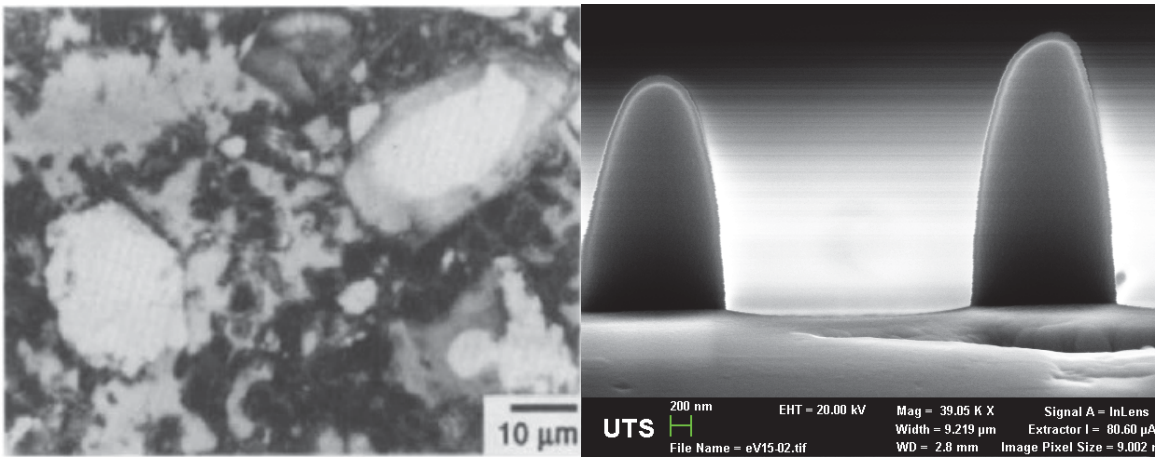

Figure 3.15 *(Left): BSE image of cement paste. Contrast is a function of atomic number in BSE imaging and thus regions of different elemental composition can be directly imaged. (Right): Image of deposits which had been coated in a layer of SiO_2 by TEOS CVD after deposition. With a 20 kV beam the SiO_2 layer can be penetrated and imaged. With a low energy beam the deposits would appear uniform.*

Image Analysis Procedure

After images were taken on the Zeiss SEM, they were analysed to estimate the deposit heights, widths, volumes and surface areas. Heights and widths were directly measured from high contrast, high resolution images using Image J. To estimate the volume and surface area I created a program using Wolfram Mathematica™. High contrast & resolution images were first transformed into binary images using ImageJ. The co-ordinates of each pixel which comprises the image of the deposit were then exported as a text file. The program measures the number of x pixels for each y value and calculates volume by adding the volume of a cylindrical slice for each y value. As long as a deposit is symmetrical about the z-axis then the calculated volume will be close to the true volume. Spot – mode EBID deposits are generally symmetrical about the z-axis.

An extensive data set was created for each EBID experimental set. The data includes charts of I_e, I_t versus deposition time (I_e and I_t curves) as well as a table recording the height, width, volume and surface area of each deposit. A record of all experimental parameters used for deposition of each set is also included.

Figure 3.16: *(Left): High contrast & resolution image for volumetric analysis. (Right): The image on the left is converted to a binary image where only the pixels of the deposit are black. The co-ordinates of the black pixels are exported as a text-file for input to the volumetric estimation program*

4. EBID Adsorption Kinetics

4.1 Abstract:

EBID experiments are performed with TEOS precursor as a function of the substrate temperature during growth (T_s). Contrary to existing models of EBID, the growth rate was found to increase after an initial decrease as T_s is increased. Furthermore, the peak growth rate at around 285 °C is around twice the rate at room temperature. Activated dissociative chemisorption of TEOS precursor at higher T_s resulting in an increase in precursor coverage is proposed as the mechanism behind enhanced growth. A model is presented which accounts for chemisorption, physisorption and adsorption state transitions of precursor molecules. The model reproduces the qualitative trends observed experimentally in simulation and displays excellent fit to experimental results. The purity of deposits grown at high T_s is found to be much higher than with EBID at room temperature. The results indicate that EBID can be performed at high T_s to achieve high purity and growth rate with a precursor which undergoes activated chemisorption.

4.2 Introduction:

As mentioned previously EBID can be likened to a localised CVD process. Thermal CVD (pyrolysis), allows for simplistic modelling as predictions upon which molecular bonds will be broken can be made easily by correlating bond strengths to available thermal energy in the system. The case of EBID however, is inherently much more complex than thermal CVD as all bonds of a precursor molecule can be broken by the wide energy range of electrons produced during electron beam at typical SEM accelerating voltages. Many different neutral and ionised fragment species can be created under electron irradiation of the typically complex molecules used for EBID precursors. Some species will react further to form yet more species. Furthermore, other electron induced processes apart from dissociation will occur simultaneously such as electron beam induced heating (EBIH), electron stimulated desorption (ESD), molecular excitation and photon production of various energies [70]. This myriad of processes occurring during EBID creates difficulties in developing an accurate model.

The model presented in chapter 1 is the basis for most EBID modelling work yet many simplifications and assumptions are involved in the model.

Studies involving EBID as a function of T_s have previously almost exclusively focused upon improving the purity of EBID structures [71, 72]. Mulders et. al. [53] studied compositional changes of EBID deposits grown at different T_s values from 25 – 360°C with a variety of precursors including TEOS. However, TEOS was studied in the range 25 – 150 °C only. EBID rates were reported to decrease with increasing temperature for all precursors. Indeed, growth rates are generally assumed to decrease with increasing T_s in EBID literature.

It would seem that adsorption kinetics, which play a vital role in the EBID process have not been considered in detail in previous EBID studies. Exclusive molecular physisorption of precursors on substrate surfaces is a standard assumption. This accounts for the general assumption of decreasing EBID rates with increasing T_s as coverage of physisorbed molecules on a surface decreases with increasing T_s. Li et. al. studied the growth rate dependence upon T_s for WF_6 precursor in a small T_s range (-30 – 75 °C) and their data is consistent with exclusively molecular physisorption. Measuring deposition yields as a function of T_s can provide insight into the adsorption kinetics of a precursor. A greater understanding of the adsorption kinetics of a precursor is desirable for accurate modelling of EBID, CVD or any similar process which utilises the precursor. It is also worthwhile simply as a valid contribution to surface sciences.

In this chapter, defocused beam EBID experiments are performed over a broad substrate temperature (T_s) range with TEOS precursor. The results provide insights into the adsorption kinetics of the TEOS molecule with the SiO_xC_y TEOS EBID material surface. Comparison of the results with results published by other authors involving TEOS, from the fields of CVD and surface science leads to conclusions about the adsorption kinetics of the system and the development of an extension to the standard model of EBID, which provides a mathematical framework for taking detailed adsorption kinetics into account for EBID modelling and future experimentation.

4.3 Experimental:

EBID experiments were performed with the ESEM cell sub-chamber configuration described in chapter 3. Depositions were made on single crystalline Si (111) with native oxide layer. The substrates were clamped upon a grounded, stainless steel sample holder which is clamped atop a ceramic heater element capable of reaching high temperatures via resistive heating. The sample holder is polished on both sides and all clamps are tight to ensure good thermal contact between substrate and holder. A k-type thermocouple is secured by a screw within the sample holder to measure the substrate temperature (T_s). Tests were performed utilising multiple thermocouples to confirm good thermal contact between holder and substrate. A Faraday cup built into sample holder connects to a picoammeter via the grounding wire and is used to measure the beam current (I_b). The emitted current (I_e) collected by the GSED detector and the transmitted current through the substrate and sample holder (I_t) are logged during deposition to monitor the deposition process (refer to chapters 2 & 3 for more information on the *in-situ* monitoring system).

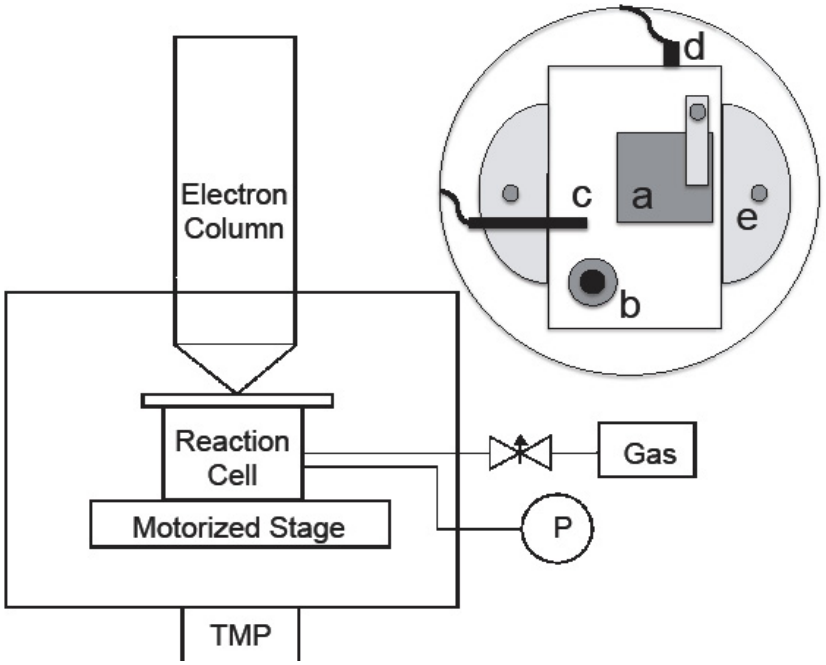

Figure 4.01: *Schematic of the system used for EBID. Inset at top-right is a representation of the sample holder.* ***a:*** *substrate,* ***b:*** *Faraday cup,* ***c:*** *GSED detector wire,* ***d:*** *K-type thermocouple for T_s measurement, grounding and specimen current flow,* ***e:*** *resistive heating element.*

The precursor gas TEOS and a 25 keV electron beam which traverses a gas path length of ≈14 mm to the substrate was used for all depositions. The total cell pressure (assumed to be > 99 % TEOS) was 0.05 torr (≈7 Pa) for all experiments. EBID was performed with a defocused beam as a function of beam diameter at room temperature (RT, 25 °C) and with a constant beam diameter as a function of T_s.

Two sets comprise the experimental data for this chapter. The EBID parameters for each were: **Set 1:** EBID as function of defocus (beam diameter), I_b: 3.5 nA, growth time t_g: 20.5 minutes, $\Delta d_{f\text{-}s}$: 0 - 0.25 mm (7 deposits). **Set 2:** Defocused EBID, function of T_s (25 – 551 °C), I_b: 9 nA, t_g: 30 minutes, $\Delta d_{f\text{-}s}$: 0.3 mm (7 deposits). Several other sets similar to these two were performed to check reproducibility of observed effects. All effects were observed to be reproducible. These two sets were chosen from several possible candidates. The beam diameter was varied by changing the focal position of electron beam to substrate distance ($\Delta d_{f\text{-}s}$). EDS was performed to analyse composition of deposits in set 2.

Depositions were made 30 – 45 minutes after each temperature increase to allow T_s to stabilise and the system to reach thermal equilibrium. Stability of substrate temperature was confirmed by monitoring T_s during deposition. Defocusing of the beam was performed with FEI software which allowed precision control of the change in focal point in order to achieve reproducible beam diameters. Other details of the general procedure developed for high quality EBID experimentation can be found in chapter 3. In this work a “Defocused beam” refers to a wide electron beam which can be modelled by a top hat function and not a broad, diffuse electron source.

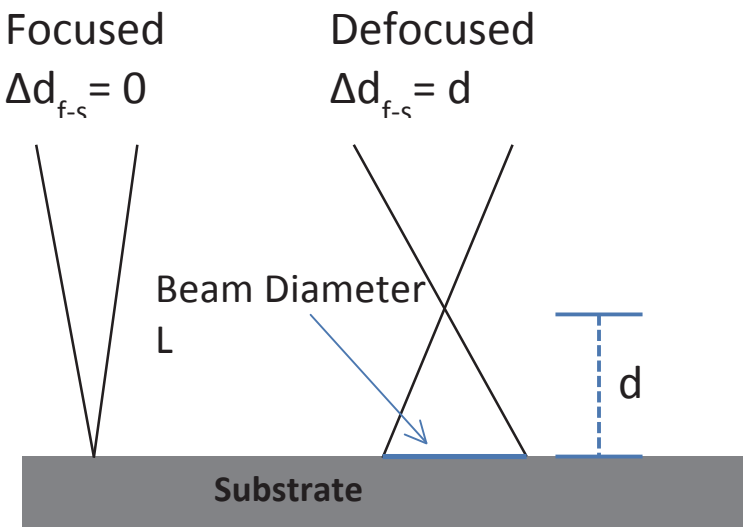

Figure 4.02: *A schematic illustrating focused and defocused electron beam sources. A defocused beam is wide with diameter = L but is not a diffuse broad beam electron source, as is used for electron stimulated desorption experiments.*

4.4 Results and Discussion:

Defocused beam EBID

Performing EBID with a defocused beam can simplify the analysis of EBID results. An approximately uniform e^- flux profile across the irradiation region can be assumed. A non – uniform electron flux across the irradiation region will result in non – uniform growth rates and internal precursor diffusion within the irradiation region. In order to validate a theoretical model, experiments must be devised with the minimum amount of unknown parameters. Hence it is desirable to use a defocused e^- beam.

A top hat beam profile can model a defocused beam whilst a Gaussian is used to model a focused beam. The functions shown in figure 4.1 below are intended to assist the reader in visualising the difference between focused and defocused electron beams and their effects on the EBID process. It should be apparent that using a defocused beam will simplify the EBID process as effects caused by a non – uniform electron flux across the irradiation region do not need to be considered.

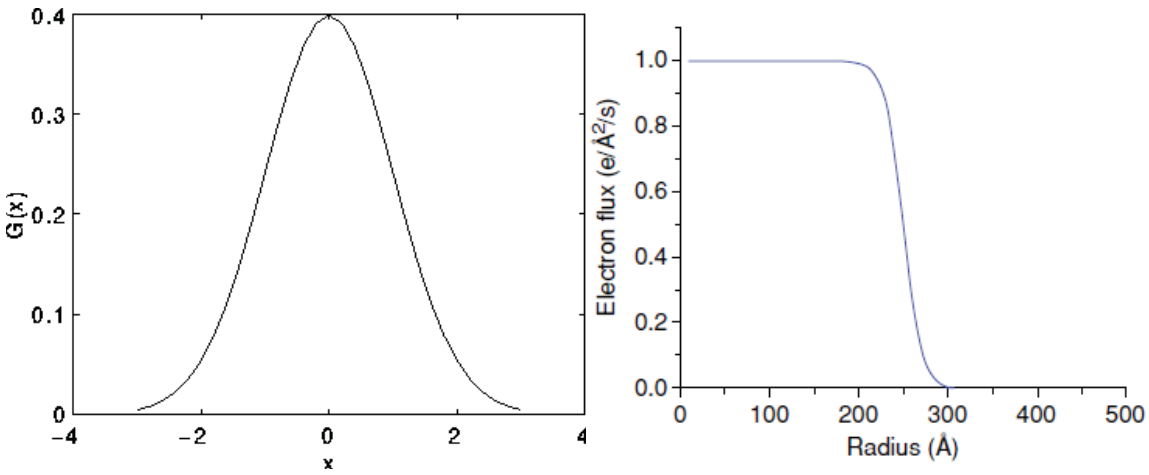

Figure 4.1: *Examples of the functions used to approximate electron beam profiles for modelling purposes for the focused and defocused case. (Left): Gaussian profile for a focused beam where G(x) represents the electron flux. (Right): Top-hat beam profile for defocused beam. From [40].*

The electron flux is much lower for a defocused beam than for a focused beam of equal beam current. As a result there will be less precursor depletion within the irradiation region. Less precursor depletion means less diffusion of precursor molecules into the irradiation region. High levels of diffusion can result in non-uniform growth rates across the irradiation region. For accurate quantitative analysis of growth rates with increasing T_s uniform growth is necessary. Furthermore, effects such as EBIH and uncontrolled charging, which can be significant for the focused EBID (FEBID) case can often be considered negligible for defocused EBID. Lateral growth and precursor diffusion are minimised. Defocused EBID is the simplest EBID process and is thus a better choice for experimental validation of an EBID model.

Defocused EBID at Room Temperature

Initial experiments were performed to determine the EBID growth behaviour using a defocused beam at RT. A reproducible trend was observed whereby an initial increase in growth rate followed by a large decrease occurred as the beam diameter was increased. This behaviour is summarised in figure 4.2 below.

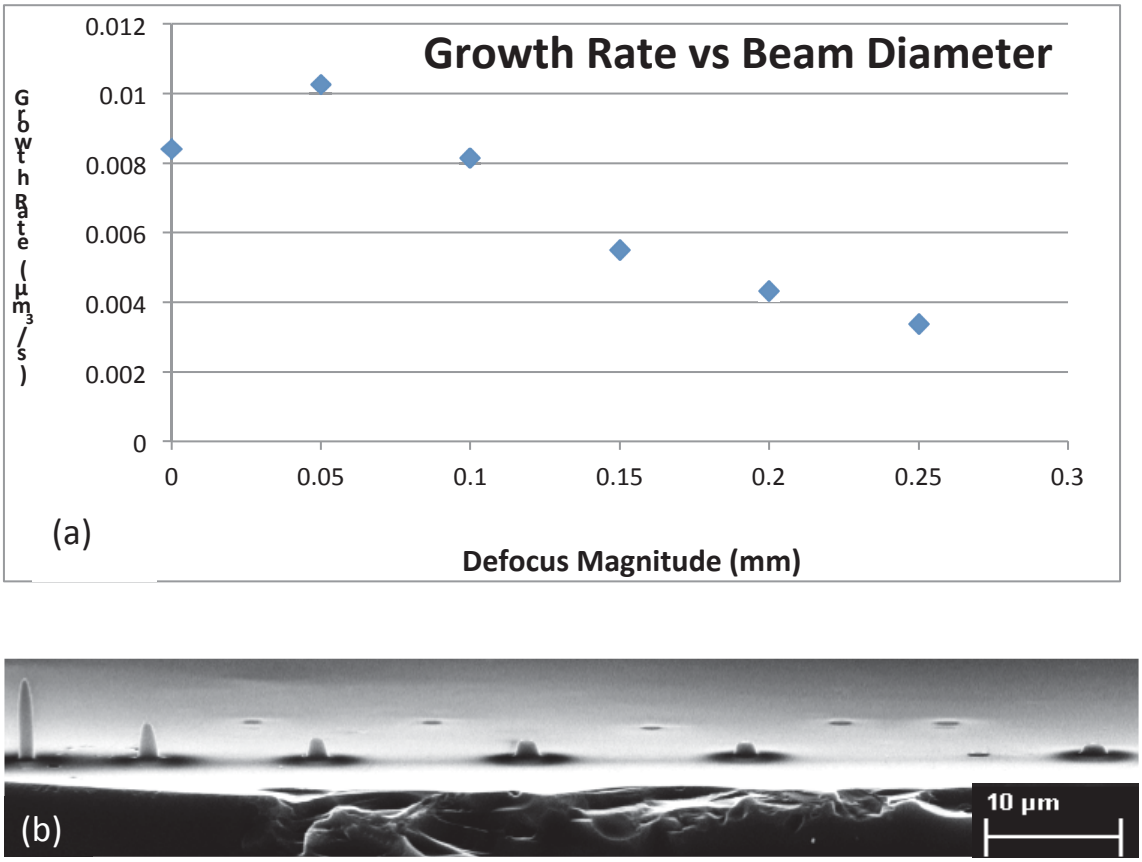

Figure 4.2: (a) *Reproducible trend in growth rate observed when perfomring EBID with increasing electron beam diameter.(b) SEM image of experimental set used for above figure.*

The initial increase is attributed to a decrease of precursor depletion in the irradiation region. This occurs as the electron flux decreases as the beam diameter increases (increasing defocus) for a constant total beam current. Decreasing precursor depletion increases the efficiency of the EBID reaction in terms of incident electrons per dissociation event. Since the same total beam current is incident over a wider area inducing a more efficient EBID reaction, the total growth rate is increased.

Effect of Substrate BSE Yield

The decrease in growth rate observed after the initial increase is attributed to a difference in the backscattered electron (BSE) yield between the substrate and the EBID material. The BSE yield of a material is proportional to the density, average atomic weight and average atomic number of the material. As an EBID deposit grows the electron beam interaction volume will become increasingly contained within the deposit. If a difference in BSE yield (γ) exists between the substrate and EBID deposit, the total electron yield emitted from the deposit surface will be proportional to the proportion of the interaction volume that is contained within each material (EBID deposit and substrate) and the difference in BSE yield between the two materials:

$$\gamma_T \, \alpha \, (\gamma_e - \gamma_s)(1 - p_s), \qquad \gamma_T = k(\gamma_e - \gamma_s)(1 - p_s) \tag{4.01}$$

where: γ_T, γ_e and γ_s are the total, EBID material and substrate material BSE yields respectively, p_s is the proportion of the electron beam interaction volume contained within the substrate and k is a material dependant constant.

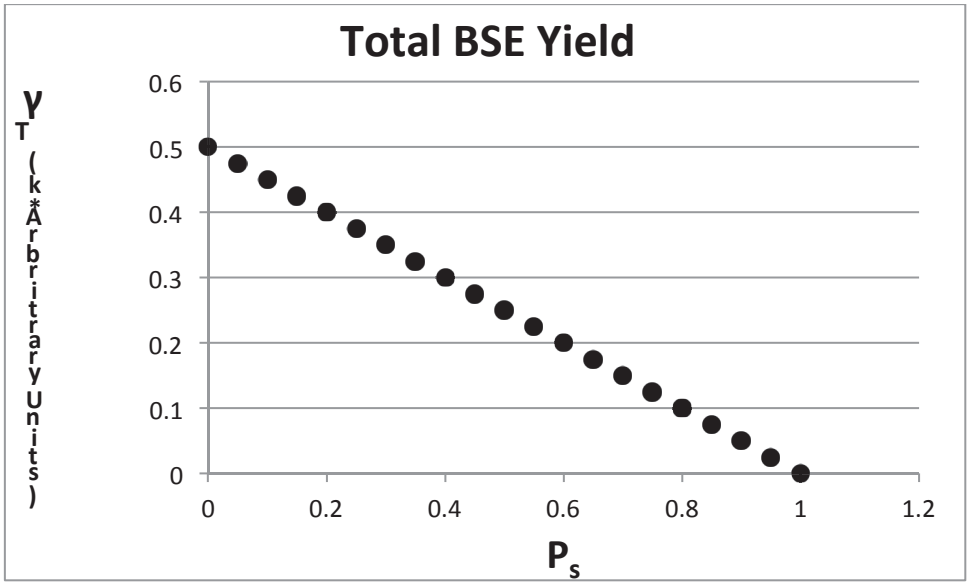

Figure 4.3: *Calculated total BSE yield using the simple model described above (exp. 4.01). Assumed input parameters: γ_s = 1, γ_e = 1.5. The values for γ_s and γ_e were arbitrarily chosen assuming that the EBID material has a higher BSE yield than the substrate. This is justified as TEOS EBID deposits are much brighter than the substrate during BSE imaging.*

The vertical growth rate of an EBID deposit decreases as the diameter of the beam used increases. This is mainly due to the decreasing electron flux. The growth will move towards the EL regime. As the vertical growth rate decreases, a larger proportion of the interaction volume will be contained within the substrate for a larger proportion of the growth time. Thus an EBID deposit grown with a wider beam will have a larger proportion of its growth determined by the BSE yield of the *substrate material.* This affect is attributed as the main contributing factor to the decrease in *volumetric growth rate* with increasing beam diameter. Deposits formed by a wider beam will have a lower BSE and SE2 flux emitted from the surface during EBID resulting in a lower growth rate. The simple model presented above predicts a linear decrease in BSE yield. It is clear that the model does not account for all factors affecting the system yet accounts for the most important parameter.

The decreasing proportion of the EBID deposit's surface area which is made up by the sidewalls with decreasing aspect ratio is another factor. Primary electrons have a higher chance to cross the deposit/vacuum boundary twice for higher aspect ratio deposits. A primary electron will initially penetrate the growing deposit at the tip and can then be scattered at a non-zero angle and exit the deposit through a sidewall. The higher the aspect ratio, the lower this scattering angle will have to be. SEs will be emitted by each interface crossing thus increasing the total electron flux for a higher aspect ratio deposit. The I_e and I_t curves collected during EBID display the decreasing vertical growth rate and allow a rough estimation of the proportion of the interaction volume in each material.

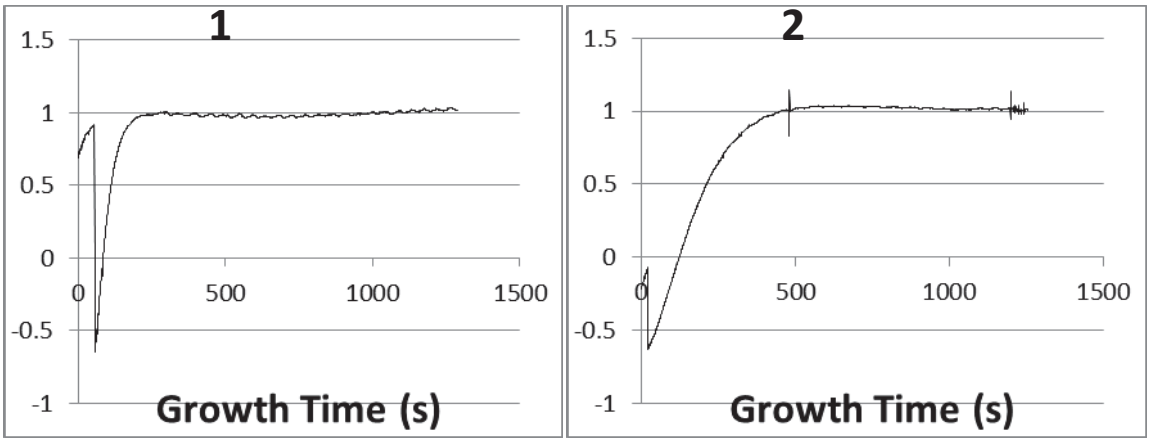

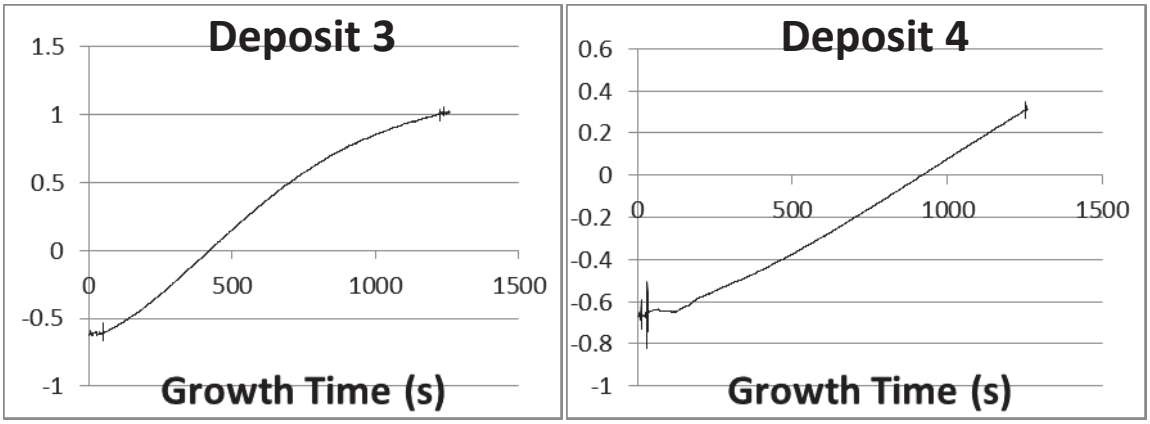

Figure 4.4: *Transmitted current curves, I(nA) versus growth time (s) collected during deposition of set shown in figure 4.2. Saturation of the curves corresponds to the height where the interaction volume is contained completely within the EBID deposit. Thus the growth of deposits 3 & 4 have a portion of their growth determined by the substrate BSE yield for a much longer time than deposits 1 & 2.*

Defocused EBID with Increasing T_s

These experiments were performed with a constant beam diameter to avoid the effects discussed above. Analysis of changes in EBID rates with increasing substrate temperature can be used to gain an insight into the adsorption kinetics of an EBID system. A continuous decrease in the EBID growth rate is predicted by the standard model with increasing T_s. This is predicted as the standard model assumes a single adsorption state. Within a single adsorption state, the adsorbate concentration present upon the surface is assumed to decrease with increasing T_s. The assumption is not valid if the nature of the adsorption changes with increasing T_s. The results observed were in direct contradiction of this assumption.

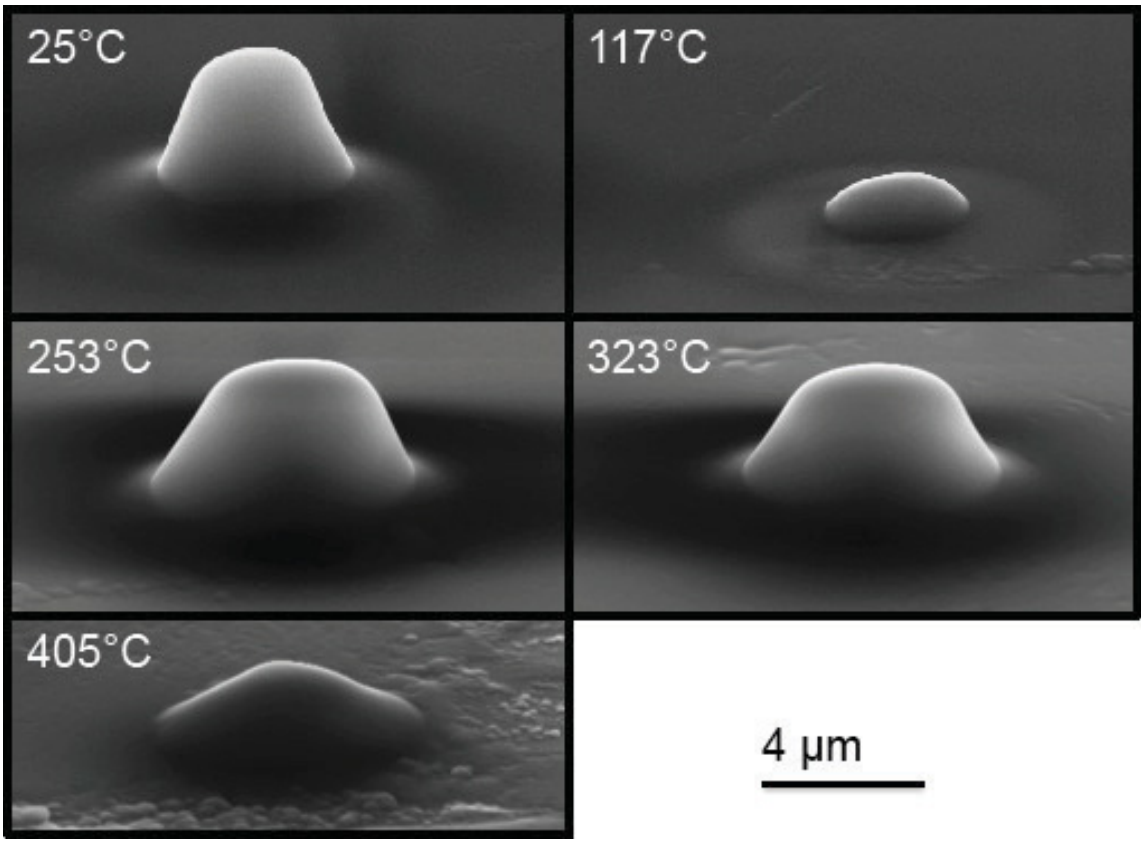

Figure 4.5: *SEM images of defocused deposits grown at increasing T_s. EBID conditions were: V_0: 25 kV, I_b: 9 nA, t_g: 30 mins. Not shown is two more EBID attempts at T_s = 467 °C & 551 °C. Minimal deposition occurred at 467 °C and no deposition at all at 551 °C. Images above were taken at a viewing tilt angle of ≈ 35°. A horizontal image is shown below.*

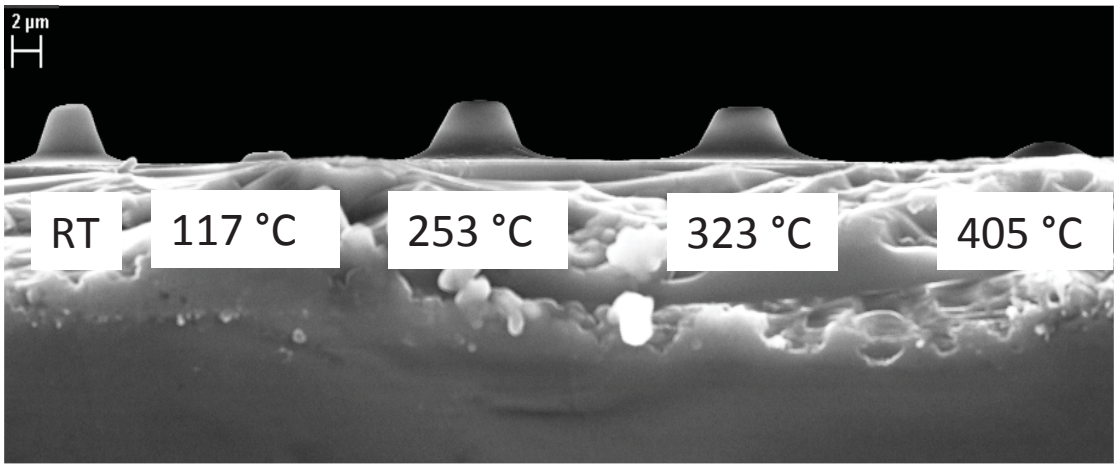

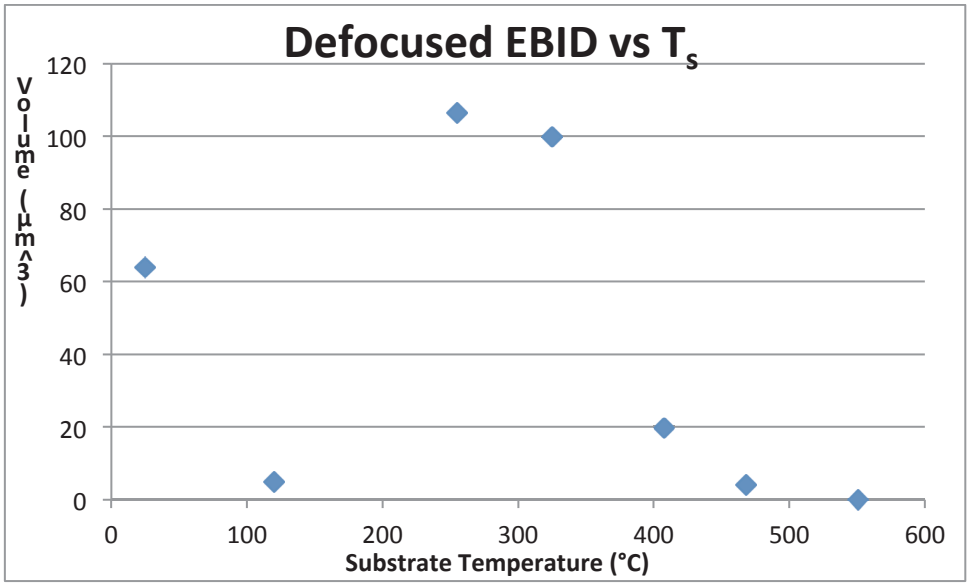

Figure 4.6: *Volume of defocused EBID deposits shown in fig. 4.3 vs the T_s at which each deposit was grown. The total EBID rate at 253 °C is nearly twice the rate at RT. Volume of deposits not shown in fig. 4.3 are included.*

Figure 4.4 outlines changes in EBID rate with a defocused beam with increasing T_s (set 2). A minimum in the growth rate is reached within the T_s range: 25 – 120 °C after which a dramatic increase occurs, surpassing the room temperature rate. The growth rate then decreases to zero as T_s is increased. Very slow deposition still occurred at 467 °C and no deposition was seen at 551 °C. Unique defocused EBID deposit geometry is observed in the high T_s region (D5, 405 °C).

The EBID behaviour shown in figures 4.3 and 4.4 is not predicted by the standard model of EBID. The standard model predicts a decrease in EBID rate as is observed in the region 25 – 120 ° with no subsequent increase. The behaviour predicted by the standard model is the behaviour expected if the adsorption kinetics of the system is limited to molecular physisorption of precursor molecules. Since the experimental results could not be explained by the existing model of EBIED, an extensive literature review was performed to determine the nature of the adsorption kinetics of the TEOS EBID system at higher T_s.

Adsorption Kinetics: Studies Concerning T_s Dependence of TEOS Adsorption

Tedder et. al. [73] studied the adsorption of TEOS upon a SiO_2 surface and found that molecular physisorption occurs exclusively when the surface is exposed at low temperatures. With TEOS exposure at T_s = 450 K, dissociative chemisorption occurs with the majority chemisorbed surface species being triethoxysiloxane, diethoxysiloxane and ethoxy groups. Danner et. al. [74], Spitzmüller et. al [75] and Gamble et. al. [76] found the same dissociative adsorption occurring with TEOS on Si(100), Si(111) and TiO_2 surfaces respectively. Reported differences in the activation temperature of the dissociative adsorption can be attributed to differences in the reactivity of each surface.

Deshmukh et. al [77] performed the most relevant study. They investigated the adsorption of TEOS upon a SiO_xC_y surface grown by CVD using TEOS. The surface they used is the closest approximation to the TEOS EBID material surface which is available in the literature. They found that "reversible" adsorption of TEOS was dominant at RT. At substrate temperatures > 100 °C, "irreversible" adsorption occurred for the majority of TEOS molecules. They attributed this to activated dissociative chemisorption of TEOS which begins above 100 °C and increases with T_s. They suggested the majority species on the surface in the chemisorption region to be di and triethoxysiloxanes as well as ethoxy and/or ethyl groups.

The available data published by various authors concerning the adsorption of TEOS leads me to conclude the following concerning the temperature dependence of TEOS adsorption upon Si and SiO_2 surfaces:

- Molecular physisorption is the dominant adsorption mechanism at room temperature.
- The physisorbed surface coverage will decrease to zero as T_s is increased.
- Dissociative chemisorption of TEOS becomes a significant adsorption mechanism above 100 °C and increases with T_s.
- The surface coverage of chemisorbed TEOS fragments increases with T_s until the temperature is high enough for desorption of chemisorbed fragments to occur. After this point the surface coverage will decrease with increasing T_s.

Adsorption Kinetics: Adsorption Kinetics in General

The adsorption of a molecule onto a surface can be classed into two categories: physisorption and chemisorption. The two adsorption types are differentiated by the strength of the bond with the surface and the forces which give rise to this bond.

Physisorption:

A physisorption bond arises due to intermolecular forces such as dipole interactions which will occur with polar molecules and surfaces and of course Van der Waal forces for all molecule/surface combinations. Inelastic scattering on impact with the surface results in an incident molecule losing some kinetic energy. If the energy loss in a direction normal to the surface is sufficient, the molecule will be unable to escape the potential well. The molecule is trapped in the well and is "physisorbed". The adsorbate will remain trapped until it absorbs sufficient phonon energy to overcome E_d and desorb. The residence time τ is the average time spent in the adsorbed state. The strength of a physisorption bond is comparatively weak. Strengths can range from 1 – 500 meV [79] and are typically around 200 meV [79]. No energy barrier exists for a gas molecule moving from the gaseous to physisorbed phase as no chemical reaction is involved. Molecular orbitals of the molecule's valence electrons are only weakly perturbed. The process can be represented by a reaction co-ordinate diagram like fig. 4.6 below.

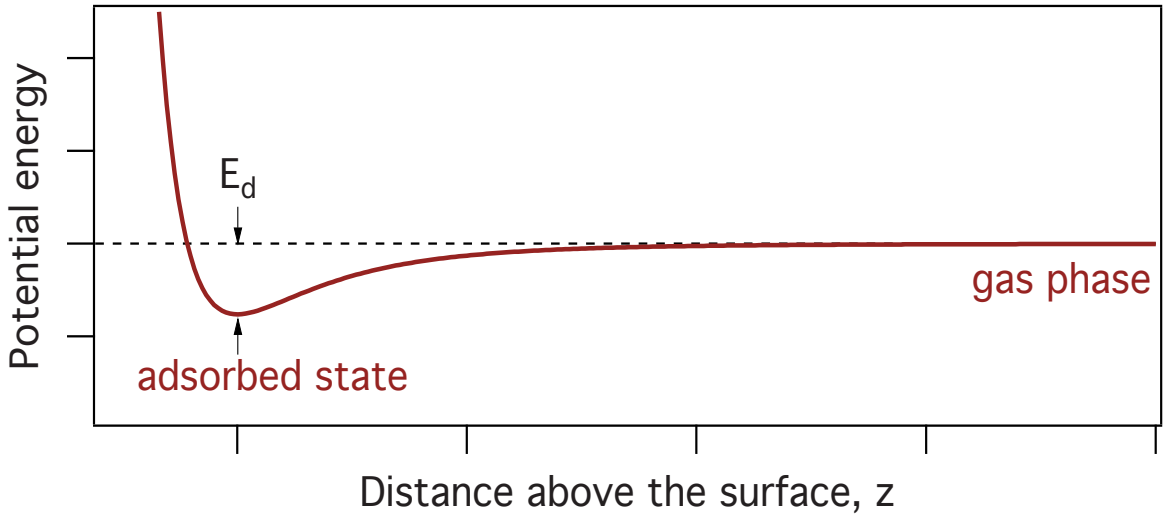

Figure 4.7: *Reaction co-ordinate diagram representing physisorption. Gas molecules colliding with the surface are trapped in the potential well E_d if enough of their kinetic energy is lost in collision. E_d is the strength of the physisorption bond.*

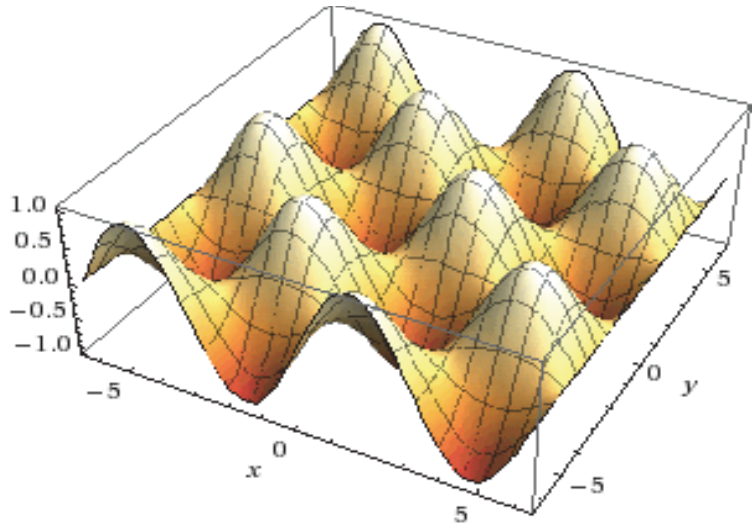

Figure 4.8: *2D schematic representing the potential at a surface as seen by an incident gas molecule. The surface could be atomically clean Si or Ge or any atomically flat elemental crystal. Molecules will become trapped in the wells and be considered physisorbed. If the molecule gains sufficient energy to overcome the bond energy E_d, it will desorb from the surface. Schematic generated using Mathematica®.*

Chemisorption:

When chemisorption occurs, there is a reaction between the adsorbate and the surface. There is a significant change in the molecule's electronic structure. Covalent bond/s are formed and the strength of the bond is much stronger than in the case of physisorption. Typical energies of chemisorption bonds can range from 0.5 – 10 eV [79]. Chemisorption can be activated or spontaneous. An energy barrier must be overcome by the molecule in the case of activated chemisorption. Thus the chemisorption will be "activated" by thermal energy at higher T_s. There is no barrier to overcome in the case of spontaneous chemisorption. A reaction co-ordinate diagram like that of figure 4.5 can represent spontaneous chemisorption although the bond strength E_d will be much higher than that of a physisorption bond. An example of spontaneous chemisorption is the case of clean reactive surfaces such as the surface formed by titanium sputtering in a getter pump [80]. The clean Ti surface is sufficiently reactive to chemisorb most gaseous species present thus reducing pressure in the high vacuum pressure regime.

Figure 4.7 below shows a reaction co-ordinate diagram which can represent the activated chemisorption process. Molecules from the gas phase must overcome the energy barrier (E_c - E_d) and physisorbed molecules the barrier E_c in order to chemisorb to the surface. The height of the barrier E_c will depend upon the nature of the chemisorption reaction which occurs. For a system with a high substrate temperature and much lower gas temperature, direct chemisorption from the gas phase will be negligible. Only molecules at the high substrate temperature will have sufficient energy to surmount the barrier E_c. Thus chemisorption will proceed through an initial physisorbed state where the molecules quickly thermalise with the surface whilst physisorbed. Once the physisorbed molecule has reached a sufficient temperature it can surmount the barrier E_c into the chemisorbed state.

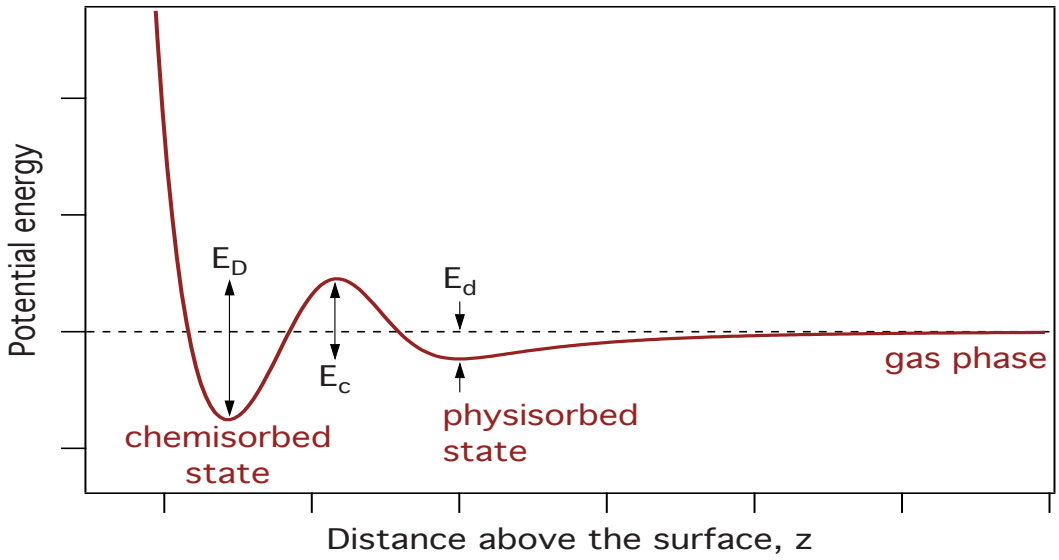

Figure 4.9: *Reaction co-ordinate diagram representing the activated chemisorption process. Typical values of E_D are of the order of 1 – 10 eV.*

For the system used in my experiments $T_s >> T_g$ (T_g = precursor gas temperature) and thus direct chemisorption from the gas phase will be negligible. This becomes important for incorporation of activated chemisorption into the standard EBID model which will be discussed below. Most chemisorption is assumed to proceed through the physisorbed state.

Precursor Residence Time:

The strength of the bond with the surface will have a large effect upon the precursor residence time τ (equation 1.3, chapter 1). Therefore the nature of the adsorption process will have a large effect upon τ. Residence times are long for chemisorbed species and short for physisorbed species. Typical values are of the order of ms for physisorbed species and hours or days for chemisorbed species [80].

Explanation of Defocused TEOS EBID Results

As was discussed previously, the experimental results shown in figures 4.3 and 4.4 cannot be explained by the standard model. Now that the adsorption kinetics of the system have been characterised, we are in a position to explain the results. Precursor molecules that are chemisorbed will have a much higher residence time upon the substrate surface than their physisorbed counterparts. This will result in an increased precursor surface coverage once activated chemisorption has become a significant adsorption mechanism. This will occur as substrate temperature is increased. For the precursor TEOS used in this work, physisorption is the dominant mechanism on SiO_2 and the surface created by TEOS EBID at RT [77]. The residence time of physisorbed TEOS will decrease with increasing T_s. Above a certain T_s which is likely around 100 °C [77], dissociative chemisorption will begin and become the dominant adsorption mechanism as T_s is increased. The physisorbed precursor concentration will approach zero whilst the chemisorbed precursor coverage will increase until a high T_s value where desorption of chemisorbed precursor can occur. The chemisorbed precursor concentration will then approach zero as T_s is increased to high values. This dissociative chemisorption process of TEOS can be visualised as shown by figure 4.9 below.

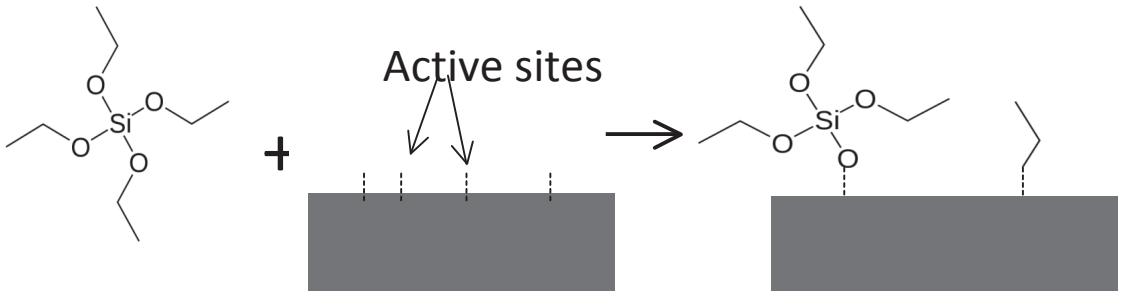

Figure 4.10: *Representation of TEOS chemisorption. The surface freshly deposited by TEOS EBID will have a proportion of active sites. A TEOS molecule which encounters an active site will dissociate and chemisorb if sufficient energy is available to break the O-C bond on one of ethoxy ligands [74].*

Silicon dangling bonds formed by surface oxygen vacancies (V_O) are a likely candidate for the active sites on the TEOS EBID material surface. These would be quickly terminated by chemisorption of species such as OH via dissociative chemisorption of H_2O if the surface was exposed to atmosphere. Since the EBID process proceeds in a pure TEOS precursor environment, the TEOS will be able to chemisorb at these active sites.

The experimental results displayed in figures 4.3 and 4.4 can now be explained. An increase in the growth rate is seen at high T_s. This is inconsistent with exclusive molecular physisorption of TEOS precursor. An increased precursor concentration due to activated chemisorption leading to an increased growth rate is consistent with the results. At higher T_s TEOS precursor adsorbs dissociatively to the freshly deposited TEOS EBID material surface. Due to the long residence time of these chemisorbed TEOS fragments, an increased precursor coverage results. This can be demonstrated mathematically by referring to the standard model:

Rate of change of adsorbed

precursor molecules: $$\frac{\partial N_d}{\partial t} = sJ\Lambda - \frac{N}{\tau} + D - dissociation$$

The complex expression presented as part of the standard model in chapter 1 is shown here in condensed form. The adsorption term is represented by Λ, diffusion term by *D* and e^- dissociation term by *dissociation*. The desorption term N/τ will be less for a higher value of residence time τ. This will result in a higher precursor concentration. This single expression can model one adsorbate species at a time. To more correctly model the situation presented by activated chemisorption we will need to have two adsorbate rate expressions. Separate expressions for chemisorption and physisorption will be required.

Extending Standard EBID model to Account for Activated Chemisorption

The standard model of EBIED was presented in chapter 1. The basis for this extended model was derived in part from [81].

The main expressions are (presented here in compacted form):

$$\frac{\partial N_p}{\partial t} = s_p F \Lambda_p - N_p(k_p \sigma_p f) \qquad (4.1)$$

$$\frac{\partial N}{\partial t} = \sigma_p f N_p \qquad (4.2)$$

Where: N_p and N are the concentrations of physisorbed precursor molecules and dissociated molecules respectively, s_p the sticking co-efficient for physisorption, σ_p the cross-section for dissociation of physisorbed precursor molecules. F and f are the molecular flux from gas phase (equation 1.1, chapter 1) and electron flux respectively. k_p is the inverse of the residence time of the physisorbed precursor (residence time τ defined in chapter 1, equation 1.3). $\boldsymbol{\Lambda}_p$ is the adsorption of precursor from gas phase and is limited to a monolayer for Langmuir adsorption. The subscript p is used to indicate physisorption.

$$k_p = {}^{1}/_{\tau} = \kappa_p e^{-E_d/kT_s} \qquad (4.3)$$

Activated chemisorption of precursor molecules can be incorporated into the standard model by the addition of an expression for the rate of change of chemisorbed molecules. The expressions must also account for transitions from gas phase to chemisorbed state (negligible for my system), physisorbed to chemisorbed state and desorption from chemisorbed state. The main expressions of the extended model are:

$$\frac{\partial N_p}{\partial t} = s_p(1-s_c)F\Lambda_p - N_p(k_p + k_c\Lambda_c + \sigma_p f), \qquad (4.4)$$

$$\frac{\partial N_c}{\partial t} = (s_c F + N_p k_c)\Lambda_c - N_c(k_c + \sigma_c f), \qquad (4.5)$$

$$\frac{\partial N}{\partial t} = f(\sigma_p N_p + \sigma_c N_c). \qquad (4.6)$$

Where: N_p and N_c are the concentrations of physisorbed and chemisorbed precursor respectively. σ_p, σ_c, Λ_p and Λ_c are the cross sections for dissociation of physisorbed and chemisorbed precursor and the concentrations of free physisorption and chemisorption sites respectively.

The sticking coefficients s_p and s_c are the probabilities of direct adsorption from gas phase for physisorption and chemisorption. As discussed previously s_c will be negligible for the experimental conditions used in this work, where $T_s >> T_g$. s_c is necessary though to allow the model to account for all possible experimental conditions. It allows modelling of systems where direct chemisorption will be a significant process. s_c is defined by the barrier (E_c-E_d) and a pre-exponential factor s_0:

$$s_c = s_0 e^{-(E_c - E_d)/kT_g} \qquad (4.7)$$

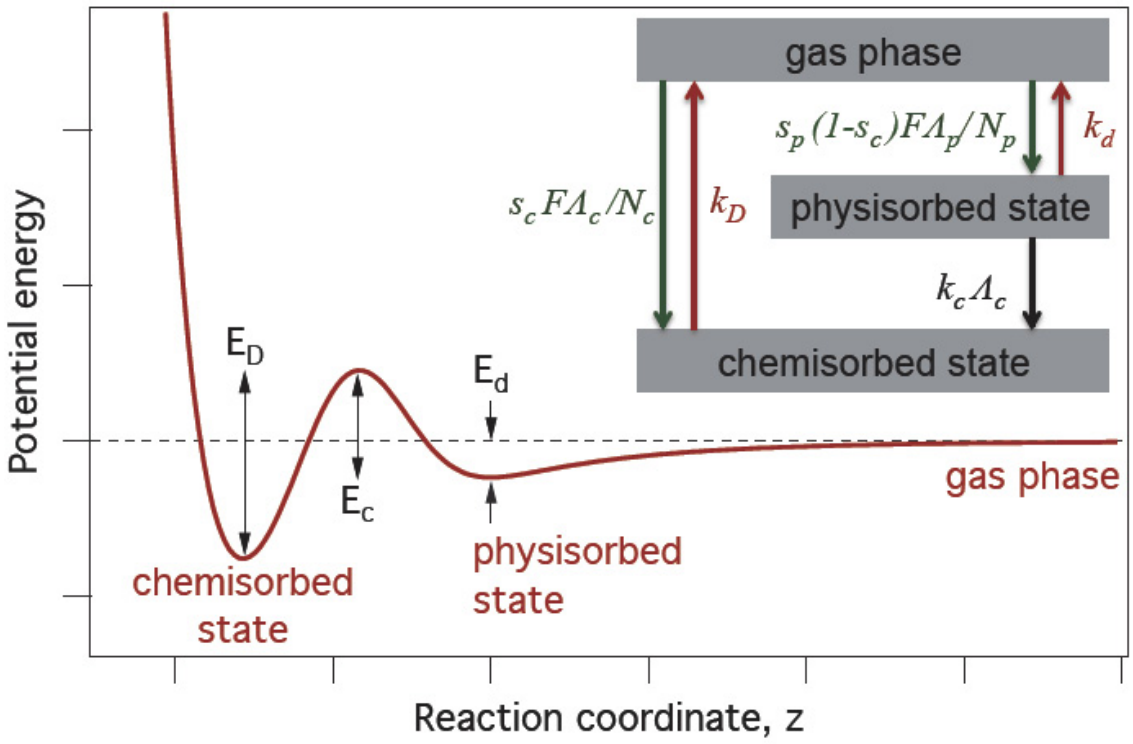

Figure 4.11: *Reaction co-ordinate diagram representing activated chemisorption with inset showing the adsorption state transitions which can occur and the terms used to represent them in the model.*

Equation 4.4 is analogous to 4.1 yet includes the term $(s_p(1- s_c)F\Lambda_p)$ to exclude molecules chemisorbed from gas phase. $(N_p k_c \Lambda_c)$ accounts for the flux of molecules that transition from the physisorbed to chemisorbed state by gaining thermal energy (kT). This will be the dominant route to chemisorption for my experimental conditions.

Λ_c is the fraction of unoccupied chemisorption sites and is limited to a monolayer (Λ_c = $(1 - A_cN_c)$, A_c = chemisorption site surface area). The rate coefficients k_c and k_D are the rates of transitions from physisorbed to chemisorbed state and desorption from chemisorbed state respectively and are given by:

$$k_c = \kappa_c e^{-E_c/kT_S} \qquad (4.8)$$

$$k_D = \kappa_D e^{-E_D/kT_S} \qquad (4.9)$$

where: E_c and E_D are the energy barriers (shown in fig. 4.9) for transition from physisorbed to chemisorbed state and desorption from chemisorbed state respectively. Equation 4.5 models the rate of change of the chemisorbed adsorbate concentration. Equation 4.6 is the sum of the dissociation of physisorbed ($\sigma_p N_p f$) and chemisorbed ($\sigma_c N_c f$) precursor molecules and models the EBID growth rate. Equations 4.4 - 4.6 can be solved to yield the equilibrium coverage of physisorbed and chemisorbed species and the simulated steady state growth rate of EBID, $\frac{\partial N}{\partial t}$. Mathematica was used to implement the model and perform simulations.

Parameters used for Simulation:

The electron flux profile was assumed to be top-hat with a beam diameter of 1.5 µm (similar to top-hat profile shown in fig. 4.1) and electron flux of f = 80 electrons/Å^{2}s. These parameters were calculated from measure of the beam current I_b and estimation of the beam diameter used for set 2. The gas temperature and pressure were set to the experimental values of T_g = 300K and P = 0:05 Torr (6.7 Pa). The sticking coefficients of the physisorbed species (s_p) and the pre-exponential for thermally activated chemisorption (s_0) were both set to unity. The surface site areas, dissociation cross-sections and desorption and transition rate pre-factors for physisorbed and chemisorbed species were assumed to be equal at $A_p = A_c$ = 100 Å^2, $\sigma_p = \sigma_c$ = 10 Å^2 and $\kappa_p = \kappa_D = 10^{15}$ s^{-1} respectively. The cross section value was taken from literature [101]. κ_p and κ_D are the attempt frequencies of molecular vibrations of adsorbed precursor and were estimated based on recommendations in literature [82] for large molecules such as TEOS. The assumption of equal parameters for the physisorbed and chemisorbed species is justified as the species are expected to be very similar [73, 75]. The energy barrier parameters E_d, E_c and E_D were adjusted to fit the

experimental growth rates. The values which gave the best fit were: E_d = 0.51 eV, E_c = 0.86 eV and E_D = 1.42 eV. These parameters seem likely given what is known about the adsorption of TEOS on SiO_2 [73, 77].

Simulation Results

The model was used to produce simulated EBID rates using the parameters discussed above. With the energy barrier values listed above, excellent fit to the experimental results was obtained. Adjusting the energy values in this way is valid as the model would not be able to reproduce the shape of the deposition rate vs T_s curve if the correct adsorption behaviour was not being accounted for. As the energy barrier values were unknowns, fitting to experimental results allows indirect measurement of adsorbate energy barriers if all other parameters of the model are representative of the system.

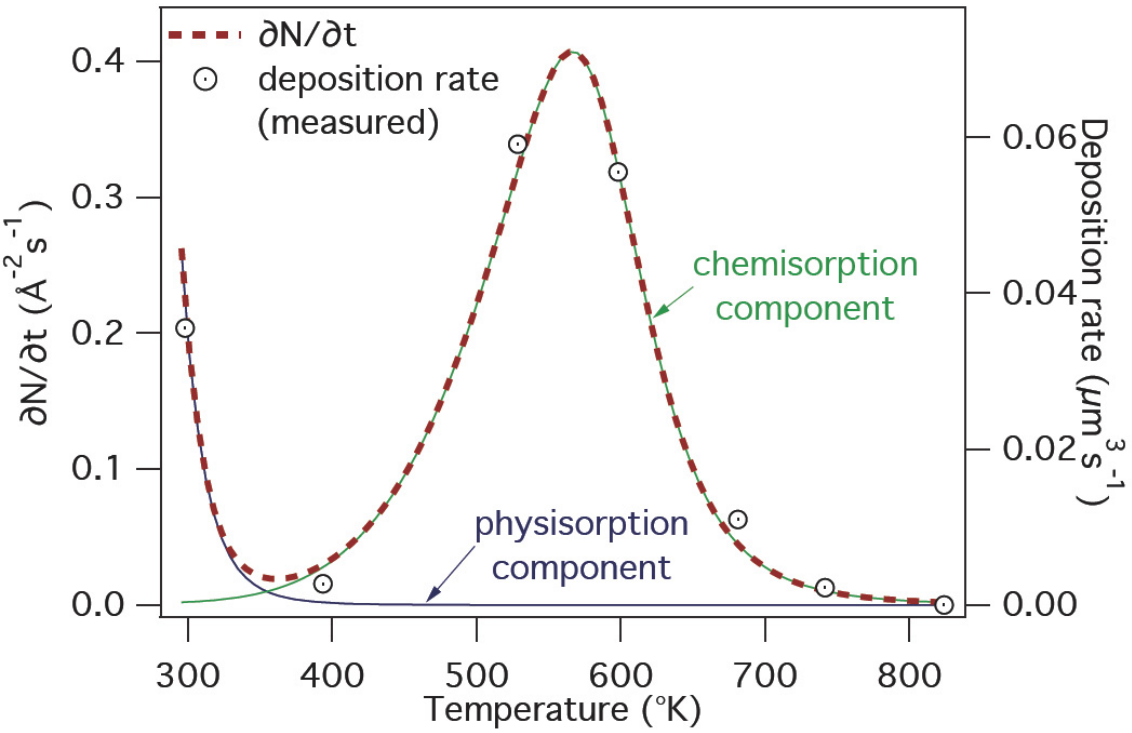

Figure 4.12: *The simulated deposition rate due to dissociation of precursor from each adsorbed state. The blue line represents dissociation of physisorbed molecules and the green line chemisorbed precursor dissociation. The total dissociation rate is the dotted red line.*

Under electron irradiation the calculated adsorbate concentrations reached a steady state within 0.1 s over the entire T_s range. T_g was fixed at 300 K for the

simulation result shown in figure 4.10. With my experiments the sub-chamber wall temperature increased up to ≈ 350 K as the substrate was heated to 800 K, due to radiative and convective heat transfer to the sub-chamber walls. T_g therefore increased with T_s, and may alter the chemisorption rate through equation 4.7. This small increase in T_g is demonstrated to have negligible effect under the experimental conditions used here, over any realistic range of T_g. This was investigated by assuming that the gas temperature takes the form: $T_g = 300 + n(T_s - 300)$, where n was varied from 0 to 0.2. The resulting behaviour, shown in fig. 4.11, is not surprising given the high value of $(E_c - E_d)$ relative to the maximum value of kT_g.

The effect of varying the parameters s_0 and A_c were also investigated. $s_0 = 0$ removes direct gas phase to substrate chemisorption from the model and as is seen in fig. 4.11, this had no effect. The effects of T_g and A_c were found to only change the height of the peak growth rate and not change the qualitative trend in any way. The results indicate that direct chemisorption is indeed negligible for the experimental conditions used and that the approximation of representing dissociative chemisorption by a single chemisorbed species is valid for the case of TEOS.

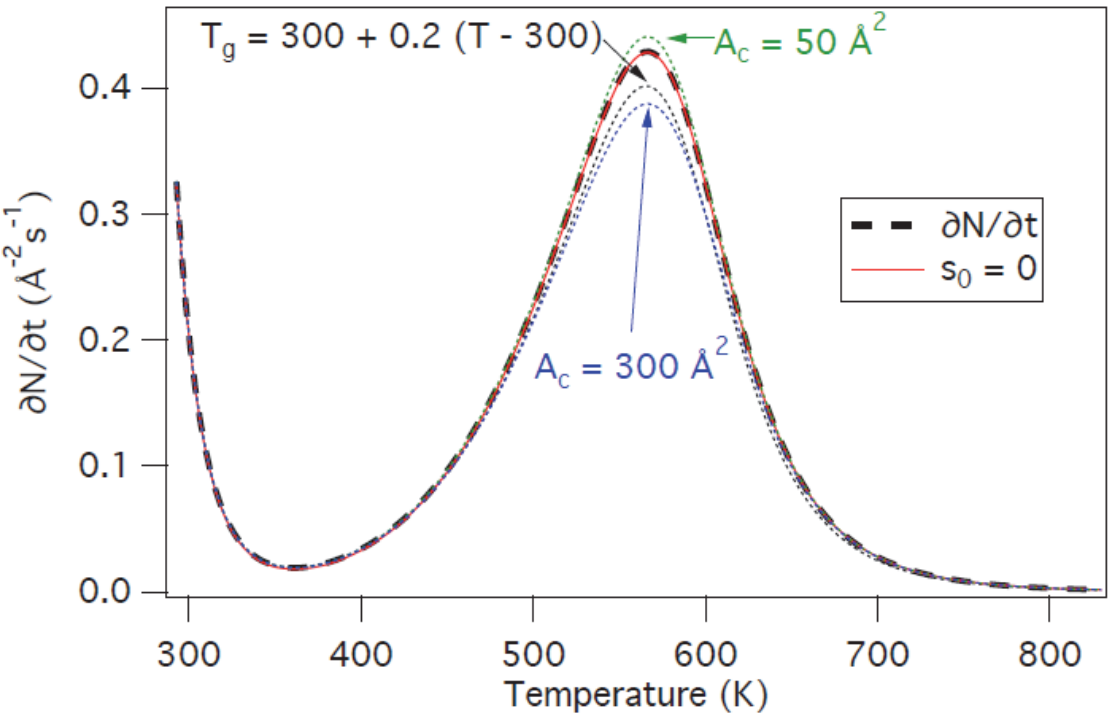

Figure 4.13: *Effects of varying s_0, A_c & T_g. The most extreme cases are plotted here. s_0 has no effect. Changing A_c or T_g only changes the height of the peak and not the shape of the curve.*

The values of the desorption energies (E_d & E_D) and pre-factors (κ_p & κ_D) compensate for each other when altered and change the shape of the $\frac{\partial N}{\partial t}$ curve. The dissociation cross section also alter the curve shape if $\sigma_p \neq \sigma_c$. Analysis of experimentally determined $\frac{\partial N}{\partial t}$ rates with fitting to this model therefore may allow determination of values for σ and E_d/E_c using EBID, if other parameters are known with reliability.

The modelling and experimental results illustrate the utility of using EBID for characterisation of physisorbed and chemisorbed adsorbates under conditions which are inaccessible by other techniques. For example, temperature programmed desorption (TPD) is currently used as a technique to characterise adsorption energies of molecules [74]. The technique involves low doses of the precursor gas on super-clean surfaces under UHV conditions. Thus the technique investigates adsorbates only in the low coverage regime. These results indicate that EBID could be used to characterise adsorbates in the high coverage regime at equilibrium conditions. Much work remains to be done to refine the model and complementary experimental procedure although the results indicate the possibility of using EBID as an adsorbate chemistry/surface science technique.

Current Limitations of the Model

The development of the model is in the early stages as yet. TEOS is known to adsorb dissociatively and several similar chemisorbed species will be the EBID precursors at higher T_s. Here the growth is modelled by a single chemisorbed species. Molecular TEOS and the products produced following dissociative adsorption are known to be very similar [73, 75]. This allows the growth to be approximated by a single chemisorbed species. The approximation may not be valid for other precursors. Furthermore, the term which accounts for diffusion has been removed from the model for this initial formulation. The term was removed as the expressions for N_p and N_c can be solved analytically without the diffusion term. This allowed rapid testing of the model. Diffusion is expected to be minimal for the experimental conditions used and thus neglecting diffusion was a valid approximation. The approximation will likely not be valid for the case of focused electron beam induced deposition (FEBID) where

diffusion is often significant. Incorporation of expressions for multiple precursor species to better account for dissociative chemisorption as well as expressions to account for diffusion are expected to be the next steps in the development of the model.

Practical Advantages of Activated Chemisorption for EBID

As the experimental results and model discussed above demonstrate, activated chemisorption can be used to increase the growth rate of an EBID process. The effect of dissociative adsorption upon the composition of EBID deposits was also investigated. Energy dispersive X-ray spectroscopy (EDS) was employed to analyse EBID deposit composition. Line scans were taken across each deposit and analysed to yield the elemental ratios of the deposits. It was found that a large decrease in the carbon content of EBID deposits grown in the chemisorption T_s region of TEOS occurs. Deposits formed primarily as a result of the electron beam induced dissociation of chemisorbed TEOS fragments have a much lower C content than those formed by dissociation of physisorbed molecular TEOS.

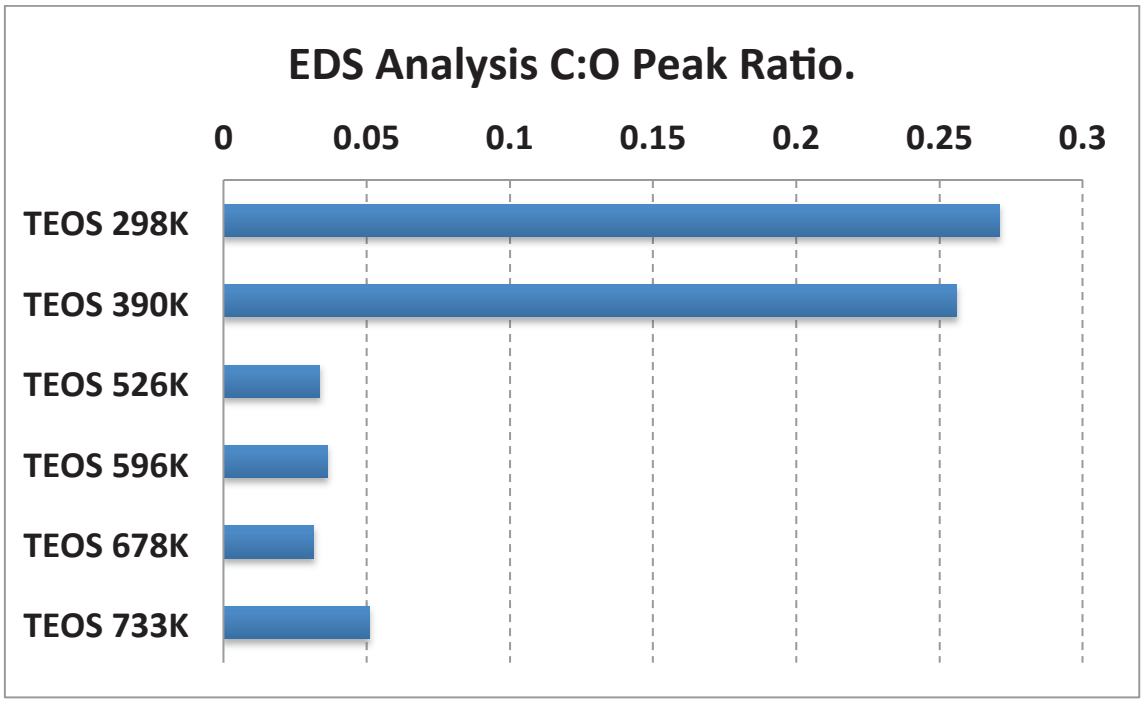

Figure 4.14: *C:O X-ray signal ratio for the defocused deposit grown at each T_s indicated. A lower value indicates less carbon content. The C:O value taken at a clean spot on the*

substrate surface was ≈ 0.03 – 0.05. Thus the C content of all deposits grown above 500 K was indistinguishable from the background level.

Figure 4.11 above displays Carbon/Oxygen X-ray signal ratios. The values can be taken as the approximate ratio of C content to O content in the EBID material. The Si:O content ratio remained approximately constant at ≈ 0.5 for all substrate temperatures. The results indicate that TEOS EBID creates deposits with O:Si content in a 2:1 ratio as is the case for SiO_2. A variable amount of carbon is co-deposited. The amount of carbon decreases with increasing T_s. The small increase seen at 733 K is within the noise level and it is considered that all deposits grown above 500 K have similarly low C contents.

At RT TEOS will be primarily physisorbed. Thus the growth will result from the e^- induced dissociation of molecular TEOS. As T_s is increased, the residence time of physisorbed precursor will decrease and decrease the growth rate. The residence time of carbonaceous fragments produced by EBID will also decrease. This will result in a decreased incorporation of these fragments into the EBID deposit resulting in higher purity. Thus prior to the onset of activated chemisorption, increasing T_s can be used to increase purity but at the cost of a lower growth rate. This approach has been used by others [44, 53] to increase purity yet it has been stated that since the growth rate generally decreases faster than the purity increases as T_s is increased, (with molecular physisorption only) the approach is not very useful [44, 53]. These results indicate that the approach can be used to increase the purity of EBID deposits to very high levels and simultaneously have an increased growth rate for the case of a precursor which undergoes activated chemisorption.

When dissociative chemisorption becomes the dominant adsorption mechanism, the majority of growth will result from dissociation of a different species to TEOS. These species are likely to be triethoxysiloxane and diethoxysiloxane [73, 74, 75, 77]. These species have a lower carbon content than TEOS and will naturally result in deposits with a lower C content.

As discussed in chapter 1, the EBID reaction results in the dissociation of a precursor molecule into many different fragments. Many carbonaceous fragments will

be formed by EBID of organometallics and organosilanes like TEOS. These carbonaceous fragments are likely to physisorb only and are "trapped" within a growing EBID deposit at lower T_s due to significant residence times. At high T_s these carbonaceous fragments will have very low residence times and be likely to desorb before being trapped in the growing EBID deposit. Thus the combination of a chemisorbed precursor of lower carbon content and efficient desorption of carbonaceous fragments will result in deposits of higher purity at high T_s.

These results indicate that not only can activated chemisorption of EBID precursors be used to enhance the growth rate of EBID, it can also be used to create deposits of higher purity. Purity of EBID deposits from most precursors has been shown to increase with T_s [44, 53]. For most precursors this increase in purity comes with a large decrease in growth rate. This has limited the use of heated substrate EBID. The results outlined in this chapter indicate that it is not the case for all precursors, namely those for which activated chemisorption occurs.

Ramifications of Compositional Analysis Results for Chemisorption Dynamics of TEOS

Authors such as Tedder *at al.* [73], Danner *et al.* [74] and Deshmukh *et al.* [77] have all independently demonstrated that the activated chemisorption of TEOS upon Si/SiO_2 surfaces results in di- and tri- ethoxysiloxane as the majority surface species. Deshmukh *et al.* concluded that the chemisorption is irreversible. This means that following activated chemisorption, the tri- and di-ethoxysiloxanes remain chemisorbed to the surface when cooling the surface down to RT. Insufficient data has been collected concerning the fate of the ethyl ligands which are cleaved from the TEOS molecule upon chemisorption. The three possibilities are:

- The ethyl molecule primarily reacts with the surface and is chemisorbed.
- The ethyl molecule does not react with the surface yet forms physisorption bonds of sufficient strength for a significant physisorbed ethyl surface population to be present at 100°C < T_s < 400°C.
- The ethyl molecule is primarily desorbed from the surface at > 100°C.

Some associative desorption could theoretically also occur. Associative desorption could occur when a physisorbed ethyl molecule encounters a chemisorbed triethoxysiloxane, reacts to form TEOS and then desorbs from the surface. The rate of associative desorption will depend upon the concentration of physisorbed ethyl molecules and the height of the energy barrier for the reaction to occur.

The EDS compositional analysis results provide evidence towards the fate of the ethyl ligands. We see a dramatic decrease in the carbon content of the TEOS EBID deposits when deposited > 100 °C, i.e when EBID proceeds primarily with chemisorbed di- and tri-ethoxysiloxanes as the precursor. This indicates that it is most likely that the ethyl ligands are primarily desorbed from the surface following TEOS chemisorption and do not contribute to the carbon content of the deposits.

Conclusions:

Activated dissociative chemisorption of TEOS occurs on the surface grown by EBID with TEOS as the substrate temperature (T_s) is increased. Dissociative chemisorption results in an increased precursor concentration at high T_s relative to the physisorbed precursor concentration at room temperature (RT). EBID with activated chemisorption can be simulated by an extended model of EBID which models physisorbed and chemisorbed precursor concentrations and accounts for adsorption state transitions. Investigation of adsorbate properties under conditions inaccessible to other techniques is likely to be possible using EBID experimentation and modelling. EBID deposits formed by dissociation of chemisorbed TEOS fragments at high T_s are of much higher purity than deposits grown at RT. The purity increase is due to a chemisorbed precursor with a lower carbon content (than TEOS) and increased desorption of carbonaceous fragments produced by EBID at high T_s. Performing EBID at high T_s can result in high purity deposits with growth rates superior to RT EBID for TEOS. EBID deposit purity and growth rate increases are expected for other precursors for which activated chemisorption occurs at higher T_s.

5. FEBID with Increasing Substrate Temperature (T_s)

5.1 Abstract:

EBID experiments are performed with a focused beam (FEBID) upon a heated substrate as a function of substrate temperature (T_s). The change in growth rates with T_s differs to that observed during EBID with a defocused beam and is not predicted by the standard model. Unexpected evolution of FEBID deposit geometries with increasing T_s is observed. The results indicate that unique FEBID deposit geometries can be obtained with T_s selection. Large dendritic-like growth is observed in the high T_s region and this is accompanied by a large increase in growth rate. The unique growth observed with TEOS FEBID at high T_s is attributed to a complex mechanism involving electron beam induced heating (EBIH), charging and high levels of chemisorbed precursor surface diffusion.

5.2 Introduction:

As was stated in the previous chapter, the standard model predicts only a decrease in EBID growth with increasing substrate temperature (T_s). Deviation from this behaviour was shown to occur when activated chemisorption of an EBID precursor occurs. A large reduction in the carbon content of EBID deposits formed by dissociation of chemisorbed TEOS fragments compared to dissociation of molecular TEOS was shown to occur. The standard model was extended to incorporate activated chemisorption. The model predicts the correct generic T_s dependence of EBID growth rates. The initial formulation of this extended model does not account for diffusion and thus will likely not perform very well when used to predict the growth rate T_s dependence for FEBID.

Experimentation involving EBID on a heated substrate has been performed by several groups [83, 71, 72]. Studies have previously focused upon changes in deposit purity and have generally used defocused beams as EBID pillars are not suitable for X-ray based compositional analysis techniques. The case of FEBID is somewhat more

complex than that of EBID with a defocused beam. Diffusion of precursor molecules into the irradiation region must be considered. This makes the modelling of FEBID much more computationally expensive. Other effects which arise due to high electron fluxes must also be considered. Electron beam induced heating (EBIH) and excess charge build up are two main processes which can have an effect during FEBID.

EBIH has been investigated by several groups through experimentation and modelling work [84, 33]. It was demonstrated that EBIH can have a significant effect on FEBID. Hochleitner *et al.* [33] observed large, spontaneous radial growth on FEBID pillars grown with $Fe(CO)_5$. They attributed this extra growth to thermal decomposition of the precursor induced by high temperatures of the FEBID pillars caused by EBIH during FEBID. For thermal decomposition to occur the increase in nanopillar temperature during FEBID must have been significant. Randolph *et al.* [84] performed simulations of EBIH using a model of a SiO_2 nanopillar. For their conditions (500 pA, 50 nm diameter beam) they estimated an increase of up to 30 K. Such an increase can have a significant effect upon the deposition rate. It was also demonstrated that the temperature of a growing FEBID pillar increases with height and deposition time.

Excess charging during EBID can have unpredictable effects. The effects of charging upon SEM imaging are well known and can cause image distortion and contrast artifacts. The electron beam is deflected by large electric fields at the surface of an insulating sample and thus such samples cannot be imaged unless coated in a conductive material in high vacuum SEM. Van Dorp *et al.* [68] observed fractal-like, branched growth when performing FEBID with an organosilane precursor. They attributed the growth to excess charging during FEBID of insulating material.

Significant diffusion of precursor molecules into the irradiation region can cause formation of asymmetrical EBID deposits. Rykaczewski *et al.* [85] observed growth of nanopillars with a surrounding ring at a radius of ≈ 1.5 µm from the pillars. They attributed the ring growth to dissociation of diffusing carbonaceous molecules (used as the precursor) into the irradiation region. Smith *et al.* [86] observed and simulated the growth of volcano shaped structures via EBID with WF_6. The results were

attributed to surface diffusion being the main precursor supply mechanism to the irradiation region.

In this work FEBID experiments are performed as a function of T_s Unexpected evolution of growth rates and FEBID deposit geometry is observed. The results are attributed to effects of activated chemisorption of TEOS precursor, high levels of diffusion, EBIH and excess charge build up during FEBID of the SiO_xC_y insulating structures.

5.3 Experimental:

EBID experiments were performed with a focused beam on a heated substrate with the ESEM cell experimental apparatus detailed in chapters 3 and 4. Substrates for deposition were clamped upon the sample holder which itself was clamped atop a resistive heating element. This setup allowed accurate control of the substrate temperature (T_s) with a range of 25 – 700 °C. Good thermal contact between the heater and substrate was confirmed for the experimental conditions used prior to experimentation. A K-type thermocouple secured within the sample holder was used to measure T_s. The precursor TEOS was used for all experiments at a pressure of 0.05 torr (≈ 7 Pa) unless stated otherwise. The emitted (I_e) and transmitted (I_t) current were logged and recorded during EBID to monitor growth as detailed in chapter 3. The T_s was allowed approximately 30 minutes to stabilise after each increase before deposition to ensure constant T_s.

Six experimental sets comprise the main data for this chapter. Depositions were made with increasing T_s. T_s was constant throughout each individual deposition. **Set 1:** FEBID at RT function of t_g, I_b: 3.5 & 9 nA, (5 FEBID deposits + 1 defocused at each I_b). **Set 2:** FEBID, function of T_s, t_g: 27 mins, I_b: 9 nA, T_s: 25 – 258 °C (6 deposits). **Set 3:** FEBID, function of T_s, t_g: 40 mins, I_b: 9 nA, T_s: 25- 368 °C (14 deposits). **Set 4:** Alternating focused (odd numbered deposits) and defocused (even numbered deposits) EBID, function of T_s, t_g: 30 mins, T_s: 25 – 341 °C, $\Delta d_{f\text{-}s}$: 0 & 0.3 mm (8 deposits). **Set 5:** FEBID, function of T_s, t_g: 25 mins, I_b: 3.5 nA, T_s: 25 – 390 °C (7

deposits). **Set 6:** FEBID, function of T_s, t_g: 25 mins, I_b: 8 nA, precursor pressure: 0.16 torr, T_s: 25 – 295 °C (5 deposits).

5.4 Results and Discussion:

Room Temperature EBID with TEOS Precursor

Typical EBID growth with TEOS precursor at room temperature (set 1) is summarised in figure 4.1 below. A focused, stationary beam produces cylindrical pillars with conical tips surrounded by a diffuse "halo" of negligible thickness. This "halo" growth generally extends far (10^2 – 10^3 x the primary beam diameter) from the beam axis and is attributed to precursor dissociation by SE2s (SEs produced by BSEs), BSEs and PEs scattered at an angle by collisions with gas molecules ("skirt" electrons) [60].

High aspect-ratio pillars are grown at lower electron fluxes in the EL or early PD regime (i.e. minimal precursor depletion). As the flux is increased, the volumetric growth rate increases while the aspect ratio of resultant EBID pillars is decreased. This can be explained by a separate analysis of the vertical and lateral growth rates. The total electron flux (PE + SE + BSE) incident upon and emitted from the pillar tip is always much higher than the flux incident upon and emitted from the sidewalls of a growing EBID pillar. As a result there will be higher precursor depletion on the pillar tip than on the sidewalls. Thus as primary electron flux is increased the vertical growth may move into the PD (some precursor depletion) or even MTL regime (approaching full precursor depletion) whilst the lateral growth of the pillar via e^- emission from pillar sidewalls remains in the EL or PD (less precursor depletion) growth regime. Therefore the vertical growth rate may saturate long before the lateral growth rate as e^- flux is increased.

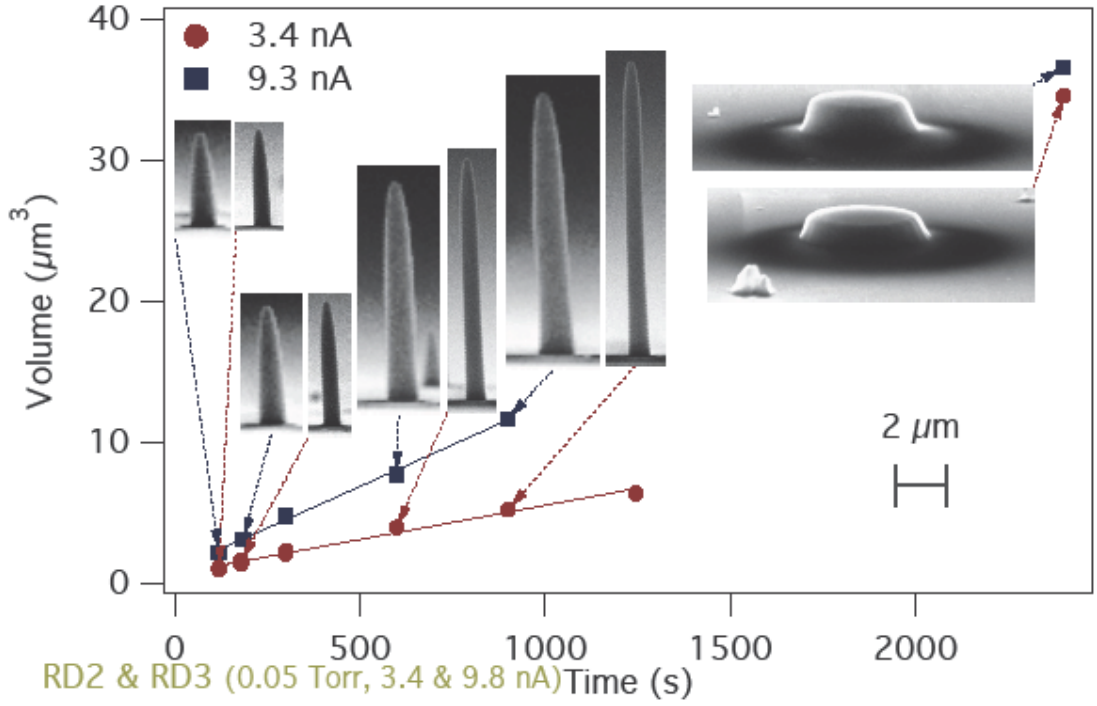

Figure: 5.1: *(Previous page): Volumetric growth rate of EBID deposits with TEOS precursor at RT (set 1). SEM images of deposits are inset.*

The EBID growth rate increases linearly with e^- flux in EL regime and sub-linearly in the PD regime. Therefore the lateral growth will increase at a faster rate than the vertical growth as e^- flux is increased, once the vertical growth has moved into the PD regime. This results in pillar aspect ratios decreasing as e^- flux increases for a constant precursor pressure. In the same way aspect ratios decrease with decreasing precursor pressure for a constant e^- flux. Set 1 shown in fig. 1 demonstrates this. The vertical growth rate increases by only 3.5 % whilst the lateral growth rate increases by 65 % when I_b is increased from 3.5 to 9 nA. The effect is likely exaggerated by an unavoidable beam diameter increase when increasing beam current whilst maintaining focus.

The overall growth rate (volumetric) of set 1 (fig. 4.1) increases by a factor of 2.15 when the electron flux is increased by a factor of 2.75. Analysis of the volumetric growth rate of an EBID experiment allows assessment of the overall level of precursor depletion and minimises error due to changing beam diameters. The sub-linear increase in growth rate with e^- flux indicates precursor depletion, PD regime growth and a lowering of EBID reaction efficiency at the higher flux. Defocusing the beam increases growth rate as depletion is reduced and hence efficiency of the EBID reaction

increased. The larger difference in growth rates between focused and defocused EBID at 3.5 nA compared to 9 nA indicates depletion is still high at 9 nA when defocused and there is depletion with a focused beam of 3.5 nA. Thus with a focused beam and TEOS pressure = 0.05 torr, growth is in PD regime at 3.5 nA and deeper in PD (maybe even MTL) regime at 9 nA. The growth is likely in the EL regime with a defocused beam of 3.5 nA.

FEBID with Increasing T_s

Growth rate and morphological changes were observed for FEBID deposits grown at increasing T_s. The changes in growth rate were similar to the defocused EBID vs T_s results however, the situation is complicated by extra effects which can be considered negligible for the defocused EBID case. These effects may include electron beam induced heating (EBIH), charge build-up and significant precursor diffusion.

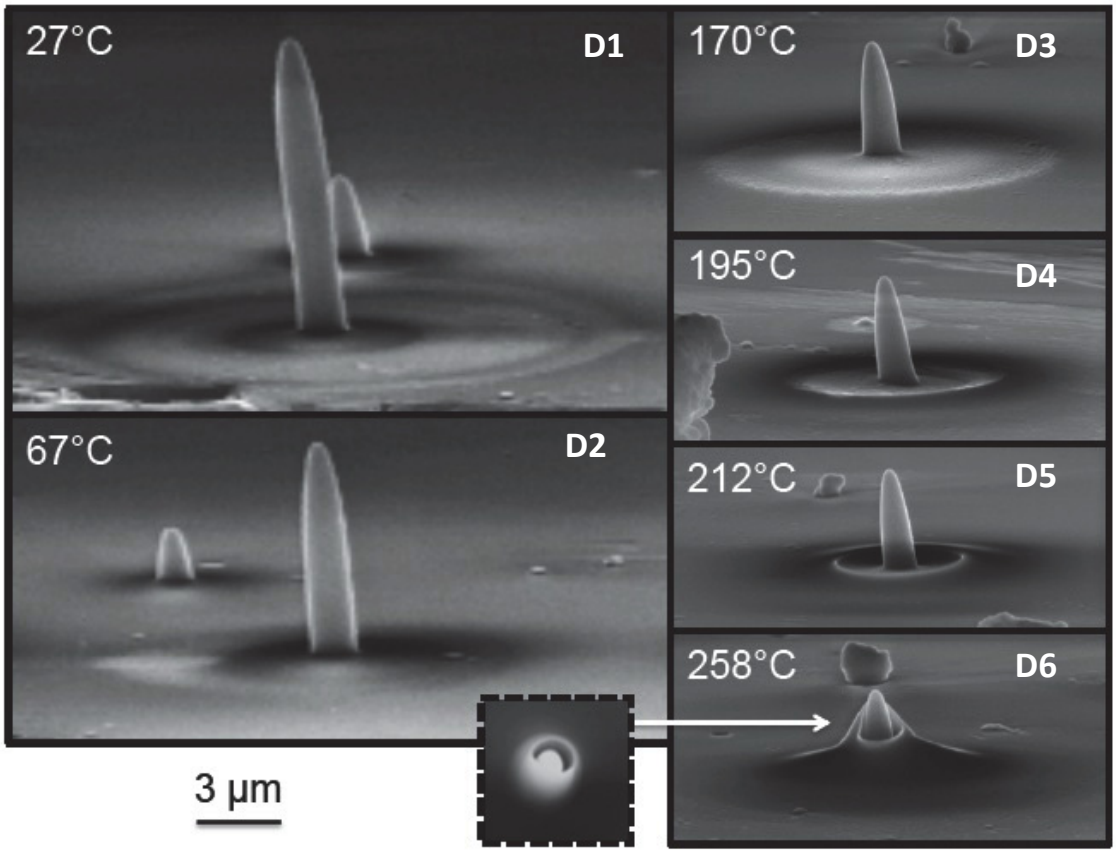

Figure 5.2 (above): *SEM images of FEBID deposits (set 2) grown on a heated substrate at the temperatures indicated. The pillar (primary growth) decreases whilst the halo (secondary growth) increases and moves inwards.* ***(below):*** *I_e curves collected during growth of the deposits shown above. Curves reflect the decreasing vertical primary*

growth rate.

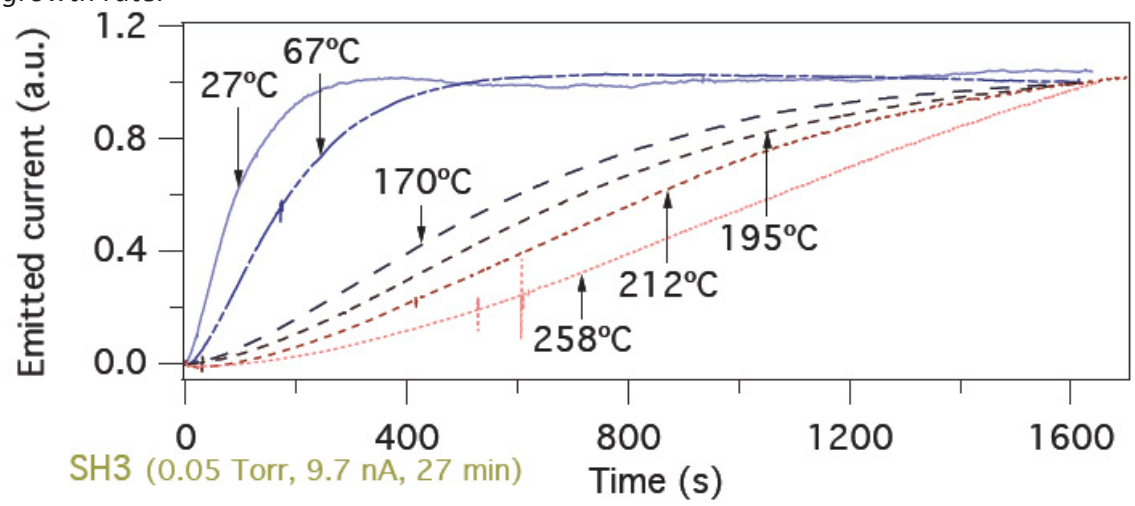

Figures 5.2 (set 1) and 5.3 (set 2) show typical EBID growth upon a heated substrate using a focused beam with TEOS precursor. A reproducible trend is observed as T_s is increased. The central pillar (primary growth) decreases in height whilst the surrounding, delocalised "halo" growth (secondary growth) decreases in diameter and increases in height. The decreasing primary growth rate is reflected in the I_e curves of figures 5.2 and 5.3 although they display no information concerning the increasing secondary growth. Unique deposit geometries can be achieved with selection of T_s for EBID.

Above 260 °C and given sufficient growth time (t_g), the primary and secondary growth regions merge and the overall EBID rate increases dramatically after merger event. t_g required for merger event decreases as T_s is increased above 260 °C. Deposits 8 - 11 with their associated I_t curves of fig. 4 show merger event. Merger is first seen in I_e curve of D8. The sudden increase in gradient at approximately 1800 s indicates merger event. Gradient of I_e curve increases due to increase in growth rate after merger. Merging occurs faster for D9 – 11 and is less evident in their I_t curves although the increasing growth rate is plainly evident.

After merger event, FEBID growth is significantly altered. The width of a deposit steadily decreases to approximately the electron beam diameter. Rapid growth with increasing surface roughness is then evident. The surface roughness evolves to the point where fractal-like growth begins to occur. EBID deposits grown above 300 °C, exhibit three characteristic growth regions: A wide base (region #1), a smooth steadily roughening narrow pillar (region #2) and then fractal-like dendritic growth (region #3).

As T_s is increased, the transition between the growth regions #1, #2 and #3 occurs faster. The height and width of region #1 as well as the height of region #2, decrease with increasing T_s. The growth behaviour of EBID deposits after merger event is summarised in figure 5.4.

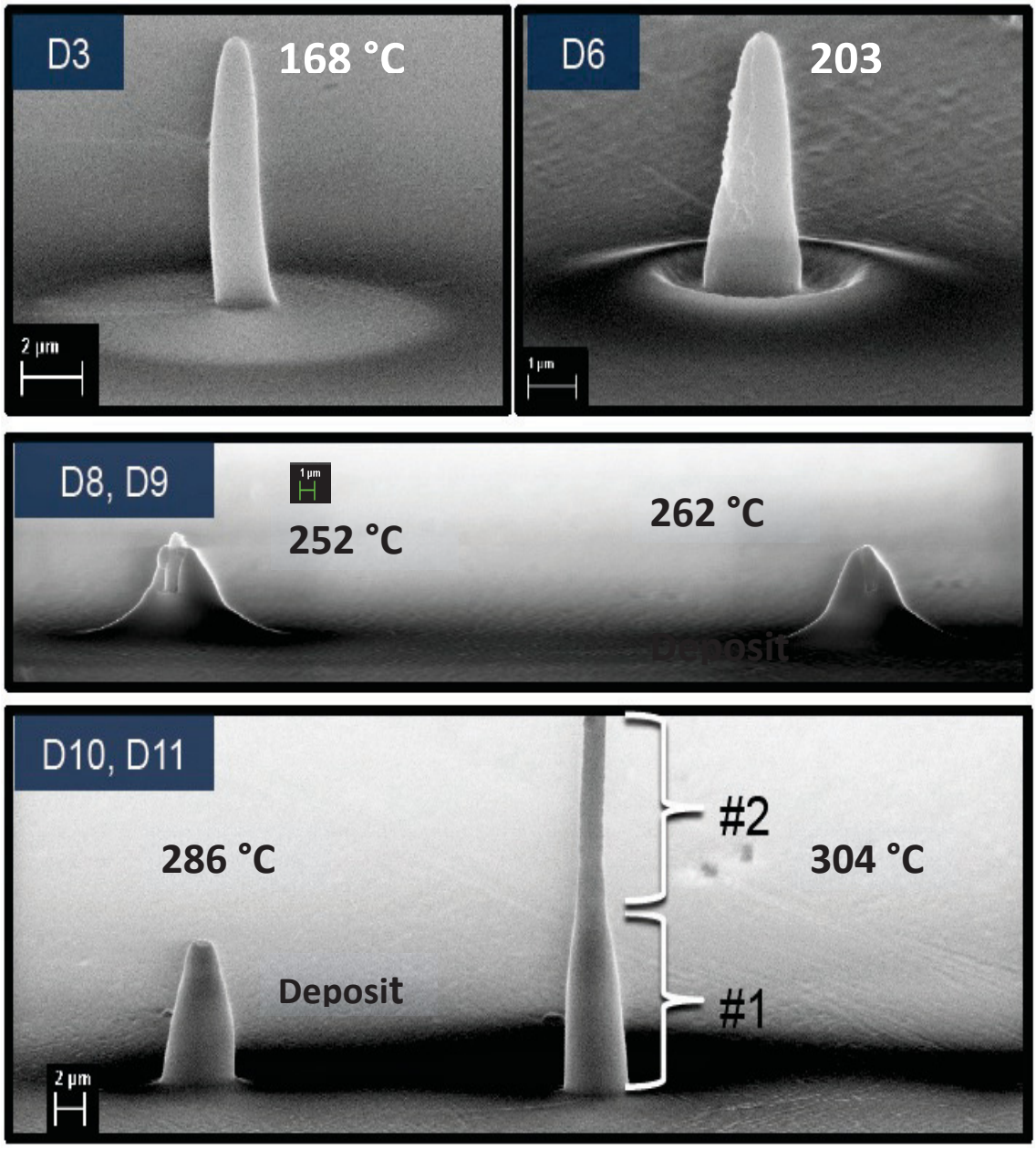

Figure 5.3: *(Above): FEBID growth into high T_s region (set 3). Primary growth decreases, secondary growth increases and merger occurs. Large increase in growth rate is observed after merger event. (Below, next page): I_e curves collected during EBID of deposits shown above. Merger event is seen in gradient increase of D8 and D9.*

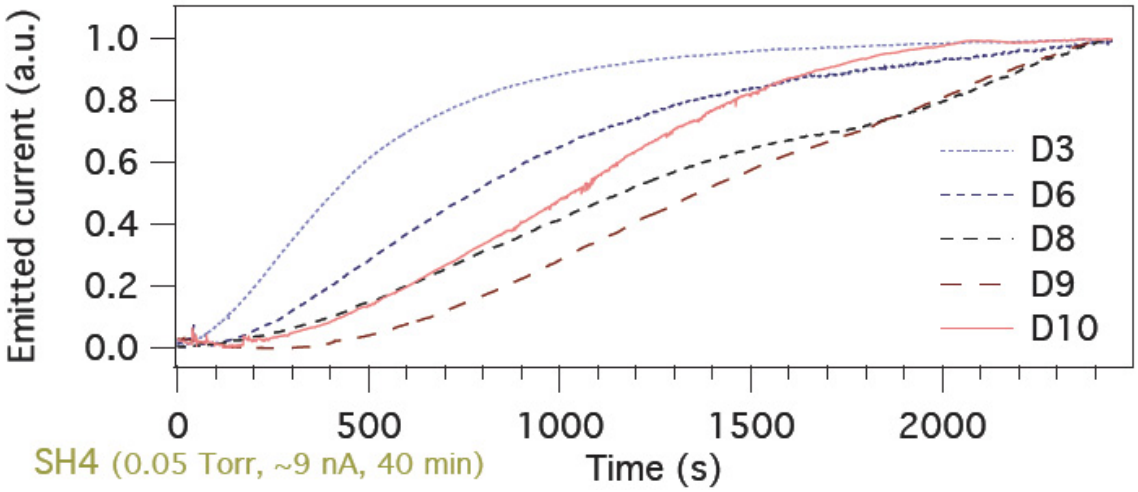
Emitted current (a.u.)
1.0
0.8
0.6
0.4
0.2
0.0
0
500
1000
1500
2000
Time (s)
D3
D6
D8
D9
D10
SH4 (0.05 Torr, ~9 nA, 40 min)

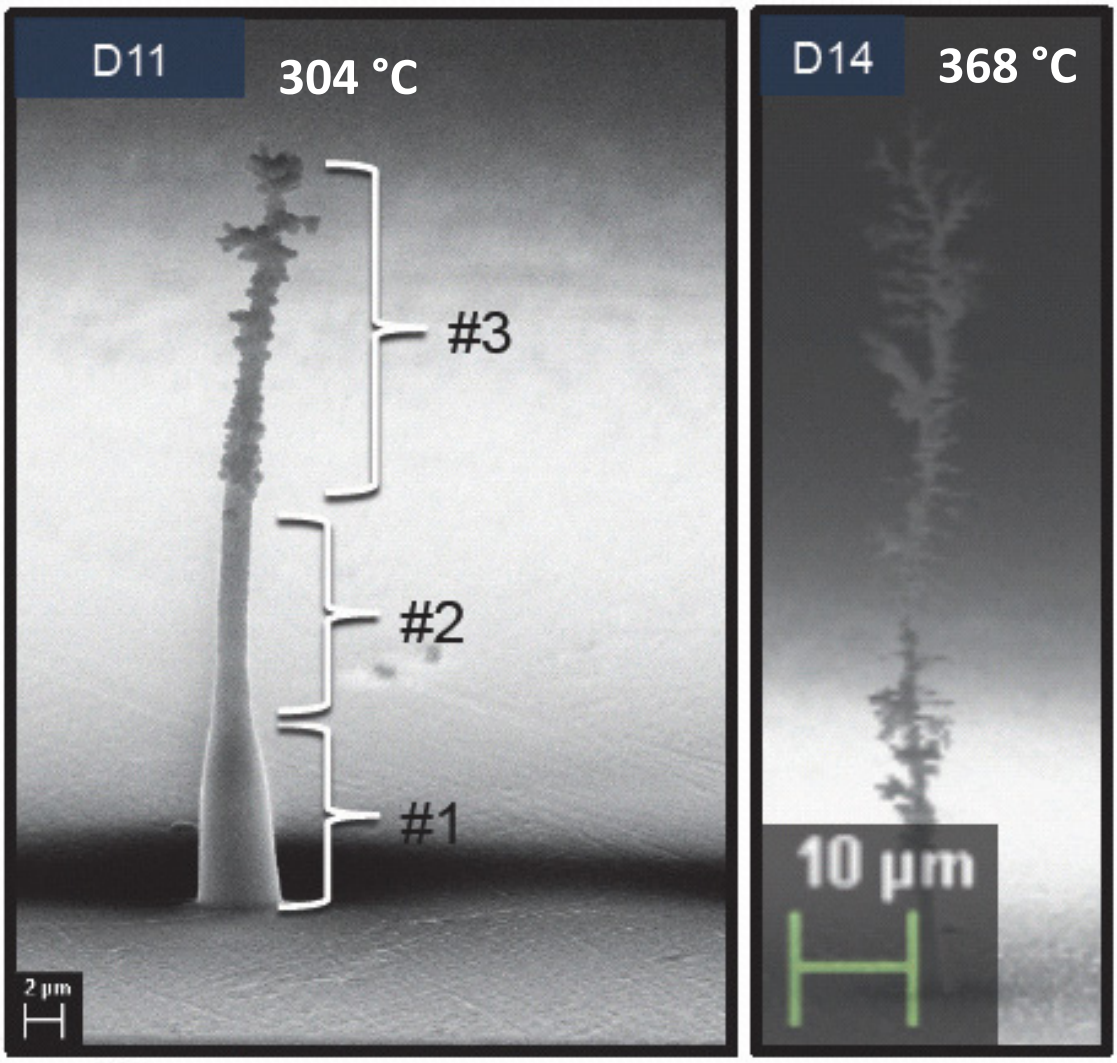
D11
304 °C
#3
#2
#1
2 µm
D14
368 °C
10 µm

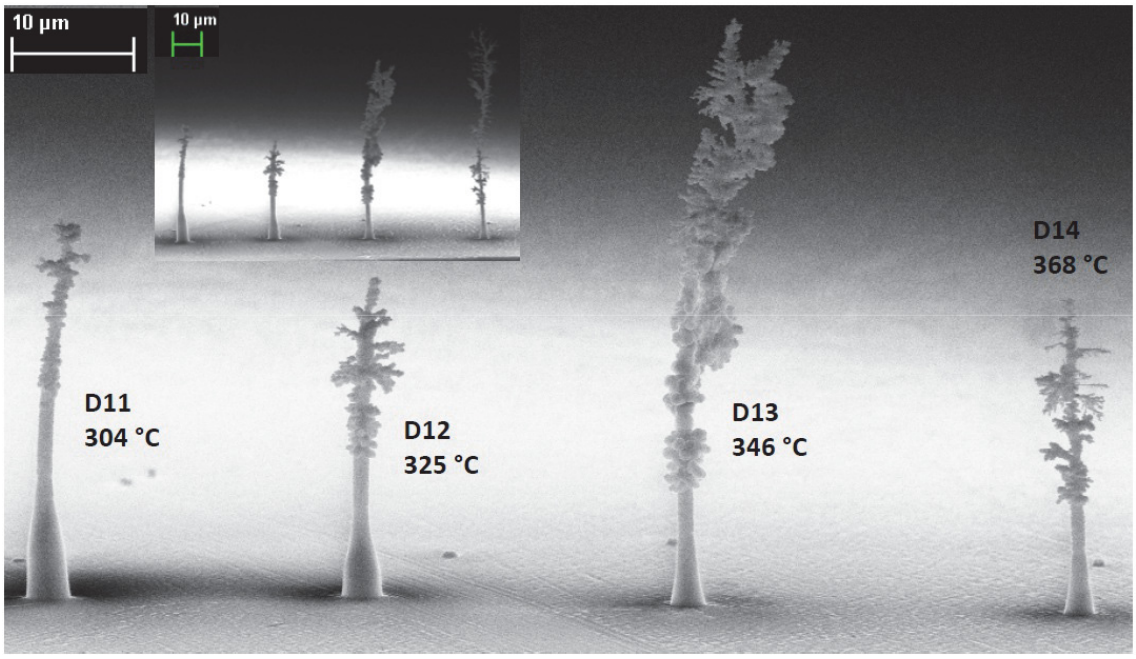

Figure 5.4 (above & previous page): *FEBID growth at T_s > 300 °C, (Top left): 3 distinct growth regions indicated on FEBID pillar. (Top Right): D14 (set 3) prior to pillar breakage, note extraordinary height. (Bottom): D11 – D14 of set 3, note decreasing height and width of region #1 and decreasing height of region #2 with increasing T_s. Top of D14 broke off due to imaging. D12 likely broke during transit to Zeiss LEO SEM. (Inset): D11 – D14 prior to D14 breakage.*

The onset of region #3 growth is indicated in I_e and I_t curves. A drop in I_e or I_t followed by erratic behaviour is indicative of region #3 growth. Region #3 growth initiates earlier with increasing T_s and reaches higher. This can be seen in the I_e & I_t curves. The fractal growth of region #3 seems to generally have increasingly finer structure with increasing T_s, although exceptions do occur. The finer structures are very delicate and the top parts of D12 and D14 were broken off. D12 was likely damaged in transferral to Zeiss SEM and the upper part of D14 was damaged in a more interesting way. The inset in figure 5.4 shows D14 prior to breakage. Increasing the magnification during imaging will increase the incident current density upon an EBID pillar. Charging occurs during imaging of finely structured region #3 EBID deposits and causes image distortion which can be indicative of deflection of the electron beam by high – strength localised electric fields. The top of D14 was broken off by increasing the magnification during imaging. This is likely due to the force exerted on the EBID deposit by the electron beam due to strong electric fields at the pillar surface.

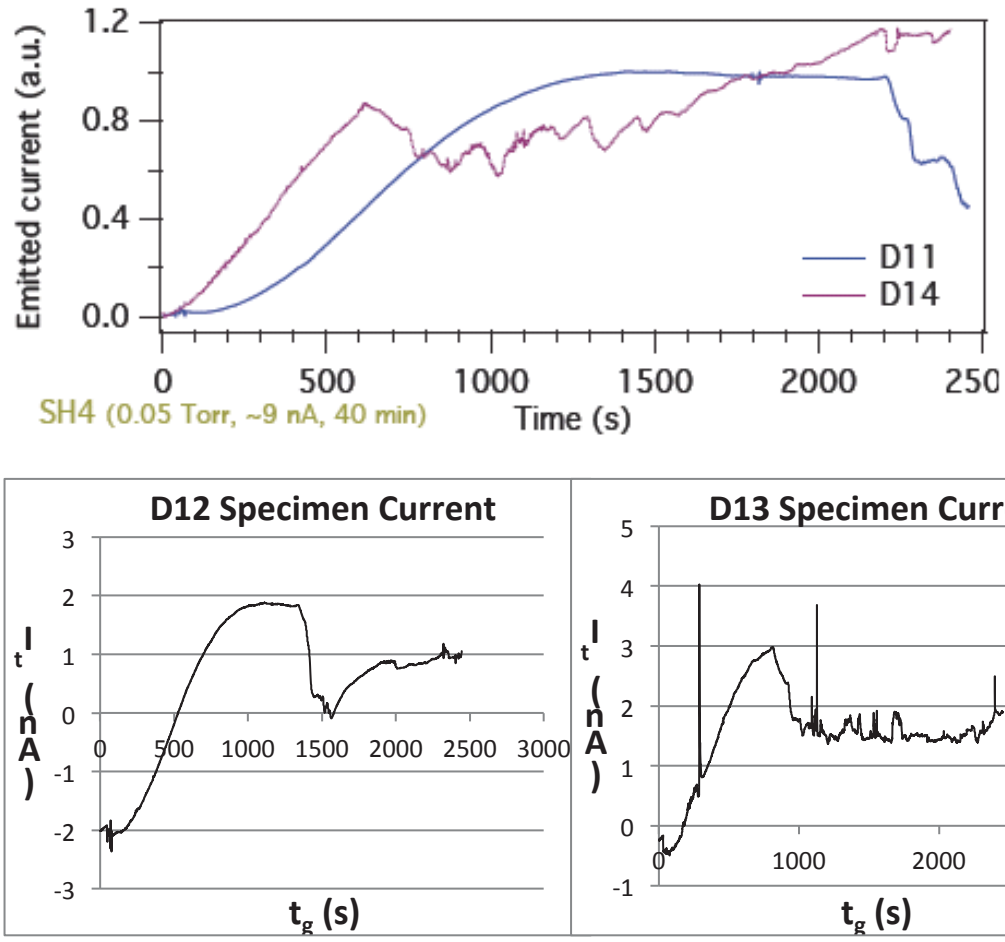

Figure 5.5: *I_e and I_t curves indicating onset of region #3 fractal-like growth. #3 initiates earlier with increasing T_s. Region #3 growth initiates after and prior to curve saturation for D11, D12 and D13, D14 respectively. Large spikes seen in D13 I_t curve are instrumental noise.*

Explanation of Results

The unique evolution of FEBID deposit geometry and growth rates with T_s likely has a number of contributing factors. The adsorption kinetics of TEOS discussed in the previous chapter will affect the growth rates and may contribute to the shape evolution. A high level of diffusion of precursor molecules is a likely contributor. Electron beam induced heating (EBIH) is surely one of the main contributing factors and evidence for EBIH is observed. Excessive charging of FEBID pillars during growth must be occurring during region #2 and #3 growth to result in the fractal patterns observed. Effects of excessive charging on EBID can be somewhat unpredictable. Determination of detailed mechanisms behind the FEBID growth presented in this

chapter would require further investigation although each likely contributing factor will be discussed in detail.

Adsorption Kinetics and Diffusion

Recalling the adsorption kinetics of TEOS as discussed in the previous chapter we can assume that the precursors for EBID at T_s > 150 °C are primarily the chemisorbed products of dissociative TEOS adsorption and are likely to be tri- and di-ethoxysiloxane. There is some dispute about the other majority species present on the surface following dissociative chemisorption of TEOS. For a surface with significant surface –OH coverage, the reaction scheme presented by Tedder *et al.* [73] is a likely route to chemisorption:

$$Si(OC_2H_5)_4 + Si\text{-}OH \rightarrow (SiO)(OC_2H_5)_3 + C_2H_5OH \qquad (5.1)$$

$$(SiO)(OC_2H_5)_3 + Si\text{-}OH \rightarrow (SiO)_2(OC_2H_5)_2 + C_2H_5OH \qquad (5.2)$$

Ethanol is likely to be the 3rd majority surface product for the case of an EBID material surface with significant –OH chemisorbed on the surface. Ethanol is likely to only physisorb and thus will desorb from the surface quickly at high T_s. H_2O could potentially be formed by EBID reactions of the chemisorbed siloxanes and result in significant –OH surface termination. Other reaction schemes presented by other authors propose ethyl groups [74] or ethoxy groups [76] as the 3rd majority surface species following dissociative chemisorption. The EDS compositional analysis results presented in the previous chapter indicate that minimal C is incorporated in deposits grown above 250 °C. This indicates that it does not matter which species is the 3rd majority species as it is quickly desorbed from the surface and not incorporated into the deposit. Thus it is safe to assume that we can treat the situation as having only 2 precursor species which contribute to the EBID growth at high T_s. These two species are likely tri- and di-ethoxysiloxane and are chemisorbed to the surface. The modelling results presented in chapter 4 indicate that the two species have similar EBID parameters (e.g dissociation cross-section, diffusivity etc.) and can be approximated by a single chemisorbed surface species.

The onset of chemisorption of precursor will result in an increased EBID rate due to a higher concentration of precursor as discussed in the previous chapter. This can in part account for the changes in growth rate but cannot, by itself explain the observed evolution of FEBID deposit morphology. Significant surface diffusion of precursor is consistent with the observed deposit morphologies. Since a chemisorbed species has a much stronger bond with a surface than a physisorbed species, one may expect that the surface mobility (diffusion) of chemisorbed species to be lower. Furthermore, it would be expected that chemisorption bonds would have to be broken, the molecule diffuse across the surface and then new bonds formed at a new active site for diffusion of chemisorbates to occur. However, it has been shown that the mobility of chemisorbed species can be high for certain systems and that the energy barrier to diffusion occurring does not necessarily depend directly upon the energy of desorption. The results lead me to conclude that there is significant surface diffusion of these chemisorbed precursor molecules occurring. The pillar and ring morphologies observed for FEBID deposits prior to merger of primary and secondary growth regions is common for FEBID with significant surface diffusion [85, 86]. As T_s is increased the diffusion coefficient, D_d of precursor molecules will increase. An increasing supply of precursor via diffusion is consistent with the increasing secondary growth. The abrupt edge of the secondary growth is indicative of diffusion influenced growth.

The mean diffusion length L_d will increase with D_d. Thus precursors diffusing inwards towards the beam axis will be more likely to travel further (before being dissociated) with increasing D_d and will simultaneously encounter an increasing electron flux with decreasing distance from e^- beam axis (r). An increasing L_d coupled with a higher total flux of precursors arriving via diffusion with increasing T_s is the best explanation for the observed decreasing diameter and increasing rate of secondary growth that can be provided without further experimental data.

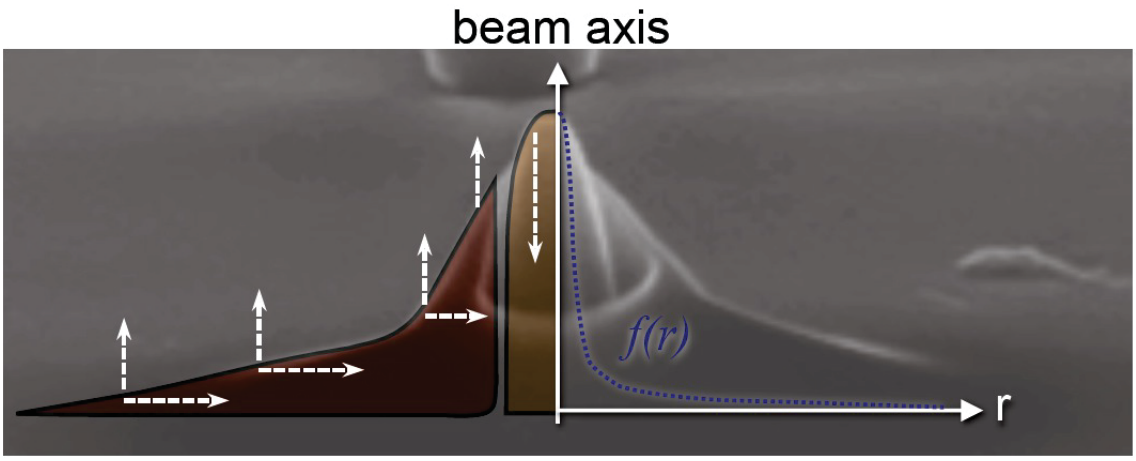

Figure 5.6: *Schematic overlayed on image of deposit illustrating trend in primary (yellow) and secondary (red) growth regions with increasing T_s. The decrease in the primary region slows down and is halted as chemisorption reaches a maximum.*

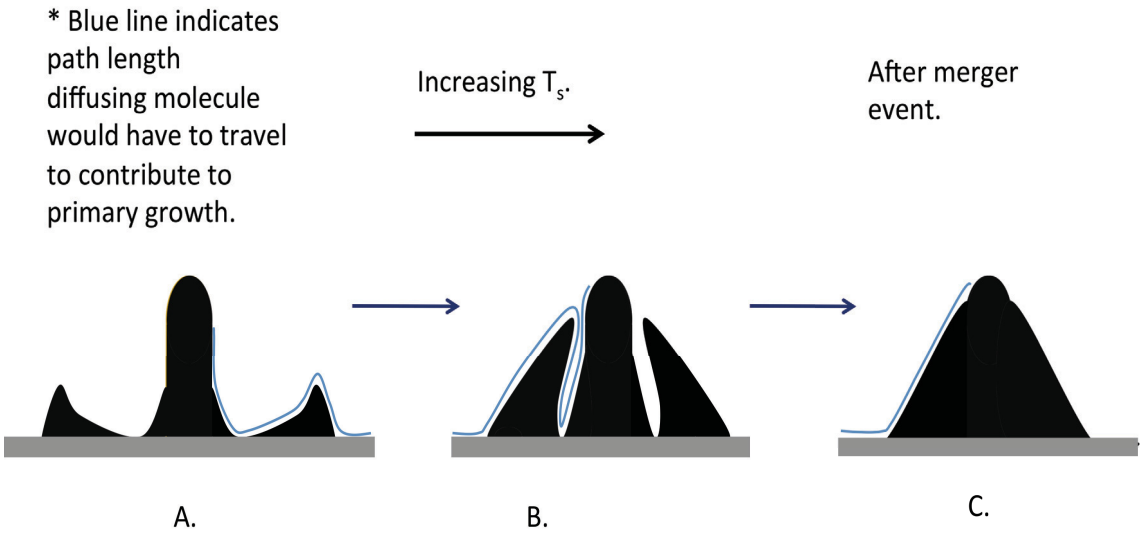

Figure 5.7: *Simple schematic illustrating the evolution of the primary and secondary growth regions with T_s and diffusion path length (l_p) which a diffusing molecule would have to travel to contribute to the primary growth. Mean diffusion length (L_d) will be increasing with T_s. After merger event l_p will suddenly be drastically reduced whilst L_d continues to increase.*

As is indicated in figure 5.7, we can define the diffusion path length l_p as the distance a diffusing molecule would have to travel to reach the primary growth region. l_p will be increasing with T_s prior to merger event. L_d will increase with T_s until desorption of chemisorbed precursor becomes significant. Thus it is likely that prior to merger event, diffusing molecules contribute only to secondary growth and the primary growth region has ≈ 0 growth contribution from diffusion as diffusing

molecules will be dissociated by SE2s and FSEs before they reach the beam axis. The decreasing diameter of the secondary growth region is attributed to increasing L_d. A significant electron flux will also be incident upon and emitted from the inner sidewall of the secondary region which will cause it to grow inwards. EBIH will also be simultaneously causing a local temperature rise and increasing L_d further. The combination of this sidewall growth and EBIH is proposed to explain the observed occurrence of the merger event with long deposition time. The merger event occurs earlier for higher T_s as the secondary growth will be closer to primary growth.

After the merger event, diffusion will be able to contribute to the primary growth. The diffusion path length l_p will suddenly and drastically be reduced by the merger event which will allow diffusing molecules to reach close to the beam axis before being dissociated. After merger event there is only the primary growth and the growth rate is increased dramatically. This increase in precursor supply due to high levels of diffusion can explain the onset of region #2 growth.

Electron Beam Induced Heating (EBIH) and Charging

Separating the effects of EBIH and charging can be very difficult. This is due to the fact that charging and EBIH are generally affected in the same way by most parameters. For example, increasing the electron flux will increase both charging and EBIH. Furthermore, materials which are good thermal insulators are generally also good electrical insulators and thus EBIH and charging can be significant for the deposition of insulating material. Material deposited by TEOS EBID is highly insulating and thermal and electrical conductivity are expected to decrease with decreasing carbon content. In the previous chapter it was demonstrated that TEOS EBID at T_s > 250 °C results in SiO_2C_x material with a very low C content. Thus it is expected that EBIH and charging levels are higher for TEOS EBID at T_s > 250 °C. It seems likely that both processes contribute significantly to the fractal-like dendritic growth of region #3.

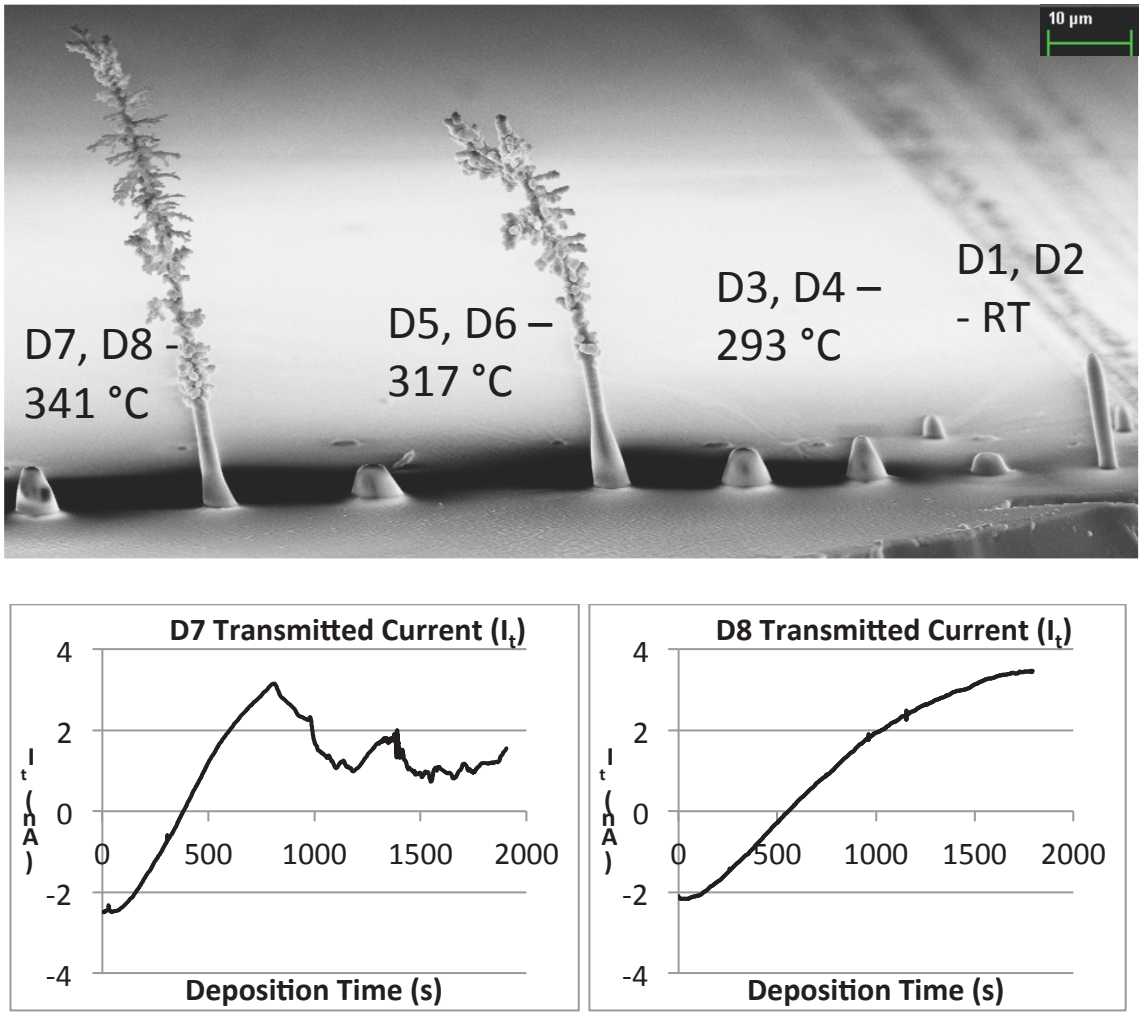

Figure 5.8: *SEM image and I_t curves of set 4. From right to left each 2nd deposit is defocused by 0.3 mm to achieve a lower electron flux over a larger area. The deposits grown with a lower e^- flux do not initiate region #2 and #3 growth.*

The experimental set shown in figure 5.8 above demonstrates the importance of EBIH and/or charging in the initiation of region #2 and #3 growth. At high T_s region #2 and #3 growth is seen using a focused beam. Using a wider, slightly defocused beam the extra growth regions do not occur. This result does not directly allow separation of the contributions of EBIH and charging.

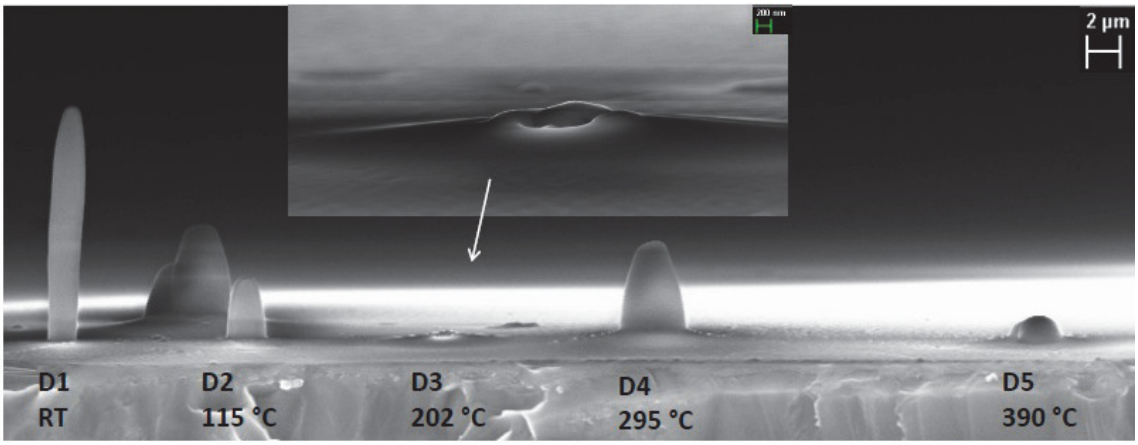

Figure 5.9: *SEM images of set 5. The set was made with a 3.5 nA focused beam. It is seen that region #2 and #3 growth is not initiated in the high T_s region with the lower e^- flux. Furthermore, curious geometry and a low growth rate are observed around 200 °C. Inset: higher magnification image of D3, scale bar is 200 nm.*

Set 5 presented in figure 5.9 above provides further evidence for the importance of EBIH and/ or charging in the initiation of region #2 and #3 growth. The lower e^- flux used (3.5 nA compared to 9 nA for set 2 & 3) results in much less charging and EBIH and no region #2 or #3 growth is observed. The growth dynamics seem to be somewhat different for TEOS FEBID with increasing T_s at lower electron flux. The case appears to be closer to the wide, defocused beam EBID case presented in chapter 4 although it is unique in some ways. Note the volcano-like deposit and low growth rate (t_g = 25 mins for each deposit) observed at 202 °C and the wide deposit grown at the highest T_s. The result serves to further demonstrate the high complexity of FEBID at high T_s with TEOS where many simultaneously occurring processes result in unpredictable results. Important processes which will be occurring include: diffusion, depletion, dissociative chemisorption, EBIH and charging.

The final set shown in figure 5.10 allows some separation of the effects of EBIH and charging. The set was grown with a high TEOS pressure of 0.16 torr. The higher pressure will allow significant charging compensation while heat dissipation will be increased to a lesser degree. We see that the growth rate is increased at all T_s which is as expected. The extra growth of regions #2 & #3 is increased using the higher precursor pressure. It is also observed that the fractal-like dendritic growth of region

#3 is less random and more ordered although not suppressed in terms of the significantly accelerated growth rate caused by the onset of region #3 growth. The decreased randomness of region #3 growth for D5 is attributed to a higher level of charge compensation by the higher precursor pressure. The difference between D4 and D5 (grown at same T_s) indicates a vastly accelerating EBID rate from region #2 to #3 growth.

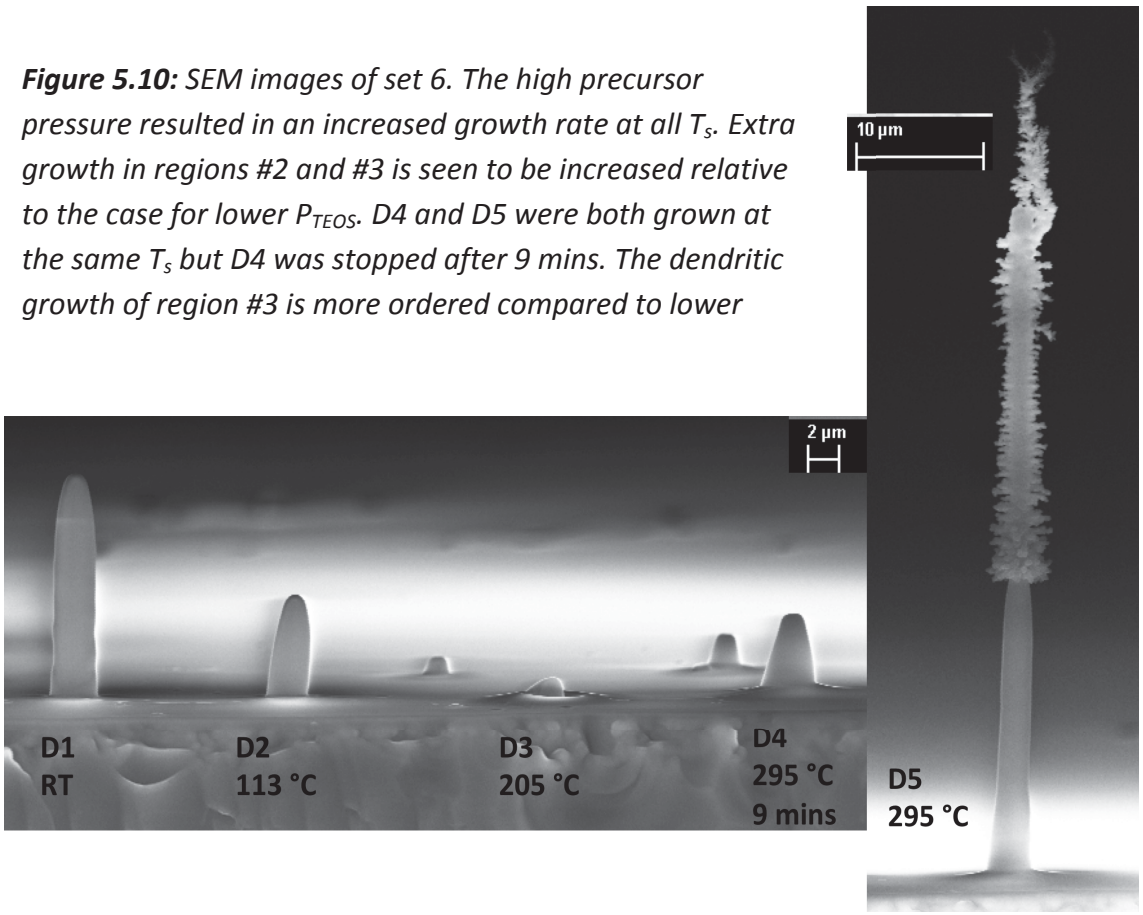

Figure 5.10: *SEM images of set 6. The high precursor pressure resulted in an increased growth rate at all T_s. Extra growth in regions #2 and #3 is seen to be increased relative to the case for lower P_{TEOS}. D4 and D5 were both grown at the same T_s but D4 was stopped after 9 mins. The dendritic growth of region #3 is more ordered compared to lower*

The evidence all points towards charging playing a significant role. High asymmetric electric fields at the surface of a growing EBID pillar caused by charging could attract ionised precursor molecules from the gas phase. A localised plasma will be present surrounding any growing EBID deposit due to gas phase electron induced ionisation events. Electric fields could attract ionised precursor molecules to the surface of a growing EBID pillar. Polarisation of precursor molecules by strong electric fields could also occur and polarised molecules be attracted to a growing EBID pillar [68, 99]. Ionised and polarised precursor molecules being induced to follow deterministic paths due to electric fields (formed by excessive charging during EBID)

and being attracted to a growing deposit, is a likely candidate to explain the fractal pattern growth observed. Banhart [99] proposed this mechanism to explain dendritic growth from a hydrocarbon precursor.

There is some evidence which indicates that EBIH must also play a role and charging is not the exclusive casual process. Region #3 growth is observed to initiate earlier with increasing T_s (fig. 5.4 & fig. 5.8). Both #2 and #3 growth does not occur under any experimental conditions investigated at lower T_s. These results indicate that a certain temperature is required to initiate the growth referred to as region #2 and #3. The rate of heating by EBIH will be constant for each T_s. Less heating (by EBIH) time will be required to bring the deposit tip up to the required temperature for region #2 and #3 growth to initiate for a higher T_s.

The possibility of thermal decomposition of TEOS at the pillar surface has been considered and dismissed due to the high temperatures needed (≈ 900 - 1000 K [73]) for spontaneous thermal decomposition of TEOS. It is unlikely that EBIH could achieve such temperatures [84]. Electron beam assisted and/or autocatalytic CVD where the decomposition temperature of a molecule is lowered has been reported for some EBID precursors [53] and was also considered. The results presented in chapter 4 with a wide beam up to high T_s allow dismissal of these processes. Beam assisted or autocatalytic CVD would have resulted in another growth rate increase by 550 °C.

A study of all the available data concerning the complex growth resulting from FEBID at high T_s leads me to propose the following possible explanation:

Material deposited by TEOS EBID at high T_s is much more pure and thus of lower thermal and electrical conductivity than the material deposited at RT. Thus EBIH and charging are both higher. After merger event, the overall growth rate of a FEBID deposit is increased due to the sudden increase in precursor supply due to diffusion. The width of the deposit decreases as growth rate accelerates due to increasing diffusion due to EBIH (which itself increases as width decreases) initiating region #2 growth. The growth rate continues to accelerate and surface roughening increase during #2 growth due to increasing temperature (EBIH) and surface charge. Increasing surface charge attracts ionised and polarised precursor molecules to the surface

increasing precursor supply and accelerating growth rate further. Region #3 growth initiates when surface roughness becomes significant, resulting in increasing asymmetry of the electric fields at the surface. Fractal growth ensues as precursor molecules follow paths according to the increasingly asymmetric electric fields. The growth rate likely is accelerated even further as the fine structures of the fractal growth have the same charge incident upon them resulting in stronger electric fields.

5.5 Conclusions:

FEBID at RT with most precursors results in high aspect ratio pillars surrounded by a diffuse “halo”. Increasing the electron flux results in pillars of decreasing aspect ratio as the vertical growth rate saturates before the lateral growth rate. As the substrate temperature (T_S) is increased, FEBID with TEOS results in unique growth. The growth rate of the pillar (primary region) decreases and saturates while the growth rate of the halo (secondary region) increases and decreases in diameter closing in on the primary region. The evolution of the secondary growth with T_S is likely due to increasing diffusion of precursor. The primary and secondary growth regions merge with T_S > 260 °C given sufficient growth time, for the experimental conditions used. The merger event is attributed to increasing diffusion, EBIH and growth of the secondary region inwards towards the primary region. After merger event growth rate is significantly increased and the rate continues to accelerate. Ionised precursor molecules are likely attracted to the growing EBID pillar and increase growth rate. Surface roughness increases as electric fields at the pillar surface increase in strength and become increasingly asymmetric. This causes a cascade effect which results in rapid fractal growth.

6. TEOS EBID with Gas Mixing

6.1 Abstract:

EBID was performed using TEOS precursor with oxygen and argon mixing. It was found that O_2 mixing increases both the purity and deposition rate of EBID deposits grown at room temperature (RT). Argon mixing was found to decrease EBID rates at RT. O_2 mixing was found to inhibit TEOS EBID growth at higher T_s where TEOS EBID proceeds through chemisorbed rather than physisorbed surface states. Increased purity and growth rate of TEOS EBID at RT with O_2 mixing is attributed to dissociation of TEOS by oxygen radicals generated by e^- induced dissociation of physisorbed O_2. Deactivation of surface sites by activated dissociative chemisorption of O_2 at high T_s is proposed to explain the inhibition of TEOS EBID with O_2 at high T_s. Unique FEBID deposit geometries are obtained during FEBID with O_2 mixing and likely growth mechanisms are explored.

6.2 Introduction:

As was briefly discussed in chapter 1, a major disadvantage of EBID as a nanofabrication technique is the typical composition of deposits produced by EBID [44]. Typically, organometallics precursors are used and the composition and structure of deposits from such precursors is often reported as nanocrystals of the target metal dispersed throughout an amorphous carbon matrix [45]. Impurity incorporation is also problematic for inorganic precursors such as WF_6 [44]. Inorganic precursors reduce C incorporation and allow higher purity yet inorganic impurity incorporation remains problematic. Residual water and organic vapours also add to impurity incorporation. Deposition onto a heated substrate has been used to improve EBID deposit purity through increased desorption of H_2O and organic species during growth [53]. Mixing of reactive gases such as O_2, N_2O, H_2O or H_2 with the precursor during EBID has been shown to increase deposit purities for many systems [53].

For the case of deposition of an oxidised material such as TiO_2, SiO_2 or CuO, O_2 or H_2O mixing during EBID has been demonstrated to produce uncontaminated

deposits [48, 68, 87]. Perentes *et al.* [48, 87] used O_2 mixing with a range of organosilane precursors to produce pure stoichiometric SiO_2. Studies involving oxidising gas mixing have thus far concentrated on improving EBID deposit composition, although Perentes *et al.* [87] and Fischer *et al.* [68] both reported an increase in EBID rate as well as deposit purity with O_2 mixing. To our knowledge no detailed mechanisms have been presented in the literature to explain increased EBID rates and deposit purity using organosilane precursors mixed with oxidant gases.

Analysis of changes in EBID rates with parameters such as substrate temperature (Ts) can allow investigation of processes occurring during EBID. In this work we have investigated oxygen mixing during EBID with tetraethoxysilane (TEOS) precursor. Growth mechanisms are proposed based upon observations of TEOS EBID growth behaviour with and without O2 mixing over a broad substrate temperature (Ts) range. The effects of oxygen mixing are found to differ according to the adsorption state of the precursor molecule. The mechanisms are consistent with results published in the literature.

6.3 Experimental:

EBID experiments were performed with the ESEM cell experimental apparatus described in detail in previous chapters. Reactive (O_2) and inert (Ar) gases were mixed with the precursor (TEOS) prior to introduction to ESEM cell for some experiments. Experiments were performed with focused and defocused electron beams at RT and elevated T_s. Standard Si(111) substrates described in previous chapters were used for all experiments. High purity mixing gases O_2 (Sigma-Aldrich > 99.9%) and Ar (Scientific & Technical Gases PTY LTD > 99.9 %) were introduced to the precursor input line of the ESEM cell via a mass-flow controller (MFC) for precision control of mixing gas partial pressure. The flow of TEOS precursor was set and fixed to achieve the desired pressure and mixing gas then added to achieve a certain total pressure in the ESEM cell. Stable and reproducible partial pressures were achieved. The apparatus for gas mixing is detailed below in figure 6.0. All experiments were performed at room temperature (RT) with a 25 kV electron beam unless stated otherwise.

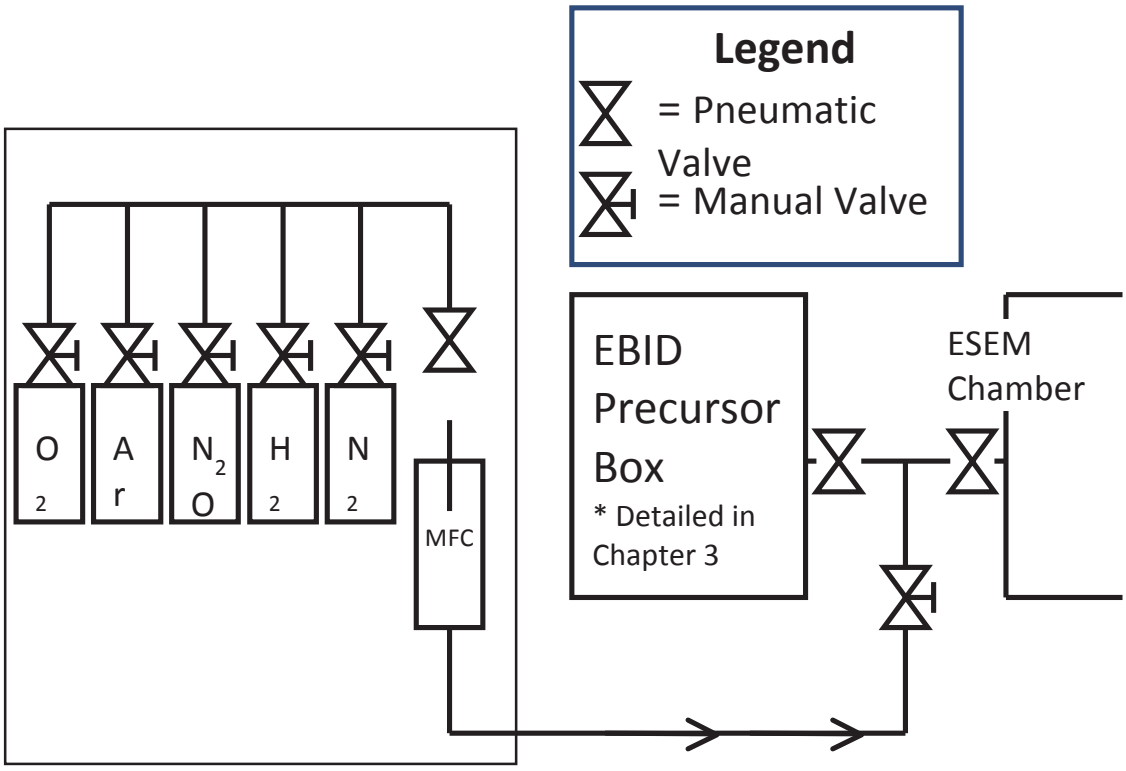

Figure 6.0: *Schematic of auxiliary gas box used for gas mixing. Any of the gases listed could be used for mixing. The MFC allows precision control of the mix gas partial pressure to within ≈ 0.01 torr.*

The majority of the data for this chapter was derived from seven experimental sets. The conditions used for each set were, **Set 1:** Slightly defocused beam (focus point moved 0.05 mm away from optimum focal point) EBID as function of t_g , I_b: 3.5 nA, 0.05 torr TEOS partial pressure (P_{TEOS}) for all parts. *Part 1:* TEOS only, total pressure P_T: 0.05 torr. *Part 2:* TEOS + Ar, P_{Ar}: 0.075 torr, P_T: 0.125 torr. *Part 3:* TEOS + O_2, P_{O2}: 0.075 torr, P_T: 0.125 torr. **Set 2:** EBID with fixed t_g as function of beam diameter, t_g: 20 mins, I_b: 3.5 nA, P_{TEOS}: 0.05 torr for all parts. *Part 1:* TEOS only, P_T: 0.05 torr. *Part 2:* TEOS + Ar, P_{Ar}: 0.075 torr, P_T: 0.125 torr. *Part 3:* TEOS + O_2, P_{O2}: 0.075 torr, P_T: 0.125 torr. **Set 3:** Wide beam EBID ($\Delta d_{f\text{-}s}$ = 0.5 mm), t_g: 40 mins, I_b: 3.5 nA, P_{TEOS}: 0.05 torr both deposits. *D1:* TEOS only, P_T: 0.05 torr. *D2:* TEOS + O_2, P_{O2}: 0.17 torr, P_T: 0.22 torr. **Set 4:** FEBID, function of T_s, I_b: 3.5 nA, T_s: 25 – 390 °C, P_{TEOS}: 0.05 torr both parts. *Part 1:* TEOS only, P_T: 0.05 torr. *Part 2:* TEOS + O_2, P_{O2}: 0.075 torr, P_T: 0.125 torr. **Set 5:** FEBID, t_g: 40 mins, I_b: 9 nA, P_{TEOS}: 0.05 torr both deposits. *D1*: TEOS only, P_T: 0.05 torr. *D2:* TEOS + O_2, P_{O2}: 0.25 torr, P_T: 0.3 torr. **Set 6:** FEBID, TEOS + O_2, function of t_g, I_b: 9 nA,

P_{TEOS}: 0.1 torr, P_{O2}: 0.2 torr, P_T: 0.3 torr. **Set 7:** FEBID, function of I_b, t_g: 30 mins, P_{TEOS}: 0.05 torr both parts. *Part 1:* TEOS only, P_T: 0.05 torr. *Part 2:* P_{O2}: 0.25 torr, P_T: 0.3 torr.

6.4 Results & Discussion:

TEOS EBID with O_2 and Ar Mixing at RT

The addition of O_2 or Ar with TEOS during EBID was found to have a significant effect on the growth. Figure 6.1 and 6.2 display volumetric growth rates of EBID deposits fabricated with a slightly defocused beam (set 1) as a function of time and with fixed t_g as a function of beam diameter (set 2) with (1) TEOS only, (2) TEOS + O_2 and (3) TEOS + Ar. With respect to the EBID rate using TEOS only, the growth rate can be significantly increased or decreased using O_2 or Ar mixing respectively. Focused and near focused beam deposits grown with TEOS + Ar maintain their geometry with respect to TEOS only deposits while deposits grown with TEOS + O_2 display a unique geometry where pillar width increases with height.

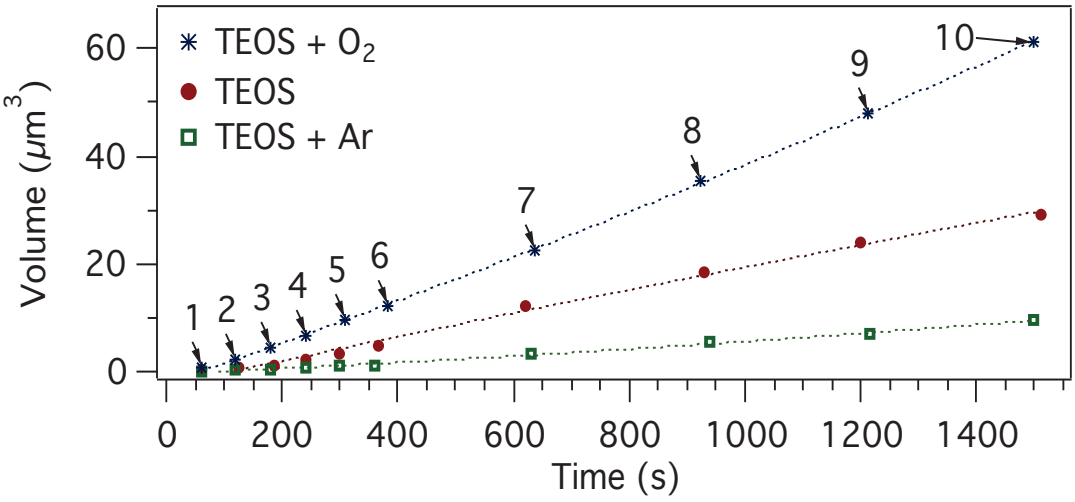

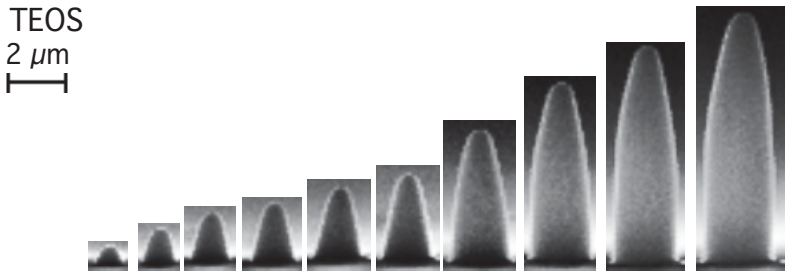

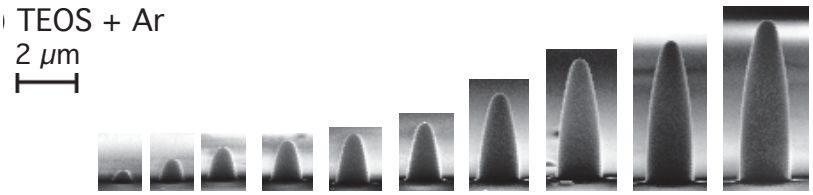

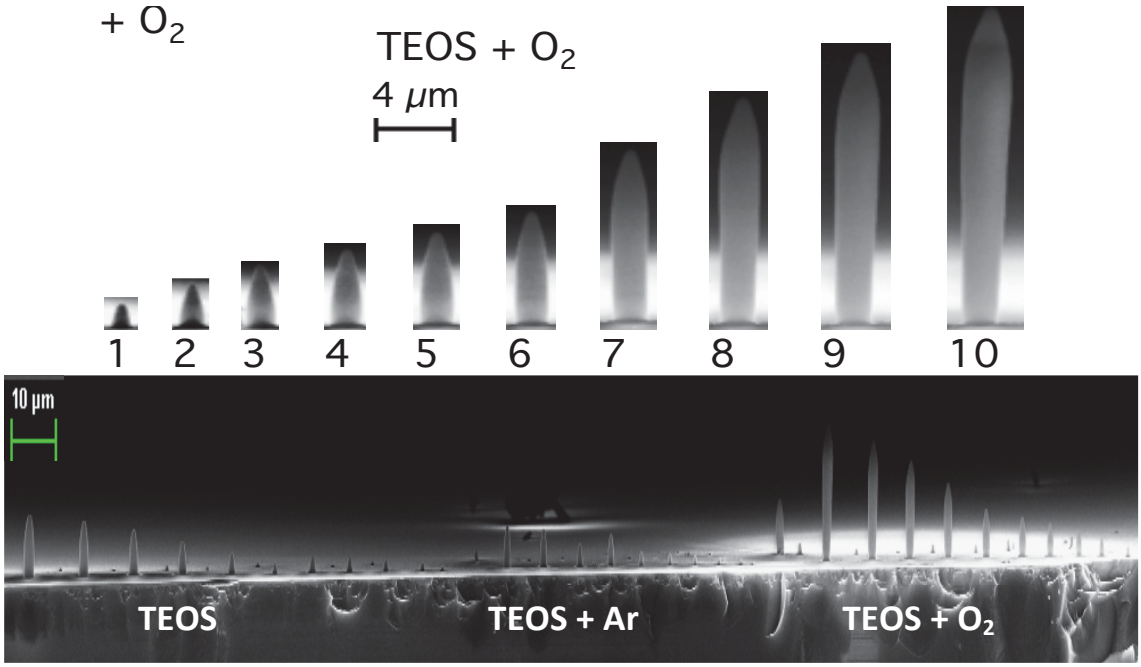

Figure 6.1 (above): *Volume vs time and SEM images of set 1. Large increase or decrease in growth rate at RT observed with O_2 or Ar mixing respectively.*

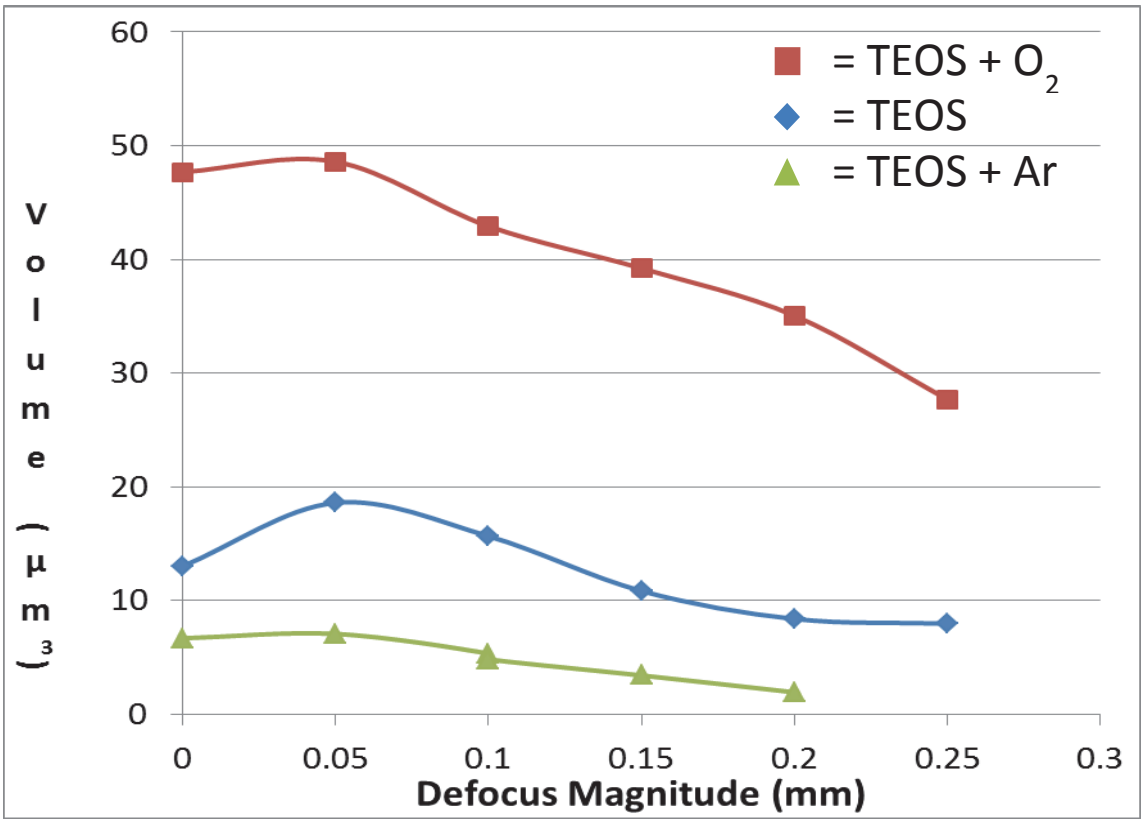

Figure 6.2 (above and next page): *Volume vs time and SEM images of set 2. The expected change in growth rate with increasing beam diameter (discussed in chapter 4) is observed for each precursor combination. Large increase or decrease in EBID rate at RT is observed with O_2 or Ar mixing respectively. D3 & D4 (left to right) of TEOS + Ar were made with same beam diameter due to I_e & I_t curve artifact of D3.*

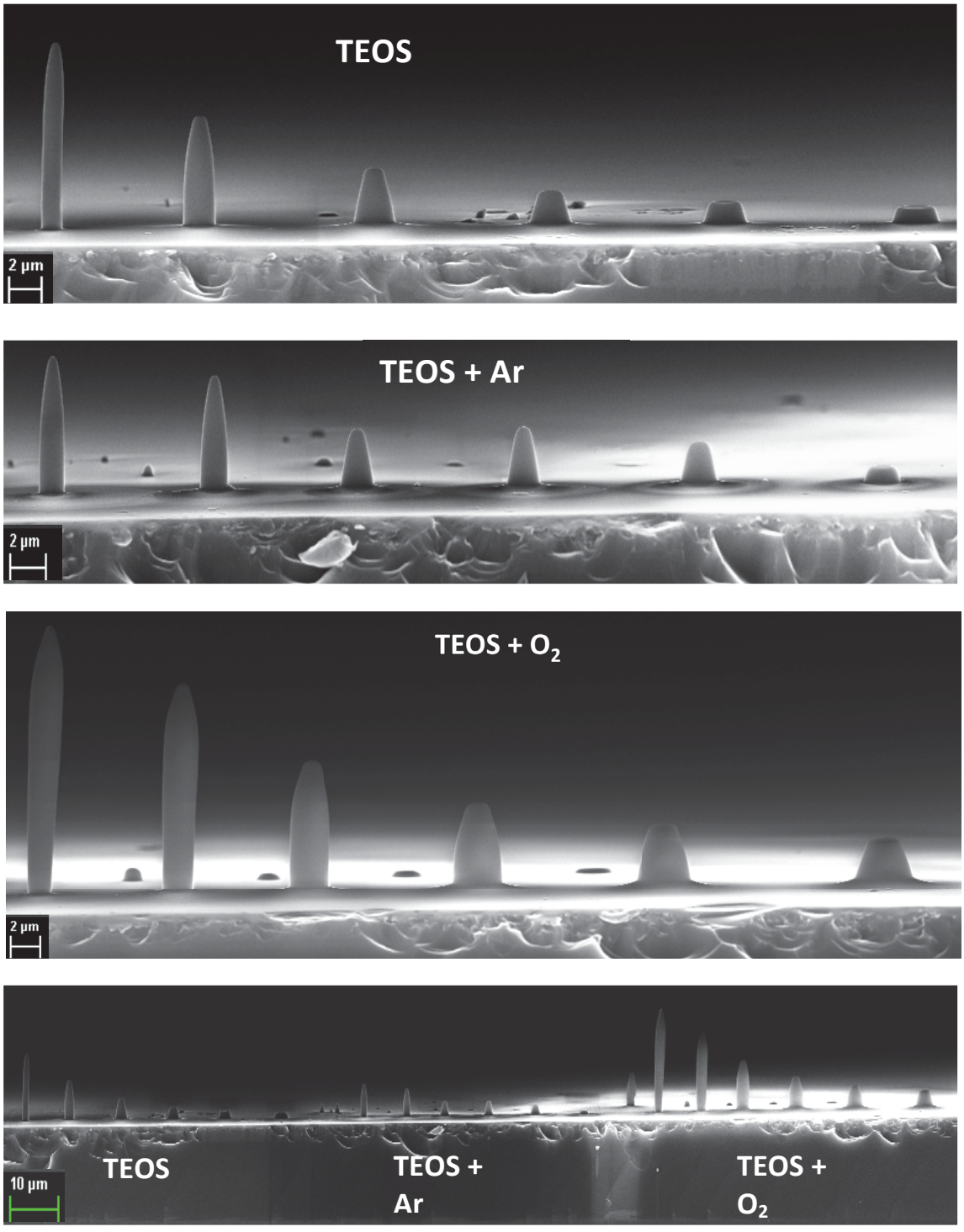

Growth Suppression with Ar Mixing

Several factors may contribute to the observed reduction in growth rate with Ar mixing. Excitation of Ar atoms by the electron beam may occur to a certain degree and it is feasible that some reactive excited Ar species (Ar^*) could exist in the system. Ar^* could react with TEOS with unpredictable effects upon the EBID growth rate. No experimental method could be devised to investigate the effect (if any) of Ar^* and it was considered unimportant as reducing growth rate is not of interest.

Physical mechanisms of growth suppression are more likely. Henry *et al.* [88] used an Ar gas jet to either increase or decrease the EBID rate from residual hydrocarbons. A low energy Ar jet (20 °C) was found to increase the supply of hydrocarbon precursor and thus EBID rate through enhanced diffusion of precursor molecules (collision induced migration, CIM) [89]. A high energy Ar jet (140 °C) was found to decrease the EBID rate through collision induced desorption (CID) [90] of precursor molecules. Ar atoms in the gas phase will be travelling in all directions with a kinetic energy distribution described by the Maxwell-Boltzmann distribution with the peak position defined by the gas temperature T_g. For Ar applying the ideal gas law, it was found that CID should be minimal for my system. For CID to occur it has been reported by several authors [90] that the minimum K.E of incident gas molecules must be at least 2 times the bond strength of the adsorbed molecule with the surface. For Ar at 300 K the proportion of gas phase atoms with sufficient energy to induce CID of adsorbed TEOS should be very low (<0.0001 %).

Another possible mechanism of EBID rate reduction with Ar mixing is surface site competition. TEOS will be unable to physisorb to a surface site occupied by a physisorbed Ar atom. This may occur in my system although the residence time of physisorbed Ar would be expected to be very low due to the inert nature of the gas. In summary, all mechanisms of growth rate reduction proposed above seem unlikely to be the cause. The inhibition of growth may be a combination of the physical mechanisms presented above or a more complex mechanism involving reactions of Ar^*. Further investigation was considered unimportant as Ar mixing was performed primarily as a control experiment to dismiss physical mechanisms of growth enhancement during O_2 mixing. Furthermore, a reduction in EBID rate is something to be avoided.

Growth Enhancement with O_2 mixing at RT

Physical mechanisms of growth enhancement are to be considered first. Collision enhanced migration (CIM) [89] of TEOS adsorbates via impact of O_2 molecules could increase precursor supply. Similarly, collision induced desorption (CID) [90] could increase supply of residual water molecules sourced from within the gas lines and chamber walls which would have an effect on growth. Van Dorp *et al.* [68] performed EBID with an organosilane precursor with H_2O mixing. They observed a similar growth enhancement effect to that observed for O_2 mixing with TEOS. The Ar mixing results discussed above allow us to deduce that both CIM of TEOS and CID of H_2O are negligible with Ar mixing. O_2 is of lower mass than Ar and thus it can be concluded that the situation is the same for O_2. It can therefore be concluded that reactive species derived from O_2 mixing increase the growth rate of TEOS EBID.

It is well documented that oxygen radicals can facilitate the decomposition of TEOS [91, 92, 77, 93]. Deshmukh *et al.* [77, 93] investigated the deposition of SiO_2 by atomic oxygen induced chemical vapour deposition (AOCVD) of TEOS in a remote plasma CVD reactor. They demonstrated that deposition of SiO_2 can proceed at RT via atomic oxygen induced decomposition of TEOS. They proposed that atomic oxygen ($O^{\cdot}$) directly oxidises adsorbed TEOS yielding $SiOH_{(s)}$, $H_2O_{(g)}$ and $CO_{(g)}$. A condensation reaction between adjacent silanol species then forms the SiO_2 film releasing H_2O. They also found that pure SiO_2 is formed by AOCVD with TEOS at RT if the $O^{\cdot}$/TEOS flux ratio is sufficiently high [93].

During EBID with TEOS/O_2 mixtures at RT both TEOS [77] and O_2 [94] will be primarily physisorbed to the surface. Physisorbed O_2 molecules are dissociated under electron beam irradiation to yield oxygen radicals [95]. Adsorbed atomic oxygen will then induce the dissociation of TEOS and will yield pure SiO_2 if the $O^{\cdot}$ concentration is sufficient [93]. This reaction will provide an alternative pathway for material deposition. The O radicals can be considered as having an effectively infinite cross-section for dissociation of TEOS. Any interaction between TEOS and $O^{\cdot}$ will result in dissociation of TEOS. This will occur with both species in the physisorbed state and

with TEOS from gas phase impacting physisorbed $O^{\cdot}$. The relative sizes of O_2 and TEOS will allow for a higher adsorbate density of O_2, promoting full oxidation of TEOS.

The effect described above could be described as localised atomic oxygen induced chemical vapour deposition (LAOCVD). The electron induced dissociation (EBID) of adsorbed TEOS molecules will also occur simultaneously. The sum of the two simultaneously occurring deposition mechanisms will result in an increased growth rate. Carbonaceous fragments produced by EBID of TEOS will also be oxidised to $H_2O_{(g)}$ and $CO_{(g)}$ by reaction with $O^{\cdot}$.

The proposed simultaneous reaction scheme leading to material deposition in the TEOS + O_2 EBID/LAOCVD system can be represented by the following stochiometric reactions:

$$Si(OC_2H_5)_{4(g)} + nO_{(ad)} \rightarrow SiO_{2(s)} + 0.625H_2O_{(g)} + (n/2)CO_{(g)} \quad \text{(LAOCVD), [77]}$$

$$Si(OC_2H_5)_{4(ad)} + nO_{(ad)} \rightarrow SiO_{2(s)} + 0.625H_2O_{(g)} + (n/2)CO_{(g)} \quad \text{(LAOCVD),}$$

$$Si(OC_2H_5)_{4(ad)} + ne^{-} \rightarrow SiO_xC_yH_z + nO_xC_yH_z \text{ fragments} \quad \text{(EBID),}$$

$$SiO_xC_yH_z \text{ fragments} + nO_xC_yH_z \text{ fragments} + nO^{\cdot} \rightarrow SiO_{2(s)} + nH_2O + nCO_2 \quad (O^{\cdot} \text{ induced purification}).$$

The value of n for the first two reactions is predictable by balancing the stoichiometric equations. Deshmukh *et al.* [77] present the first equation as the overall reaction for AOCVD of TEOS with n = 16. For the other two equations, many different species will be created by e^{-} induced dissociation of TEOS and as a result n, x, y and z could take many different values. Accurate quantification of products produced by EBID with TEOS is likely to be impossible. The best that can be done is to measure the elemental composition of EBID deposits and use the results to predict the non-volatile products produced by EBID. Since the proportion of total precursor molecules in an EBID system which are dissociated by electrons is very small, techniques like residual gas analysis (RGA) cannot be used.

Compositional Enhancement with O_2 Mixing

The composition of TEOS EBID deposits grown with and without O_2 mixing were analysed with energy dispersive x-ray spectroscopy (EDS). Comparison of EDS results for compositional analysis is not reliable unless the x-rays come from a relatively flat surface and from the EBID deposits only. For reliable compositional comparisons, EBID deposits were grown for significant time with and without oxygen mixing with a defocused beam to provide a flat surface. A 5 kV beam was used for EDS so that the interaction volume would be contained completely within the EBID deposits.

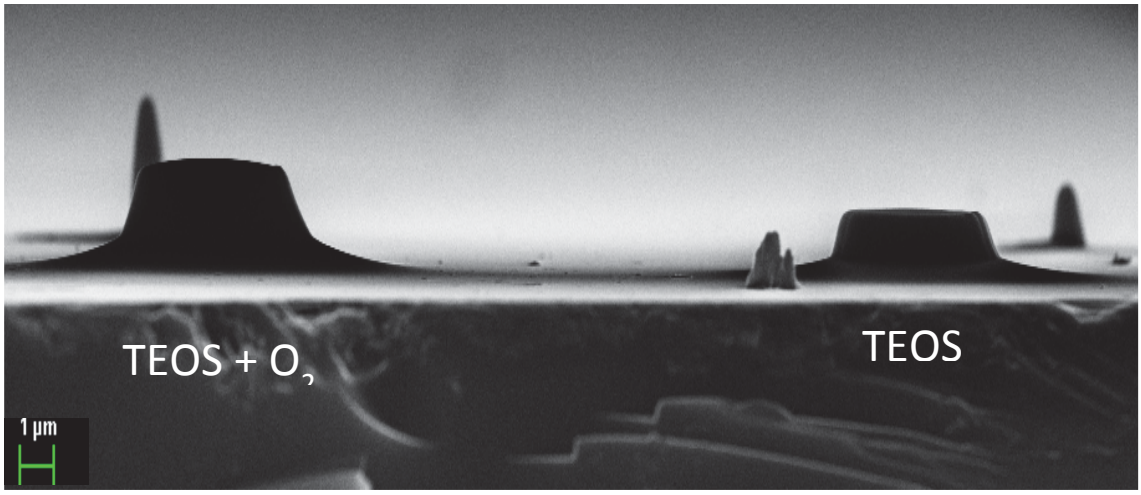

Figure 6.3: *SEM images of deposits (set 3) created for EDS compositional analysis.*

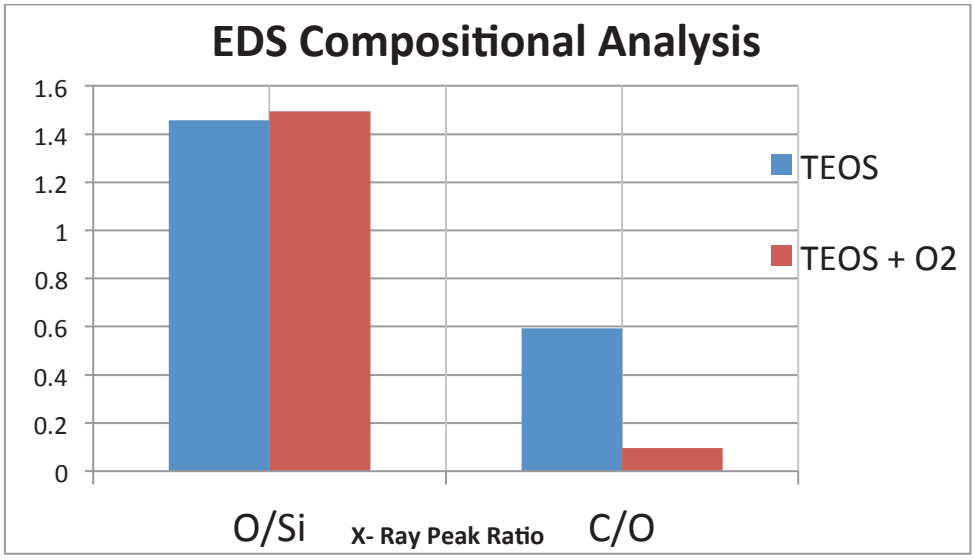

Figure 6.4: *EDS compositional analysis results of the deposits shown in figure 6.3. The O/Si ratio remains constant (difference within noise levels of technique) while the C/O ratio decreases dramatically with O_2 mixing. The C level detected in the TEOS + O_2 deposit was the same as the background level indicating minimal C content in deposit grown with O_2 mixing.*

EDS was performed on several sets of EBID deposits grown with different beam currents and beam diameters with and without O_2 mixing. All results were consistent and we can conclude that C incorporation is drastically reduced in TEOS EBID deposits grown with O_2 mixing. The detected C level in most deposits grown with O_2 mixing was the same as the background level. That is, a spectrum taken at a clean section of the substrate far from the EBID deposits gave the same C x-ray signal. The result indicates that the C level in the deposits is very low.

Perentes *et al.* [48, 87] investigated EBID with TEOS/O_2 precursor mixture using different [O_2]/[TEOS] ratios. They found that C contamination in the EBID material can be reduced significantly with a low [O_2]/[TEOS] ratio. C incorporation was eliminated entirely using [O_2]/[TEOS] = 1.75, producing stoichiometric SiO_2. No further compositional changes occurred with increasing [O_2]/[TEOS] ratio after 1.75. They also observed a corresponding increase in growth rate of material with a more than threefold increase from [O_2]/[TEOS] = 0 to [O_2]/[TEOS] = 1.75. Minimal EBID rate increase occurred with further O_2 addition. Their results are consistent with localized atomic oxygen induced decomposition (LAOCVD) of TEOS during EBID. Observed reduction of C incorporation in the EBID material is likely due to a combination of the LAOCVD reaction, which can produce pure SiO2 and volatilization of any remaining carbon by atomic oxygen. Their results show excellent consistency with my results. They published the data with no detailed mechanism to explain the observed increase in growth rate and purity of TEOS EBID deposits with O_2 mixing. The proposed mechanism of LAOCVD coupled with $O^{\cdot}$ induced volatilisation of carbonaceous EBID fragments provides an explanation for their results.

T_s Dependence of TEOS EBID with O_2 Mixing

The substrate temperature dependence of TEOS EBID with O_2 mixing was also investigated. Since the growth rate and purity of EBID deposits from TEOS was found to be significantly enhanced at high T_s (chapter 4) and growth rates and purity were also significantly enhanced by O_2 mixing at RT, it was reasoned that with both high T_s

and O_2 mixing growth rates should be very high and deposits very pure. The observed results were not as expected.

Fig. 6.5 shows volumetric EBID growth rates (set 4) on a heated substrate with increasing (T_s) using (a): TEOS and (b): TEOS + O_2 precursor mixture. The growth rate of deposits grown with O_2 mixing is very low at elevated T_s. The growth rate which is enhanced with O_2 mixing at RT (compared to EBID with TEOS only) steadily decreases with increasing T_s and remains low in the T_s region where chemisorption of TEOS is known to occur.

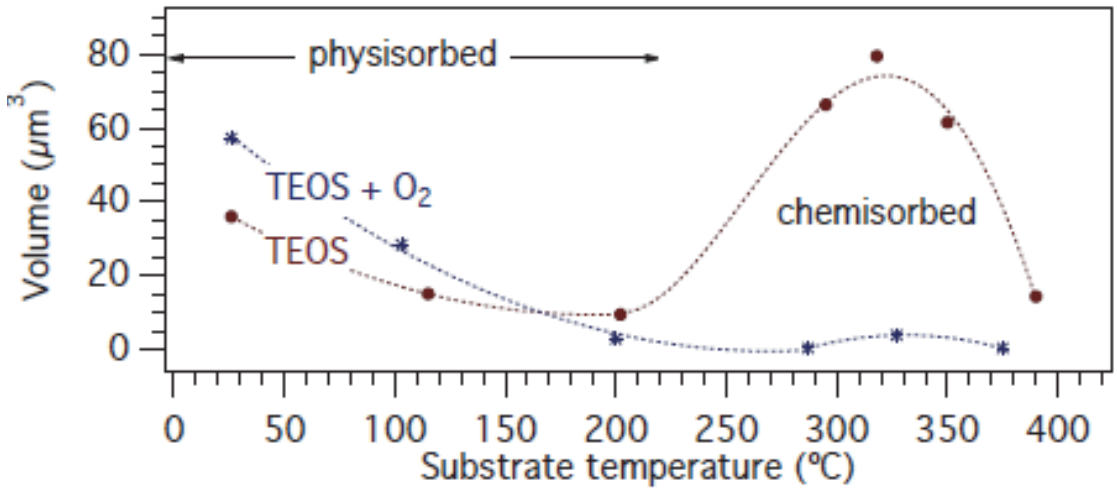

Figure 6.5: (Above): *Volumetric growth rate of EBID deposits (set 4) grown on a heated substrate with (a): TEOS only and (b): TEOS + O_2. Deposits not included in the SEM images below are included in the chart.* ***(Below):*** *SEM images of set 4.*

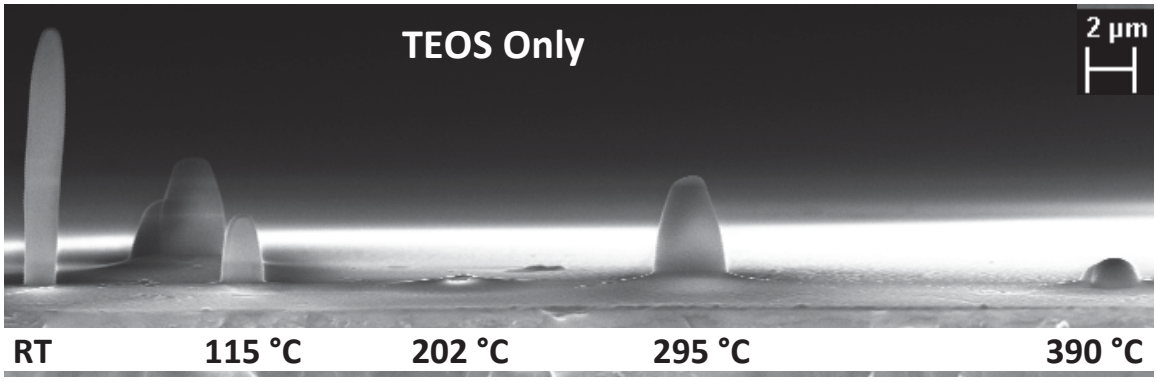

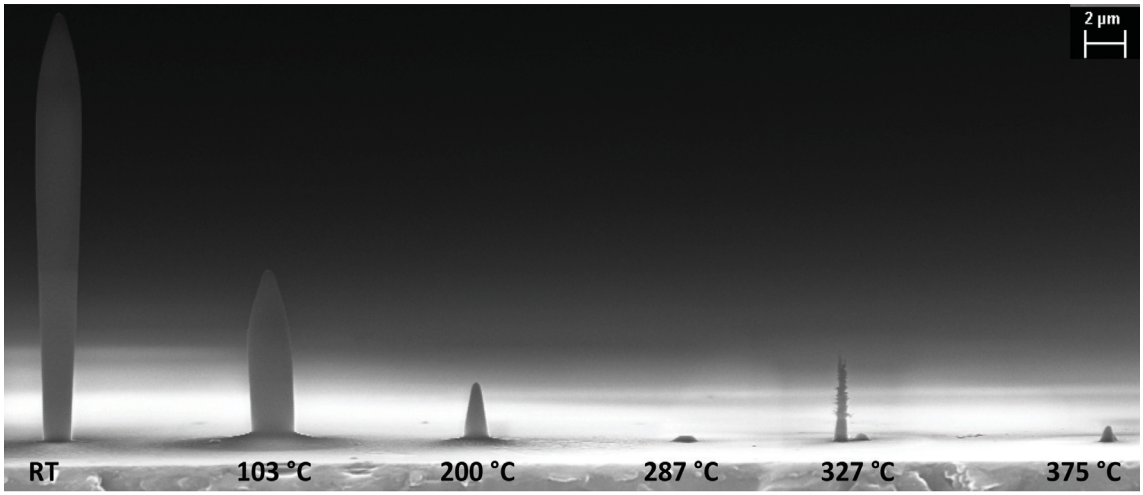

O_2 is known to adsorb dissociatively at higher T_s on a range of surfaces [94]. Activated dissociative chemisorption will occur for both TEOS and O_2 at higher T_s on SiO_2 [73, 77, 94]. As T_s is increased the dominant adsorption mechanism for both species (TEOS & O_2) will change from physisorption to chemisorption. The transition in dominant adsorption state will also be a gradual process. Activated chemisorption will proceed through an initial physisorbed state for a system with $T_s >> T_g$ which is the case for my experimental conditions.

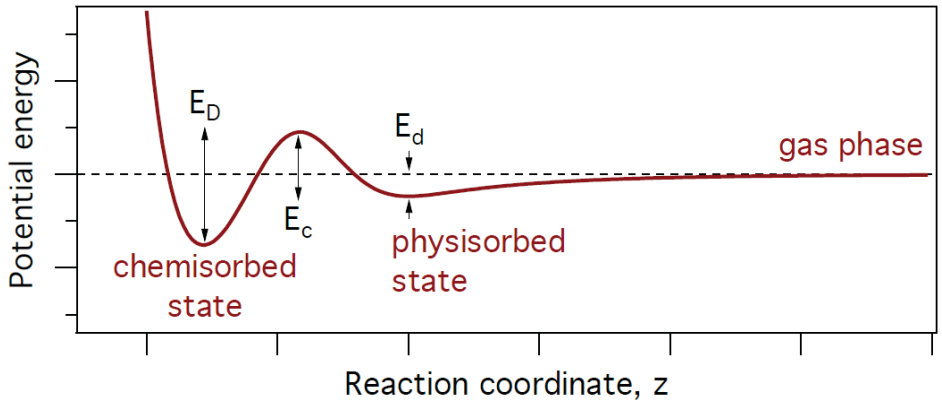

Figure 6.6: *Reaction co-ordinate diagram representing energy differences of possible adsorption states of gaseous molecules.*

It is a reasonable assumption that the adsorption behaviour of TEOS and O_2 on the TEOS + O_2 EBID material surface is very similar to the behaviour on SiO_2. At RT both species (TEOS & O_2) will primarily be in the molecular physisorbed state. As T_s is increased, both species will begin to chemisorb dissociatively to the substrate/ EBID material surface. The height of the barrier E_c (see fig. 6.6) for each species will

determine the temperature required for chemisorption to become the dominant adsorption mechanism. From my results and comparison with results published in literature [77, 94] concerning the adsorption of TEOS and O_2, I can infer that these temperatures are around 100 - 130 °C and 200 - 250 °C for TEOS and O_2 respectively for the EBID surface created under the experimental conditions used.

The T_s value of the thermal desorption peak and the surface mobility of an adsorbate is proportional to the strength of the adsorption bond with the surface. Thus in general, the surface mobility is higher and the desorption temperature lower for physisorbed species than chemisorbed species. The chemisorption bond strength E_D of each species will play a significant role in the T_s dependence of the adsorption kinetics. The value of E_D has been reported to be very high for O atoms chemisorbing to a SiO_2 surface. Boudart *et al.* [96] investigated recombination efficiency of $O^{\cdot}$ on a quartz surface. They estimated an E_D value of ≈ 3 eV for O chemisorbed on SiO_2. They reported that this desorption energy corresponds to a desorption peak of chemisorbed O at ≈ 1200 K. Thus desorption of chemisorbed O is not expected for the T_s range used for my experiments.

Determination of the nature of the active sites for chemisorption of both TEOS and O on the EBID material surface is beyond the scope of this thesis. However, a likely candidate would be a surface oxygen vacancy (V_O). V_O would result in Si dangling bonds which would leave an active site. An O terminated surface site is expected to be unreactive [73, 77] and thus chemisorption would not proceed at these sites. The chemisorption of O at a V_O site would fill the vacancy and leave an unreactive site. Chemisorbed O is expected not to be mobile upon the surface until T_s values higher than those used in my experiments due to the high E_D value [96]. Dissociative chemisorption of O_2 will therefore deactivate active surface sites.

Deactivation of active surface sites by dissociative adsorption of O_2 is thus proposed as the mechanism for EBID rate suppression at high T_s with TEOS/O_2 mixtures. There will be a lower proportion of active sites available for TEOS chemisorption at high T_s with O_2 present during EBID which will result in a lower concentration of precursor at high T_s. This will result in a much reduced EBID growth rate.

The LAOCVD mechanism is also suppressed at high T_s as dissociative chemisorption is the dominant adsorption mechanism for O_2. The LAOCVD mechanism increases the growth rate at RT via direct dissociation of TEOS by physisorbed $O^{\cdot}$. The mechanism requires a high concentration of physisorbed O_2 as a precursor to physisorbed $O^{\cdot}$. Physisorbed O_2 and $O^{\cdot}$ will have a very low residence time on the surface at high T_s resulting in a very low concentration of the species required for LAOCVD. Thus the LAOCVD mechanism will be low at high T_s.

Examining the change of growth rate of TEOS + O_2 shown in figure 6.5, we can attribute the changes to the processes discussed above. The decrease in growth rate from RT to 200 °C is attributed to a decrease in residence time of physisorbed O_2, $O^{\cdot}$ and TEOS, resulting in a decreasing coverage of all physisorbed species. The growth rate above 200 °C remains low as the chemisorbed TEOS fragment coverage is low due to the deactivation of surface sites by the dissociative adsorption of O_2 and the physisorbed precursor coverage is even lower. As a result all mechanisms of growth are suppressed at high T_s for TEOS EBID with O_2 mixing.

Unique Geometry of TEOS FEBID Deposits with O_2 Mixing

EBID deposits grown with a focused beam (FEBID) from TEOS/O_2 precursor mixtures display a unique geometry for FEBID pillars. Pillars grown by FEBID from most precursors display a cylindrical geometry with a conical tip. To my knowledge, all published EBID simulation modelling work have all predicted cylindrical EBID pillars resulting from a focused Gaussian beam [97] for longer growth periods. The growth observed from FEBID with TEOS + O_2 indicates that other processes which are not accounted for in EBID models can have large effects on EBID growth under certain conditions.

Figure 6.7: *Two FEBID pillars (set 5) grown under identical conditions excepting the addition of 0.24 torr of O_2 for the pillar on the right. TEOS partial pressure was 0.05 torr.*

The addition of O_2 results in a unique geometry for TEOS FEBID pillars as can be seen in figure 6.7 above. The pillar width increases with pillar height. The pillar width is seen to saturate with very long growth times as seen in figure 6.8 below. An increase in $I_{e/t}$ curve gradient after the point where saturation would occur for TEOS FEBID without O_2 mixing is characteristic of increasing pillar width for TEOS + O_2 FEBID. This

increase is seen to level off with long t_g and is assumed to reflect the saturation in pillar width.

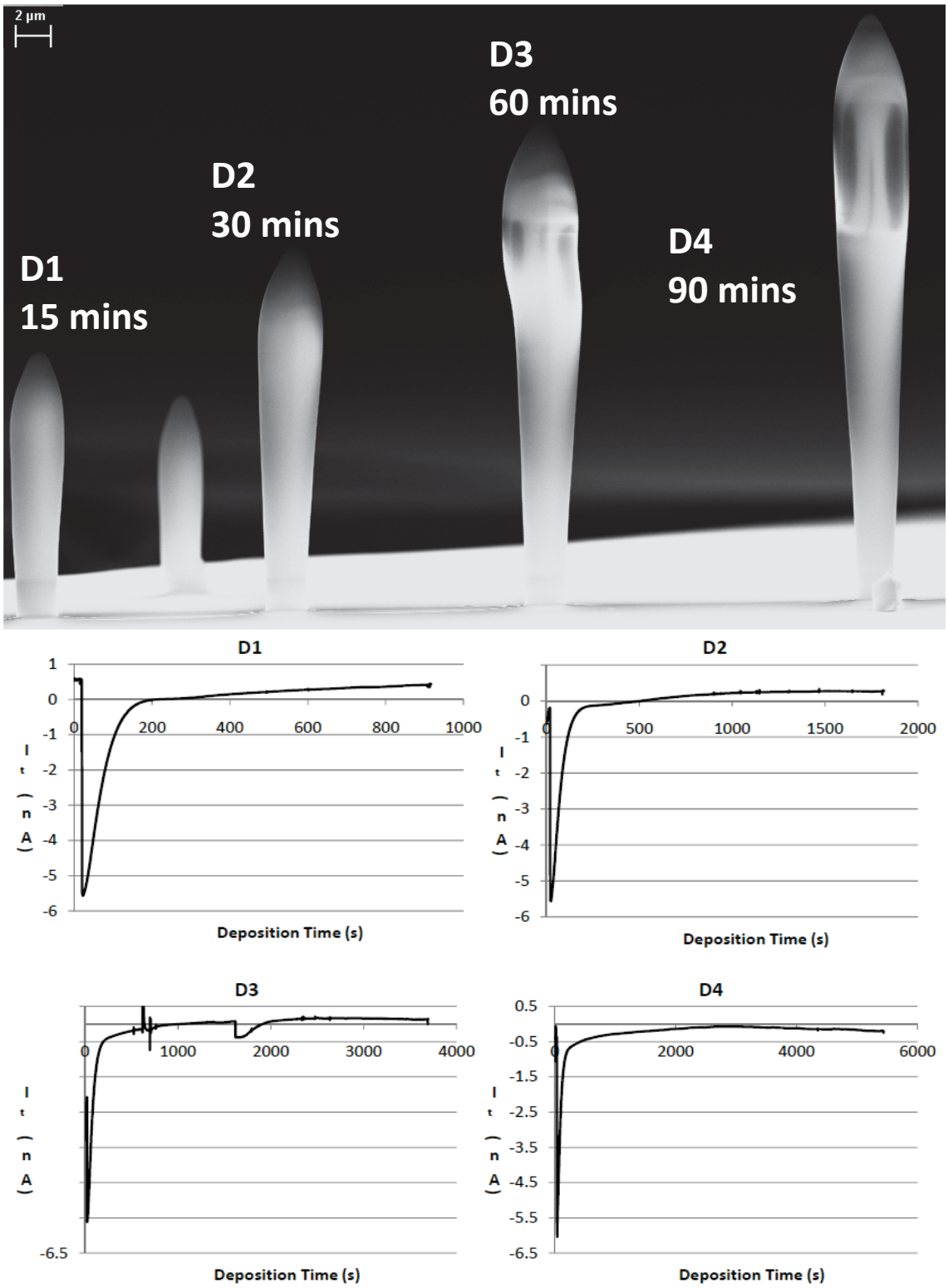

Figure 6.8 (previous page): *(Top): FEBID deposits grown with TEOS + O_2 as a function of time (set 6). Deposit 3 had a temporary drop in pressure of O_2. This may have caused the beam shift which caused the warped growth or the shift may have been*

coincidental. (Bottom): I_t curves collected during the growth of set 6. The increase in curve gradient characteristic of TEOS + O_2 FEBID growth is seen to saturate at long t_g and correlates with FEBID pillar width. The temporary pressure drop is seen in the curve for D3 at ≈ 1700 s. The spike prior to this is an artifact.

Factors Contributing to TEOS + O_2 FEBID Pillar Geometry

The precise mechanism/s behind the unique geometry observed for TEOS FEBID with O_2 mixing remain unclear. However, based on the available data we can conclude that electron beam induced heating (EBIH) is likely to play the major role in the process. Charging of deposits during growth may also play a role. The contribution of each mechanism is very hard to differentiate as most factors which affect EBIH also affect the degree of charging.

It has been demonstrated that O_2 mixing with TEOS during EBID decreases the C content of deposits and results in material with the stoichiometric composition of SiO_2 [48]. The thermal and electrical conductivity of the TEOS EBID material would thus be expected to decrease with increasing $[O_2]/[TEOS]$ ratio. The degree of EBIH and charging will therefore be higher for deposits grown with O_2 mixing. Randolph *et al.* [84] simulated EBIH in a SiO_2 nanopillar with a simple EBIH model. They concluded that the tip temperature of a growing EBID deposit increases with growth time and height. Thermal equilibrium will eventually be reached when the temperature of the tip is sufficiently high that thermal losses (radiation, conduction, convection) equal the heat input due to EBIH.

An increasing FEBID pillar tip temperature during growth is consistent with the increasing width with height which is observed. As the tip temperature increases during growth, precursor depletion will increase due to decreasing residence time of physisorbed precursor molecules. As was discussed in chapter 5, the e^- flux incident and emitted vertically from a pillar tip is always higher than that emitted from the sidewalls of a pillar. Thus vertical growth can be in the PD or MTL regime while the lateral growth remains in the EL or PD regime. When pillar tip temperature is increased during FEBID by EBIH, the vertical growth rate will thus be affected more than the lateral growth rate by the increasing precursor depletion. Since the vertical growth rate is decreasing faster than the lateral growth rate, pillar widening will result.

Other Evidence for EBIH

A decrease in the volumetric growth rate with extended deposition time is expected due to EBIH. This is observed experimentally (fig. 6.9). An increase in electron flux will certainly increase EBIH during EBID. As beam current I_b is increased the widening of FEBID pillars grown with O_2 mixing become more significant (see fig. 6.10 below). The widening effect is decreased for a small magnitude of defocus of the e^- beam (set 2, see fig. 6.2). Both observations are consistent with decreasing EBIH due to decreasing e^- flux.

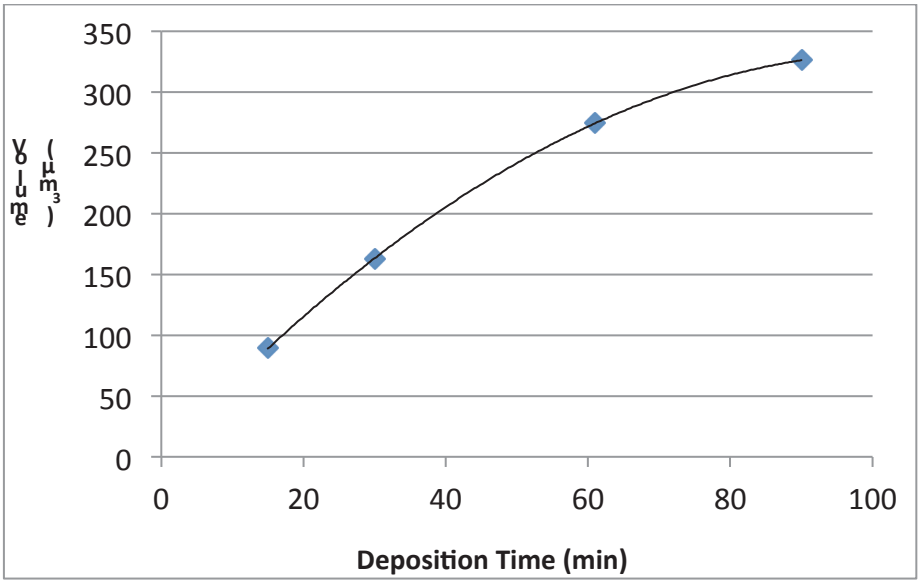

Figure 6.9: *Decreasing volumetric growth rate with increasing growth time observed for set 6. This is consistent with EBIH.*

Figure 6.10 below shows FEBID deposits made with TEOS only and TEOS + O_2 as a function of I_b. Deposits were made with TEOS only first and then TEOS + O_2 deposits were made in between. The first deposit was seen to bend towards the TEOS + O_2 deposit made next to it. This is a common effect and occurs with high aspect ratio FEBID deposits made too close to one another. The bending effect is attributed to attractive forces due to charging during growth and is documented in literature [98].

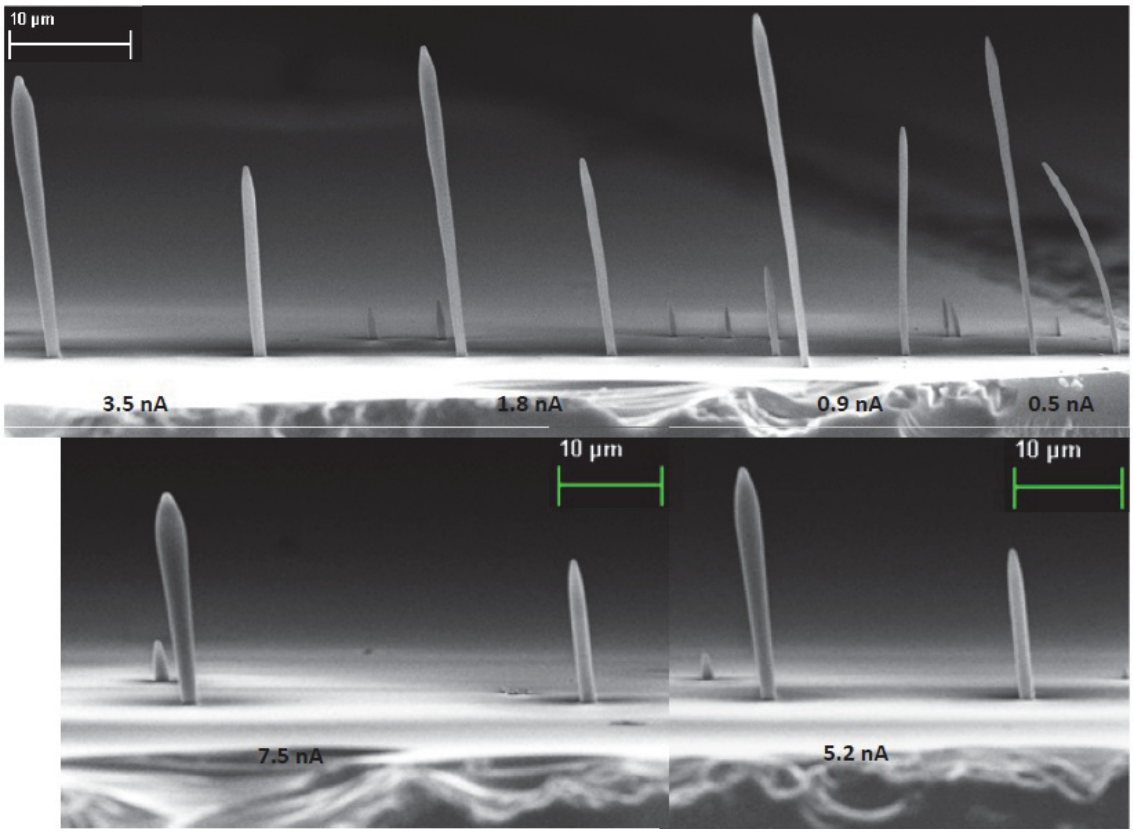

Figure 6.10: *SEM images of set 7. The set was grown as a function of I_b with and without TEOS. From right to left, every 2nd deposit was grown with O_2 mixing. The degree of pillar widening with height can be seen to increase with I_b.*

The magnitude of the widening effect increases with I_b and this is consistent with increasing EBIH and/or charging being the cause of the increasing widening. Most parameters which increase EBIH also increase charging.

Difficulties in Separating the Role of EBIH and Charging

Charging could increase the EBID rate by the mechanism proposed by Banhart [99] and discussed in the previous chapter. Charging would be expected to decrease with increasing total gas pressure in the ESEM cell. A higher gas pressure results in increased charging compensation by gaseous ions formed by electron induced ionisation events in the gas phase [19]. Charge compensation efficiency correlates directly with the average ionisation probability [19] per unit length α:

$$\alpha(P,\chi) = APe^{-BP/\chi} \qquad (6.1)$$

where: χ is the electric field strength determined by the bias on and distance to the GSED detector. P is the partial pressure of the gas. A and B are gas specific constants. So the charge compensation efficiency of a gas is a strong function of the gas composition. A much higher imaging signal is obtained using the GSED detector with TEOS only, relative to the signal obtained for the same pressure of O_2. Thus we can conclude that the gas cascade amplification gain of TEOS is much higher than that of O_2. Therefore the charge compensation efficiency will be higher for TEOS compared to an equal pressure of O_2.

It is observed that with a higher $[O_2]/[TEOS]$ ratio the magnitude of the widening effect is increased. Also using the same total gas pressure but a lower $[O_2]/[TEOS]$ ratio (i.e higher TEOS partial pressure) the magnitude of the widening is less. This is observed when comparing set 6 (figure 6.8) to set 5 (figure 6.7). Both sets were grown with $I_b \approx 9$ nA and the same total gas pressure of ≈ 0.3 torr. The difference is in the $[O_2]/[TEOS]$ ratio. Set 6 had an $[O_2]/[TEOS]$ ratio of 2:1 whereas set 5 had $[O_2]/[TEOS]$ = 5:1. We see that the magnitude of the widening is much more significant for the higher $[O_2]/[TEOS]$ ratio. Charging should be less for the lower $[O_2]/[TEOS]$ ratio and the magnitude of the widening is also seen to be less. The purity and therefore thermal and electrical conductivity of the deposits will be lower for the higher $[O_2]/[TEOS]$ ratio and this will increase both EBIH and charging.

In summary, insufficient data has been collected to enable a conclusion to be made regarding whether the widening effect is due to EBIH, charging or both. It may be that both processes contribute significantly. Although the specific mechanism cannot be isolated, this growth is another good example of processes which are not accounted for in EBID models playing a significant role in EBID growth kinetics.

6.5 Conclusions:

At RT, the growth rate of TEOS EBID deposits can be significantly increased or decreased by mixing the precursor gas with O_2 or Ar respectively. The purity of TEOS EBID deposits is also significantly enhanced with O_2 mixing. The increased growth rate and purity of TEOS EBID at RT is due to direct dissociation of TEOS by $O^{\cdot}$ formed by e^- induced dissociation of physisorbed O_2 (LAOCVD). At high T_s, dissociative chemisorption of O_2 deactivates surface sites which would be available for

chemisorption of TEOS in the absence of O_2. The LAOCVD mechanism is also limited at high T_s as it requires physisorbed O_2 and the physisorbed O_2 concentration is low at high T_s. Unique geometries for FEBID pillars obtained with TEOS + O_2 are likely to be caused by EBIH and/or charging during growth which are both increased with O_2 due to the higher purity of TEOS EBID deposits obtained with O_2 mixing.

Main Conclusions of Thesis

The adsorption kinetics of precursor molecules is a factor which can have a large impact upon the EBIED process yet has been neglected in EBIED theory and models thus far. A model has been developed which correctly predicts EBID growth rates in the case of activated chemisorption of an EBID precursor molecule. This model has been experimentally validated using tetraethoxysilane (TEOS) for EBID. TEOS is demonstrated to undergo activated chemisorption upon the surface of the material produced by EBID with TEOS as T_s is increased. It is likely that EBID can successfully be used as an analytical technique for the characterisation of molecule – surface interactions under conditions inaccessible to other surface science techniques. Increasing the substrate temperature for EBID can result in an increase in the growth rate of an EBID deposit as well as the purity of the deposit if activated chemisorption of the EBID precursor occurs as T_s is increased.

Focused electron beam induced deposition can result in many effects which are not accounted for by current models of EBID. These include electron beam induced heating (EBIH), charging and non – uniform precursor diffusion. These effects result in deviation from model behaviour and are demonstrated in the formation of large fractal – like, branched deposits formed at high T_s by FEBID with TEOS. These effects can be minimised by use of an electron source which provides a lower, uniform electron flux.

The addition of O_2 or Ar gas to TEOS precursor vapour results in an increase or decrease respectively in the growth rate at RT. The purity of TEOS EBID deposits is also significantly enhanced with O_2 mixing. At high T_s the growth rate of TEOS EBID is significantly reduced by the presence of O_2. TEOS and O_2 both undergo activated chemisorption which affects the growth rate of TEOS EBID at high T_s with and without O_2 mixing.

Appendix I: Preliminary EBID Experimentation

Abstract:

EBID experiments are performed with a rudimentary precursor delivery system. Carbonaceous deposits are grown as functions of deposition parameters and the geometries obtained are explained in the context of existing models of EBID. Qualitative trends are identified for FEBID as a function of beam current (I_b) with TEOS precursor. Unique geometries of TEOS FEBID deposits are obtained using residual TEOS as precursor. The unique geometries obtained are attributed to diffusion limited growth. Deposits are grown by EBID using condensed TEOS in the liquid phase. The growth rate from liquid TEOS is found to be orders of magnitude higher than the rate of TEOS EBID using gas phase precursor. Irreproducibility of results indicated that apparatus upgrades were necessary for quality EBID experimentation.

Introduction:

Information concerning the details of constructing a system for the study of EBIED is not available in EBIED literature. Most publications provide only a brief description of the experimental setup and methods used. Thus it is not surprising that the original PDS used for EBIED study had several critical design flaws. It required many experiments for the flaws in design to become apparent. These flaws and how to avoid them in construction of an experimental EBIED system are discussed in chapter 3. Although the experimental results were irreproducible, they allowed some conclusions to be drawn. As discussed in chapter 1, simple experimental setups for EBIED study involve the addition of a GIS to a standard SEM or a precursor delivery system to an ESEM. The latter setup was chosen as a simple precursor delivery system (PDS) could be easily constructed and attached to an ESEM available for use in the Microstructural Analysis Unit at UTS. A simple PDS had been constructed and attached to the XL30 ESEM prior to the commencement of my project by a technical officer and previous student who performed EBID experimentation using the setup with limited success.

The results presented in this appendix are not discussed in detail due to the irreproducibility. Qualitative conclusions are drawn concerning EBID with carbonaceous precursors and TEOS. No quantitative comparisons are made.

Experimental:

EBID experiments were performed in stationary mode as a function of different deposition parameters such as beam current (I_b), precursor pressure (unreliable), accelerating voltage (V_0) and with raster scanning for area deposition. A range of carbonaceous precursors were used to deposit amorphous carbon structures and tetraethoxysilane (TEOS) was used to deposit $Si_xO_yC_z$ structures. The experimental setup used for these experiments is discussed in chapter 3, section

The experimental parameters used to grow the EBID sets are not presented in this chapter as in other chapters as the recorded values for each parameter are unreliable. For example, beam current was measured prior to each experiment yet the crude faraday cup used was likely to underestimate the beam current. The natural decay in beam current was also not accounted for. The gas pressure in the chamber was recorded yet the precursor partial pressure was unknown. Certain experimental parameters were also not recorded as their importance had not yet become apparent at the time of the experiments.

Results & Discussion:

Carbonaceous EBID

Alkane precursors were used to deposit amorphous carbon structures: n-hexane (C_6H_{14}), n-octane (C_8H_{18}), n-dodecane ($C_{12}H_{26}$) and n-hexadecane ($C_{16}H_{34}$). The initial idea was to investigate the change in deposition rates from precursor molecules which are very similar with increasing chain length as the only difference. The hypothesis was that only the sticking coefficient of the precursor molecules would be different and thus the effect of the sticking coefficient could be investigated. I now know that other parameters such as the dissociation cross section (σ), residence time (τ) and diffusion coefficient (D) are likely to change significantly between alkanes of

different chain lengths. Furthermore, the significant amount of residual gases, including water vapour, present in the ESEM chamber during EBID using the initial apparatus allows no quantitative comparison of results.

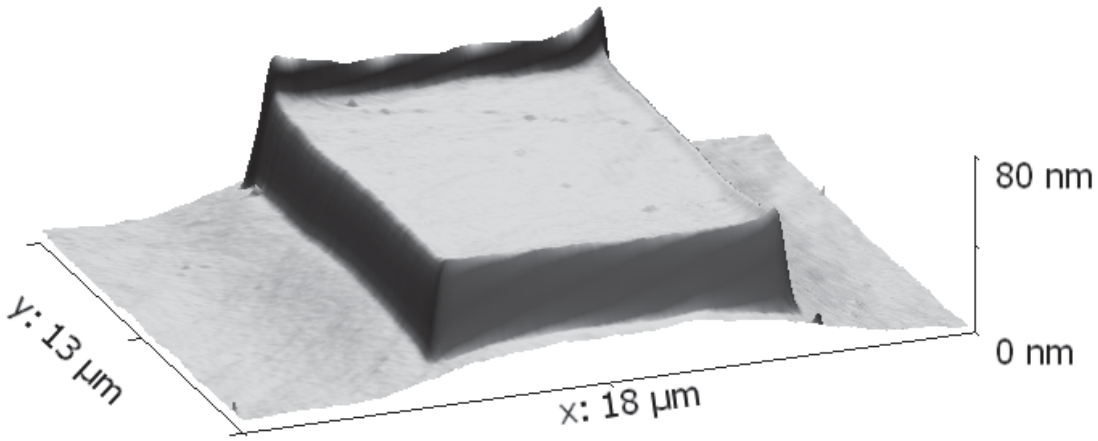

Figure AI.1: *Rectangular EBID deposits created by raster scanning of a fixed area with using the same conditions with different precursors. Deposits were imaged with AFM and growth rates calculated for comparison of growth rates with different alkane precursors.*

Rectangular EBID deposits were created to attempt to quantitatively compare different growth rates with different chain length alkane precursors. The data analysis procedure was good yet contamination by residual gases gave irreproducible results and allowed no quantitative comparison. If the experiments could be repeated using the experimental apparatus and procedure outlined in chapter three, quantitative comparison would be possible. The approach could potentially yield valuable data concerning the physisorption of alkanes.

Pillar and Ring Geometries of Carbonaceous FEBID

Pillar and ring style geometries were obtained for carbonaceous EBID deposits grown with a highly focused beam (FEBID). Such geometries are common for carbonaceous FEBID from residual hydrocarbon precursors where diffusion is a significant precursor supply mechanism [85].

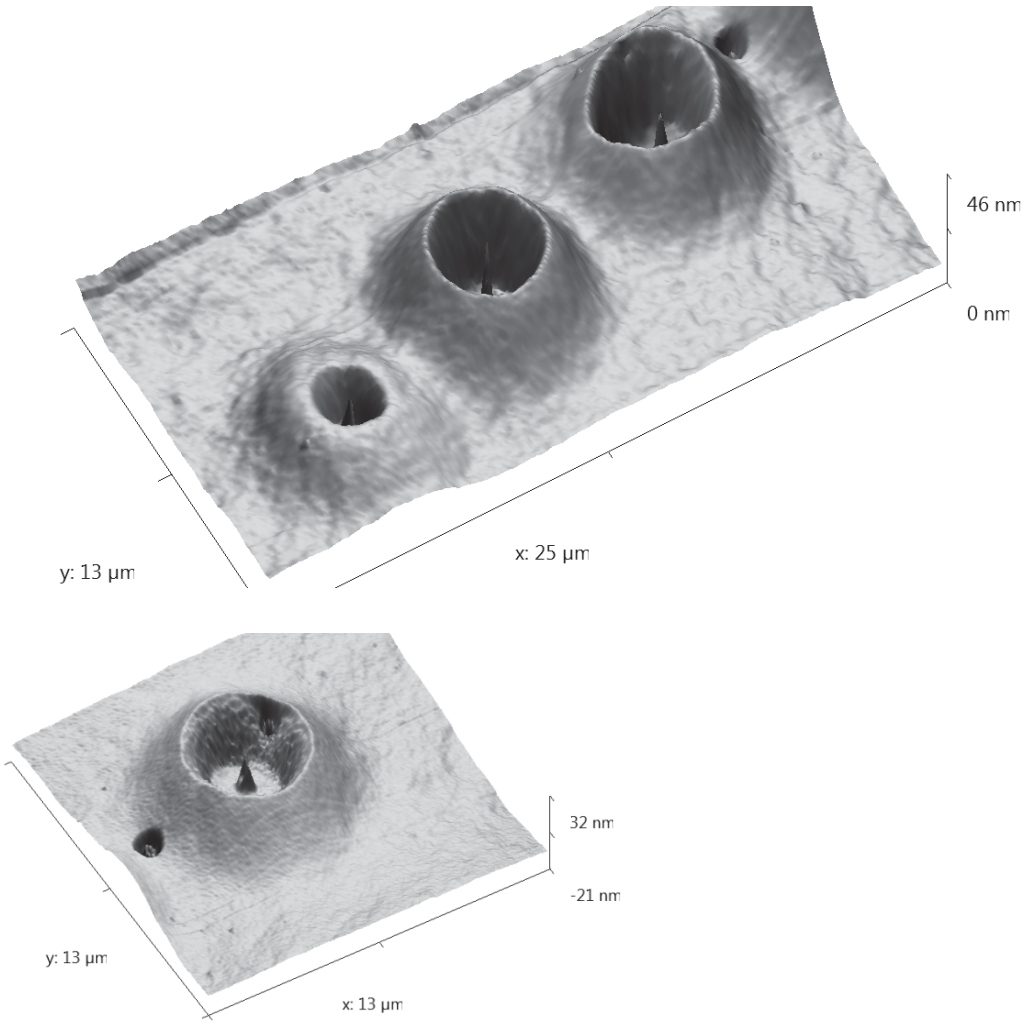

Figure AI.2: *3D AFM images of pillar and ring deposits obtained by FEBID with alkane precursor.*

The geometries observed above would be expected for FEBID using only residual hydrocarbons. There should be a much higher partial pressure of organic vapour for these experiments than for the case of residual hydrocarbon FEBID. The pillar would be expected to be much higher than the ring for this case. There will also be considerable H_2O vapour present due to leaks in the PDS. We can interpret this result in the context of the model of simultaneous electron beam induced deposition and etching (SEBIED) presented by Toth *et al.* [42, 43] discussed in chapter 1.

The significant proportion of H_2O vapour present in the system will result in the net carbonaceous deposition rate being lowered in the centre where the electron flux is high. Etching is not significant for the ring as the electron flux is low and the carbonaceous EBID reaction is much more efficient than the H_2O mediated EBIE reaction. Thus with significant etching in the centre only a small pillar is formed and is shorter than the ring. Further confirmation of SEBIED playing a role in this system is observed with other experimental sets where a crater is observed in the top of a carbonaceous pillar. One can postulate that it should be possible to tailor the pillar height to ring height ratio by adjusting the organic precursor to water vapour ratio. A high level of control of precursor partial pressures would be necessary for this and could be achieved with the improved EBID apparatus used for the rest of the work of this thesis.

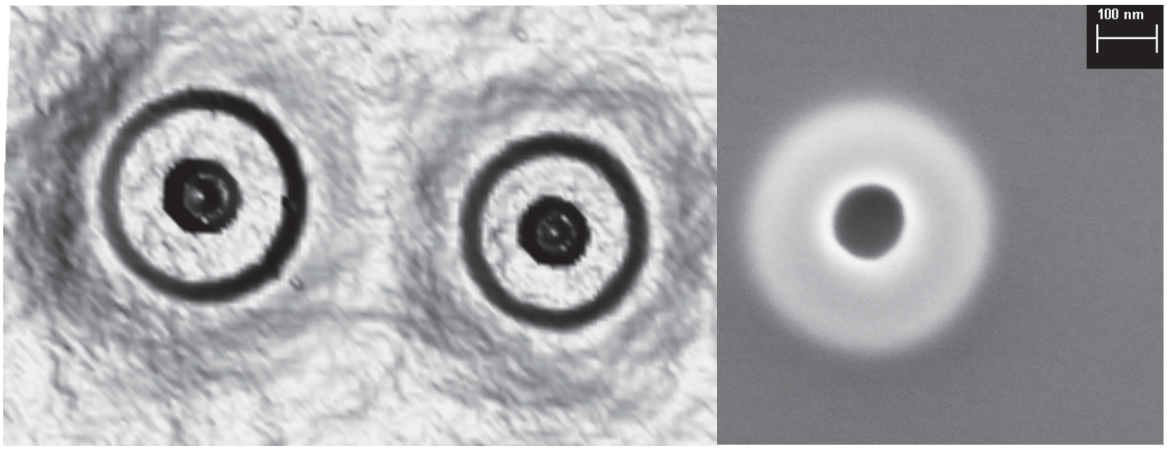

Figure AI.3: *Bird's eye 3D AFM image (left) and close up SEM image showing depressions in the centre of carbonaceous pillars grown by FEBID with alkane precursors.*

FEBID with TEOS Precursor

FEBID experiments were performed with TEOS precursor. The results were irreproducible due to the deficiencies in apparatus described above. However, several qualitative trends were observed which remain valid.

FEBID Pillar Geometry Evolution with Beam Current

Characteristic behaviour was observed for TEOS pillars grown with increasing beam current. The mechanisms behind the geometry evolution will be discussed in detail in later chapters.

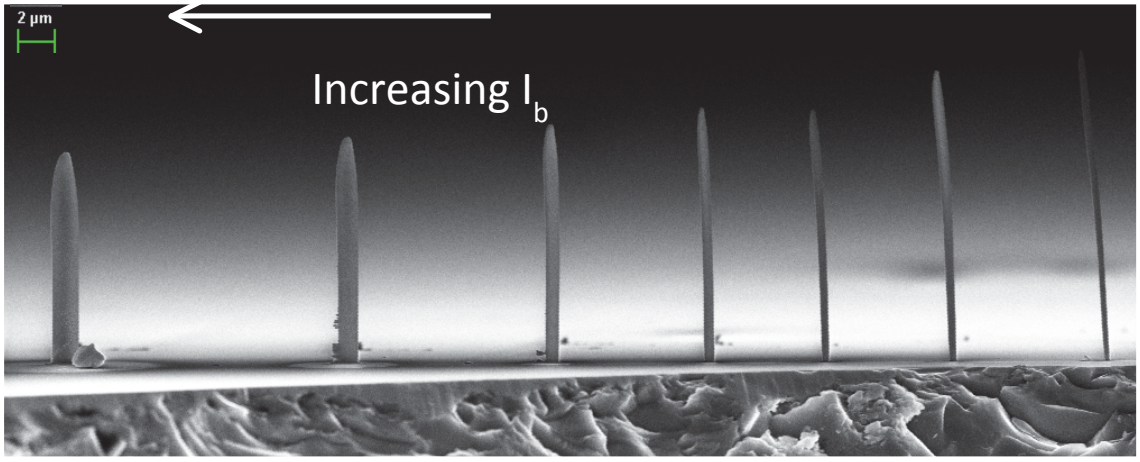

Figure AI.4: *Set grown by FEBID using a focused beam and TEOS precursor. Aspect ratio of deposits decreases with increasing I_b.*

FEBID Deposits Using Residual TEOS

Unique geometries of TEOS FEBID deposits can be achieved using a very low partial pressure of TEOS. The ESEM chamber was pumped to high vacuum and only residual TEOS was present. TEOS seems to take a long time to fully remove from a vacuum system, a consequence of the unique adsorption behaviour of the molecule which will be discussed in later chapters. It was found that TEOS based EBID deposits could still be grown weeks after filling the ESEM chamber with a certain pressure of TEOS. Only by flushing the vacuum system with significant N_2 flow and days of plasma cleaning of the ESEM chamber could TEOS be fully removed.

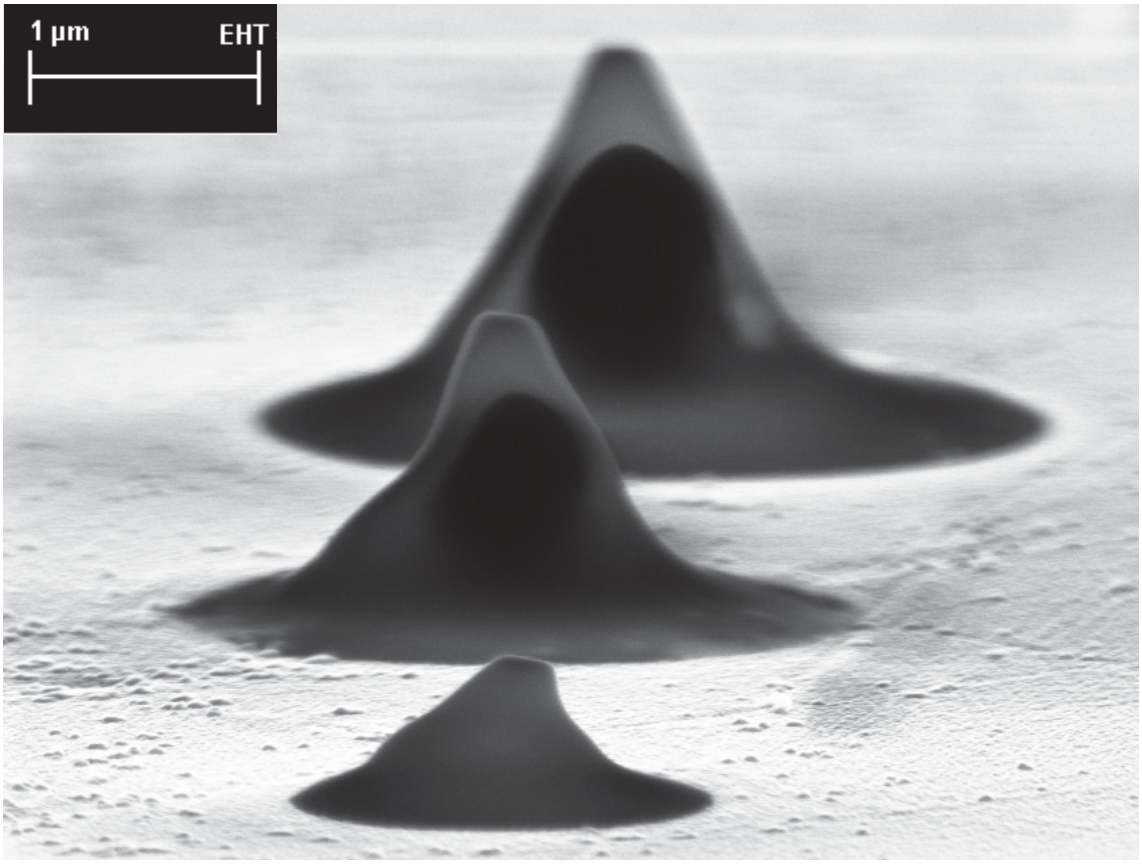

Figure AI.5: *Deposits grown by FEBID using residual TEOS as precursor. The warping is image distortion caused by charging during imaging. The true geometry is that of a witch's hat. This represents a unique geometry for EBID deposits.*

The deposits shown in figure 2.7 above represent a unique geometry for FEBID deposits. This geometry is attributed to the fact that the main mechanism of precursor supply will be diffusion across the substrate surface into the irradiation region rather than adsorption from the gas phase. This could be referred to as "diffusion limited EBID growth" and could be considered as a special case of MTL regime EBID. This will limit the vertical growth and result in cone/witch's hat like structures as shown above. The effect can be expected to occur only for precursors which are said to be "sticky". That is, precursors with characteristically long residence times and thus remain in vacuum systems even after considerable high vacuum pumping time.

FEBID with Liquid TEOS

The substrate temperature (T_s) dependence of TEOS FEBID was attempted to be investigated through initial experiments using a Peltier heating/cooling stage installed within the ESEM chamber of the XL30 ESEM. The stage had an effective range of – 10 to 45 °C. The growth rate of TEOS pillars was found to decrease slightly with increasing T_s up to 45 °C. It was discovered that TEOS condenses upon the substrate at around – 5 °C. The electron beam was set to remain stationary incident upon a droplet of liquid TEOS to form liquid phase FEBID deposits. A macroscopic and highly insulating film was observed to be deposited on the substrate in all areas where TEOS had condensed. This film is likely to be SiO_2 formed by reaction of TEOS with H_2O: $Si(OC_2H_5)_4 + 2H_2O \rightarrow SiO_2 + 4C_2H_5OH$, which occurs spontaneously and quickly with both reactants mixed in the liquid phase.

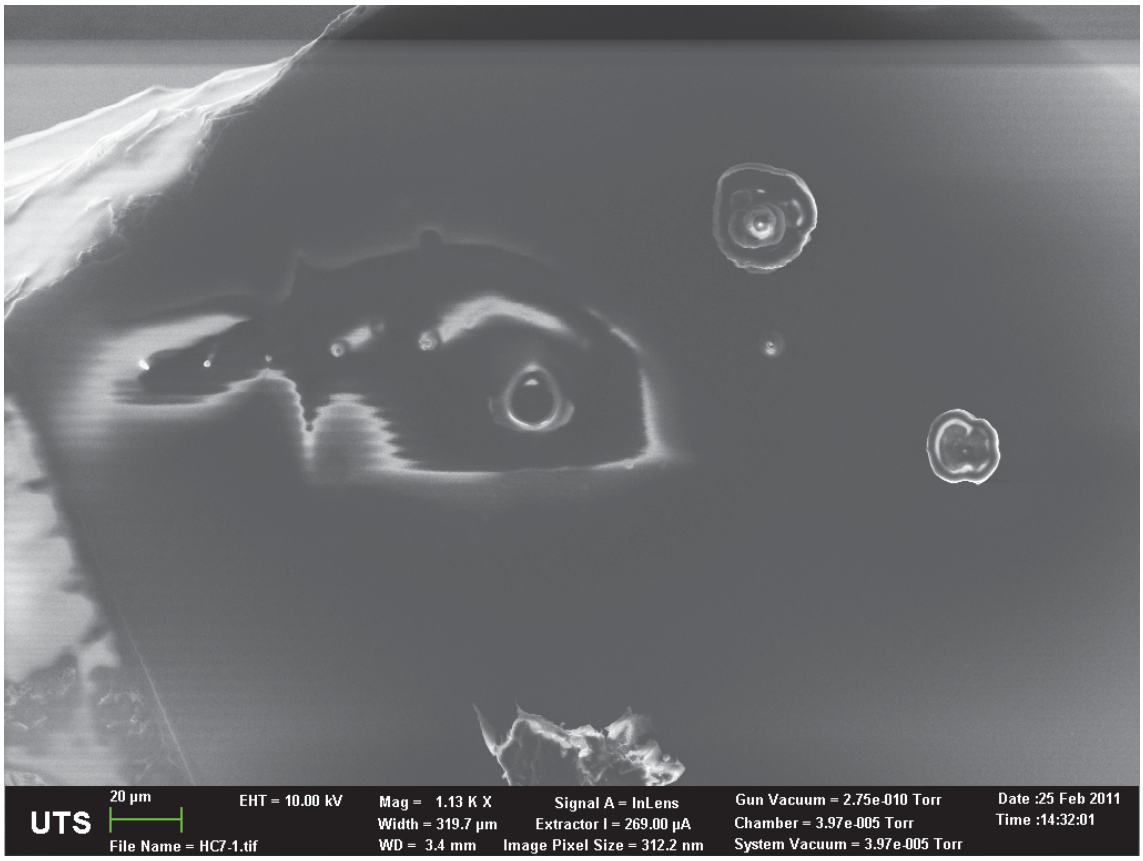

Figure AI.6: *Deposition area after liquid phase EBID. Highly insulating film makes imaging in HIVAC near impossible.*

A thin layer of gold was then sputtered on the substrate to allow for imaging. The results were found to be interesting. Enormous structures were created through liquid phase EBID. This indicates a growth rate that is orders of magnitude above gas phase EBID. A major problem is that EBID growth would initiate at the top of an EBID droplet and proceed downwards and not necessarily be anchored to the substrate. A condensed precursor approach to EBID was used by Mitchell *et al.* [100] and they noted large growth rates. If an approach can be determined to reliably control condensed film thickness and uniformity, condensed precursor EBID may have much potential.

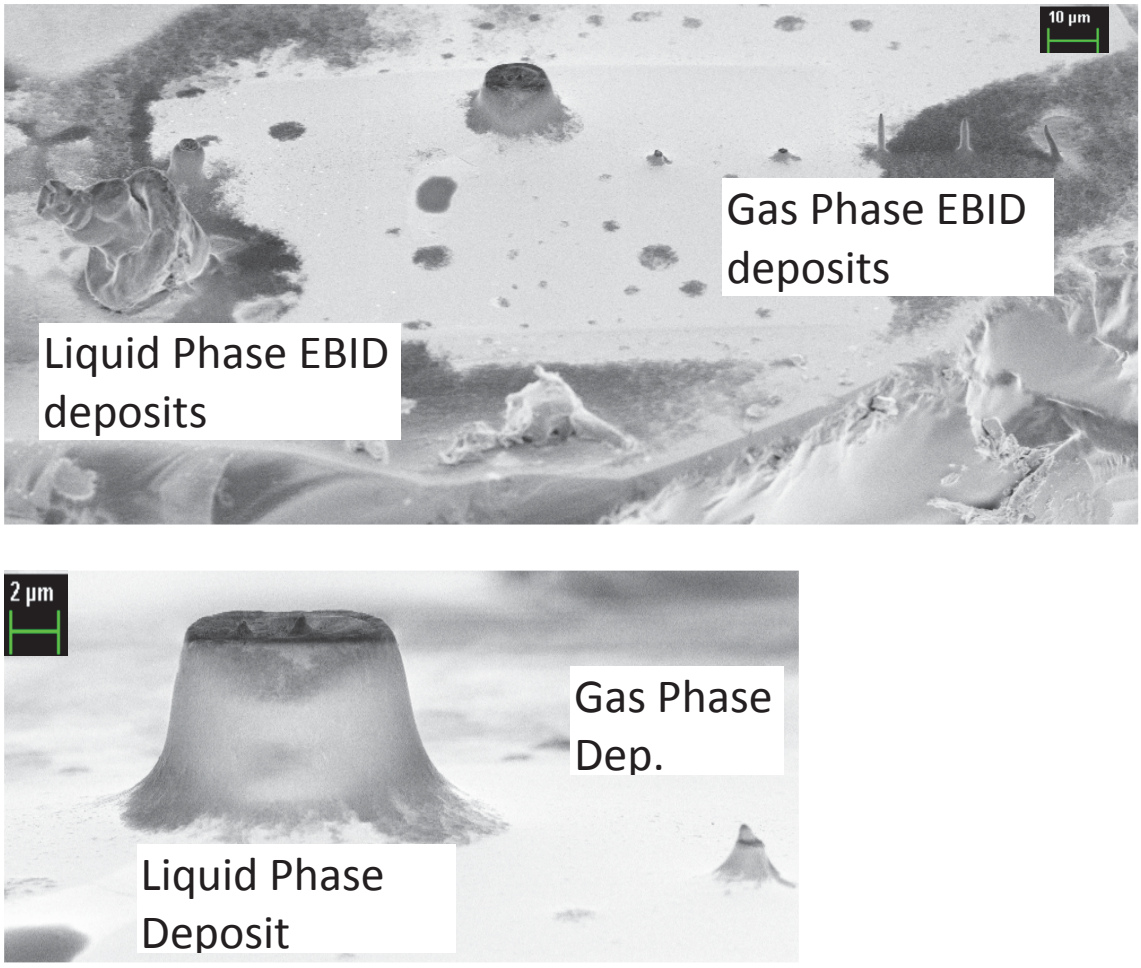

Figure AI.7: *Liquid phase deposits near gas phase deposits to allow for comparison. Liquid phase deposits display a volumetric growth rate which is orders of magnitude larger than gas phase deposits. Two of the gas phase EBID pillars were snapped off prior to imaging.*

Conclusions:

For quantitative EBIED study, ensuring a flux of pure precursor gas with minimal residual gases is crucial. Pillar and ring EBID deposit geometries can be achieved using carbonaceous precursors mixed with water vapour. With high control over the carbonaceous precursor to H_2O flux ratio and the electron flux it should be possible to tailor the pillar height to ring height ratio. Diffusion limited growth using residual precursor molecules can result in EBID deposit geometries unachievable with higher precursor pressures. EBID growth using condensed, liquid-phase TEOS as the precursor allows for growth rates orders of magnitude above gas phase TEOS EBID growth rates.

Appendix II: EBID Parameter Dependence

Factors which Affect the EBIED Process

The EBIED process is complex and involves many parameters and simultaneously occurring processes. The mind map below may help the reader to appreciate this complexity.

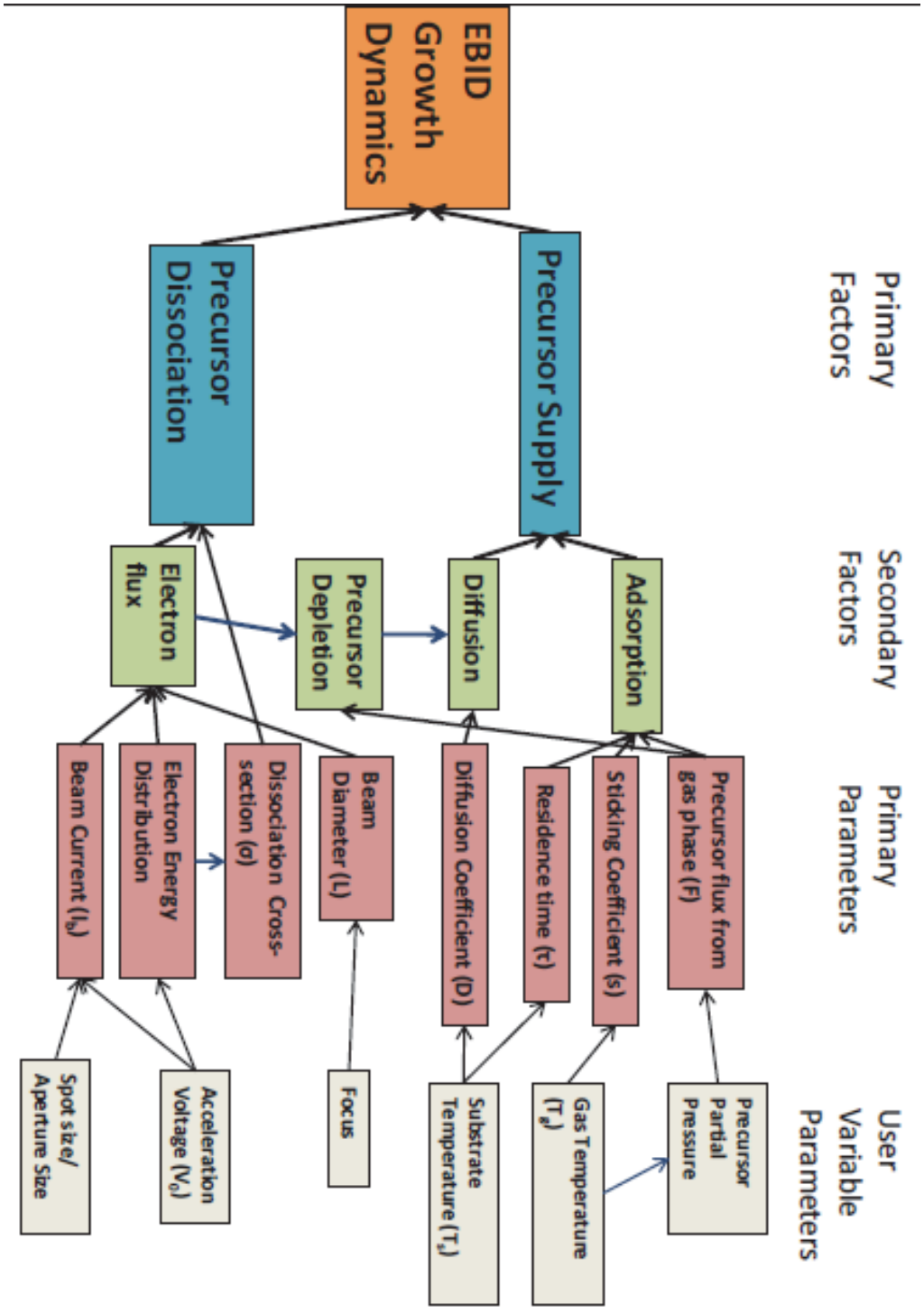

Figure AII.0 (previous page): *Mind map representing the main factors and parameters which affect the EBIED process. A black arrow indicates that the parameter affects the parameter/ factor to which it points. A blue arrow indicates parameters/ factors which affect each other. More complex processes not accounted for by the standard model such as EBIH, charging, activated chemisorption and multiple gas species are not included. The map is rotated 90° to fit page.*

A large amount of experimental data was collected during the course of the project. Only part of it has been presented in chapters 2 – 6. Some of the remaining data shall be presented below in order to illustrate the standard trends in EBID growth with 3 important parameters.

The system parameters used for deposition of the experimental sets presented in this appendix were: **Set 1:** FEBID, function of I_b, V_0: 25 kV, T_s: RT, t_g: 10 mins, I_b: 0.5 – 44 nA, $P_T = P_{TEOS}$ = 0.05 torr. Set was grown with tungsten filament forward for maximum electron flux. **Set 2:** FEBID, function of P_{TEOS}, V_0: 25 kV, t_g: 10 mins, I_b: 8.5 nA, $P_T = P_{TEOS}$: 0.02 – 0.16 torr. **Set 3:** EBID, function of beam diameter, V_0: 25 kV, t_g: 20.5 mins, I_b: 3.5 nA, $P_T = P_{TEOS}$ = 0.05 torr, beam diameters: range of focal point to substrate distances ($\Delta d_{f\text{-}s}$): 0 – 0.3 mm. **Set 4:** EBID, function of beam diameter, V_0: 25 kV, t_g: 20.5 mins, I_b: 3.5 nA, $P_T = P_{TEOS}$ = 0.05 torr, $\Delta d_{f\text{-}s}$: 0 – 0.35 mm.

Electron Beam Current (I_b)

The affect of this parameter has been discussed in other chapters already. Most tungsten filament SEM's have an adjustable parameter called the "spot size" which affects the amount of current that is allowed through the final aperture of the SEM column. Increasing the spot size increases the beam current in an exponential fashion and increases the minimum beam diameter which can be achieved. The important thing to consider is that using a standard SEM for the study of EBIED, the user does not have a high level of control over the most important EBIED parameter: the electron flux. The spot size (ss) can be changed to increase beam current (I_b) yet the e^- flux will be increased or decreased depending upon the minimum beam diameter that can be achieved by the electron optics of the system.

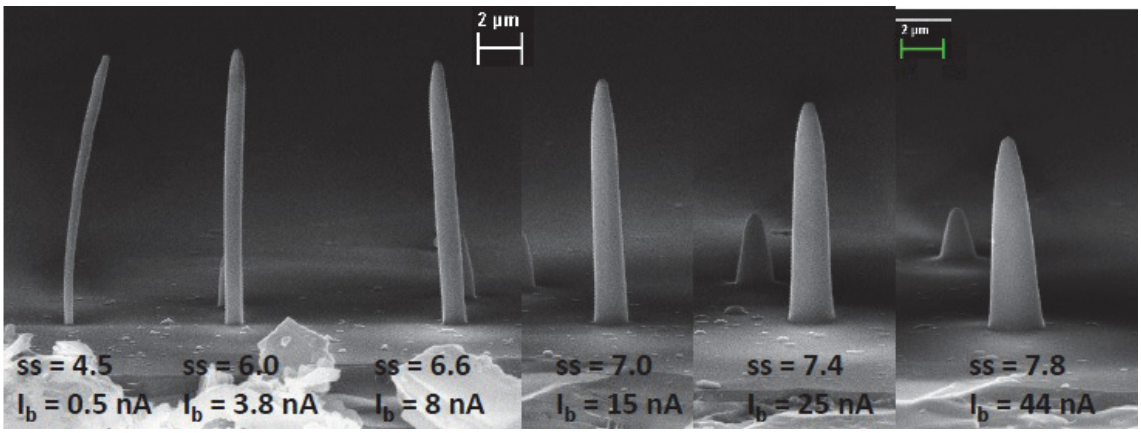

Figure AII.1: *Composite SEM image of set 1 grown with increasing ss. Refocused after each ss change to acheive minimum beam diameter at each beam current. All images are at approximately equal magnification thus relative sizes are shown.*

For deposition of the set shown above in figure A.1, the filament position in the Wehnelt emitter housing was adjusted to achieve maximum electron flux. The filament position can be adjusted to achieve a higher electron flux but the lifetime of the filament is significantly reduced. A tungsten filament may last < 20 hours when operating at the maximum electron flux. A typical filament can last > 200 hours when operating at optimum conditions. Furthermore, venting of the chamber and column will be necessary to make the adjustment. Adjusting the ss and/or the beam diameter (by changing focal point to substrate distance) are the only reliable methods of controlling the electron flux.

The observed trend in TEOS FEBID pillar geometry evolution with ss/I_b shown in figure A.1 is the typical case. Aspect ratio of pillars decreases as ss/I_b is increased. The height decreases with increasing ss/I_b as the beam width increases and diffusing molecules are less and less able to contribute to the vertical growth. Molecules diffusing up the sidewalls of an EBID pillar will be likely to reach the tip and contribute to the vertical growth if the electron flux from the sidewalls is low. As I_b is increased, e^- flux from pillar sidewalls is increased and consumes more diffusing molecules. This effect is more significant for this effect as I_b reaches very high levels. The deposits are seen to move further towards cone geometry with increasing I_b. All EBID growth is likely in the MTL regime for the last pillar at 44 nA. Since the growth is at a maximum at all points along the pillar the cone geometry will result.

Precursor Pressure (P_{TEOS})

Increasing the precursor pressure generally has the opposite effect to increasing the beam current. EBID growth will move further towards the EL regime. Aspect ratio of pillars will increase. If growth begins in MTL regime at low pressure, growth rate will increase, reach a maximum and decrease slightly. The growth rate will decrease slightly as depletion becomes minimal and precursor supply due to diffusion becomes negligible as EL regime is approached. Increasing the pressure further after EL regime growth is achieved will have minimal effect. The trend is nicely illustrated by set 2 shown below.

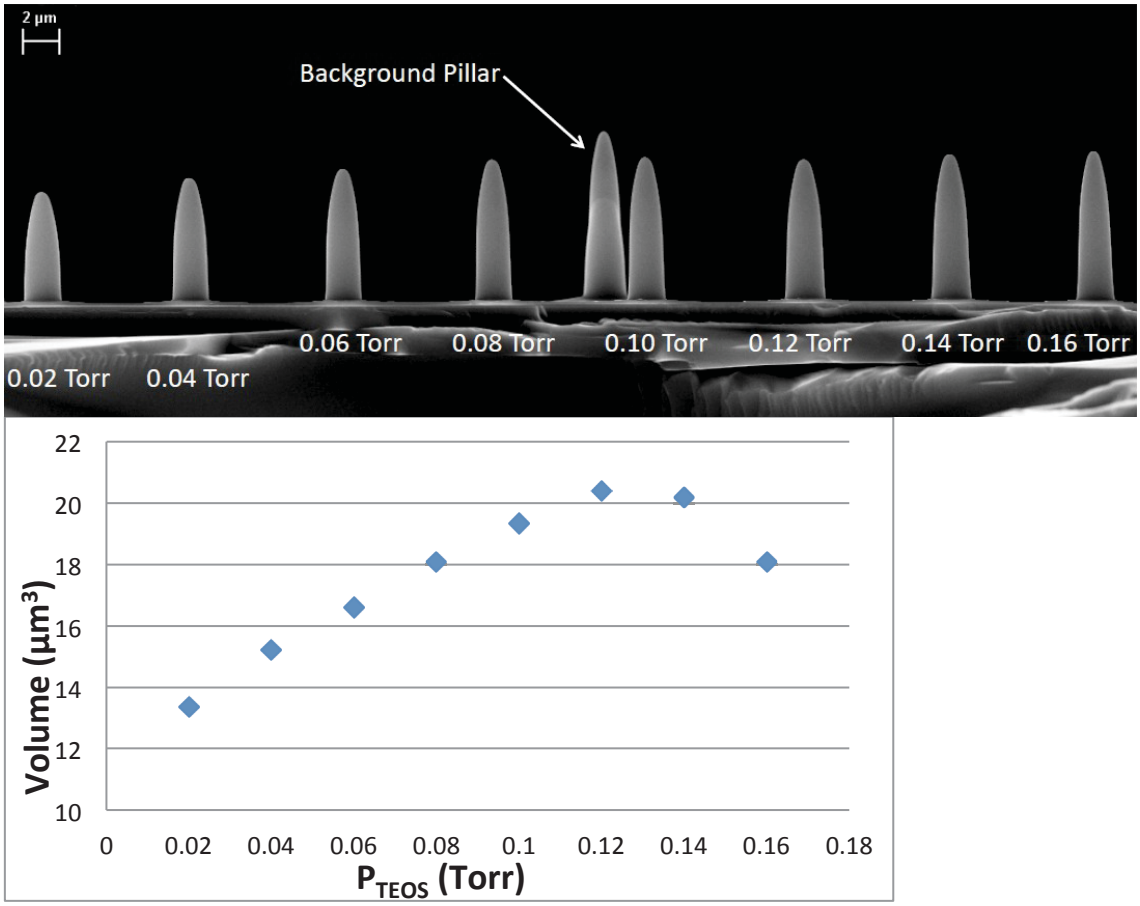

Figure AII.2: *SEM image and volume vs P_{TEOS} for set 2. Set was grown (from left to right) with increasing P_{TEOS}.*

The volumetric growth rate trend displayed in figure A.2 above indicates that diffusion is a significant precursor supply mechanism for TEOS EBID at lower pressures and higher electron fluxes. The behaviour is predicted by the standard EBID model.

Diffusion is highest in the MTL regime and becomes negligible as the EL regime is approached. The precursor flux from gas phase will be increasing with pressure yet precursor flux from diffusion decreases as the adsorbate gradient into the irradiation region decreases. The magnitude of this growth rate decrease would be expected to decrease with decreasing T_s as diffusivity of molecules is decreased. Conversely it would be expected to increase with T_s.

Acceleration Voltage (V_0)

Growth rates of EBID processes generally increase with decreasing V_0. The peak energy of BSE and SE emission from a substrate/EBID deposit shifts to lower energy with decreasing V_0. This results in a greater proportion of electrons which have a higher cross section for dissociation of precursor molecules. Lower V_0 is desirable for achieving high growth rates and less delocalised EBID. A drawback to this is that beam diameters generally increase with decreasing V_0 due to limitations of electron optics systems. Such is the case for the instrument used in this project. I_b also decreases with V_0. 25 kV was chosen as the main V_0 to use for this project as it allowed small beam diameters and high electron fluxes.

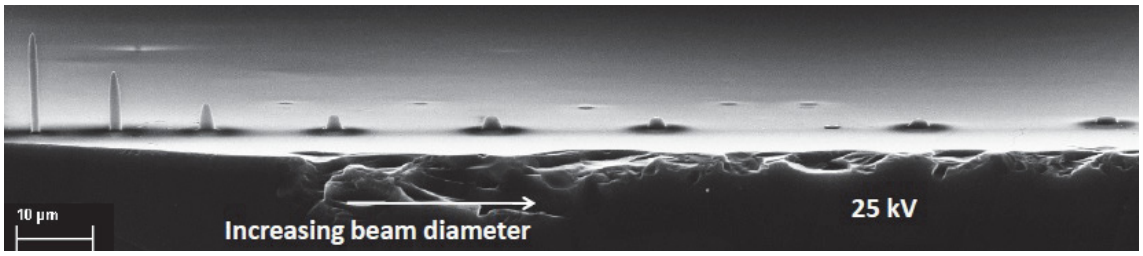

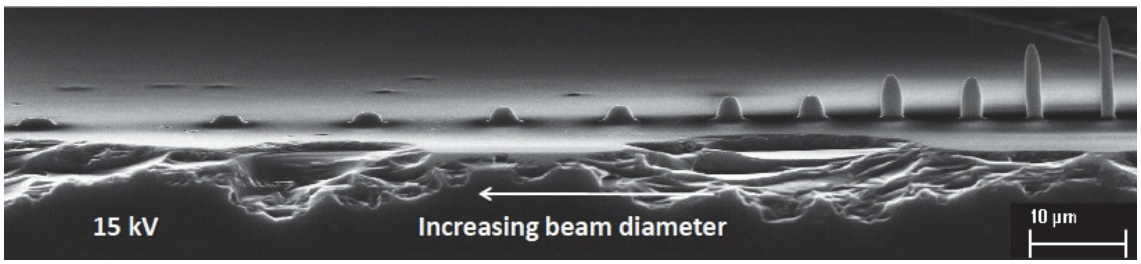

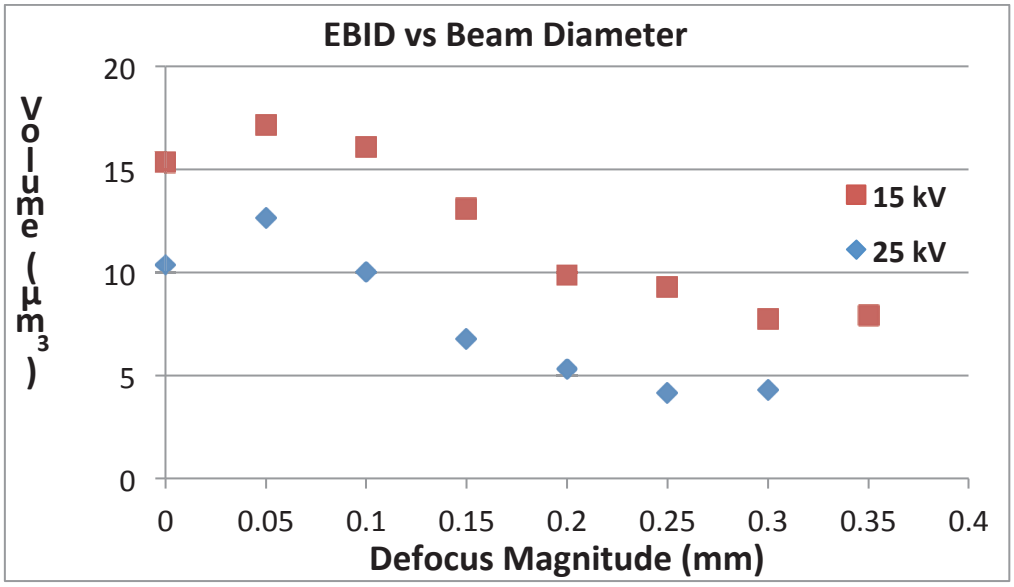

Figure AII.3: *SEM images and volume vs beam diameter (defocus magnitude) for set 3 and 4 (grown with same total I_b). Sets display the typical trend with increasing beam diameter and the growth rate at 15 kV is higher than at 25 kV. 15 kV set has several deposits at the same defocus as deposits were repeated due to artifacts in their I_e curves.*

Deposit Shape Evolution with V_0

FEBID deposits grown with increasing V_0 display a characteristic shape evolution. FEBID pillars generally display a cylindrical geometry with a conical tip. The base of the tip generally coincides with the extent of the interaction volume of the electron beam inside the FEBID pillar. A notable exception is the case presented by the deposit grown with I_b = 44 nA in figure A.1 above. The growth continues below the tip region due to BSE's scattered back into the base of the pillar from the substrate. Growth from electrons like these is generally negligible but with the extreme beam current used, growth from all electron species becomes significant. I shall refer to the general FEBID pillar growth regions as the body (cylindrical region) and tip (approximately conical region) as outlined in figure A.4 below.

Tips of pillars become increasingly sharp with increasing V_0 as is seen in figure A.5 below. The height of the tip region also increases with V_0. This is due to the shape and size of the electron beam interaction volume inside the FEBID pillar. Electrons of lower energy have a higher chance of being scattered at higher angles resulting in an

interaction volume with a more rounded top for lower kV. High energy electrons penetrate through with minimal change in direction giving a sharp top to the

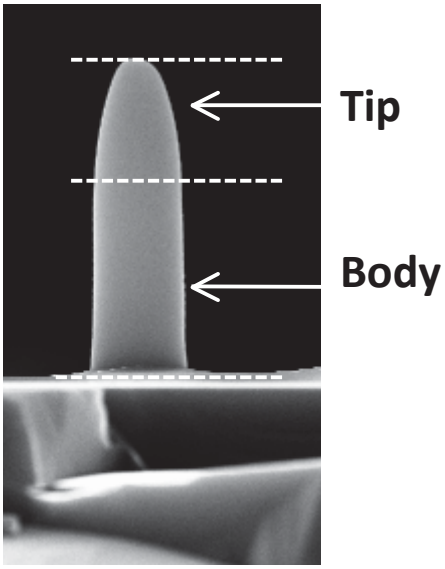

Figure AII.4: *Growth regions of a standard FEBID pillar.*

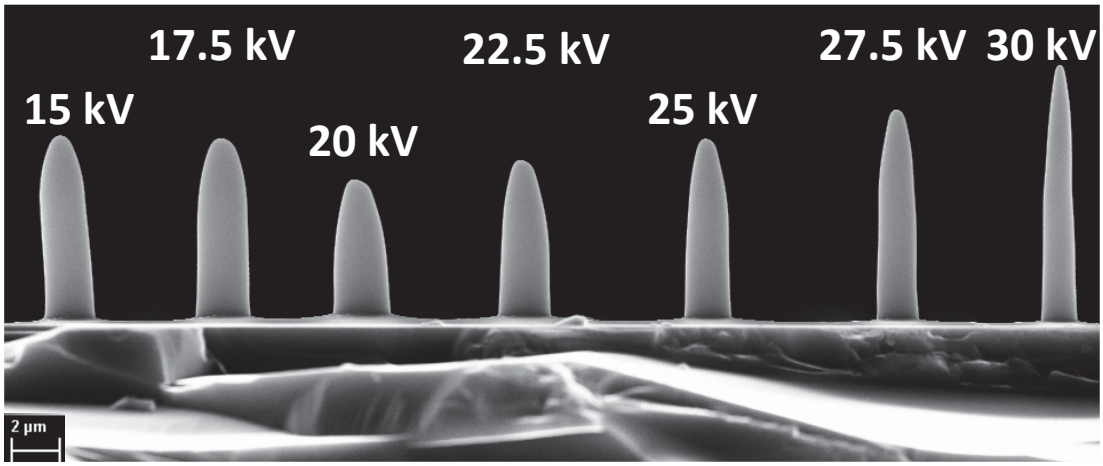

Figure AII.5: *SEM image of set 5 grown as a function of V_0. The ss was adjusted at each V_0 to achieve a constant I_b. The beam diameter will be increasing with decreasing V_0 due to increasing ss and natural effect of decreasing V_0. The set illustrates the evolution of FEBID pillar geometry with V_0 quite nicely.*

interaction volume. The pillars reflect the shape of the interaction volume of the electron beam used for deposition. The height of the tip region decreases with decreasing V_0 due to the decreasing penetration range of the interaction volume. In summary, V_0 can be chosen to achieve a particular FEBID pillar geometry although it is not recommended to alter V_0 and make quantitative comparison as it changes many parameters for EBID.

Bibliography

[1] L. Stewart, R., “Insulating films formed under electron and ion bombardment,” *Physical Review*, vol. 45, p. 488, 1934.

[2] R. W. Christy, “Formation of Thin Polymer Films by Electron Bombardment,” *Journal of Applied Physics*, vol. 31, no. 9, p. 1680, 1960.

[3] A. G. Baker and W. C. Morris, “Deposition of Metallic Films by Electron Impact Decomposition of Organometallic Vapors,” *Review of Scientific Instruments*, vol. 32, p. 458, 1961.

[4] B. H. Chin and G. Ehrlich, “Formation of silicon nitride structures by direct electron beam writing,” *Applied Physics Letters*, vol. 38, no. 2012, p. 253, 2011.

[5] S. Matsui and M. Mito, “Si deposition by electron beam induced surface reaction”, *Applied Physics Letters*, vol. 53, p. 1492, 1988.

[6] S. Lipp et al., “Tetramethoxysilane as a precursor for focused ion beam and electron beam assisted insulator (SiO_x) deposition,” *Journal of Vacuum Science & Technology B*, vol. 14, no. 6, p. 3920, Nov. 1996.

[7] W. J. Mitchell and E. L. Hu, “Selective area chemical vapor deposition of titanium oxide films: Characterization of $Ti(OC_3H_7)_4$ as an electron beam resist,” *Journal of Vacuum Science & Technology B*, vol. 17, pp. 1622-1626, 1999.

[8] V. Scheuer, H. W. P. Koops, and T. Tschudi, “Electron Beam Decomposition of Carbonyls On Silicon,” *Microelectronic Engineering*, vol. 5, pp. 423-430, 1986.

[9] F. Banhart, “LAPLACIAN GROWTH OF AMORPHOUS-CARBON FILAMENTS IN A NON-DIFFUSION-LIMITED EXPERIMENT”, *Physical Review E*, vol. 52, no. 5, p. 5156, 1995.

[10] M. Waiblinger et al., “e-beam induced EUV photomask repair – a perfect match.”. Carl Zeiss SMS GmbH, promotional material, www.zeiss.com.

[11] K. Edinger et al., “Electron-beam-based photomask repair,” *Journal of Vacuum Science & Technology B*, vol. 22, no. 6, p. 2902, 2004.

[12] S. Lipp et al., “A COMPARISON OF FOCUSED ION BEAM AND ELECTRON BEAM INDUCED DEPOSITION PROCESSES,” *Microelectronics Reliability*, vol. 36, no. 11, pp. 1779-1782, 1996.

[13] K. Murakami and M. Takai, “Characteristics of nano electron source fabricated using beam assisted process,” *Journal of Vacuum Science & Technology B*, vol. 22, no. 3, p. 1266, 2004.

[14] T. Tsuda, S. Seino, and S. Kuwabata, “Gold nanoparticles prepared with a room-temperature ionic liquid-radiation irradiation method”, *Chemical communications (Cambridge, England)*, Vol. 44, p6792, Nov. 2009.

[15] H. W. P. Koops and M. Weber, “Tips for scanning tunneling microscopy produced by electron-beam-induced deposition,” *Ultramicroscopy*, vol. 42-44, pp. 1519-1525, 1992.

[16] K. Mølhave et al., “Solid Gold Nanostructures Fabricated by Electron Beam Deposition”, *Nano Letters*, vol. 3, no. 11, pp. 1499-1503, Nov. 2003.

[17] D. J. Burbridge, S. Crampin, G. Viau, and S. N. Gordeev, “Selected immobilization of individual nanoparticles by spot-exposure electron-beam-induced deposition”, *Nanotechnology*, vol. 21, no. 4, p. 045302, Jan. 2010.

[18] K. T. KOHLMANN, “E-BEAM INDUCED X-RAY MASK REPAIR WITH OPTIMIZED GAS NOZZLE GEOMETRY”, *Microelectronic Engineering*, vol. 13, pp. 279-282, 1991.

[19] B. L. Thiel, “Imaging and Microanalysis in Environmental Scanning Electron Microscopy”, *Microchimica Acta*, vol. 155, pp. 39-44, 2006.

[20] S. Randolph, J. Fowlkes, and P. Rack, “Focused, Nanoscale Electron-Beam-Induced Deposition and Etching”, *Critical Reviews in Solid State and Material Sciences*, vol. 31, no. 3, pp. 55-89, Sep. 2006.

[21] H. W. P. Koops, “High-resolution electron-beam induced deposition,” *Journal of Vacuum Science & Technology B*, vol. 6, no. 1, p. 477, Jan. 1988.

[22] P. A. Crozier, “Synthesis of uniform GaN quantum dot arrays via electron nanolithography,” *Applied Physics Letters*, vol. 84, no. 18, p. 3441, 2004.

[23] C. W. Hagen and P. Kruit, “Direct fabrication of nanowires in an electron microscope,” *Applied Physics Letters*, vol. 82, no. 20, pp. 3514-3517, 2003.

[24] S. Rubel, M. Trochet, E. E. Ehrichs, W. F. Smith, and A. L. D. Lozanne, “Nanofabrication and rapid imaging with a scanning tunneling microscope,” *Journal of Vacuum Science & Technology B*, vol. 12, pp. 1894-1897, 1994.

[25] X. Yang and M. L. Simpson, “Integrated tungsten nanofiber field emission cathodes selectively grown by nanoscale electron beam-induced deposition”, *Applied Physics Letters*, vol. 86, p. 183106, 2005.

[26] J. D. Fowlkes, S. J. Randolph, and P. D. Rack, “Growth and simulation of high-aspect ratio nanopillars by primary and secondary electron-induced deposition,” *Journal of Vacuum Science & Technology B*, vol. 23, no. 6, p. 2825, 2005.

[27] W. White, K. Rykaczewski, and A. Fedorov, “What Controls Deposition Rate in Electron-Beam Chemical Vapor Deposition?”, *Physical Review Letters*, vol. 97, no. 8, pp. 3-6, Aug. 2006.

[28] W. L. Morgan, “Electron collision cross sections for tetraethoxysilane,” *Journal of Applied Physics*, vol. 92, no. 3, p. 1663, 2002.

[29] H. Dietrich, P. Geng, K. Jacobi, and G. Ertl, “Sticking coefficient for dissociative adsorption of N_2 on Ru single crystal surfaces”, *Journal of Chemical Physics*, vol. 104, p. 375, 1996.

[30] J. Fowlkes and P. Rack, “Fundamental Electron-Precursor-Solid Interactions Derived from Time-Dependant Electron-Beam-Induced Deposition Simulations and Experiments,” *ACS Nano*, vol. 4, no. 3, pp. 1619-1629, 2010.

[31] K. Kanaya and S. Okayama, “Penetration and energy-loss theory of electrons in solid targets,” *Journal of Physics D: Applied Physics*, vol. 5, no. 1, pp. 43-58, Jan. 1972.

[32] T. R. Groves, “Theory of beam-induced substrate heating,” *Journal of Vacuum Science & Technology B*, vol. 14, no. May, pp. 3839-3844, 1996.

[33] G. Hochleitner, H. D. Wanzenboeck, and E. Bertagnolli, “Electron beam induced deposition of iron nanostructures,” *Journal of Vacuum Science & Technology B*, vol. 26, no. 3, p. 939, 2008.

[34] P. Roy, R. Lynch, and P. Schmuki, “Electron beam induced in-vacuo Ag deposition on TiO_2 from ionic liquids,” *Electrochemistry Communications*, vol. 11, no. 8, pp. 1567-1570, Aug. 2009.

[35] P. C. Hoyle, J. R. A. Cleaver, and H. Ahmed, “Ultralow-energy focused electron beam induced deposition,” *Applied Physics Letters,* vol. 64, no. 11, pp. 1448-1450, 1994.

[36] H. W. P. Koops, A. Kaya, and M. Weber, “Fabrication and characterization of platinum nanocrystalline material grown by electron-beam induced deposition,” *Journal of Vacuum Science & Technology A*, vol. 13, no. June, pp. 2400-2403, 1995.

[37] N. Mason, “Cross Sections for Electron Collisions with Water Molecules,” *Journal of Physical Chemistry Reference Data*, vol. 34, no. 1, pp. 1-22, 2005.

[38] H. Sugai and H. Toyoda, “Measurements of Electron-Impact-Dissociation Cross Section for Neutral Products,” *AIP Conference Proceedings*, vol. 500, pp. 349-358, 2000.

[39] W. L. Morgan, “A Critical Evaluation of Low-Energy Electron Impact Cross Sections for Plasma Processing Modelling”, *Plasma Chemistry and Plasma Processing*, vol. 12, no. 4, pp. 477-493, 1992.

[40] I. Utke, S. Moshkalev, P. Russell, "Nanofabrication Using Focused Ion and Electron Beams: Principles and Applications (Oxford Series in Nanomanufacturing), Oxford University Press, USA (May 1, 2012), Hardcover, 840 pages.

[41] R. Ghez, "Diffusion Phenomena: Cases and Studies", Springer; 1 edition (July 1, 2001), Hardcover, 328 Pages.

[42] M. Toth, C. J. Lobo, G. Hartigan, and W. Ralph Knowles, “Electron flux controlled switching between electron beam induced etching and deposition,” *Journal of Applied Physics*, vol. 101, no. 5, p. 054309, 2007.

[43] C. J. Lobo, M. Toth, R. Wagner, B. L. Thiel, and M. Lysaght, “High resolution radially symmetric nanostructures from simultaneous electron beam induced etching and deposition,” *Nanotechnology*, vol. 19, no. 2, p. 025303, Jan. 2008.

[44] A. Botman, J. J. L. Mulders, and C. W. Hagen, “Creating pure nanostructures from electron-beam-induced deposition using purification techniques: a technology perspective.,” *Nanotechnology*, vol. 20, no. 37, p. 372001, Sep. 2009.

[45] K. Mølhave et al., “Solid Gold Nanostructures Fabricated by Electron Beam Deposition”, *Nano Letters*, vol. 3, no. 11, pp. 1499-1503, Nov. 2003.

[46] J. Li, M. Toth, V. Tileli, K. a Dunn, C. J. Lobo, and B. L. Thiel, “Evolution of the nanostructure of deposits grown by electron beam induced deposition,” *Applied Physics Letters*, vol. 93, no. 2, p. 023130, 2008.

[47] K. Landheer et al., “Low-Energy Electron-Induced Decomposition and Reactions of Adsorbed Tetrakis (trifluorophosphine) platinum [Pt $(PF_3)_4$]”, *The Journal of Physical Chemistry C*, vol. 115, pp. 17452-17463, 2011.

[48] A. Perentes and P. Hoffmann, “Focused Electron Beam Induced Deposition of Si-Based Materials From SiO_xC_y to Stoichiometric SiO_2: Chemical Compositions, Chemical-Etch Rates, and Deep Ultraviolet Optical Transmissions,” *Chemical Vapor Deposition*, vol. 13, no. 4, pp. 176-184, Apr. 2007.

[49] N. Silvis-Cividjian, C. W. Hagen, and P. Kruit, “Spatial resolution limits in electron-beam-induced deposition,” *Journal of Applied Physics*, vol. 98, no. 8, p. 084905, 2005.

[50] L. R. Baylor et al., *Progress in Field Emitter Sources for Digital Electrostatic E-beam Array Lithography*", Oak Ridge National Laboratory, Promotional Material.

[51] L. R. Baylor, W. L. Gardner, X. Yang, R. J. Kasica, M. A. Guillorn, and B. Blalock, "Initial lithography results from the digital electrostatic e-beam array lithography concept," *Journal of Vacuum Science & Technology B*, vol. 22, no. 6, pp. 3021-3024, 2004.

[52] A. Botman, M. Hesselberth, and J. J. L. Mulders, "Improving the conductivity of platinum-containing nano-structures created by electron-beam-induced deposition," *Microelectronic Engineering*, vol. 85, no. 5-6, pp. 1139-1142, May. 2008.

[53] J. J. L. Mulders, L. M. Belova, and a Riazanova, "Electron beam induced deposition at elevated temperatures: compositional changes and purity improvement", *Nanotechnology*, vol. 22, no. 5, p. 055302, Feb. 2011.

[54] E. Unger and K. Michael, "Making electrical contact to single molecules," *Nanotechnology*, vol. 9, p. 177, 1998.

[55] D. J. Burbridge, S. Crampin, G. Viau, and S. N. Gordeev, "Selected immobilization of individual nanoparticles by spot-exposure electron-beam-induced deposition.," *Nanotechnology*, vol. 21, no. 4, p. 045302, Jan. 2010.

[56] L. M. Belova, E. D. Dahlberg, A. Riazanova, J. J. L. Mulders, C. Christophersen, and J. Eckert, "Rapid electron beam assisted patterning of pure cobalt at elevated temperatures via seeded growth.," *Nanotechnology*, vol. 22, no. 14, p. 145305, 08-Apr-2011.

[57] A. Perentes, "Focused electron beam induced deposition of a periodic transparent nano-optic pattern," *Microelectronic Engineering*, vol. 73-74, pp. 412-416, Jun. 2004.

[58] J. D. Fowlkes, M. J. Doktycz, and P. D. Rack, "An optimized nanoparticle separator enabled by electron beam induced deposition", *Nanotechnology*, vol. 21, no. 16, p. 165303, Apr. 2010.

[59] H. Ximen and P. E. Russel, "Microfabrication of AFM tips using focused ion and electron beam techniques," *Ultramicroscopy*, vol. 42-44, pp. 1526-1532, 1992.

[60] W. F. van Dorp and C. W. Hagen, "A critical literature review of focused electron beam induced deposition," *Journal of Applied Physics*, vol. 104, no. 8, p. 081301, 2008.

[61] X. Yang and M. L. Simpson, "Integrated tungsten nanofiber field emission cathodes selectively grown by nanoscale electron beam-induced deposition", *Applied Physics Letters*, vol. 86, p. 183106, 2005.

[62] K. Murakami and M. Takai, “Characteristics of nano electron source fabricated using beam assisted process”, *Journal of Vacuum Science & Technology B*, vol. 22, no. 3, p. 1266, 2004.

[63] A. C. Adams and C. D. Capio, “The Deposition of Silicon Dioxide Films at Reduced Pressure”, *Journal of the Electrochemical Society*, vol. 126, no. 6, pp. 1042-1046, 1976.

[64] J. Spitzmüller, J. Braun, H. Rauscher, and R. J. Behm, “Thermal decomposition of tetraethoxysilane (TEOS) on Si(111)-(7×7),” *Applied Physics A: Materials Science & Processing*, vol. 66, no. 7, p. S1021-S1024, Mar. 1998.

[65] J. E. Crowell, L. L. Tedder, and F. M. Cascarano, “THE CHEMICAL VAPOR DEPOSITION OF $Si0_2$ FROM TEOS,” *Journal of Electron Spectroscopy and Related Phenomena*, vol. 54/55, pp. 1097-1104, 1990.

[66] A. Granier, C. Vallée, A. Goullet, K. Aumaille, and G. Turban, “Experimental investigation of the respective roles of oxygen atoms and electrons in the deposition of SiO_2 in O_2/TEOS helicon plasmas,” *Journal of Vacuum Science & Technology A*, vol. 17, no. 5, p. 2470, 1999.

[67] A. M. Svetlichnyi, V. V. Polyakov, and Y. N. Varzarev, “The Formation of Silicon Dioxide Films by TEOS Photochemical Decomposition,” *Russian Microelectronics*, vol. 30, no. 1, pp. 27-31, 2001.

[68] S. K. de Boer, W. F. van Dorp, and J. T. M. De Hosson, “Charging effects during focused electron beam induced deposition of silicon oxide,” *Journal of Vacuum Science & Technology B*, vol. 29, no. 6, p. 06FD01, 2011.

[69] T. Bret, I. Utke, A. Bachmann, and P. Hoffmann, “In situ control of the focused-electron-beam-induced deposition process,” *Applied Physics Letters*, vol. 83, no. 19, pp. 4005-4008, 2003.

[70] Educational material by Darrell Henry of Lousiana State University, http://serc.carleton.edu/research_education/geochemsheets/electroninteractions.html

[71] M. Tanaka et al., “Position- and size-controlled fabrication of iron silicide nanorods by electron-beam-induced deposition using an ultrahigh-vacuum transmission electron microscope by electron-beam-induced deposition using an ultrahigh-vacuum,” *Applied Physics Letters*, vol. 86, p. 183104, 2005.

[72] H. W. P. Koops and M. Weber, “Conductive dots , wires , and supertips for field electron emitters produced by electron-beam induced deposition on samples having increased temperature,” *Journal of Vacuum Science & Technology B*, vol. 14, no. 6, pp. 4105-4109, 2000.

[73] L. L. Tedder, G. Lu, and J. E. Crowell, “Mechanistic studies of dielectric thin film growth by low pressure chemical vapor deposition: The reaction of tetraethoxysilane with SiO2 surfaces,” *Journal of Applied Physics*, vol. 69, no. 10, p. 7037, 1991.

[74] J. B. Danner, M. A. Rueter, and J. M. Vohs, “Pathways and Intermediates in the Reaction of Tetraethoxysilane on Si (100) -2X1,” *Langmuir*, vol. 9, pp. 455-459, 1993.

[75] J. Braun, H. Rauscher, and R. J. Behm, “Dissociative adsorption and site specificity in the initial stages of tetraethoxysilane (TEOS) interaction with Si (111) - (7 × 7),” *Surface Science*, vol. 400, pp. 356-366, 1998.

[76] L. Gamble and J. W. Rogers, “Adsorption and Reactions of TEOS on Clean and Water-Dosed Titanium Dioxide (110),” *Journal of the American Chemical Society*, vol. 115, no. 13, pp. 12096-12105, 1993.

[77] S. C. Deshmukh and E. S. Aydil, “Investigation of SiO2 plasma enhanced chemical vapor deposition through tetraethoxysilane using attenuated total reflection Fourier transform infrared spectroscopy,” *Journal of Vacuum Science and Technology A*, vol. 13, no. 5, pp. 2355-2367, 1995.

[78] I. Utke, P. Hoffmann, and J. Melngailis, “Gas-assisted focused electron beam and ion beam processing and fabrication,” *Journal of Vacuum Science & Technology B*, vol. 26, no. 4, p. 1197, 2008.

[79] G.C Bond - "Hetrogenous Principles and Applications", Clarendon Press 1974, Hardcover, 376 pages.

[80] Kimo M. Welch - " Capture Pumping Technology" 2001 Elsevier Science B.V, Hardcover, 361 pages.

[81] S. G. Brass and G. Ehrlich, “Activated Chemisorption: Internal Degrees of Freedom and Measured Activation Energies,” *Physical Review Letters*, vol. 57, no. 20, p. 2532, 1986.

[82] K. A. Fichthorn and R. A. Miron, “Thermal Desorption of Large Molecules from Solid Surfaces,” *Physical Review Letters*, vol. 89, no. 19, p. 196103, 2002.

[83] S. Wang, Y. Sun, Q. Wang, and J. M. White, “Electron-beam induced initial growth of platinum films using $Pt(PF_3)_4$”, *Journal of Vacuum Science & Technology B*, vol. 22, pp. 1803-1806, 2004.

[84] S. J. Randolph, J. D. Fowlkes, and P. D. Rack, “Effects of heat generation during electron-beam-induced deposition of nanostructures,” *Journal of Applied Physics*, vol. 97, no. 12, p. 124312, 2005.

[85] K. Rykaczewski, A. Marshall, W. B. White, and A. G. Fedorov, “Dynamic growth of carbon nanopillars and microrings in electron beam induced dissociation of residual hydrocarbons.,” *Ultramicroscopy*, vol. 108, no. 9, pp. 989-92, Aug. 2008.

[86] D. A. Smith, J. D. Fowlkes, and P. D. Rack, “Simulating the effects of surface diffusion on electron beam induced deposition via a three-dimensional Monte Carlo simulation,” *Nanotechnology*, vol. 19, p. 415704, 2008.

[87] A. Perentes and P. Hoffmann, “Oxygen assisted focused electron beam induced deposition of Si-containing materials: Growth dynamics,” *Journal of Vacuum Science & Technology B*, vol. 25, no. 6, p. 2233, 2007.

[88] M. R. Henry, S. Kim, K. Rykaczewski, and a G. Fedorov, “Inert gas jets for growth control in electron beam induced deposition,” *Applied Physics Letters*, vol. 98, no. 26, p. 263109, 2011.

[89] D. P. Fogarty, N. A. Kautz, and S. A. Kandel, “Collision-induced diffusion and vacancy migration in alkanethiol monolayers on Au (1 1 1),” *Surface Science*, vol. 601, pp. 2117-2124, 2007.

[90] M. Asscher and Y. Zeiri, “Surface Processes Induced by Collisions,” *Journal of Physical Chemistry B*, vol. 107, no. 29, pp. 6904-6919, 2003.

[91] S. Wickramanayaka and A. Matsumoto, “Remote Plasma SiO2 Deposition by Tetraethoxysilane with Chemically and Energetically Different Atomic Species,” *Japanese Journal of Applied Physics*, vol. 33, pp. 3520 - 3527, 1994.

[92] A. M. Wrobel and A. Walkiewicz-pietrzykowska, “Mechanism of Amorphous Silica Film Formation from Tetraethoxysilane in Atomic Oxygen-Induced Chemical Vapor Deposition”, *Journal of the Electrochemical Society*, vol. 145, no. 8, p. 2866, 1998.

[93] S. C. Deshmukh, E. S. Aydil, S. C. Deshmukh, and E. S. Aydil, “Lowtemperature plasma enhanced chemical vapor deposition of SiO_2”, *Applied Physics Letters*, vol. 65, no. May, p. 3185, 2012.

[94] C. Goletti, L. Moretti, W. Yian, G. Chiarotti, and S. Selci, “Activated chemisorption of oxygen on Si(111)-2 × 1,” *Surface Science*, vol. 356, pp. 68-74, 1996.

[95] P. C. Cosby, “Electron-impact dissociation of oxygen,” *Journal of Chemical Physics*, vol. 98, p. 9560, 1993.

[96] Y. C. Kim and M. Boudart, “Recombination of 0, N, and H Atoms on Silica: Kinetics and Mechanism,” *Langmuir*, vol. 7, pp. 2999-3005, 1991.

[97] D. A. Smith, P. D. Rack, J. D. Fowlkes, and T. Liang, “Understanding the growth mechanisms of electron beam induced deposition via a Monte - Carlo based , 3D growth simulation,” in *Nanotechnology, 2006. IEEE-NANO 2006. Sixth IEEE Conference on*, 2006, pp. 659-661.

[98] K. Mitsuishi and M. Shimojo, “Proximity Effect in Electron-Beam-Induced Deposition,” *Japanese Journal of Applied Physics*, vol. 45, no. 6, pp. 5517-5521, 2006.

[99] F. Banhart, “Laplacian growth of amorphous carbon filaments in a non-diffusion-limited experiment,” *Physical Review E*, vol. 52, no. 5, p. 5156, 1995.

[100] W. J. Mitchell and E. L. Hu, “High-resolution in situ electron beam patterning using Ti(OC3H7)4 as a negative-type resist,” *Journal of Vacuum Science & Technology B*, vol. 20, no. 2, p. 596, 2002.

[101] W. L. Morgan, “Electron collision cross sections for tetraethoxysilane”, *Journal of Applied Physics*, vol. 92, no. 3, p. 1663, 2002.